



# THE UNIVERSITY *of* EDINBURGH

This thesis has been submitted in fulfilment of the requirements for a postgraduate degree (e.g. PhD, MPhil, DClinPsychol) at the University of Edinburgh. Please note the following terms and conditions of use:

This work is protected by copyright and other intellectual property rights, which are retained by the thesis author, unless otherwise stated.

A copy can be downloaded for personal non-commercial research or study, without prior permission or charge.

This thesis cannot be reproduced or quoted extensively from without first obtaining permission in writing from the author.

The content must not be changed in any way or sold commercially in any format or medium without the formal permission of the author.

When referring to this work, full bibliographic details including the author, title, awarding institution and date of the thesis must be given.

---

# Interference Mitigation in LiFi Networks

---

*Zhihong Zeng*



A thesis submitted for the degree of Doctor of Philosophy.  
**The University of Edinburgh.**  
March 28, 2022

---

# Abstract

---

Due to the increasing demand for wireless data, the radio frequency (RF) spectrum has become a very limited resource. Alternative approaches are under investigation to support the future growth in data traffic and next-generation high-speed wireless communication systems. Techniques such as massive multiple-input multiple-output (MIMO), millimeter wave (mmWave) communications and light-fidelity (LiFi) are being explored. Among these technologies, LiFi is a novel bi-directional, high-speed and fully networked wireless communication technology. However, inter-cell interference (ICI) can significantly restrict the system performance of LiFi attocell networks. This thesis focuses on interference mitigation in LiFi attocell networks.

The angle diversity receiver (ADR) is one solution to address the issue of ICI as well as frequency reuse in LiFi attocell networks. With the property of high concentration gain and narrow field of view (FOV), the ADR is very beneficial for interference mitigation. However, the optimum structure of the ADR has not been investigated. This motivates us to propose the optimum structures for the ADRs in order to fully exploit the performance gain. The impact of random device orientation and diffuse link signal propagation are taken into consideration. The performance comparison between the select best combining (SBC) and maximum ratio combining (MRC) is carried out under different noise levels. In addition, the double source (DS) system, where each LiFi access point (AP) consists of two sources transmitting the same information signals but with opposite polarity, is proven to outperform the single source (SS) system under certain conditions.

Then, to overcome issues around ICI, random device orientation and link blockage, hybrid LiFi/WiFi networks (HLWNs) are considered. In this thesis, dynamic load balancing (LB) considering handover in HLWNs is studied. The orientation-based random waypoint (ORWP) mobility model is considered to provide a more realistic framework to evaluate the performance of HLWNs. Based on the low-pass filtering effect of the LiFi channel, we firstly propose an orthogonal frequency division multiple access (OFDMA)-based resource allocation (RA) method in LiFi systems. Also, an enhanced evolutionary game theory (EGT)-based LB scheme with handover in HLWNs is proposed.

Finally, due to the characteristic of high directivity and narrow beams, a vertical-cavity surface-emitting laser (VCSEL) array transmission system has been proposed to mitigate ICI. In order to support mobile users, two beam activation methods are proposed. The beam activation based on the corner-cube retroreflector (CCR) can achieve low power consumption and almost-zero delay, allowing real-time beam activation for high-speed users. The mechanism based on the omnidirectional transmitter (ODTx) is suitable for low-speed users and very robust to random orientation.

---

# Lay summary

---

The sixth-generation (6G) communication is required to support a variety of services such as the internet of things (IoT), augmented reality, virtual reality, video streaming and online gaming with extremely high data and low latency. However, the current sub-6 GHz band is congested, and lower-band communication is not enough to support high data rate transmission. Such a critical issue has motivated industrial and research communities to look for new solutions and even-higher frequency bands for communication. The presented work investigating the optical wireless communication (OWC) falls into this category.

By improving the spatial reuse of spectrum resources, cellular networks can achieve a higher spectral efficiency. Light-fidelity (LiFi) attocell networks use smaller cell sizes as the light beams from light-emitting diodes (LEDs) are intrinsically narrow. Thus, with the densely deployed optical access points (APs), the LiFi attocell network can achieve a better bandwidth reuse and a higher area spectral efficiency. However, inter-cell interference (ICI) in LiFi attocell networks significantly limits the system performance.

Many aspects need to be carefully studied in order to mitigate the ICI and realize the full potential of LiFi cellular networks. In this work, in order to improve the network performance, the angle diversity receiver (ADR), the hybrid LiFi/WiFi network (HLWN) as well as the vertical-cavity surface-emitting laser (VCSEL) array system are designed and investigated separately. Relying on the presented results, this study deepens the understanding of ICI, its influence on the network performance and the usefulness of the proposed interference mitigation methods.



---

## Declaration of originality

---

I hereby declare that the research recorded in this thesis and thesis itself have been composed solely by myself and that it has not been submitted, either in whole or in part, in any previous application for a degree. Except where otherwise acknowledged, the work presented is entirely my own.

Zhihong Zeng  
Edinburgh, UK  
September 2021

---

# Acknowledgments

---

First of all, I would like to offer my sincerest gratitude to my supervisor, Prof. Harald Haas. This research would not have been accomplished without his constant support and great guidance. Harald has been beyond a supervisor to me and I have learned a lot from him. I truly appreciate his patience and encouragement throughout my Ph.D studies.

I would like to give special thanks to my second supervisor, Dr. Majid Safari. Majid was also my supervisor during my undergraduate studies and is the one who guided me into the field of LiFi. My thanks also go to Ms Hannah Brown and Dr. Mohammad Dehghani Soltani for proof-reading this thesis and all my Ph.D publications. In addition, I would like to thank Dr. Hanaa Abumarshoud for proof-reading this thesis.

I wish to offer my sincere gratitude to my parents for encouraging me to be who I am. I could not accomplish this thesis without their unconditional love, help and support.

I would like to thank my friends and colleagues in Edinburgh, who have encouraged me throughout my academic experience and gave me precious memories. I am surely blessed to have met you all. Also, I would like to thank pureLiFi Ltd for providing the financial support necessary to support my Ph.D studies.

Finally, I would like to express my gratitude and love to my wife, Yuejun Wang, who I met during my undergraduate studies. Although, for the past four years, we have been separated from each other and living in different countries, I have always received her support that has allowed me to get through any difficulties.

---

# Contents

---

Lay summary . . . . .	iii
Declaration of originality . . . . .	iv
Acknowledgments . . . . .	v
Contents . . . . .	vi
List of figures . . . . .	ix
List of tables . . . . .	xi
Acronyms and abbreviations . . . . .	xii
Nomenclature . . . . .	xv
<b>1 Introduction . . . . .</b>	<b>1</b>
1.1 Motivation . . . . .	2
1.2 Contribution . . . . .	4
1.3 Thesis Layout . . . . .	6
1.4 Summary . . . . .	6
<b>2 Background . . . . .</b>	<b>9</b>
2.1 Introduction . . . . .	10
2.2 Optical Transmitter . . . . .	11
2.2.1 Light-emitting Diode . . . . .	11
2.2.2 Laser Diode . . . . .	12
2.3 Optical Receiver . . . . .	14
2.3.1 P-intrinsic-n Diode . . . . .	14
2.3.2 Avalanche Photodiode . . . . .	14
2.3.3 Single-photon Avalanche Diode . . . . .	14
2.3.4 Noise Analysis . . . . .	15
2.3.5 Concentrator . . . . .	16
2.3.6 Angle Diversity Receiver Structure . . . . .	17
2.3.7 Signal Combining Schemes for an Angle Diversity Receiver . . . . .	19
2.3.8 Receiver Bandwidth vs Photodiode Area . . . . .	20
2.4 Digital Modulation Techniques . . . . .	20
2.4.1 DCO-OFDM . . . . .	21
2.4.2 ACO-OFDM . . . . .	22
2.5 VLC Channel Model . . . . .	22
2.5.1 Line-of-sight Link . . . . .	23
2.5.2 Non-line-of-sight Link . . . . .	23
2.6 LiFi Attocell Networks . . . . .	25
2.6.1 Interference Mitigation . . . . .	25
2.6.2 Multiple Access Techniques . . . . .	26
2.7 User Orientation and Mobility . . . . .	27
2.7.1 Random Orientation Model . . . . .	27
2.7.2 Random Waypoint Mobility Model . . . . .	28
2.7.3 Orientation-based Random Waypoint Mobility Model . . . . .	28
2.8 Summary . . . . .	29

<b>3</b>	<b>Interference Mitigation using Optimized Angle Diversity Receiver in LiFi Cellular Network</b>	<b>31</b>
3.1	Introduction . . . . .	32
3.2	LiFi Cellular Network Model . . . . .	32
3.3	Visibility of an Angle Diversity Receiver . . . . .	35
3.4	The Optimum Field of View . . . . .	36
3.4.1	Optimization Problem . . . . .	36
3.4.2	Projection area of Angle Diversity Receiver on the Ceiling . . . . .	37
3.4.3	Lower Bound of Field of View . . . . .	39
3.5	Double Source Cell Configuration . . . . .	44
3.6	Results and Discussions . . . . .	46
3.6.1	Simulation Setups . . . . .	47
3.6.2	Importance of Reflection and Orientation . . . . .	47
3.6.3	Performance Analysis for Single Source cells . . . . .	48
3.6.4	Performance Analysis for Double Source cells . . . . .	52
3.7	Summary . . . . .	55
<b>4</b>	<b>Realistic Indoor Hybrid WiFi and OFDMA-Based LiFi Networks</b>	<b>57</b>
4.1	Introduction . . . . .	58
4.2	Hybrid LiFi/WiFi Network Model . . . . .	59
4.2.1	System Setup . . . . .	59
4.2.2	LiFi System . . . . .	61
4.2.3	WiFi System Model . . . . .	63
4.2.4	Handover . . . . .	65
4.3	Dynamic Load Balancing Scheme in Hybrid LiFi/WiFi Networks . . . . .	66
4.3.1	Resource Allocation in OFDMA LiFi Systems . . . . .	66
4.3.2	Proposed Evolutionary-game-theory-based Load Balancing Scheme . . . . .	68
4.3.3	Convergence Analysis of Proposed Scheme . . . . .	71
4.4	Performance Evaluation . . . . .	72
4.4.1	Simulation Setups . . . . .	72
4.4.2	Performance Analysis . . . . .	73
4.5	Summary . . . . .	79
<b>5</b>	<b>A VCSEL Array Transmission System with Novel Beam Activation Mechanisms</b>	<b>81</b>
5.1	Introduction . . . . .	82
5.2	Multi-beam System Setup . . . . .	83
5.3	Beam Activation . . . . .	85
5.3.1	Systems with a Corner-cube Retroreflector . . . . .	86
5.3.2	Systems with Omnidirectional Transmitter on the User Equipment . . . . .	89
5.4	System Level Analysis . . . . .	92
5.4.1	System with Single User . . . . .	92
5.4.2	System with Multiple Users . . . . .	94
5.5	Simulation Results . . . . .	95
5.6	Summary . . . . .	104
<b>6</b>	<b>Conclusions, Limitations and Future Research</b>	<b>105</b>
6.1	Summary and Conclusions . . . . .	106

6.2	Limitations and Future Research . . . . .	107
<b>A</b>	<b>Maximum Transmit Power Considering Eye Safety</b>	<b>109</b>
<b>B</b>	<b>Publications</b>	<b>111</b>
B.1	Journal Papers . . . . .	111
B.2	Conference Papers . . . . .	111
	<b>References</b>	<b>186</b>

---

## List of figures

---

2.1	A typical LiFi downlink transmission with commonly used front-end elements at the transmitter and receiver. . . . .	11
2.2	Geometrical representation of the elliptical Gaussian beam. . . . .	13
2.3	ADR structures. . . . .	18
2.4	Typical nonlinear transfer characteristic of an LED. . . . .	20
2.5	Downlink geometry of LOS light propagation in VLC. . . . .	23
2.6	Representation of random UE orientation. . . . .	27
3.1	The LiFi cellular network using the ADR as the receiver . . . . .	33
3.2	Projection area of PDs on the ceiling . . . . .	37
3.3	Projection area of PD on the $xy$ -plane . . . . .	39
3.4	Projection area of PR and TPR with different number of PDs. . . . .	40
3.5	Projection area of ADR in $xz$ -plane. . . . .	41
3.6	The geometrical representation of $\Psi_c$ , $\Theta_{PD}$ , $\Psi_{total}$ and $d_c$ in the spherical coordinate system. . . . .	42
3.7	DS cell configuration. . . . .	45
3.8	Comparisons among received optical power for LOS link, LOS + diffuse link up to order $L$ and infinite reflections in 2 different positions with different orientations. . . . .	47
3.9	The relationship between $\Psi_{c,min}$ and the number of PD, $N_{PD}$ , on an ADR for the SS system. . . . .	48
3.10	The performance comparison between PR and TPR configurations considering different Tx bandwidth in the SS system (MRC, $N_0 = 10^{-21}$ A <sup>2</sup> /Hz). . . . .	49
3.11	Rx bandwidth versus the number of PD, $N_{PD}$ . . . . .	50
3.12	The performance comparison between MRC and SBC for the SS (PR, $B_t=100$ MHz). . . . .	51
3.13	The relationship between $\Psi_{c,min}$ and the number of PD, $N_{PD}$ , on an ADR for the DS system. . . . .	52
3.14	The performance comparison between MRC and SBC in DS cells (PR, $N_0 = 10^{-22}$ A <sup>2</sup> /Hz, $B_t=100$ MHz). . . . .	53
3.15	The performance comparison between PR and TPR in DS cells (MRC, $N_0 = 10^{-21}$ A <sup>2</sup> /Hz). . . . .	54
3.16	The performance comparison between the DS and SS systems. . . . .	55
4.1	(a) Illustration of AP deployment in HLWN and (b) polar and azimuth orientation angle of LiFi Rx. . . . .	60
4.2	Illustration of CSMA/CA with DCA mechanism. . . . .	63
4.3	Average user data rate versus the iteration number. . . . .	72
4.4	Evaluation of average data rate with different 3 dB bandwidth in LiFi OFDMA network. A comparison between proportional fairness (PF) and max-min fairness (MF). ( $N_{UE} = 80$ , 16 LiFi APs and no WiFi AP considered) . . . . .	74

4.5	Evaluation of the system performance by using different LB and RA schemes in HLWN. ( $B_L = 300$ MHz, $f_0 = 30$ MHz, $\epsilon = 2$ , $\eta_{0,\text{HHO}} = 0.9$ , $\eta_{0,\text{VHO}} = 0.6$ and $N_{\text{UE}} = 200$ ) . . . . .	75
4.6	Evaluation of the effects of WiFi utilization ratio on the user data rate in HLWN ( $B_L = 300$ MHz, $f_0 = 30$ MHz, $\eta_{0,\text{HHO}} = 0.9$ , $\eta_{0,\text{VHO}} = 0.6$ and $N_{\text{UE}} = 200$ ) and a stand-alone WiFi network ( $N_{\text{UE}} = 40$ ). . . . .	76
4.7	Evaluation of average handover rate corresponding to user speed. (The EGT-based LB scheme is applied, $B_L = 300$ MHz, $f_0 = 30$ MHz, $\epsilon = 2$ , $\eta_{0,\text{HHO}} = 0.9$ , $\eta_{0,\text{VHO}} = 0.6$ and $N_{\text{UE}} = 200$ ) . . . . .	77
4.8	Evaluation of the effects of $\eta_{\text{HHO}}$ and $\eta_{\text{VHO}}$ on the user data rate. ( $B_L = 300$ MHz, $f_0 = 30$ MHz, $\epsilon = 2$ and $N_{\text{UE}} = 200$ ) . . . . .	78
5.1	The downlink geometry of a VCSEL array system. . . . .	84
5.2	Corner-Cube retroreflector. . . . .	86
5.3	The setup of the AP in the VCSEL array system using a CCR ( $N_{\text{beam}} = 9$ ). . . . .	87
5.4	Beam activation mechanism. . . . .	88
5.5	Localization using the ODTx. . . . .	90
5.6	The ANN structures . . . . .	91
5.7	The UE locations and received power matrix, $N_{\text{beam}} = 9$ . . . . .	96
5.8	The comparison of beam activation accuracy between the ODTx and the single-PD Tx for both orientation models (M1 and M2) with different number of hidden neurons. . . . .	97
5.9	The comparison of beam activation accuracy between the ODTx and the IS-based VLP system for different positioning error. . . . .	98
5.10	SNR distribution in a single user system. . . . .	99
5.11	Probability density function of the SNR for the central beam ( $\theta_{\text{FWHM}} = 4^\circ$ ). . . . .	100
5.12	Average data rate in a single user system. . . . .	101
5.13	Average data rate for the VCSEL array system with multiple users. ( $N_{\text{beam}} = 10 \times 10$ , $d_{\text{cell}} = 10$ cm). . . . .	102
5.14	Evaluation of system throughput and outage probability corresponding to user speed. ( $N_{\text{beam}} = 10 \times 10$ , $d_{\text{cell}} = 10$ cm, $\theta_{\text{FWHM}} = 4^\circ$ ), $N_{\text{UE}} = 5$ . . . . .	103
A.1	Maximum transmit power considering eye safety . . . . .	110

---

## List of tables

---

3.1	Parameters Lists [1] . . . . .	46
4.1	Modulation and Coding Table [2]. . . . .	62
4.2	Simulation Parameters . . . . .	73
5.1	APD parameters. [3] . . . . .	85
5.2	Parameters of beam activation mechanism. . . . .	89
5.3	Parameters in Zemax simulation . . . . .	95
A.1	Parameters for eye safety . . . . .	110



---

## Acronyms and abbreviations

---

6G	Sixth-generation
ACK	Acknowledgment
ACO-OFDM	Asymmetrically clipped optical orthogonal frequency division multiplex
ADC	Analog to digital converter
ADR	Angle diversity receiver
ADT	Angle diversity transmitter
ANN	Artificial neural network
AOA	Angle of arrival
AP	Access point
APD	Avalanche photodiode
APA	Access point assignment
AR	Autoregressive
ASE	Average spectral efficiency
AWGR	Arrayed waveguide grating router
BS-ILC	Beam-steered infrared light communication
CCR	Corner-cube retroreflector
CIR	Channel impulse response
CPC	Compound parabolic concentrator
CSI	Channel state information
CSMA/CA	Carrier sense multiple access with collision detection
CTS	Clear to send
CU	Central unit
DAC	Digital to analog converter
DC	Direct current
DCA	Downlink compensation access
DCO-OFDM	Direct current biased optical orthogonal frequency division multiplex
DD	Direct detection
DIFS	Distributed inter-frame space
DMT	Discrete multitone modulation
DS	Double source
DSP	Digital signal processor
EE	Evolutionary equilibrium
EGC	Equal gain combining
EGT	Evolutionary game theory
FDMA	Frequency division multiple access
FFR	Fractional frequency reuse
FFT	Fast Fourier transform
FOV	Field of view
FWHM	Full width at half maximum
HCPP	hard-core pointprocess
HHO	Horizontal handover

HLWN	Hybrid LiFi/WiFi Network
HT	Hard threshold
ICI	Inter-cell interference
IFFT	Inverse fast Fourier transform
INR	Interference to noise ratio
IoT	Internet of things
IR	Infrared
IS	Image sensor
ISI	Inter-symbol interference
IM	Intensity modulation
JT	Joint transmission
LB	Load balancing
LCD	Liquid crystal display
LD	Laser diode
LED	Light-emitting diode
LiFi	Light-Fidelity
LOS	Line-of-sight
LSSA	Least-squares spectral analysis
MAC	Medium access control
MEMS	Microelectromechanical systems
MF	Max-min fairness
MHP	Most hazardous position
MIMO	Multiple-input multiple-output
mmWave	Millimeter wave
MPE	Maximum permissible exposure
MRC	Maximum ratio combining
NLOS	Non-line-of-sight
ODTx	Omnidirectional transmitter
OFDM	Orthogonal frequency division multiplex
O-OFDM	Optical-OFDM
OOK	On-off keying
ORWP	Orientation-based random waypoint
OWC	Optical wireless communication
PAM	Pulse amplitude modulation
PD	Photodiode
PDF	Probability density function
PF	Proportional fairness
PIN	P-intrinsic-n
PIFS	Point inter-frame space
PPM	Pulse position modulation
PPP	Poisson point process
PR	Pyramid receiver
PSD	Power spectral density
PWM	Pulse width modulation
QoS	Quality of service
RA	Resource allocation
RAA	Random access point assignment

RB	Resource block
ReLU	Rectified linear unit
RF	Radio frequency
RFID	Radio frequency identification
RGB	Red-green-blue
RIN	Relative intensity noise
RP	Random process
RS	Reflected signal
RSS	Received signal strength
RTS	Request to send
RU	Resource unit
RWP	Random waypoint
Rx	Receiver
SBC	Select best combining
SDMA	Space division multiple access scheme
SLM	Spatial light modulation
SNR	Signal-to-noise ratio
SIFS	Short inter-frame space
SINR	Signal to interference-plus-noise ratio
SPAD	Single-photon avalanche diode
SS	Single source
SSS	Signal strength strategy
STA	Station
TDMA	Time division multiple access
TDOA	Time differential of arrival
TIA	Transimpedance amplifier
TPR	Truncated pyramid receiver
TS	Test signal
Tx	Transmitter
UE	User equipment
UWB	Ultra-wideband
VCSEL	Vertical-cavity surface-emitting laser
VHO	Vertical handover
VLC	Visible light communication
VLP	Visible light positioning
WiGig	Wireless gigabit alliance

---

# Nomenclature

---

$\langle \cdot, \cdot \rangle$	Inner product operator
$(\cdot)$	Dot product
$(\cdot)^T$	Transpose of vectors
$\ \cdot\ $	Norm operator
$\ln(\cdot)$	Natural logarithm
$\mathbb{E}[\cdot]$	The expectation operator
$(\cdot)^*$	Complex conjugate operator
$\alpha$	Index of a LiFi AP
$\alpha_s$	Index of the serving LiFi AP
$\alpha_i$	Index of the interfering LiFi AP
$\mathcal{A}$	The set of LiFi APs
$A_p$	Physical area of the PD
$A_{\text{eff}}$	Effective area of the APD
$B_L$	Baseband modulation bandwidth in the LiFi system
$C_{\text{max}}$	The maximum backoff stage
$C_r$	Capacitance of a PD
$C_T$	Capacitance of the APD
$d$	Distance between the Tx and Rx
$d_{\text{cell}}$	Side length of each cell
$d_0$	Distance from the Tx to the UE along the beam axis
$\mathbf{d}$	The distance vector between the LiFi AP and the UE
$D$	Displacement of input and output apertures
$D_{\mu, \alpha}$	LiFi data rate of user $\mu$
$f$	Frequency
$f_m$	Frequency of the subcarrier $m$
$f_0$	The 3 dB cut-off frequency of the front-end filtering effect
$F_A$	Excess noise factor
$g(\psi)$	Gain of the optical concentrator
$G_{\text{APD}}$	Gain of the APD
$\mathbf{G}_\rho$	Reflectivity matrix
$h$	The vertical distance between the Tx and the UE is denoted as
$H(f)$	Frequency response of the LiFi channel
$H_{\text{diffuse}}$	Diffuse DC channel gain
$H_F(f)$	Front-end device frequency response
$H_{\text{LOS}}$	LOS DC channel gain in a VLC system
$H_{\text{neg}}$	Channel gain between the negative source and the PD
$H_{\text{pos}}$	Channel gain between the positive source and the PD
$H_{\mu, \alpha}(f)$	Channel gain between user $\mu$
$\mathbf{H}$	Room-intrinsic transfer matrix
$I$	Index of the serving beam
$I_F$	Fairness index

$I_G$	Gaussian beam intensity
$\mathbf{I}$	The unity matrix
$k_A$	Dimensionless parameter
$k_B$	Boltzmann's constant
$k_{\mu,m}$	Number of RUs allocated to user $\mu$ on subcarrier $m$ in each RB
$K$	Number of subframes in the time domain
$L$	Length of the CCR
$L_{\text{Data}}$	Average data packet length
$L_p$	The PD thickness
$m$	Sequence number of OFDM subcarriers
$m_{\text{LED}}$	The Lambertian order of a LED
$m_{\text{wall}}$	The Lambertian order of the wall surface
$M$	The number of OFDM subcarriers
$\mathcal{M}_e$	The effective subcarrier set
$n$	Sequence number of a quasi state
$\hat{n}$	the index of narrow-beam Tx's in the VCSEL array system
$\mathbb{N}$	The set of natural numbers
$n_{\text{re}}$	Refractive index of the retroreflector
$n_{\text{ref}}$	Internal refractive index of the concentrator
$\mathbf{n}_{\text{PD}}$	Normal vector of the PD
$\mathbf{n}_{\text{tx}}$	Normal vector of the Tx
$\mathbf{n}_{\text{UE}}$	Normal vector of a UE
$N_0$	Noise power spectral density of the receiver
$N_{\text{beam}}$	the number of narrow-beam Tx's in the VCSEL array system
$N_E$	The number of small surface elements
$N_{\text{hidden}}$	Number of neurons in the hidden layer
$N_L$	Total number of LiFi APs
$N_{\text{UE}}$	Total number of UEs
$N_{\text{PD}}$	The total number of PDs on an ADR
$N_{\text{PR}}$	The number of PDs on a PR
$N_{\text{TPR}}$	The number of PDs on a TPR
$N_W$	The number of users served by the WiFi AP
$\tilde{N}_a$	Average number of active beams
$p$	Index of a PD on an ADR
$p_c$	Probability that a user transmits a data frame in a backoff counter time
$p_d$	Probability that a data frame is transmitted by the DCA
$p_s$	Probability of successful transmission
$p_t$	Probability that there is at least one transmission in a backoff unit time
$p_{\mu}^{<t>}$	Probability of mutation for user $\mu$
$p_v$	Probability of visibility of an ADR
$\mathbf{p}_c$	Critical point
$\mathbf{p}_{\text{cell}}$	Center of the VCSEL cell
$\mathbf{p}_{\text{tx}}$	Position of the Tx
$\mathbf{p}_{\text{UE}}$	Location of the UE
$P_{\text{elec}}$	The electrical power
$P_n$	Average ambient power
$P_{\text{tx,OD}}$	Transmitted optical power of a single infrared LED in the ODTx

$P_{\text{out}}$	Outage probability
$P_{\text{rx,opt}}$	The optical power of the received signal at the Rx
$P_{\text{tx}}$	Transmitted optical power of a LiFi AP
$P_{\text{tx,opt}}$	Transmitted optical power of a single VCSEL beam
$\mathcal{P}$	The set of PDs on an ADR
$q$	The electron charge
$q_{\mu,\alpha,m}$	Spectral efficiency of subcarrier $m$ for the user $\mu$ served by the LiFi AP $\alpha$
$r_{\text{cell}}$	Side length of a square cell
$r_{\text{I}}$	A measure of the noise level of the optical signal
$r_0$	Distance from the UE to the $z_{\text{beam}}$ -axis
$\mathbf{r}$	Receiver transfer vector
$R$	Radius of the service region of the central beam
$R_{\text{APD}}$	APD responsivity
$R_{\text{c}}$	Channel bit rate in the WiFi system
$R_{\text{F}}$	Feedback resistor of the transimpedance amplifier
$R_{\text{T}}$	Required threshold data rate
$R_{\mu,\text{wifi}}$	Downlink data rates for user $\mu$ in the WiFi cell
$\text{RIN}(f)$	Intensity noise spectrum
$\mathbf{R}$	Rotation matrix
$s_{\text{pos}}(t)$	Time domain signal of the positive source in a double source cell
$s_{\text{neg}}(t)$	Time domain signal of the negative source in a double source cell
$S_{\text{RIN}}$	PSD of the relative noise intensity for an APD
$S_{\text{shot}}$	PSD of the shot noise for an APD
$S_{\text{thermal}}$	PSD of thermal noise for an APD
$\mathcal{S}_{\mu}$	Strategy Set
$t$	The iteration
$t_{\text{c}}$	Average time that the channel is sensed to be busy because of a collision
$t_{\text{d}}$	Time duration for DCA.
$t_{\text{delay}}$	Delay time
$t_{\text{Data}}$	Average data transmission time
$t_{\text{f}}$	Duration of an empty slot time
$t_{\text{p}}$	Average transmission time of the frame payload
$t_{\text{p}}$	Propagation delay
$t_{\text{s}}$	Average time that the channel is sensed as busy as a successful transmission
$t_{\text{tot}}$	Total time required to complete the transmission of a packet
$t_{\text{ACK}}$	Time duration of ACK
$t_{\text{CTS}}$	Time duration of CTS
$t_{\text{DIFS}}$	Time duration of DIFS
$t_{\text{H}}$	Time duration of frame header
$t_{\text{PIFS}}$	Time duration of PIFS
$t_{\text{RTS}}$	Time duration of RTS
$t_{\text{SIFS}}$	Time duration of SIFS
$\mathbf{t}$	Transmitter transfer vector
$T$	Absolute temperature
$T_{\text{c},\theta}$	Coherence time of the RP for $\theta$
$T_{\text{L}}$	Coherence time of LiFi channels
$T_{\text{p}}$	The quasi-static period

$T_s$	Sampling time of the RP for $\theta$
$T_W$	Coherence time of WiFi channels
$T_s(\psi)$	Gain of the optical filter
$\mathcal{T}_{\text{eff}}$	The effective throughput
$\mu$	Index of a UE
$\mathcal{U}$	The set of users
$\mathcal{U}_\alpha$	The set of users served by the AP $\alpha$
$U_{\text{down}}$	The ratio of the downlink utilization and the total transmission time
$U_{\text{up}}$	The ratio of the uplink utilization and the total transmission time
$v_{\alpha,p}$	Visibility factor between the $p$ -th PD on the ADR and the $\alpha$ -th AP
$v_e$	Fitting coefficient
$v_s$	User movement speed
$v_{\text{Tx,Rx}}$	Visibility factor between the Tx and Rx
$V$	Visibility of the ADR
$w_p$	The combining weight of PD $p$
$W$	The VCSEL beam width
$W_{\text{AP}}$	The WiFi AP
$W_k(\cdot)$	Lambert W function
$W_0$	The VCSEL beam waist
$x_{\text{DC}}$	The DC bias
$x_i$	Achievable data rate of user $i$
$z_{\text{AP}}$	Height of the AP
$z_{\text{beam}}$	The beam axis
$z_{\text{UE}}$	Height of the UE
$Z_{\mu,m}$	Aggregate data rate from subcarries $m$ to $M/2$ for user $\mu$
$\beta$	Fairness coefficient
$\epsilon$	Utilization ratio of $U_{\text{down}}$ and $U_{\text{up}}$
$\epsilon_0$	Required utilization ratio
$\eta_{0,\text{HHO}}$	Average handover efficiency for HHO
$\eta_{0,\text{VHO}}$	Average handover efficiency for VHO
$\eta_{\text{H}}$	Estimated HHO efficiency
$\eta_{\text{V}}$	Estimated VHO efficiency
$\gamma$	SNR/SINR
$\kappa$	The ratio of DC optical power to the square root of electric signal power
$\lambda$	Operating wavelength of the VCSEL
$\lambda_m$	Lagrangian multiplier for the $m$ -th constraint
$\omega$	Azimuth angle
$\omega_{\text{PD}}$	Azimuth angle of a PD
$\omega_{\text{PD}}$	Azimuth angle of a UE
$\pi_{\mu,\alpha}$	Payoff function of user $\mu$ served by the AP $\alpha$
$\phi$	Irradiance angle of the Tx
$\Phi_{1/2}$	Half-intensity radiation angle of the LED
$\psi$	Incidence angle of the Rx
$\Psi_c$	FOV of the Rx
$\Psi_{c,\text{min}}$	The lower bound of the FOV of a Rx
$\Psi_{\text{total}}$	Total FOV of an ADR
$\rho$	Reflective coefficient

$\sigma_I^2$	Variance of power fluctuations
$\sigma_n^2$	The total noise power for a receiver
$\sigma_{\text{thermal}}^2$	Power of thermal noise
$\sigma_{\text{RIN}}^2$	Power of RIN
$\sigma_{\text{shot}}^2$	Power of shot noise
$\sigma_\theta$	Variance of $\theta$
$\tau$	Receiver's optical to electrical conversion efficiency
$\theta$	Polar angle
$\theta_{\text{beam}}$	Beam divergence of a VCSEL
$\theta_{\text{FWHM}}$	Angle for FWHM intensity points
$\theta_{\text{PD}}$	Elevation angle of a PD
$\theta_{\text{UE}}$	Elevation angle of a PD
$\Upsilon_{\mu,\text{wifi}}$	Uplink data rate for a WiFi user
$\varepsilon_0$	Permittivity of vacuum
$\varepsilon_r$	Relative permittivity of silicon
$\zeta$	Data rate
$\bar{\zeta}$	Average data rate
$\zeta_{\mu,\alpha}^{\text{Link}}$	Total LiFi link data rate of user $\mu$ served by the LiFi AP $\alpha$
$\zeta_{\mu,m}$	Communication link data rate of user $\mu$ on subcarrier $m$ for each subframe





---

# Chapter 1

## **Introduction**

---

## 1.1 Motivation

Due to the increasing demand for wireless data, the radio frequency (RF) spectrum has become a very limited resource. Alternative approaches are investigated to support the future growth in data traffic and next-generation high-speed wireless communication systems. Techniques such as massive multiple-input multiple-output (MIMO), millimeter wave (mmWave) communications and light-fidelity (LiFi) are being explored. Among these technologies, LiFi is a novel bi-directional, high-speed and fully networked wireless communication technology. A typical LiFi system uses off-the-shelf low-cost commercially available light-emitting diodes (LEDs) and photodiodes (PDs) as front end devices [4]. Intensity modulation (IM) is used to encode the information in visible light communication (VLC) since the LED is an incoherent optical source. Direct detection (DD) is adopted at the receiver (Rx) end. LiFi utilizes visible light as the downlink propagation medium to provide connectivity on top of the illumination functionality. It may use infrared (IR) light in the uplink in order to allow the illumination constraint of the room to be unaffected, and also to avoid interference with the visible light in the downlink [5]. The overall license-free bandwidth of visible light is more than 10,000 times greater than the whole RF spectrum [5]. Also, LiFi can provide enhanced security as the light does not penetrate through opaque objects [6]. In many large indoor environments, multiple light fixtures are installed and these luminaries can act as VLC access points (APs). A network consisting of multiple VLC APs is referred to as a LiFi attocell network [5]. Given the widespread use of LED lighting, a LiFi attocell network can use the existing lighting infrastructures to offer fully networked wireless connectivity. Moreover, LiFi attocells can be regarded as an additional network layer within the existing wireless networks because there is no interference to the RF counterparts, such as femtocell networks [5]. These benefits of LiFi have made it favorable for recent and future research.

By improving the spatial reuse of spectrum resources, cellular networks can achieve a higher area spectral efficiency [7]. In comparison with RF femtocell networks, LiFi attocell networks use smaller cell sizes as the light beams from LEDs are intrinsically narrow [8]. Thus, with the densely deployed optical APs, the LiFi attocell network can achieve a better bandwidth reuse and a higher area spectral efficiency. However, similar to other cellular systems, inter-cell interference (ICI) in LiFi attocell networks limits the system performance. This is because the signal transmitted to a user will interfere with other users who are receiving signals from the same frequency resource. Particularly, cell-edge users suffer from severe ICI. Despite the dense deployment of APs, due to ICI, LiFi may not provide uniform coverage concerning data rate. Interference coordination mechanisms have been extensively investigated for VLC systems [9–13]. The commonly used technique is static resource partitioning [9]. By separating any two cells that reuse the same frequency resource with a minimum reuse distance, ICI is effectively mitigated. However, there is a significant loss in spectral efficiency. A combined wavelength division and code division multiple access scheme was proposed in [10]. Although this approach enhances the system bandwidth, it requires separate filters for each color band and thus creates additional cost. In [11], the fractional frequency reuse (FFR) technique is proposed to mitigate ICI. The FFR scheme is a cost-effective approach to provide improvements both in cell-edge user performance and average spectral efficiency (ASE), but a low user-density will decrease the ASE significantly. Joint transmission (JT) has been proven to improve signal quality for cell-edge users [12]. The downside of the JT system is the extra signaling overhead. Moreover, the space division multiple access scheme (SDMA) scheme using angle diversity

transmitters (ADTs) proposed in [13] can mitigate ICI by generating concentrated beams to users at different locations.

Many aspects need to be carefully studied in order to mitigate the ICI and realize the full potential of LiFi cellular networks. In this study, we tried to reduce the interference from three aspects. One of these aspects is the Rx structure. A narrow field of view (FOV) and high optical gain can be achieved by using a PD in conjunction with a concentrator. Therefore, with careful design, the interference signal can be mitigated and the desired signal can be amplified. The second factor is the setup of APs. Combining LiFi with existing RF networks, the users who suffer severe ICI in a LiFi system can be assigned to a RF AP and achieve a better connection. Transmitter design is another important factor. Instead of using wide-spread beams emerging from illumination systems with visible light, narrow well-directed beams emerging from a dedicated source with infrared light can be adopted. In the following, these aspects are explained in more detail.

The angle diversity reception, first proposed in [14], allows the Rx to achieve a wide FOV and high optical gain simultaneously. An angle diversity receiver (ADR) is composed of multiple narrow-FOV PDs facing in different directions. In [15–22], the ADR is used to address the issue of ICI as well as frequency reuse in LiFi cellular systems, and different signal combining schemes are investigated. However, the proposed ADR structure is hard to implement and the optimum ADR design is not given. Moreover, the system is assumed to be interference limited instead of noise limited in [18], which is not always true as the ADR can mitigate most of the ICI and thus noise becomes the dominated factor. Recently, due to the lower channel correlation achieved from angle diversity schemes, ADRs are introduced to improve the performance of indoor MIMO-VLC systems. In addition, the pyramid receivers (PRs) are proposed [23]. The generalized structure of truncated pyramid receivers (TPRs) is given in [24] to reduce the signal to interference-plus-noise ratio (SINR) fluctuation. This motivates us to propose the optimum structures for the ADRs in order to fully exploit the performance gain.

With the use of novel optical devices, LiFi can potentially utilize more than 300 THz of the visible light spectrum, which is approximately 139,000 times greater than the 2.16 GHz wireless gigabit alliance (WiGig) channel in the IEEE 802.11ad standard [25]. Despite a wide variety of advantages provided by LiFi, the limitations of this technology should also be considered in order to develop feasible solutions. Link blockage is one factor that can affect LiFi performance significantly. Another limiting factor is ICI, which can significantly restrict the spectrum efficiency, especially for cell-edge users. An effective solution is to combine LiFi with existing RF networks, e.g. wireless fidelity (WiFi), to form a hybrid LiFi/WiFi network (HLWN) [26, 27]. Such a network cannot only achieve high data rates through LiFi, but can also provide ubiquitous coverage through WiFi in case of any link blockage within the optical channels or severe ICI. As LiFi uses a different spectrum from WiFi, there is no interference between LiFi and WiFi systems. Thus, the HLWN is able to offer a total system throughput greater than that of a stand-alone LiFi or WiFi network [27]. In order to explore the full potential of the HLWN system, we proposed an evolutionary game theory (EGT)-based load balancing (LB) scheme, which considers the effect of resource allocation, handover and random device orientation.

The VLC systems use wide-spread beams emerging from illumination systems. Due to the wide coverage of the LEDs, multiple user equipment (UE) may be served by the same LED

and may share the same resources, which may lead to traffic congestion when the load is high. In [13], an ADT which consists of multiple narrow-beam visible light LEDs has been proposed for optical wireless communication (OWC) networks with the SDMA. Multiple users at different locations can be served simultaneously by activating different LED elements on an ADT. The results show that SDMA schemes can mitigate ICI and thus can greatly increase the ASE. However, VLC systems require illumination to be switched-on, which may not always be desired and thus may increase the power consumption. Moreover, white LEDs, which are typically used for illumination, have limited bandwidth as they utilize blue LEDs with phosphor coating [28]. To solve the above limitations, the beam-steered infrared light communication (BS-ILC) system can be deployed. Due to the small cell coverage, it is more likely that each beam will only serve a single UE. Hence, capacity sharing among multiple UEs as well as traffic congestion can be avoided. Since narrow beams with high directivity can send a greater portion of the transmitted power to the corresponding UE, the BS-ILC systems provide better energy-efficiency. Moreover, the link can support higher capacity due to the high bandwidth of narrow beam sources. A vertical-cavity surface-emitting laser (VCSEL) transmission system is introduced in this study. Moreover, novel beam activation mechanisms are proposed to support high data rate, low latency and multiple UEs.

In this thesis, and in order to achieve the full potential of LiFi networks, the aforementioned aspects and challenges are discussed and effective solutions are provided. The detailed contributions of this research thesis are presented in the next section.

## **1.2 Contribution**

In this thesis, a LiFi network is considered and different interference mitigation are introduced. This thesis aims to address the following objectives:

- Reducing the ICI in LiFi networks by proposing optimized ADR structures.
- Focusing on system LB optimization in HLWNs so as to improve the performance of data rate and user fairness.
- Supporting high data rate, low latency and multiple UEs through the VCSEL array transmission system.

With respect to the first research objective, the structure of PRs and TPRs are studied. The projection area of ADRs is defined to differentiate from the coverage area of APs. Analytical expressions for the projection area of both PRs and TPRs are given. Based on the constraint set by the projection area of ADRs, the lower bound of FOV of PDs on an ADR is given for the single source (SS) system. The performance of PRs and TPRs are compared, and optimized ADR structures are proposed to fully exploit the performance gain of ADRs. In addition, the joint effect of the Rx and transmitter (Tx) bandwidth on the average data rate are analyzed. The performance comparison between the select best combining (SBC) and maximum ratio combining (MRC) are given regarding different levels of noise power spectral density. It is shown, for the first time, that under certain circumstances, the SBC can outperform the MRC. The double source (DS) cell system is considered to further mitigate the non-line-of-sight (NLOS) interference. The lower bound of FOV of PDs on an ADR is derived and the optimized

ADR structures are proposed for the DS system. By comparing the average SINR between the DS system and the SS system under different levels of noise power spectral density, we present that, in a noise-dominated scenario, the SS system should be applied, otherwise, the DS system is preferred. The contributions of this work are published in two conference papers *IEEE ICC* [21] and *IEEE WCNC* [22], and one submitted journal paper in *IEEE Transactions on Communications* [1].

Following the second research goal, an enhanced EGT-based algorithm for LB in HLWN is proposed. The joint effect of random orientation and mobility is considered to evaluate the performance of HLWN in a more realistic scenario by using the orientation-based random waypoint (ORWP) mobility model. The handover management takes into account the effect of the handover overhead. The impact of vertical and horizontal handover (HHO) on the average throughput of a HLWN is evaluated. A low-complexity orthogonal frequency division multiple access (OFDMA) resource allocation (RA) scheme in LiFi systems is proposed for HLWNs. The performance of user data rate and fairness is evaluated compared to the HLWN system where time division multiple access (TDMA) is used in LiFi. An enhanced EGT-based dynamic LB scheme for HLWNs is proposed. In the proposed HLWN, the LiFi system adopts the OFDMA scheme while the WiFi system applies the carrier sense multiple access with collision detection (CSMA/CA). The CSMA/CA scheme benefits from a utilization ratio to fairly allocate WiFi resources between the uplink and downlink. Then, LB is achieved based on these two schemes and the EGT algorithm. Also, the impact of the WiFi utilization ratio on the average data rate of a HLWN is assessed. The contributions of this work are published in one conference paper, *IEEE VTC* [29], and one published journal, *IEEE Transactions on Communications* [30].

Finally, regarding the third research goal, we propose a VCSEL array system which can support high data rate, low latency and multiple UEs without the requirement of expensive/complex hardware, such as spatial light modulation (SLM), microelectromechanical systems (MEMS) and fiber. Two beam activation methods are proposed based on the small cell property of the VCSEL array system. The beam activation based on the corner-cube retroreflector (CCR) can achieve low power consumption and almost-zero delay, allowing real-time beam activation for high-speed users. The other beam activation is based on an omnidirectional transmitter (ODTx), which serves the purpose of the uplink transmission and beam activation simultaneously. By collecting the received signal strength (RSS) values, an artificial neural network (ANN) is trained to predict the index of the serving beam directly without estimating the UE position first. This method is robust against random device orientation and is suitable for low-speed users. For a single UE scenario, regarding the central beam, the probability density function (PDF) of the signal-to-noise ratio (SNR) is derived. The analytical derivation for the average data rate is provided for the central beam and an upper bound is presented for the VCSEL array system. In terms of scenarios with multiple users, the optical SDMA is adopted and an analytical upper bound for the average data rate is developed. The effects of the cell size and beam divergence angle are considered in this study. By evaluating the system performance, the choices of cell size and beam divergence angle are proposed for the VCSEL array system. This contribution has been submitted to the *IEEE Transactions on Communications* [3].

### **1.3 Thesis Layout**

The rest of this thesis is organized as follows. In Chapter 2, different channel models are presented. The device orientation, mobility model and Rx structures are also introduced in this Chapter.

The coverage problems of PRs and TPRs are defined and investigated in Chapter 3, and the lower bound on the FOV for each PD is given analytically. The impact of random device orientation and diffuse link signal propagation are taken into consideration. The performance comparison between SBC and MRC is given under different noise levels. In addition, the DS system, where each LiFi AP consists of two sources transmitting the same information signals but with opposite polarity, is compared with the SS system.

In Chapter 4, based on the low-pass filtering effect of the LiFi channel, we firstly propose an RA method for LiFi systems. Also, a LB scheme considering handover in HLWNs is proposed. Monte-Carlo simulations have been carried to evaluate the performance of the proposed system.

Device orientation models supported by experimental measurements for static and mobile users are proposed in Chapter 4. The effect of random device orientations on the channel gain and SNR has been investigated, where an analytical model for the PDF of channel gain and SNR are developed. Finally, the effect of random orientation on the error performance of point-to-point communication is assessed and a closed-form approximation for the BER of a UE with the random orientation is derived.

In Chapter 5, a novel VCSEL array is proposed for indoor OWC systems. To activate the best beam for a mobile user, two beam activation methods are proposed for the system. The method based on a CCR provides very low latency and allows real-time activation for high-speed users. The other method uses the ODTx. The ODTx can serve the purpose of uplink transmission and beam activation simultaneously. Moreover, systems with ODTx are very robust to the random orientation of a UE. System level analyses are carried out for the proposed VCSEL array system. For a single user scenario, the PDF of the SNR for the central beam of the VCSEL array system can be approximated as a uniform distribution. In addition, the average data rate of the central beam and its upper bound are given analytically and verified by Monte-Carlo simulations. For a multi-user scenario, an analytical upper bound for the average data rate is given. The effects of the cell size and the full width at half maximum (FWHM) angle on the system performance are studied.

Conclusions and the key findings of this thesis are summarized in Chapter 6. In addition, limitations and subjects for future work are discussed.

### **1.4 Summary**

The sixth-generation (6G) communication is required to support a variety of services such as the internet of things (IoT), augmented reality, virtual reality, video streaming and online gaming with extremely high data and low latency. However, the current sub-6 GHz band is already congested, and lower-band communication may fail short in supporting high data rate transmission. As a bidirectional and high-speed wireless networked system, LiFi is a promising

solution to support the extremely high rate transmission in a new band. Hence, it has gained a lot of attention recently. However, ICI limits the performance of LiFi cellular networks. To realize the full potential of LiFi attocell networks, ICI should be reduced, mitigated or avoided. Moreover, to provide seamless connectivity for users, aspects such as random device orientation and user mobility must be studied carefully. In this thesis, different methods have been proposed to reduce the interference in LiFi networks.





---

## Chapter 2

# **Background**

---

## 2.1 Introduction

Optical wireless communication (OWC) is considered to be a promising technology which will alleviate traffic burden caused by the increasing number of mobile devices. The main applications of OWC are free-space optical (FSO) communication for long distance transmission, infrared (IR) communication and visible light communication (VLC) for short-range indoor applications [31].

In 1979, Gfeller and Bpist introduced wireless IR communication and achieved a diffuse link with data rates of 100 kbps [32]. In 1996, Marsh and Kahn proposed a faster IR system which enables transmission speeds of 50 Mb/s [33]. Later, Kahn and Barry developed channel models for line-of-sight (LOS) and non-line-of-sight (NLOS) optical wireless links in 1997 [14]. A data rate of 70 Mb/s was achieved in quasi-diffuse systems by Carruther and Kahn in 2000 [15]. Also, it has been demonstrated that IR indoor OWC systems preferably adopt the wavelengths range of 780 nm to 950 nm. In this range, not only inexpensive optical sources are already available but also the peak sensitivity of cheap photodiodes (PDs), as the main elements of a receiver, coincides with this band [34].

As another part of the optical spectrum, visible light uses the frequency spectrum between 400 THz to 790 THz and has been considered as a potential technology for high-speed broadband data communication. In the 19th century, the photophone was invented by Alexander Graham Bell [35]. By utilizing a selenium photocell and reflected sunlight on a vibrating mirror, the photophone could convey voice via a visible beam. It was demonstrated that the photophone could transmit voice messages at a distance of 200 m [35]. In the late 19th century, the British Navy used the signal lamps as a means of communication. Afterwards, in 2000, the experiment for data transmission using light-emitting diodes (LEDs) was implemented by the KEIO research group in Japan [36]. In 2003, the VLC Consortium (VLCC) was established. In 2004, the initial concept of the VLC channel model was developed [37]. In 2017, by using orthogonal frequency division multiplex (OFDM), a single LED achieved a data rate of 10 Gbit/s [38]. In 2019, a data rate of 15.73 Gbit/s was achieved using off-the shelf LEDs [39].

Light-fidelity (LiFi) was first introduced by Haas during a TED Talk in year 2011 [40]. Unlike VLC, LiFi is claimed as a fully-networked bidirectional system, rather than a point-to-point communication technique [5]. LiFi could utilize visible light or IR spectra in the downlink and uplink, and provide high data rates over short distances [41]. There are two main LiFi technologies: VLC and the beam-steered infrared light communication (BS-ILC) [28]. The VLC systems use wide-spread beams emerging from illumination systems while the BS-ILC systems use narrow well-directed beams emerging from a dedicated source.

The BS-ILC systems have been explored in [28,42–44]. Wavelength-controlled 2D beam-steered systems based on fully-passive crossed-grating devices were introduced and 1D beam steering was demonstrated in [42], which shows a multi-beam system with a capacity of 2.5 Gbit/s. The 2D steering of the multi-beam system has been first demonstrated in [43] and with adaptive discrete multitone modulation (DMT) using 512 tones, a gross bit rate of 42.8 Gbit/s has been achieved. In addition, by using 60 GHz radio signal in the uplink, upstream delivery of 10 Gbit/s per upstream has been presented. In [44], the authors proposed a novel OWC receiver (Rx) concept, which can enlarge the Rx aperture without reducing the bandwidth. Also, a multi-beam system with downstream capacities of up to 112 Gbit/s per IR

beam was demonstrated. In [28], an alternative approach, which is based on a high port count arrayed waveguide grating router (AWGR) and a high-speed lens, was proposed. With pulse amplitude modulation (PAM)-4 modulation, a total system throughput beyond 8.9 Gbit/s over 2.5 m was achieved by using 80-ports C-band AWGR.

## 2.2 Optical Transmitter

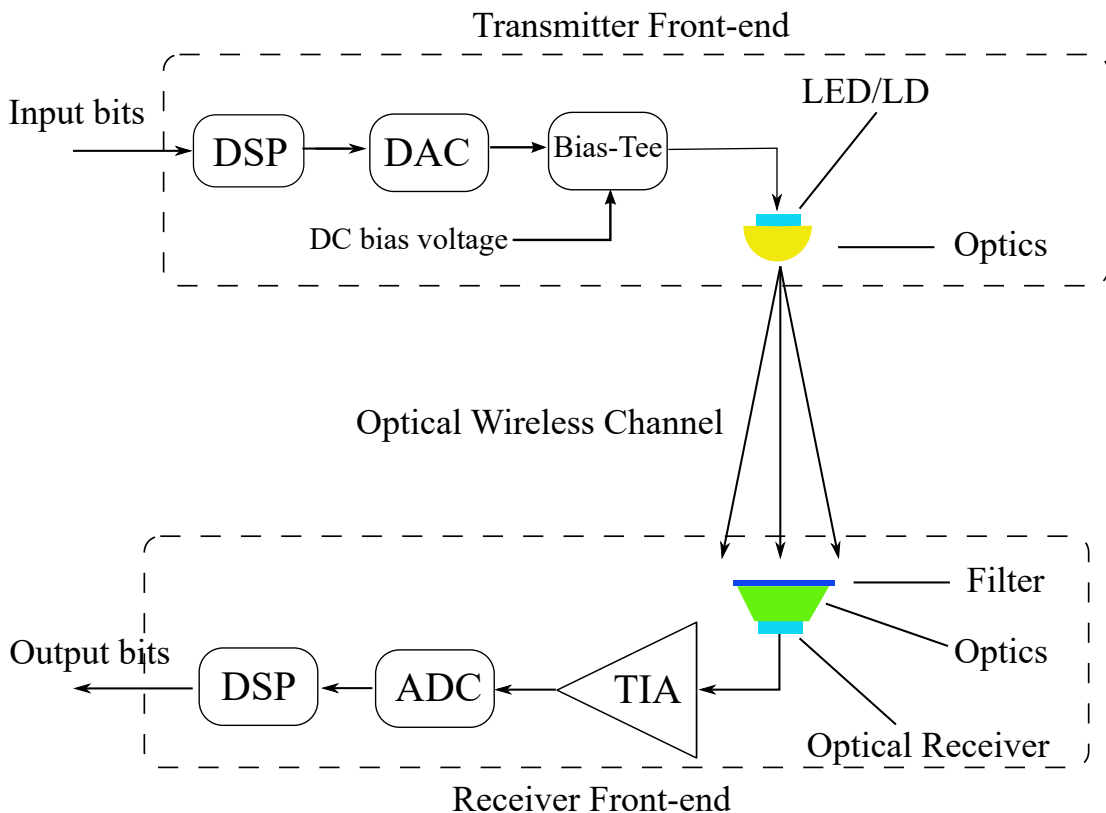


**Figure 2.1:** A typical LiFi downlink transmission with commonly used front-end elements at the transmitter and receiver.

A typical OWC downlink transmission is shown in Fig. 2.1. The front-end elements can be classified as transmitter (Tx)/Rx front-end elements. At the Tx side, the digital signal processor (DSP) converts the input information bits to digital signals. Afterwards, the digital signals are converted to analogue signals through the digital to analog converter (DAC). Then, the analogue voltage is converted to analogue current by the bias-Tee. Finally, IM is adopted using the LEDs/laser diodes (LDs), which converts the analogue current signals into optical light power with various intensities.

### 2.2.1 Light-emitting Diode

LEDs are the most commonly used optical sources in VLC systems since LEDs are widely used for the purpose of illumination [45–48]. In general, there are two types of commercial white

LEDs: the red-green-blue (RGB) LED and the blue LED chip covered by a yellow-phosphor coating. The RGB LEDs produce white optical light by combining three color components which are emitted by different devices [49]. The blue LED chip emits light in the narrow blue spectrum, which can be absorbed and efficiently re-emitted by phosphor coating. The emitted light has a wide emission profile across the entire visible light spectrum [49]. However, due to the slow absorption and re-emission time of phosphor, the 3-dB bandwidth of these LEDs is about 2 MHz [49]. A blue filter can be applied to remove the slow signal components from phosphor so that the modulation bandwidth can be increased. The most important factors that limit the modulation speed of the LED [49, 50] are carrier lifetime and innate junction capacitance. To reduce the lifetime of the carrier, the current density within the junction should be increased, which can be achieved by reducing the size of a LED. In [50], McKendry designed a Gallium Nitride based LED, named  $\mu$ LED, to provide a modulation bandwidth over 400 MHz. However, due to the issue of heat generation, the current efficiency of  $\mu$ LED drops when the current density increases [51].

Generally, the LED follows the Lambertian radiation pattern. The radiant intensity using a generalized Lambertian model is given as [14]:

$$I_L = \frac{(m_{\text{LED}} + 1)}{2\pi} \cos^{m_{\text{LED}}}(\phi), \quad (2.1)$$

where  $I_L$  is the radiant intensity;  $\phi$  is the irradiance angle of the LED;  $m_{\text{LED}}$  is the Lambertian order. Note that  $\phi$  and  $m_{\text{LED}}$  can be obtained separately as:

$$\phi = \cos^{-1} \left( \frac{\mathbf{n}_{\text{tx}} \cdot \mathbf{d}}{\|\mathbf{d}\|} \right), \quad (2.2a)$$

$$m_{\text{LED}} = -\frac{\ln(2)}{\ln(\cos(\Phi_{1/2}))}, \quad (2.2b)$$

where  $\mathbf{d}$  defines the distance vector between the transmitter (Tx) and the Rx. The dot product is denoted as  $(\cdot)$  and  $\|\cdot\|$  denotes the Euclidean distance. Furthermore,  $\mathbf{n}_{\text{tx}}$  is the normal vector of the Tx and  $\Phi_{1/2}$  denotes the half-power semi-angle of the LED.

## 2.2.2 Laser Diode

Although the Laser diode (LD) are much more expensive than the LED, it offers many advantages: 1) The LD achieves an electro-optic conversion efficiency of 30-70% while LED only achieves 10-20%; 2) compared to modulation bandwidths that are limited to tens of MHz in typical low-cost LEDs, LDs have wide modulation bandwidths, which range from hundreds of MHz to more than 10 GHz; 3) very narrow spectral widths, ranging from several nm to well below 1 nm, are available. Among different types of LDs, vertical-cavity surface-emitting lasers (VCSELs) are one of the promising candidates to ensure high-data rate communications due to several outstanding features such as [52]: high-speed modulation (bandwidths of larger than 10 GHz), high power conversion efficiency, low cost and compact in size. These attributes make VCSELs appealing to many applications, particularly for high-speed indoor wireless networks [53]. Depending on the bias current, the VCSEL output beam profile is Gaussian [54–56]. The

geometrical representation of the Gaussian beam is shown in Fig. 2.2 and the Gaussian beam intensity can be expressed as given in [57]:

$$I_G(r_0, d_0) = \frac{2P_{\text{tx,opt}}}{\pi W^2(d_0)} \exp\left(-\frac{2r_0^2}{W^2(d_0)}\right), \quad (2.3)$$

where  $P_{\text{tx,opt}}$  is the transmitted optical power of a single beam and  $r_0$  is the distance from the user equipments (UEs) to the beam axis, which is represented as  $z_{\text{beam}}$ -axis; the distance from the Tx to the UEs along the beam axis is given as  $d_0$ ; the beam width at  $z_{\text{beam}} = d_0$  is denoted as  $W(d_0)$  and it can be obtained as:

$$W(d_0) = W_0 \sqrt{1 + \left(\frac{\lambda d_0}{\pi W_0^2}\right)^2}, \quad (2.4)$$

where  $\lambda$  is the operating wavelength of the VCSEL. The beam waist is denoted as  $W_0 = \frac{\lambda}{\pi \theta_{\text{beam}}}$ , where  $\theta_{\text{beam}}$  is the divergence angle. The relation between the beam divergence and the angle for full width at half maximum (FWHM) intensity points,  $\theta_{\text{FWHM}}$ , is given as  $\theta_{\text{beam}} = \theta_{\text{FWHM}} / \sqrt{2 \ln(2)}$ , where  $\ln(\cdot)$  represents the natural logarithm. The distance vector from the Tx to the Rx is  $\mathbf{d}$  and the distance is  $d$ . The radiance angle of the Tx,  $\phi$ , can be obtained by (2.2). It should be noted that  $r_0 = d \sin \phi$  and  $d_0 = d \cos \phi$ . Hence, the intensity of the beam at the position of the UE can be reformulated as:

$$I_G(d, \phi) = \frac{2P_{\text{tx,opt}}}{\pi W^2(d \cos \phi)} \exp\left(-\frac{2d^2 \sin^2 \phi}{W^2(d \cos \phi)}\right). \quad (2.5)$$

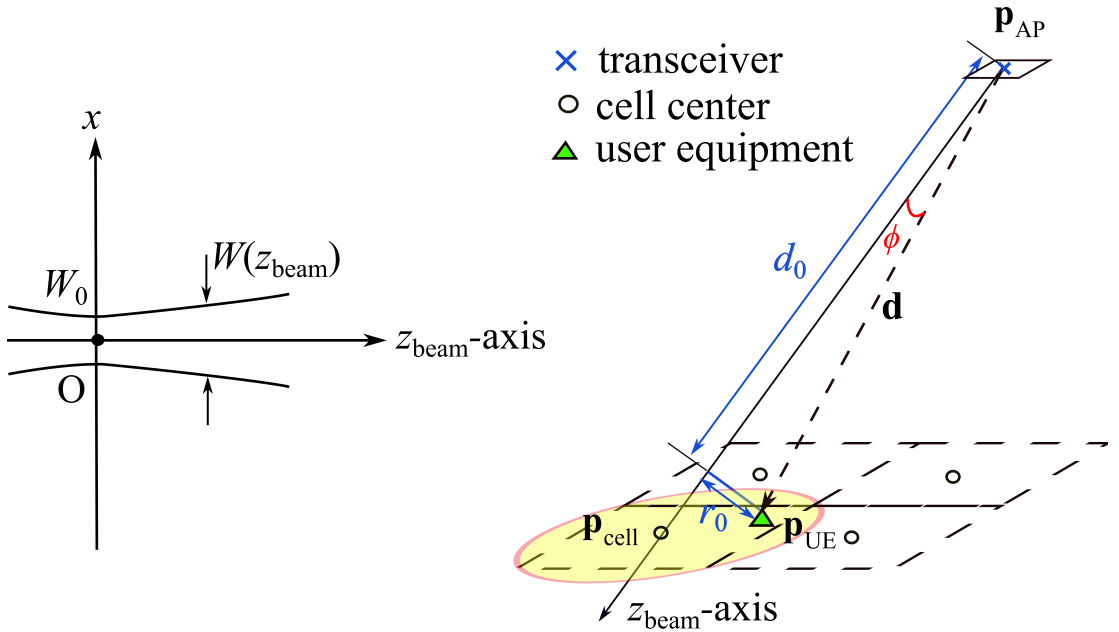


**Figure 2.2:** Geometrical representation of the elliptical Gaussian beam.

## **2.3 Optical Receiver**

As depicted in Fig. 2.1, at the Rx end, bandpass filters are required to exclude unnecessary color components. Then, various methods such as PDs [58], LEDs [59], image sensors (ISs) [60, 61] and solar cell panels [62] can be applied to turn the received optical power into electrical signals. This is known as direct detection (DD), which is the favorable and viable practical down-conversion method in OWC. In DD, a photodetector produces a current proportional to the received instantaneous power, i.e., proportional to the square of the received electric field [14]. These devices can work under different circumstances in various applications. Due to the shorter response time, which leads to a wider bandwidth and high-speed data communication, PDs are the preferred Rx unit. Afterwards, as shown in Fig. 2.1, the transimpedance amplifier (TIA) will transfer the current signal captured by the optic element at the Rx to output voltage. Then, the analog to digital converter (ADC) converts the analogue voltage signals to digital signals which are then fed into the digital signal processor (DSP) unit to recreate the information bits. Generally, based on the operation mode, PDs are classified into three types: p-intrinsic-n (PIN) diode, avalanche photodiode (APD), and single-photon avalanche diode (SPAD).

### **2.3.1 P-intrinsic-n Diode**

The PIN diode is composed of a negative-type semiconductor region and a wide undoped intrinsic semiconductor region between a positive-type semiconductor. As a photodetector, the PIN diode is reverse-biased. Under reverse bias, the diode ordinarily does not conduct. When a photon of sufficient energy enters the depletion region of the diode, it creates an electron-hole pair. The reverse-bias field sweeps the carriers out of the region, creating current. The current generated by PIN diode is approximately linear to the energy of received photons [58].

### **2.3.2 Avalanche Photodiode**

For the APD, a high reverse bias needs to be applied, and more than one hundred internal current gain can be achieved due to the avalanche effect. Therefore, the APD is very suitable to the environment with low light intensity. However, the APD is very vulnerable to ambient shot noise and the internal excess noise, which is introduced during the multiplication process. The number of initial, optically generated charge carriers in the APD is multiplied within the multiplication process and the photocurrent is amplified. By increasing the area of an APD, the light energy received by the APD increases. However, the increase in the APD area leads to a growth in switching times, which means that there is always a trade-off between the received energy and receiver bandwidth [14].

### **2.3.3 Single-photon Avalanche Diode**

Similar to the APD, a reverse biasing of p-n junction is applied to the SPAD in order to exploit the avalanche effect. However, unlike APDs, the reverse bias of a SPADs is designed to be well above the breakdown voltage of an p-n junction, which is named as Geiger mode [63, 64]. Due to the high gain of a SPAD, even a single photon can trigger a current pulse. By counting the number of pulses during a measurement time slot, the intensity of the output signal is obtained.

SPADs are preferred under environments with extremely low light. However, due to the gain of a SPAD, it can be easily saturated. When environment light level is high, a proper filter should be applied to reject ambient light. In addition, the pulse counting process causes the SPAD to be highly nonlinear [65].

### 2.3.4 Noise Analysis

Like radio frequency (RF) systems, noise can also degrade the system performance in LiFi systems. In a LiFi system, when LEDs are used as the TxS, the total Rx noise is comprised of shot noise and thermal noise. Hence, the total noise power affecting the photocurrent at the Rx is thus given by [14]:

$$\sigma_n^2 = \sigma_{\text{shot}}^2 + \sigma_{\text{thermal}}^2. \quad (2.6)$$

Thermal noise is mainly caused by the random motions of electrons in the circuit due to the temperature fluctuation. The resistance used in the TIA is the primary source of thermal noise at the Rx. The power of thermal noise at the Rx is given by [14]:

$$\sigma_{\text{thermal}}^2 = \frac{4k_B T}{R_L} B_L, \quad (2.7)$$

where  $k_B$  is the Boltzmanns constant which is  $1.38 \times 10^{-23}$  J/K;  $T$  is the absolute temperature in Kelvin;  $R_L$  is the load resistance in the Rx circuit.

In optical communication, shot noise is due to the random nature of photon arrivals with an average rate determined by the incidence optical power. Shot noise may be generated because of many factors in the environment. This encompasses ambient light due to sunlight, street lights, fluorescent and incandescent lamps [32]. The power of shot noise at a PD is then given by [14]:

$$\sigma_{\text{shot}}^2 = 2qR P_{\text{rx,opt}} B_L + 2qI_{\text{BG}} I_2 B_L, \quad (2.8)$$

where  $P_{\text{rx,opt}}$  denotes the average received optical power;  $q$  is the electron charge which is  $1.6 \times 10^{-19}$  C;  $B_L$  is the modulation bandwidth;  $I_{\text{BG}}$  is the background current; and  $I_2$  is the noise bandwidth factor. Optical RxS that use an APD are able to provide high signal-to-noise ratio (SNR). This enhancement in SNR is due to the internal gain of the APD,  $G_{\text{APD}}$ . If the noise of the Rx was independent of the internal gain, the SNR would increase by a factor of  $G_{\text{APD}}^2$ . Unfortunately, the noise depends on  $G_{\text{APD}}$  so that the SNR improvement is less than  $G_{\text{APD}}^2$  [66]. As the noise of the APD depends on the internal gain  $G_{\text{APD}}$ , the power of shot noise for an APD is given as [67]:

$$\sigma_{\text{shot}}^2 = 2qG_{\text{APD}}^2 F_A R_{\text{APD}} (P_{\text{rx,opt}} + P_n) B_L. \quad (2.9)$$

where  $P_n$  denotes the average ambient power. We note that under the condition of  $P_n \gg P_{\text{rx,opt}}$ , the shot noise is signal independent and is only affected by the ambient light. In (2.9),  $F_A$  is called the excess noise factor and can be obtained as:

$$F_A = k_A G_{\text{APD}} + (1 - k_A) \left( 2 - \frac{1}{G_{\text{APD}}} \right), \quad (2.10)$$

where  $0 < k_A < 1$  is a dimensionless parameter.



When a laser/VCSEL is applied as the Tx of a LiFi system, relative intensity noise (RIN) is another type of noise, which induced mainly due to the instability in the transmit power. Cavity variation and fluctuations in the laser gain are two major contributors to the RIN. The variance of power fluctuations is given as [67]:

$$\sigma_I^2 = (R_{\text{APD}} P_{\text{rx,opt}} r_I)^2, \quad (2.11)$$

where  $r_I$ , is a measure of the noise level of the optical signal and is given as:

$$r_I^2 = \int_{-\infty}^{\infty} \text{RIN}(f) df, \quad (2.12)$$

where  $\text{RIN}(f)$  is the intensity noise spectrum. For a limited bandwidth Rx, the above integral should be calculated over the Rx bandwidth. It is noted that  $r_I$  is simply the inverse of the transmit optical power. For simplicity, we assume that  $\text{RIN}(f)$  is a constant value over the whole bandwidth, i.e.,  $\text{RIN}(f) = \text{RIN}$ . Hence, the power of the RIN can be denoted as:

$$\sigma_{\text{RIN}}^2 = \text{RIN}(R_{\text{APD}} P_{\text{rx,opt}})^2 B_L. \quad (2.13)$$

Therefore, the total noise power for an APD can be expressed as:

$$\sigma_n^2 = \frac{4k_B T}{R_F} B_L + 2qG_{\text{APD}}^2 F_A R_{\text{APD}} (P_{\text{rx,opt}} + P_n) B_L + \text{RIN}(R_{\text{APD}} P_{\text{rx,opt}})^2 B_L. \quad (2.14)$$

### 2.3.5 Concentrator

In general, the received optical power of a PD is proportional to its physical area. Hence, more received optical power can be captured using a PD with large physical area. However, the increase in the PD area results in a growth in switching times, which reduces the receiver bandwidth [14]. In order to capture more light energy without compromising the bandwidth of a PD, the optical concentrator is utilized. There are two main kinds of concentrators: imaging concentrators as well as non-imaging concentrators. Imaging concentrators capture light signals and project the original image from the optical transmitter on a PD. Hence, optical links from different LEDs can be well separated with the utilization of imaging concentrators, which increases the optical channel capacity and reduces the complexity of detection [68]. Thus, imaging concentrators are favorable in a multiple-input multiple-output (MIMO) configuration. Instead of separating different optical channels, non-imaging concentrators focus all light energy into a small area. With the use of non-imaging concentrators, light energy can be effectively collected and a higher gain can be achieved. Therefore, non-imaging concentrators will be considered in the rest of the studies. Typically, the effective signal collection area,  $A_{\text{eff}}$ , is expressed as [14]:

$$A_{\text{eff}} = A_p \cos \psi \times \text{rect}\left(\frac{\pi}{2}\right), \quad (2.15)$$

where  $A_p$  is the physical area of a PD;  $\text{rect}(\cdot)$  denotes the rectangular function;  $\psi$  represents the incidence angle of a PD. Note that  $\psi$  can be obtained as:

$$\psi = \cos^{-1} \left( \frac{\mathbf{n}_{\text{PD}} \cdot (-\mathbf{d})}{\|\mathbf{d}\|} \right), \quad (2.16)$$

where  $\mathbf{d}$  defines the distance vector between the Tx and the Rx. The dot product is denoted as  $(\cdot)$  and  $\|\mathbf{d}\|$  denotes the Euclidean distance. Furthermore,  $\mathbf{n}_{PD}$  is the normal vector of the PD. With a concentrator and a filter, the effective area becomes [14]:

$$A_{\text{eff}} = A_p T_s(\psi) g(\psi) \cos \psi \times \text{rect}(\Psi_c), \quad (2.17)$$

where  $T_s(\psi)$  represents the signal transmission gain of the optical filter;  $\Psi_c$  denotes the field of view (FOV) of the PD with concentrator;  $g(\psi)$  is the gain of concentrator. With the use of non-imaging concentrators, there is a trade-off between FOV and gain. Ideally, the gain of non-imaging concentrator is defined as [14]:

$$g(\psi) = \frac{n_{\text{ref}}^2}{\sin^2(\Psi_c)}, \quad (2.18)$$

where  $n_{\text{ref}}$  represents the internal refractive index of the concentrator.

### 2.3.6 Angle Diversity Receiver Structure

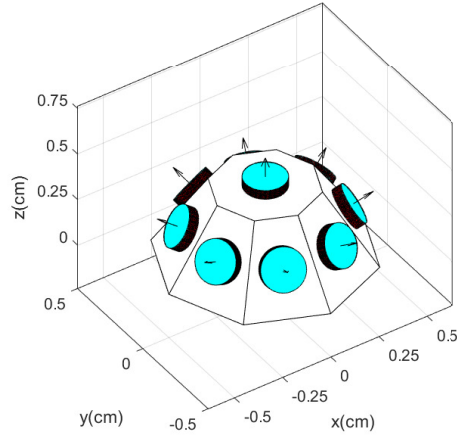
An angle diversity receiver (ADR) is composed of multiple narrow-FOV PDs facing different directions. The angle diversity reception, first proposed in [14], allows the Rx to achieve a wide FOV and high optical gain simultaneously. The high optical gain comes from the narrow-FOV of each PD while the wide FOV is the result of combining multiple narrow-FOV PDs as one Rx. In [15–24], the ADR is used to address the issue of inter-cell interference (ICI) as well as frequency reuse in LiFi cellular systems, and different signal combining schemes are investigated. By using a PD in conjunction with a compound parabolic concentrator (CPC), a narrow FOV and high optical gain can be achieved [14]. The CPC is one type of non-imaging concentrator that is widely used. It can achieve much higher gain than the hemisphere concentrator. However, the narrow FOV is achieved at the expense of the longer length of the CPC [14]. Therefore, the number of PDs on the ADR should be limited due to the size limitation on the mobile devices and smartphones.

In this study, the truncated pyramid receiver (TPR) [24] and the pyramid receiver (PR) [23] are considered as they are both suitable for hand-held devices. The number of PDs on the TPR and PR are separately denoted as  $N_{\text{TPR}}$  and  $N_{\text{PR}}$ . The structure of the TPR with  $N_{\text{TPR}} = 9$  and the PR with  $N_{\text{PR}} = 8$  are presented in Fig. 2.3 (a) and Fig. 2.3 (b), respectively. The ADR designs are analyzed in the following parts.

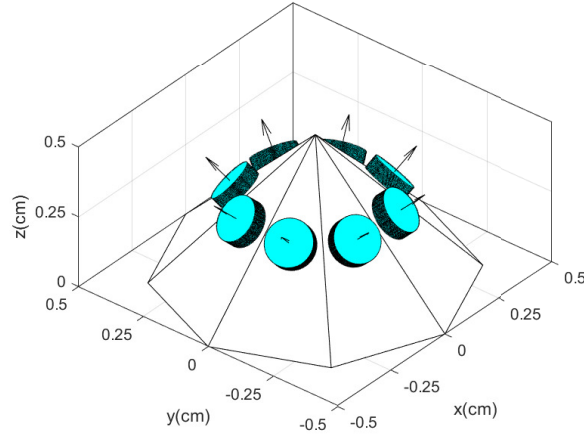
#### 2.3.6.1 Truncated Pyramid Receiver

The TPR is composed of a central PD and a ring of  $N_{\text{TPR}} - 1$  equally separated side PDs. The side PDs are arranged uniformly in a circle of radius  $r$  on the horizontal plane. Thus, the coordinate of the  $p$ -th PD on a TPR is represented as [22]:

$$(x_{PD,p}, y_{PD,p}, z_{PD,p}) = \begin{cases} \left( x_{UE} + r \cos \frac{2(p-1)\pi}{N_{\text{TPR}}-1}, y_{UE} + r \sin \frac{2(p-1)\pi}{N_{\text{TPR}}-1}, z_{UE} \right), & \text{if } 1 \leq p < N_{\text{TPR}} \\ (x_{UE}, y_{UE}, z_{UE}), & \text{if } p = N_{\text{TPR}} \end{cases}, \quad (2.19)$$



(a) The structure of truncated pyramid receiver with  $N_{\text{TPR}} = 9$ .



(b) The structure of pyramid receiver with  $N_{\text{PR}} = 8$ .

**Figure 2.3: ADR structures.**

where  $(x_{\text{UE}}, y_{\text{UE}}, z_{\text{UE}})$  is the UE position, denoted as  $\mathbf{p}_{\text{UE}}$ . As the distance between the access point (AP) and the UE is much larger than  $r$ , the distances between the AP and all PDs on a TPR are approximately the same. The normal vector of each PD can be described by two angles: the azimuth angle of a PD,  $\omega_{\text{PD}}$ , and the elevation angle of a PD,  $\theta_{\text{PD}}$  [21]. When the UE is pointing vertically upward, the TPR has one vertically orientated central PD and  $N_{\text{TPR}} - 1$  inclined side PDs with identical elevation angles  $\Theta_{\text{PD}}$ . In other words, the elevation angle of the  $p$ -th PD on a TPR can be expressed as:

$$\theta_{\text{PD,vert},p} = \begin{cases} \Theta_{\text{PD}}, & \text{if } 1 \leq p < N_{\text{TPR}} \\ 0, & \text{if } p = N_{\text{TPR}} \end{cases}. \quad (2.20)$$

The azimuth angle of the  $p$ -th PD is given by:

$$\omega_{\text{PD,vert},p} = \begin{cases} \frac{2(p-1)\pi}{N_{\text{TPR}} - 1}, & \text{if } 1 \leq p < N_{\text{TPR}} \\ 0, & \text{if } p = N_{\text{TPR}} \end{cases}. \quad (2.21)$$

### 2.3.6.2 Pyramid Receiver

The PR can be regarded as a TPR without the central PD. Therefore, the coordinate of the  $p$ -th PD on a PR is given by:

$$(x_{\text{PD},p}, y_{\text{PD},p}, z_{\text{PD},p}) = \left( x_{\text{UE}} + r \cos \frac{2(p-1)\pi}{N_{\text{PR}}}, y_{\text{UE}} + r \sin \frac{2(p-1)\pi}{N_{\text{PR}}}, z_{\text{UE}} \right). \quad (2.22)$$

When the UE is vertically orientated, the elevation angle and the azimuth angle of the  $p$ -th PD are separately expressed as:

$$\theta_{\text{PD,vert},p} = \Theta_{\text{PD}}, \quad (2.23a)$$

$$\omega_{\text{PD,vert},p} = \frac{2(p-1)\pi}{N_{\text{PR}}}. \quad (2.23b)$$

## 2.3.7 Signal Combining Schemes for an Angle Diversity Receiver

With the use of proper signal combining schemes, ADRs can significantly mitigate ICI from the cell in the vicinity without losing the coverage. Therefore, in this section, we introduce three popular signal combining schemes namely equal gain combining (EGC), select best combining (SBC) as well as maximum ratio combining (MRC).

### 2.3.7.1 Equal Gain Combining

The EGC is one of the most simple signal combining schemes as signals from all PDs are combined with equal weights. EGC does not require any knowledge from any AP to a user. Hence, only a simple adder is demanded for the combining circuit of the EGC scheme, which means optical power from multiple PDs is added up directly. However, ICI cannot be mitigated effectively since the signal from each PD is equally weighted, which could lead to poor overall signal to interference-plus-noise ratio (SINR) performance.

### 2.3.7.2 Select Best Combining

The SBC scheme only select the signal from the PD having the highest received SNR and discard the signals from other PDs. This requires the knowledge of channel state information (CSI) from the desired APs to the user. The knowledge of CSI from the other interfering APs to the user is unnecessary. With regard to the design of the combining circuit, a switch is necessary for selecting the signals from the desired PD.

### 2.3.7.3 Maximum Ratio Combining

In terms of MRC, the weight of each combining circuit is proportional to the SNR on each PD. Similar to SBC, only the knowledge of CSI from the desired AP to a user is required. Regarding the design of the combining circuit, instead of a switch, a multiplier and an adder are required to weight and combine the received signals.

In general, although the EGC scheme is easy to implement, it is not recommended as its SINR performance is similar to the performance using a single PD Rx. Although the received optical power using SBC is lower than the optical power using EGC, it achieves better SINR performance as the signals from PD with poor SNR are discarded. Among all these schemes, MRC is the most complicated scheme. However, it achieves the best performance as it could boost the desired signal and reduce interference. Therefore, a high overall SINR can be achieved when MRC is adopted [18].

### 2.3.8 Receiver Bandwidth vs Photodiode Area

The bandwidth of a PD is affected by its physical area,  $A_p$ , and the PD thickness,  $L_p$ . The capacitance of the each PD is denoted as:

$$C_r = \varepsilon_0 \varepsilon_r \frac{A_p}{L_p}, \quad (2.24)$$

where  $\varepsilon_0$  and  $\varepsilon_r$  are the permittivity of vacuum and the relative permittivity of silicon, respectively. The load resistance is defined as  $R_{load}$  while the hole velocity is denoted as  $v_p$ . Therefore, the Rx bandwidth can be written as [69]:

$$B_r = \frac{1}{\sqrt{(2\pi R_{load} C_r)^2 + \left(\frac{L_p}{0.443 v_p}\right)^2}}. \quad (2.25)$$

By solving  $\frac{\partial B_r}{\partial L_p} = 0$ , the optimum  $L_p$  can be denoted as  $L_{p,opt} = \sqrt{0.886\pi R_{load} \varepsilon_0 \varepsilon_r A_p v_p}$ .

## 2.4 Digital Modulation Techniques

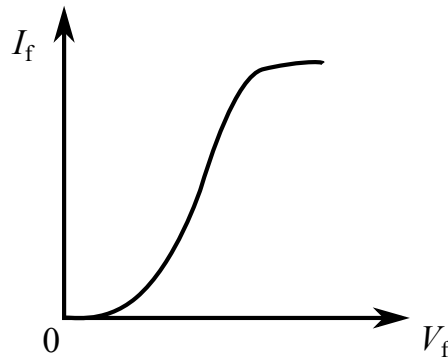


**Figure 2.4:** Typical nonlinear transfer characteristic of an LED.

The most commonly used modulation techniques can be categorized into: single carrier modulation and multiple carrier modulation. Real single carrier modulation scheme can be adapted to LiFi from RF without major modification. These modulation schemes include on-off keying (OOK), pulse position modulation (PPM), pulse width modulation (PWM) and unipolar PAM. They are prone to unwanted effects such as inter-symbol interference (ISI) and non-linear signal distortion at the LED [5]. In general, because of the p-n junction barrier and the saturation effect of the LED, there is a non-linear relation between the forward current,  $I_f$ , and the forward voltage,  $V_f$  as shown in Fig. 2.4. Therefore, appropriate equalization methods, which require complex digital filters, are required to deal with these challenges. In comparison, multiple carrier modulation techniques are more bandwidth-efficient and can offer higher data rates. One of the most common and widely used multiple carrier modulation methods is OFDM. Benefits of using OFDM include: 1) robustness against the frequency selectivity of channel by splitting the channel into narrowband flat fading subcarriers, 2) simple channel equalization by using single-tap equalizer (while adaptive equalization techniques are being used in single carrier modulation schemes), 3) as the entire available bandwidth is split into multiple narrowband subcarriers, it is possible to adaptively allocate information bits and energy to individual subcarriers according to their channel properties. This can effectively exploit the communication resources, 4) computationally efficient by using fast Fourier transform (FFT) and inverse fast Fourier transform (IFFT) techniques. 5) OFDM technique can be directly used as a multiple access scheme at the medium access control (MAC) level, where different subcarriers of OFDM can be effectively allocated to different users [70, 71].

In conventional OFDM, the transmitted signals are bipolar and complex, but bipolar signals cannot be transmitted in an IM/DD OWC system, because the intensity of light cannot be negative. Therefore, optical-OFDM (O-OFDM) is developed to ensure real and positive signals [72]. Direct current biased optical orthogonal frequency division multiplex (DCO-OFDM) and asymmetrically clipped optical orthogonal frequency division multiplex (ACO-OFDM) are two of the most well-known and commonly used optical-OFDM (O-OFDM) schemes.

### 2.4.1 DCO-OFDM

The number of OFDM subcarriers is denoted as  $M$ , where  $M$  is an even and positive integer, and the sequence number of OFDM subcarriers is denoted by  $m \in \{0, 1, \dots, M-1\}$ . In a DCO-OFDM system, to ensure real and positive signals, Hermitian symmetry is applied to the OFDM frame and the following constraints should be satisfied [73]:

$$X(0) = X(M/2) = 0, \quad (2.26a)$$

$$X(m) = X^*(M-m), \text{ for } m \neq 0, \quad (2.26b)$$

where  $(\cdot)^*$  denotes the complex conjugate operator. Therefore, the effective subcarrier set bearing information data is defined as:

$$\mathcal{M}_e = \{m | m \in [1, M/2-1], m \in \mathbb{N}\}, \quad (2.27)$$

where  $\mathbb{N}$  is the set of natural numbers. The time-domain samples can be obtained through the IFFT operation as:

$$x[n] = \frac{1}{\sqrt{M}} \sum_{m=0}^{M-1} X(m) \exp\left(\frac{j2\pi mn}{M}\right), \quad 0 \leq n \leq M-1. \quad (2.28)$$

Afterwards, to combat the inter-symbol interference (ISI) caused by the dispersive wireless channel, a cyclic prefix (CP) will be added to the samples. And then the digital to analog converter (DAC) module will convert the samples to a analog waveform. To ensure the real and positive signal, a direct current (DC) bias should be added to the analog signal  $\tilde{x}(t)$  as:

$$x_e(t) = x_{\text{DC}} + \tilde{x}(t), \quad (2.29)$$

where

$$x_{\text{DC}} = \kappa \sqrt{\mathbb{E}[\tilde{x}^2(t)]}, \quad (2.30)$$

where  $\kappa$  is the conversion factor and  $\mathbb{E}[\cdot]$  denotes the expectation operator. By setting  $\kappa = 3$ , it is guaranteed that less than 0.3% of the signals are clipped and therefore the clipping noise is neglectable [41].

## 2.4.2 ACO-OFDM

Another well-known type of O-OFDM is ACO-OFDM, which prevents adding the DC bias to the signal and is energy-efficient. In ACO-OFDM, only odd subcarriers are used to bear information which results in a loss of spectral efficiency. Spectral efficiency refers to the information rate that can be transmitted over a given bandwidth in a specific communication system. It is a measure of how efficiently a limited frequency spectrum is utilized by the physical layer protocol, and sometimes by the medium access control [74]. Compared to DCO-OFDM, half of the spectrum is sacrificed by ACO-OFDM to ensure real and positive signals. In return, ACO-OFDM is more energy efficient than DCO-OFDM.

## 2.5 VLC Channel Model

In VLC, the signal propagation consists of two components: the LOS link and the NLOS link. The LOS link represents that there is a signal path between a Tx and a Rx without blocking by opaque objects. The existence of LOS links can maximize the received SNR while minimizing the effect of multi-path distortion. For the NLOS link, light signals from a Tx require one or multiple reflections to reach a Rx. The NLOS link design is robust to the blockage and is suitable to achieve ubiquitous coverage. Therefore, the overall channel DC gain is the sum of the LOS and diffuse components:

$$H_{\text{total}} = H_{\text{LOS}} + H_{\text{diffuse}}, \quad (2.31)$$

where  $H_{\text{LOS}}$  represents the LOS DC channel gain between the Tx and Rx, and  $H_{\text{diffuse}}$  is the diffuse DC channel gain which is the superposition of all NLOS components that are caused by reflections from the surfaces of the walls.

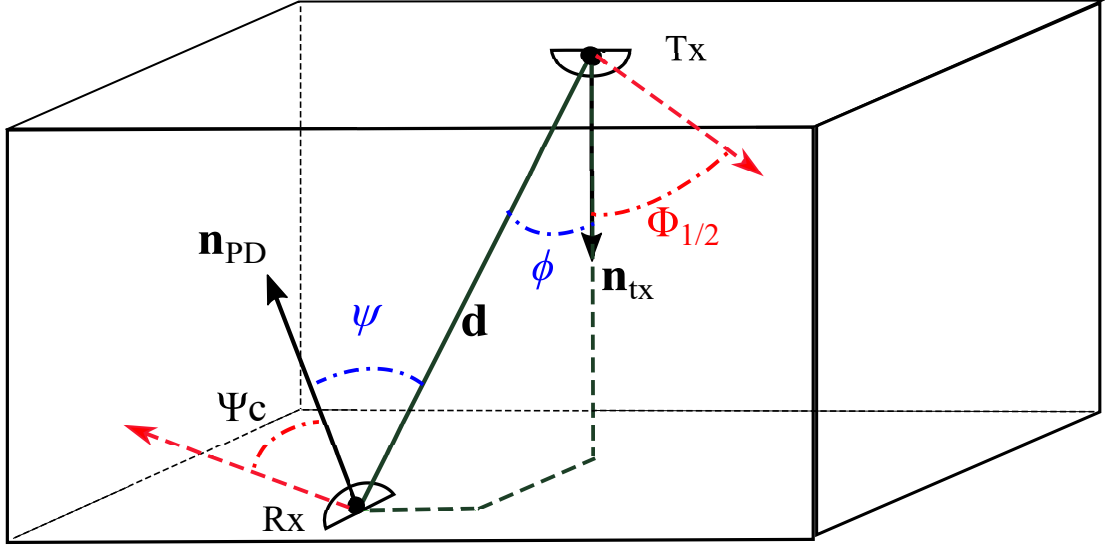


**Figure 2.5:** Downlink geometry of LOS light propagation in VLC.

### 2.5.1 Line-of-sight Link

The downlink geometry of LOS light propagation is illustrated in Fig. 2.5. As described previously in Section 2.2.1, the LED follows the Lambertian radiation pattern. The LOS DC channel gain is thus given by [75]:

$$H_{\text{LOS}} = \frac{I_L}{d^2} A_{\text{eff}} v_{\text{Tx,Rx}}, \quad (2.32)$$

where  $d$  is the distance from the Tx to the Rx.  $v_{\text{Tx,Rx}}$  is the visibility factor, which is equal to one if the Tx and Rx are within LOS, and equal to zero if not. In other words,  $v_{\text{Tx,Rx}}$  can be written as [75]:

$$v_{\text{Tx,Rx}} = \begin{cases} 0 & \phi > \pi/2 \text{ or } \psi > \Psi_c \\ 1 & \text{otherwise} \end{cases}. \quad (2.33)$$

The radiant intensity,  $I_L$ , is denoted in (2.1). The effective area of the PD,  $A_{\text{eff}}$  is presented in (2.17). Hence, (2.32) can be rewritten as:

$$H_{\text{LOS}} = \frac{(m_{\text{LED}} + 1)}{2\pi d^2} \cos^{m_{\text{LED}}}(\phi) A_p T_s(\psi) g(\psi) \cos(\psi) v_{\text{Tx,Rx}}. \quad (2.34)$$

### 2.5.2 Non-line-of-sight Link

The diffuse link is due to the reflection from the walls. A microscopic frequency-domain method for the simulation of the indoor VLC channel is presented in [75]. A closed form for the transfer function that contains all reflection orders is formulated. The method can be extended to multi-spot transmission without a significant increase in the computational complexity. Therefore, in this study, we will use the frequency-domain method to simulate the impact of the diffuse link. As mentioned earlier, the frequency-domain method in [75] is used to obtain the diffuse link DC channel gain. We assume that all the wall surfaces are purely



diffuse Lambertian reflectors with  $m_{\text{wall}} = 1$ . All of the surfaces are divided into a number of small surface elements numbered by  $k = 1, \dots, N_E$ , with areas  $A_k$  and reflective coefficients  $\rho_k$ . To calculate the diffuse link DC channel gain, the propagation of light is divided into the following three parts. The first part of the diffuse link propagation is the light path between the Tx and all the reflective surface elements of the room. The LOS DC channel gain between the Tx and the surface element  $k$  is defined as:

$$H_{\text{Tx},k} = \frac{m_{\text{LED}} + 1}{2\pi d_{\text{Tx},k}^2} \cos^{m_{\text{LED}}}(\phi_{\text{Tx},k}) A_k \cos(\psi_{\text{Tx},k}), \quad (2.35)$$

where  $d_{\text{Tx},k}$  denotes the distance between the Tx and the surface element  $k$ .  $\phi_{\text{Tx},k}$  represents the radiant angle while  $\psi_{\text{Tx},k}$  is the incident angle of the surface element  $k$ . Therefore, the Tx transfer vector,  $\mathbf{t}$ , is defined as:

$$\mathbf{t} = (H_{\text{Tx},1}, H_{\text{Tx},2}, \dots, H_{\text{Tx},N_E})^T, \quad (2.36)$$

where  $(\cdot)^T$  defines the transpose of vectors. The second part of the diffuse link is the LOS link from all the  $N_E$  surface elements to all the  $N_E$  surface elements. The LOS DC channel gain between the surface elements  $k$  and the surface element  $i$  is given as:

$$H_{k,i} = \frac{m_{\text{wall}} + 1}{2\pi d_{k,i}^2} \cos(\phi_{k,i}) A_i \cos(\psi_{k,i}). \quad (2.37)$$

To describe the LOS links between all surfaces inside the room, the  $N_E \times N_E$  room-intrinsic transfer matrix,  $\mathbf{H}$ , is defined by its elements  $[\mathbf{H}]_{k,i} = H_{k,i}$ . In order to include the reflective coefficient  $\rho_k$  of the surface elements, the  $N_E \times N_E$  reflectivity matrix is defined as [75]:

$$\mathbf{G}_\rho = \text{diag}(\rho_1, \rho_2, \dots, \rho_{N_E}). \quad (2.38)$$

In the third part of the diffuse link, the light propagates from all the surfaces of the room to the Rx. Similarly, we denote the LOS DC channel gain between the surface element  $k$  and the Rx as:

$$H_{k,\text{Rx}} = \frac{m_{\text{wall}} + 1}{2\pi d_{k,\text{Rx}}^2} \cos(\phi_{k,\text{Rx}}) A_p T_s(\psi) g(\psi) \cos(\psi_{k,\text{Rx}}), \quad (2.39)$$

The LOS DC channel gain between all the reflective elements of the room and the Rx are grouped to give the Rx transfer vector  $\mathbf{r}$  which is defined by its transpose:

$$\mathbf{r}^T = (H_{1,\text{Rx}}, H_{2,\text{Rx}}, \dots, H_{N_E,\text{Rx}}). \quad (2.40)$$

According to [75], the total diffuse DC channel gain with infinite reflection can be calculated by the matrix product:

$$H_{\text{diff}} = \mathbf{r}^T \mathbf{G}_\rho (\mathbf{I} - \mathbf{H} \mathbf{G}_\rho)^{-1} \mathbf{t}. \quad (2.41)$$

where  $\mathbf{I}$  denotes the unity matrix.

### 2.5.2.1 Channel Impulse Response

According to [76], the VLC channel impulse response between the Tx and the Rx in the frequency domain can be modeled as:

$$H(f) = H_{\text{total}}(f)H_F(f), \quad (2.42)$$

where  $H_F(f)$  represents the front-end device frequency response. The effect of front-end elements is considered in this study. It has been shown in [70,71,77] that the front-end elements follow low-pass filter characteristics. Therefore, the front-end frequency response can be modeled by a first order low pass filter as [70, 73, 78]:

$$H_F(f) = \exp\left(-\frac{f}{v_e f_0}\right), \quad (2.43)$$

where  $f_0$  is the 3 dB cut-off frequency of the front-end filtering effect;  $v_e$  is the fitting coefficient and  $|H_F(f_0)|^2 = -3$  dB when  $v_e = 2.88$  [78].

## 2.6 LiFi Attocell Networks

In a typical point-to-point VLC system, the coverage area is in the order of a few square meters. In order to support wide coverage, mobility and seamless connectivity, the networked VLC system, namely LiFi attocell network is required. The LiFi attocell network utilizes multiple LED TxS or APs, needs to be implemented. Compared with a single Tx or AP, LiFi attocell networks can provide higher power efficiency as well as higher spectral efficiency by means of frequency reuse [79]. In a LiFi attocell network, APs deployment can be mainly classified into 4 categories: 1) square deployment; 2) hexagonal deployment; 3) poisson point process (PPP) deployment and 4) hard-core pointprocess (HCPP) deployment [73]. Typically, the deployment of LEDs in offices and rooms follows the square network. Therefore, the square network is considered in this study. Unlike RF TxS that are normally omnidirectional, optical TxS are intrinsically directional. The emitted light of an LED can be confined within a limited region. Therefore, optical attocell networks can be deployed in high density. When LDs or VCSELs is used as the TxS, narrow well-directed beams can result in extremely high density.

### 2.6.1 Interference Mitigation

Similar to other cellular systems, ICI in LiFi attocell networks can significantly compromise the system performance. The ICI is inevitable as APs are placed close to each other. Particularly, cell-edge users suffer from severe ICI. Despite the dense deployment of APs, due to ICI, LiFi may not provide a uniform coverage concerning data rate. Interference coordination mechanisms have been extensively investigated for VLC systems [9–13]. The commonly used technique is static resource partitioning [9]. By separating any two cells that reuse the same frequency resource with a minimum reuse distance, ICI is effectively mitigated. However, there is a significant loss in spectral efficiency. A combined wavelength division and code division multiple access scheme was proposed in [10]. Although this approach enhances the system bandwidth, it requires separate filters for each color band and thus creates additional

cost. In [11], the fractional frequency reuse (FFR) technique is proposed to mitigate ICI. The FFR scheme is a cost-effective approach to provide improvements both in cell-edge user performance and average spectral efficiency (ASE), but a low user-density will decrease the ASE significantly. Joint transmission (JT) has been proven to improve signal quality for cell-edge users [12]. In a JT system, a UE can be served by multiple nearby APs, thereby improving the acquired signal quality. The downside of the JT systems is the extra signaling overhead. Moreover, the space division multiple access scheme (SDMA) scheme using angle diversity transmitters (ADTs) proposed in [13] can mitigate ICI by generating concentrated beams to users at different locations.

## **2.6.2 Multiple Access Techniques**

Multiple access techniques are required to support multi-user data communications in optical attocell networks. In multi-user LiFi systems, an efficient multiple access scheme can help to avoid intra-cell interference and achieve multi-user diversity gains. In the following parts, we introduce four widely used multiple access schemes in LiFi cellular networks. These techniques include time division multiple access (TDMA), orthogonal frequency division multiple access (OFDMA), SDMA and carrier sense multiple access with collision detection (CSMA/CA).

### **2.6.2.1 TDMA**

When TDMA is adopted, all active users under the same optical cell utilize the whole available bandwidth in different time slots. In each time slot, only one of the active users can be served in an attocell. Although the TDMA scheme can be directly used in a LiFi attocell network, it requires synchronization which is difficult for mobile UEs [41]. In addition, ICI can significantly degrade the performance of TDMA [5]. Therefore, interference mitigation techniques are required to attenuate ICI.

### **2.6.2.2 OFDMA**

Due to the flexibility in resource allocation (RA), OFDMA has been widely adopted in RF networks [80]. By means of the OFDMA scheme, resources can be allocated in both time and frequency domains, where the minimum and indivisible time-frequency slots are known as resource units (RUs). A resource block (RB) is composed of a number of RUs. It is evident that allocating those RUs to different users is more efficient and flexible than only allocating subcarriers or time slots. Therefore, OFDMA has been recently considered as a promising and viable solution for downlink transmission. Detailed analysis of the OFDMA scheme are discussed in Chapter 4.

### **2.6.2.3 SDMA**

SDMA is a well-known multiple access scheme in RF [81]. In RF, by changing the amplitude and phase of the signals transmitted by an antenna array, directional narrow beams are generated. This method cannot be directly implemented in a LiFi attocell since intensity

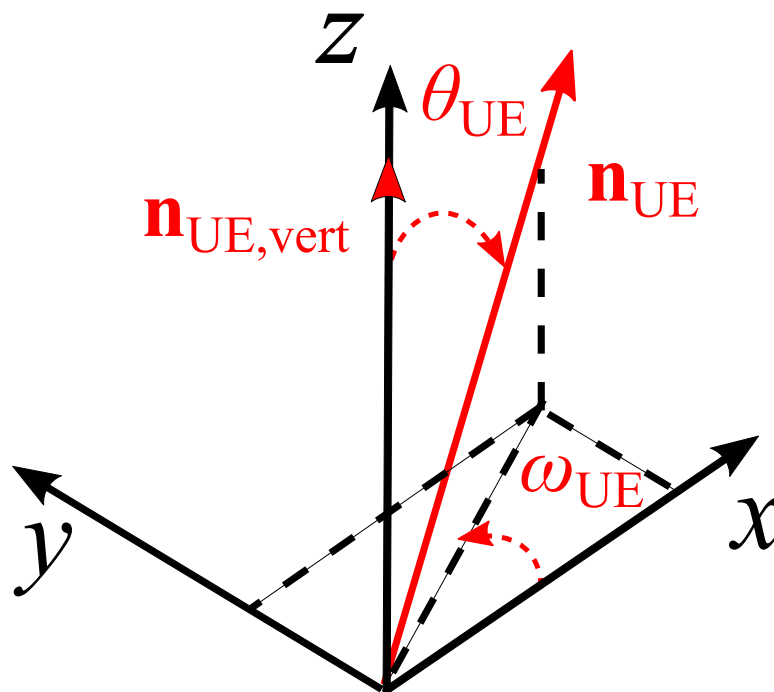


**Figure 2.6:** Representation of random UE orientation.

modulation (IM)/DD is adopted. However, directional light beams can be generated easily in LiFi as optical TxS have an inherent feature of a confined FOV. In an optical SDMA system, the AP is composed of multiple optical TxS with narrow well-directed beams. Unlike TDMA, the SDMA scheme enables simultaneous transmission to different active users. Therefore, within a single time slot, multiple active users can be served. With the knowledge of user location, the interference between these narrow beams can be substantially reduced [18].

#### 2.6.2.4 CSMA/CA

In CSMA/CA, the nodes try to avoid collision by listening to the channel. Then, the data packet will only be transmitted when the channel is found to be idle. In CSMA/CA, the request to send (RTS) and clear to send (CTS) signals are exchanged between the Rx and Tx, which is known as the RTS/CTS handshake mechanism. With the implementation of the handshake protocol, the hidden node problem, which happens when a node is visible to the AP while not to other nodes, can be addressed. A detailed explanation and performance analysis of the CSMA/CA with RTS/CTS mechanism is provided in [82].

## 2.7 User Orientation and Mobility

### 2.7.1 Random Orientation Model

The orientation of a UE has a great impact on the channel DC gain according to (2.34). In [83], a model for the random orientation of mobile devices based on experiments is proposed

so that the system performance of LiFi attocell networks can be evaluated more accurately. The random orientation model can be described by two angles: the elevation angle of a UE,  $\theta_{\text{UE}}$ , and the azimuth angle of a UE,  $\omega_{\text{UE}}$ . The geometrical representation of  $\theta_{\text{UE}}$  and  $\omega_{\text{UE}}$  is manifested in Fig. 2.6. The probability density function (PDF) of  $\theta_{\text{UE}}$  can be modeled as the truncated Laplace distribution and it can be simplified as [83]:

$$f_{\theta}(\theta_{\text{UE}}) \cong \frac{\exp(-\frac{|\theta_{\text{UE}} - \mu_{\theta}|}{b_{\theta}})}{2b_{\theta}}, \quad 0 \leq \theta \leq \frac{\pi}{2}, \quad (2.44)$$

where  $b_{\theta} = \sqrt{\sigma_{\theta}^2/2}$ . The mean and scale parameters are set as  $\mu_{\theta} = 41.39^{\circ}$  and  $\sigma_{\theta} = 7.68^{\circ}$  [83]. In addition, the PDF of the azimuth angle of a UE,  $\omega_{\text{UE}}$ , is modeled as a uniform distribution. It is assumed that the UE is initially pointing vertically upward and  $\mathbf{n}_{\text{UE,vert}} = [0, 0, 1]^T$ . The normal vector of the UE after rotation becomes  $\mathbf{n}_{\text{UE}}$ . The rotation can be simplified as rotating around the y-axis with  $\theta_{\text{UE}}$  and then rotating around z-axis with  $\omega_{\text{UE}}$ , which can be described by rotation matrices  $\mathbf{R}(\theta_{\text{UE}})$  and  $\mathbf{R}(\omega_{\text{UE}})$  separately [84]. Thus,  $\mathbf{n}_{\text{UE}}$  is given by:

$$\begin{aligned} \mathbf{n}_{\text{UE}} = \mathbf{R}(\omega_{\text{UE}})\mathbf{R}(\theta_{\text{UE}})\mathbf{n}_{\text{UE,vert}} &= \begin{bmatrix} \cos \omega_{\text{UE}} & -\sin \omega_{\text{UE}} & 0 \\ \sin \omega_{\text{UE}} & \cos \omega_{\text{UE}} & 0 \\ 0 & 0 & 1 \end{bmatrix} \begin{bmatrix} \cos \theta_{\text{UE}} & 0 & \sin \theta_{\text{UE}} \\ 0 & 1 & 0 \\ -\sin \theta_{\text{UE}} & 0 & \cos \theta_{\text{UE}} \end{bmatrix} \begin{bmatrix} 0 \\ 0 \\ 1 \end{bmatrix} \\ &= [\sin \theta_{\text{UE}} \cos \omega_{\text{UE}}, \sin \theta_{\text{UE}} \sin \omega_{\text{UE}}, \cos \theta_{\text{UE}}]^T \end{aligned} \quad (2.45)$$

## 2.7.2 Random Waypoint Mobility Model

There are plenty of mobility models proposed in the literature. Among them, the random waypoint (RWP) mobility model is one of the most simple and well-known models that is considered for the simulation of the user mobility either for indoor or outdoor environments [85]. In [86], the random waypoint (RWP) mobility model was initially introduced to model human movement in a random manner. At each waypoint, the following properties need to be satisfied in order to move to the next waypoint: i) the random destinations are chosen uniformly; ii) the movement path is a straight line; and iii) during the movement, the speed is constant. At the  $n$ -th movement period, the current waypoint is  $\mathbf{P}_{n-1} = (x_{n-1}, y_{n-1})$  and the next waypoint is  $\mathbf{P}_n = (x_n, y_n)$ . The velocity of UE at the  $n$ -th movement period is denoted at  $V_n$ . Therefore, the RWP mobility model can be mathematically expressed as an infinite sequences of triples:  $\{(\mathbf{P}_{n-1}, \mathbf{P}_n, V_n)\}_{n \in \mathbb{N}}$ .

## 2.7.3 Orientation-based Random Waypoint Mobility Model

In this section, we describe the orientation-based random waypoint (ORWP) which provides a more realistic framework for the analysis of system performance in LiFi networks [83, 87, 88]. In fact, the ORWP model incorporates the device orientation, which is modeled based on the experimental measurements, into the RWP mobility model. This method was developed in [89]. It is shown that the random orientation for walking users can be modeled as a correlated Gaussian distribution with the mean of  $\mathbb{E}[\theta] = 30^{\circ}$  and variance of  $\sigma_{\theta}^2 = 7.78^{\circ}$ . A first-order autoregressive (AR) model can be exploited to generate correlated random samples of device

orientation. Therefore, the  $i$ -th sample of AR(1) can be obtained as [83]:

$$\theta[i] = c_0 + c_1\theta[i-1] + w[i], \quad (2.46)$$

where  $w[i]$  is a white noise process with the variance of  $\sigma_w$ . To guarantee that the random process (RP),  $\theta$ , is wide-sense stationary, the condition  $|c_1| < 1$  should be met. The factors  $c_0$ ,  $c_1$  and the variance  $\sigma_w$  can be obtained based on the mean, variance and coherence time of the experimental measurements as follow:

$$c_0 = (1 - c_1)\mathbb{E}[\theta], \quad c_1 = 0.05^{\frac{T_s}{T_{c,\theta}}}, \quad \sigma_w^2 = (1 - c_1^2)\sigma_\theta^2, \quad (2.47)$$

where  $T_s$  is the sampling time and  $T_{c,\theta}$  is the coherence time of the RP,  $\theta$ . The coherence time is obtained based on the least-squares spectral analysis (LSSA) technique from the experimental measurements, which is described in detail in [90].

## 2.8 Summary

In this chapter, a brief history of LiFi has been introduced. Then, the characteristic of optical Tx and Rx front-end elements have been explained, which include: LED, LD, PIN diode, APD, SPAD, concentrator as well as ADR. Also, O-OFDM has been described as it is one of the most widely used multiple carrier modulation methods. With these fundamental concepts, the VLC channel models including both LOS and NLOS links have been provided. Moreover, the concept of LiFi attocell networks have been presented. Interference mitigation and different multiple access techniques have been discussed as well. Afterwards, two limiting factors of the LiFi system have been introduced, which are random device orientation and user mobility.



---

## Chapter 3

# **Interference Mitigation using Optimized Angle Diversity Receiver in LiFi Cellular Network**

---



### 3.1 Introduction

The angle diversity reception, first proposed in [14], allows the receiver (Rx) to achieve a wide field of view (FOV) and high optical gain simultaneously. An angle diversity receivers (ADRs) is composed of multiple narrow-FOV photodiodes (PDs) facing different directions. In [15–20], the ADR is used to address the issue of inter-cell interference (ICI) as well as frequency reuse in light-fidelity (LiFi) cellular systems, and different signal combining schemes are investigated. However, the proposed ADR structure is hard to implement and the optimum ADR design is not given. Moreover, the system is assumed to be interference limited instead of noise limited in [18], which is not always true as the ADR can mitigate most of ICI with noise being the dominated part. Recently, due to the lower channel correlation achieved from the angle diversity scheme, ADRs are introduced to improve the performance of indoor multiple-input multiple-output (MIMO)-visible light communication (VLC) systems, and the pyramid receivers (PRs) are proposed [23]. The generalized structure of truncated pyramid receivers (TPRs) are given in [24] to reduce the signal to interference-plus-noise ratio (SINR) fluctuation. However, the optimum structures of the ADRs are not given and therefore the performance gain is not fully exploited. In addition, to obtain a more accurate evaluation of the system performance, the following three factors must be taken into consideration: 1) *User Device Orientation*: Most of the studies on ADRs assume that the receiving device is pointed vertically upward. However, the random orientation of mobile devices can significantly affect the direct current (DC) channel gain and thus the system performance [29, 83]. Therefore, the random orientation model of the user equipment (UE) in Chapter 2.7.1 needs to be considered. This model will be applied in this study to evaluate the system more accurately; 2) *Diffuse Link Signal Propagation*: The non-line-of-sight (NLOS) link is neglected in most LiFi and VLC studies and only the line-of-sight (LOS) channel is considered [7–12]. In [73], it is shown that the LOS link is the dominant link and the effect of the reflected signal can be neglected. However, the UE is assumed to be positioned vertically upward, which is not realistic for mobile devices. In this study, we consider the effect of reflection when random device orientation is applied and the results show that the diffuse link cannot be ignored. The frequency-domain method of the indoor VLC channel in Chapter 2.5.2 is used to simulate the impact of the diffuse link; 3) *Noise Power Spectral Density*: The noise power spectral density of the PD has a huge impact on the analysis of system performance. For different levels of noise power spectral density, the system could be noise-limited, interference-limited or noise-plus-interference limited, which could affect the choice of the signal combining schemes and the cell configurations.

### 3.2 LiFi Cellular Network Model

An indoor LiFi network is studied and it is assumed that the total number of UE and LiFi access points (APs) are  $N_{\text{UE}}$  and  $N_{\text{L}}$ , respectively. The set of APs is denoted by  $\mathcal{A} = \{\alpha \mid \alpha \in [1, N_{\text{L}}]\}$ . The set of users is denoted as  $\mathcal{U} = \{\mu \mid \mu \in [1, N_{\text{UE}}]\}$ . In order to mitigate the ICI in LiFi systems, one of the most effective ways is to use ADR as optical Rx [19]. An ADR consists of multiple directional PD with narrow FOV. Therefore, the ADR is used as the Rx in this chapter and the set of PDs on an ADR is denoted as  $\mathcal{P} = \{p \mid p \in [1, N_{\text{PD}}]\}$ , where  $N_{\text{PD}}$  denotes the total number of PDs on the ADR. The geometrical representation of the LiFi cellular network, where the ADR is used as the Rx, is

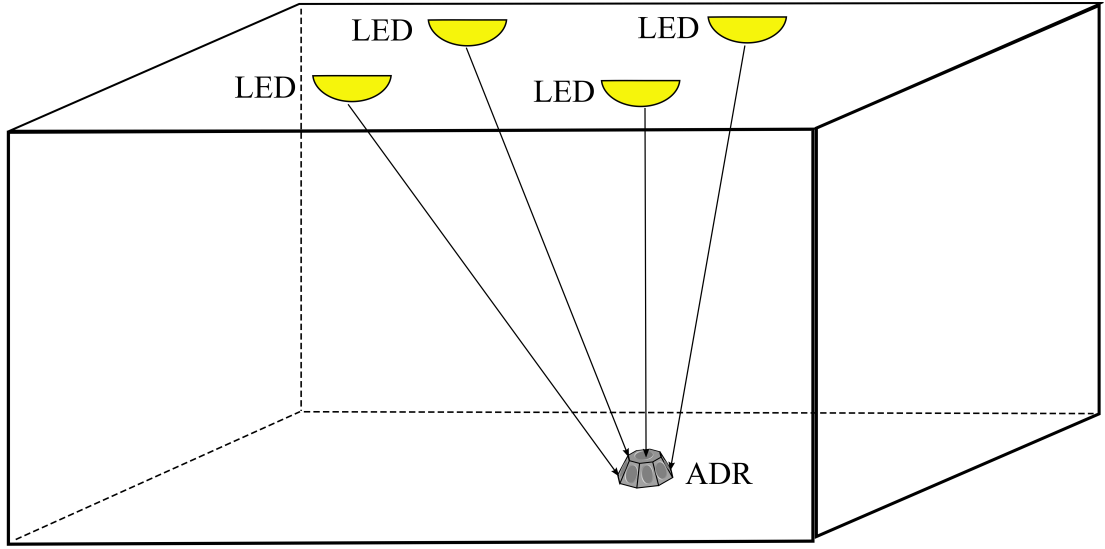


**Figure 3.1:** The LiFi cellular network using the ADR as the receiver

presented in Fig. 3.1. When the UE is pointing vertically upward, for both PRs and TPRs, the normal vector of the  $p$ -th PD is obtained as:

$$\mathbf{n}_{\text{PD,vert},p} = \begin{bmatrix} \sin(\theta_{\text{PD,vert},p}) \cos(\omega_{\text{PD,vert},p}) \\ \sin(\theta_{\text{PD,vert},p}) \sin(\omega_{\text{PD,vert},p}) \\ \cos(\theta_{\text{PD,vert},p}) \end{bmatrix}^T, \quad (3.1)$$

where  $\theta_{\text{PD,vert},p}$  and  $\omega_{\text{PD,vert},p}$  are the elevation angle and the azimuth angle of the  $p$ -th PD for vertical-orientated UEs, respectively.  $\theta_{\text{PD,vert},p}$  is denoted in (2.23a) while  $\omega_{\text{PD,vert},p}$  is given in (2.23b). However, the normal vector of the UE will change due to the random rotation. The random orientation model is described in Section 2.7.1. The rotation matrices  $\mathbf{R}(\theta_{\text{UE}})$  and  $\mathbf{R}(\omega_{\text{UE}})$  are presented in (2.45). Thus, the normal vector of the  $p$ -th PD after the random rotation is obtained by:

$$\begin{aligned} \mathbf{n}_{\text{PD},p} &= \mathbf{R}(\omega_{\text{UE}}) \mathbf{R}(\theta_{\text{UE}}) \mathbf{n}_{\text{PD,vert},p} \\ &= \begin{bmatrix} C_1 \cos \omega_{\text{UE}} \cos \theta_{\text{UE}} - C_2 \sin \omega_{\text{UE}} + \sin \theta_{\text{UE}} \cos \omega_{\text{UE}} \cos(\theta_{\text{PD,vert},p}) \\ C_1 \sin \omega_{\text{UE}} \cos \theta_{\text{UE}} + C_2 \cos \omega_{\text{UE}} + \sin \theta_{\text{UE}} \sin \omega_{\text{UE}} \cos(\theta_{\text{PD,vert},p}) \\ -C_1 \sin \theta_{\text{UE}} + \cos \theta_{\text{UE}} \cos(\theta_{\text{PD,vert},p}) \end{bmatrix}, \end{aligned} \quad (3.2)$$

where

$$C_1 = \sin(\theta_{\text{PD,vert},p}) \cos(\omega_{\text{PD,vert},p}), \quad (3.3a)$$

$$C_2 = \sin(\theta_{\text{PD,vert},p}) \sin(\omega_{\text{PD,vert},p}). \quad (3.3b)$$

Based on (3.2), after the random rotation, the elevation angle of the  $p$ -th PD can be obtained as:

$$\theta_{\text{PD},p} = \cos^{-1} \left( -C_1 \sin \theta_{\text{UE}} + \cos \theta_{\text{UE}} \cos(\theta_{\text{PD,vert},p}) \right), \quad (3.4)$$

and the azimuth angle of the  $p$ -th PD can be expressed as:

$$\omega_{PD,p} = \tan^{-1} \left( \frac{C_1 \sin \omega_{UE} \cos \theta_{UE} + C_2 \cos \omega_{UE} + \sin \theta_{UE} \sin \omega_{UE} \cos(\theta_{PD,vert,p})}{C_1 \cos \omega_{UE} \cos \theta_{UE} - C_2 \sin \omega_{UE} + \sin \theta_{UE} \cos \omega_{UE} \cos(\theta_{PD,vert,p})} \right). \quad (3.5)$$

According to (2.16), the incidence angle of the  $p$ -th PD,  $\psi_p$ , can be obtained as:

$$\psi_p = \cos^{-1} \left( \frac{\mathbf{n}_{PD,p} \cdot \mathbf{d}}{\|\mathbf{d}\|} \right) \quad (3.6)$$

With the knowledge of  $\psi_p$ , the overall DC channel gain between the  $p$ -th PD of user  $\mu$  and the  $\alpha$ -th AP,  $H_{\alpha,\mu,p}$  can be obtained according to (2.34). In order to achieve high data rates, the direct current biased optical orthogonal frequency division multiplex (DCO-OFDM) described in Chapter 2.4.1 is used in this chapter. For an ADR, multiple PDs are receiving signals simultaneously. Thus, attention should be paid to the selection of the signal combining schemes. With the use of proper signal combining schemes, ADRs can reject ICI from the cell in the vicinity without losing the coverage. The details of the signal combining schemes are described in Chapter 2.3.7. There are different combining schemes such as equal gain combining (EGC), select best combining (SBC) and maximum ratio combining (MRC). An important metric to evaluate the link quality and capacity is the SINR. The number of orthogonal frequency division multiplex (OFDM) subcarriers is denoted as  $M$ . The SINR of user  $\mu$  on subcarrier  $m$  can be obtained based on [18] and [73]:

$$\begin{aligned} \gamma_{\mu,m} &= \frac{(\sum_{p=1}^{N_{PD}} \tau P_{tx} w_p H_{\alpha_s,\mu,p})^2 / (M-2)}{\sum_{p=1}^{N_{PD}} w_p^2 \kappa^2 N_0 B_L / M + \sum_{\alpha_i \in \mathcal{A} \setminus \{\alpha_s\}} (\tau P_{tx} \sum_{p=1}^{N_{PD}} w_p H_{\alpha_i,\mu,p})^2 / (M-2)} \\ &= \frac{(\sum_{p=1}^{N_{PD}} \tau P_{tx} w_p H_{\alpha_s,\mu,p})^2}{\sum_{p=1}^{N_{PD}} w_p^2 \kappa^2 N_0 B_L (M-2) / M + \sum_{\alpha_i \in \mathcal{A} \setminus \{\alpha_s\}} (\tau P_{tx} \sum_{p=1}^{N_{PD}} w_p H_{\alpha_i,\mu,p})^2} \end{aligned} \quad (3.7)$$

where  $\tau$  is the optical-to-electrical conversion efficiency;  $P_{tx}$  is the transmitted optical power of the AP;  $w_p$  denotes the combining weight of PD  $p$ ;  $H_{\alpha_s,\mu,p}$  is the overall DC channel gain between the PD  $p$  of user  $\mu$  and the serving AP  $\alpha_s$ ;  $\kappa$  is the ratio of DC optical power to the square root of electrical signal power;  $N_0$  represents the noise power spectral density of the additive white Gaussian noise and  $B_L$  is the baseband modulation bandwidth;  $H_{\alpha_i,\mu,p}$  is the overall DC channel gain between the PD  $p$  of user  $\mu$  and the interfering LiFi AP  $\alpha_i$ . The serving AP  $\alpha_s$  for user  $\mu$  is selected based on the signal strength strategy (SSS) where the UEs are connected to the APs providing the best received signal strength. Hence, the serving AP  $\alpha_s$  for user  $\mu$  can be expressed as:

$$\alpha_s = \arg \max_{\alpha \in \mathcal{A}} \sum_{p=1}^{N_{PD}} |H_{\alpha,\mu,p}|^2. \quad (3.8)$$

When the EGC scheme is adopted, the signals received by the PDs are simply combined with equal weights, which can be described as:

$$w_p = 1, \text{ for any } p \in \mathcal{P}. \quad (3.9)$$

In terms of the SBC scheme, a switch circuit is required to output the information from the PD with the highest SINR. Hence, the weight of each PD is given as:

$$w_p = \begin{cases} 1, & p = p_s \\ 0, & \text{otherwise} \end{cases}, \quad (3.10)$$

where  $p_s$  can be obtained by:

$$p_s = \arg \max_{p \in \mathcal{P}} \frac{(\tau P_{\text{tx}} H_{\alpha_s, \mu, p})^2}{\kappa^2 N_0 B_L (M - 2)/M + \sum_{\alpha_i \in \mathcal{A} \setminus \{\alpha_s\}} (\tau P_{\text{tx}} H_{\alpha_i, \mu, p})^2}. \quad (3.11)$$

On the subject of the MRC schemes, the weight for each PD is denoted as [18]:

$$w_p = \frac{(\tau P_{\text{tx}} H_{\alpha_s, \mu, p})^2}{\kappa^2 N_0 B_L (M - 2)/M + \sum_{\alpha_i \in \mathcal{A} \setminus \{\alpha_s\}} (\tau P_{\text{tx}} H_{\alpha_i, \mu, p})^2}. \quad (3.12)$$

Based on the Shannon capacity, assuming electrical signals after optical to electrical conversion, the data rate of the  $\mu$ -th UE on subcarrier  $m$  can be expressed as [91]:

$$\zeta_{\mu, m} = \begin{cases} \frac{B_L}{M} \log_2(1 + \gamma_{\mu, m}), & m \in [1, M/2 - 1] \\ 0, & \text{otherwise} \end{cases} \quad (3.13)$$

Hence, the data rate of the  $\mu$ -th UE can be obtained by  $\zeta_\mu = \sum_{m=1}^{M/2-1} \zeta_{\mu, m}$ .

### 3.3 Visibility of an Angle Diversity Receiver

The visibility of an ADR was first defined in [21]. An AP is visible to a PD when the AP is within the FOV of the PD. Hence, with the UE location  $\mathbf{p}_{\text{UE}}$  and the  $p$ -th PD orientation  $(\theta_{\text{PD}, p}, \omega_{\text{PD}, p})$ , the visibility factor between the  $p$ -th PD on the ADR and the  $\alpha$ -th AP can be expressed as:

$$v_{\alpha, p}(x_{\text{UE}}, y_{\text{UE}}, \theta_{\text{PD}, p}, \omega_{\text{PD}, p}, \Psi_c) = \begin{cases} 0, & \psi_{\alpha, p} > \Psi_c \\ 1, & \text{otherwise} \end{cases}, \text{ and } \psi_{\alpha, p} = \arccos \left( \frac{\mathbf{n}_{\text{PD}, p} \cdot \mathbf{d}_\alpha}{\|\mathbf{d}_\alpha\|} \right), \quad (3.14)$$

where  $\mathbf{d}_\alpha = (x_\alpha - x_{\text{UE}}, y_\alpha - y_{\text{UE}}, z_\alpha - z_{\text{UE}})$  is the distance vector between the AP  $\alpha$  and the UE;  $\mathbf{n}_{\text{PD}, p}$  is the normal vector of the  $p$ -th PD;  $\Psi_c$  denotes the FOV of the PD;. The dot product is denoted as  $(\cdot)$  and  $\|\cdot\|$  is the norm operator. In terms of ADR, an AP is visible to an ADR if and only if the AP is visible to at least one of the PDs on the ADR. Hence, for a given UE position  $(x_{\text{UE}}, y_{\text{UE}})$  and UE orientation  $(\theta_{\text{UE}}, \omega_{\text{UE}})$ , the visibility of the ADR can be written

as [21]:

$$V(x_{\text{UE}}, y_{\text{UE}}, \theta_{\text{UE}}, \omega_{\text{UE}}, \Psi_c) = \begin{cases} 1, & \text{if } \sum_{\alpha \in \mathcal{A}} \sum_{p \in \mathcal{P}} v_{\alpha,p} \neq 0 \\ 0, & \text{otherwise} \end{cases}. \quad (3.15)$$

It is assumed that both  $x_{\text{UE}}$  and  $y_{\text{UE}}$  follow a uniform distribution. Also, as discussed in Chapter 2.7.1, the azimuth angle of a UE follows uniform distribution. The probability of visibility of an ADR is defined as the probability that there is at least one AP within the projection area of the ADR for all UE positions and orientations, and it can be expressed as follows:

$$\begin{aligned} p_v(\Psi_c) &= \int_{x_{\text{UE}}} \int_{y_{\text{UE}}} \int_{\theta_{\text{UE}}} \int_{\omega_{\text{UE}}} V(x_{\text{UE}}, y_{\text{UE}}, \theta_{\text{UE}}, \omega_{\text{UE}}, \Psi_c) \frac{1}{X_{\text{UE}}} \frac{1}{Y_{\text{UE}}} \frac{1}{\Omega_{\text{UE}}} f_{\theta}(\theta_{\text{UE}}) dx_{\text{UE}} dy_{\text{UE}} d\theta_{\text{UE}} d\omega_{\text{UE}} \\ &= \int_{x_{\text{UE}}} \int_{y_{\text{UE}}} \int_{\theta_{\text{UE}}} \int_{\omega_{\text{UE}}} \frac{V(x_{\text{UE}}, y_{\text{UE}}, \theta_{\text{UE}}, \omega_{\text{UE}}, \Psi_c)}{X_{\text{UE}} Y_{\text{UE}} \Omega_{\text{UE}}} f_{\theta}(\theta_{\text{UE}}) dx_{\text{UE}} dy_{\text{UE}} d\theta_{\text{UE}} d\omega_{\text{UE}} \end{aligned}, \quad (3.16)$$

where  $X_{\text{UE}}$ ,  $Y_{\text{UE}}$  and  $\Omega_{\text{UE}}$  are the range of  $x_{\text{UE}}$ ,  $y_{\text{UE}}$  and  $\omega_{\text{UE}}$ , respectively. Hence, it can be obtained that  $X_{\text{UE}} = \max(x_{\text{UE}}) - \min(x_{\text{UE}})$ ,  $Y_{\text{UE}} = \max(y_{\text{UE}}) - \min(y_{\text{UE}})$  and  $\Omega_{\text{UE}} = \max(\omega_{\text{UE}}) - \min(\omega_{\text{UE}})$ .

## 3.4 The Optimum Field of View

### 3.4.1 Optimization Problem

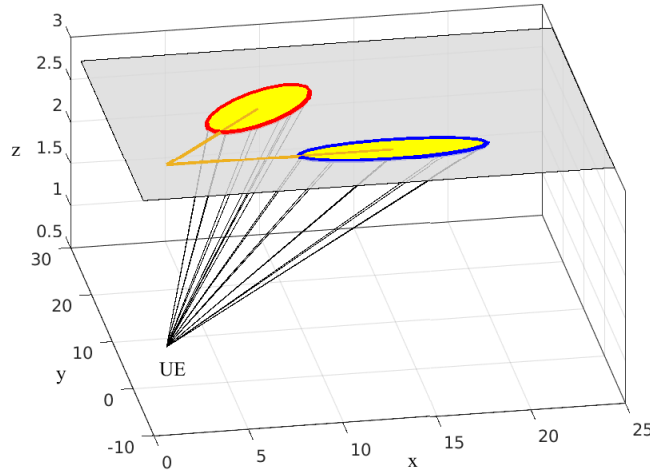
In (2.34), the LOS channel gain  $H_{\text{LOS}}$  is a convex function of  $\Psi_c$  and decreases monotonically. Hence, the smaller the  $\Psi_c$ , the higher the channel gain. However, when the  $\Psi_c$  of the PD is too small, there is a high chance that no APs are visible to the ADR and the LOS link cannot be constructed. Thus, there is a trade off between the LOS channel gain and visibility. The optimization problem is formulated as maximizing the LOS channel gain based on the constraint that the ADR should provide visibility for all UE locations. Thus, the optimization function is written as:

$$\begin{aligned} &\arg \max_{\Psi_c} H_{\text{LOS}}(\Psi_c), \\ &\text{subject to } p_v(\Psi_c) = 1. \end{aligned} \quad (3.17)$$

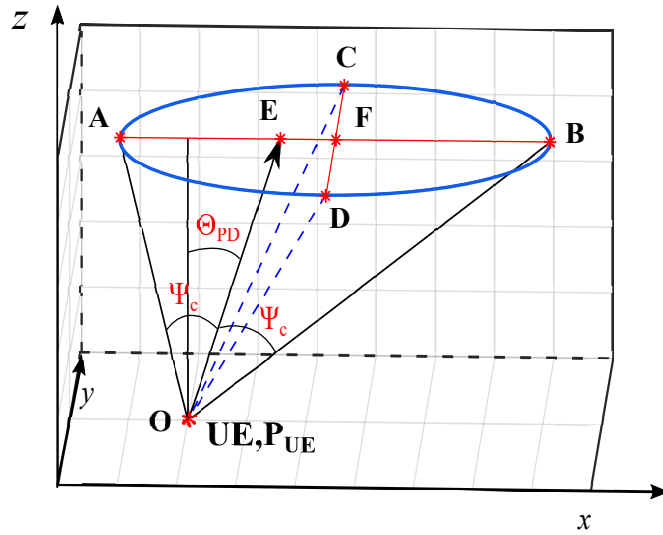
The solution set of  $p_v(\Psi_c) = 1$  is denoted as  $\mathbb{R}$  and  $\Psi_{c,\min}$  is the minimum value in  $\mathbb{R}$ . As  $H_{\text{LOS}}(\Psi_c)$  is a monotonically decreasing function, the maximum  $H_{\text{LOS}}(\Psi_c)$  is achieved when  $\Psi_c = \Psi_{c,\min}$ . Hence, the optimization problem can be solved by finding the minimum value of  $\Psi_c$ ,  $\Psi_{c,\min}$ , which satisfies  $p_v = 1$ . Based on (3.16),  $\Psi_{c,\min}$  cannot be solved in a closed form. Therefore, in the following parts, we will study the ADRs' projection area on the ceilings to solve the solution set  $\mathbb{R}$  and find a closed form for  $\Psi_{c,\min}$ .

### 3.4.2 Projection area of Angle Diversity Receiver on the Ceiling

Firstly, we study the projection area of a PR for a vertical-orientated UE. Fig. 3.2 (a) demonstrates that the projection area of the PD mounted on the PR is an ellipse on the ceiling. The projection area of the 1-st PD with  $(\theta_{PD,1} = \Theta_{PD}, \omega_{PD,1} = 0)$  is illustrated in Fig. 3.2 (b).



(a) Projection area of PDs on the ceiling.



(b) Projection area of the 1-st PD.

**Figure 3.2:** Projection area of PDs on the ceiling

The point  $\mathbf{O}$  represents the location of the UE,  $\mathbf{p}_{UE}$ , and  $\mathbf{OE}$  represents the normal vector of the PD. The intersection point of the normal vector with the ceiling is  $\mathbf{E}$ . The coordinate of  $\mathbf{E}$  is denoted as  $(x_e, y_e, z_e)$  and points  $\mathbf{A}$ ,  $\mathbf{B}$ ,  $\mathbf{C}$ ,  $\mathbf{D}$ ,  $\mathbf{F}$  are denoted in the same way. Points  $\mathbf{A}$  and  $\mathbf{B}$  are the vertices of the ellipse. Points  $\mathbf{C}$  and  $\mathbf{D}$  are the co-vertices of the ellipse. The center point of the ellipse is denoted as  $\mathbf{F}$ . The angle between each of the four vectors,  $\mathbf{OA}$ ,  $\mathbf{OB}$ ,

**OC**, **OD** with **OE** is  $\Psi_c$ . The length of the semi-major and semi-minor axes of the ellipse are represented by  $a$  and  $b$  separately. The length of semi-major axes  $a$  is denoted as:

$$\begin{aligned} a &= \frac{|\mathbf{AB}|}{2} = \frac{h \tan(\Psi_c + \Theta_{PD}) + h \tan(\Psi_c - \Theta_{PD})}{2} \\ &= \frac{h \sin(2\Psi_c)}{\cos(2\Psi_c) + \cos(2\Theta_{PD})}. \end{aligned} \quad (3.18)$$

where  $h$  is the vertical distance between the AP and UE. As **A**, **B**, **E**, **F** and **O** are on the same  $xz$ -plane,

$$y_a = y_b = y_e = y_f = y_{UE}. \quad (3.19)$$

As **A**, **B**, **C**, **D**, **E** and **F** are on the ceiling,

$$z_a = z_b = z_c = z_d = z_e = z_f = z_{AP}, \quad (3.20)$$

where  $z_{AP}$  is the height of the AP. As **C** and **D** are on the same  $yz$ -plane with **F**, the coordinates  $x$  of these points are represented by:

$$\begin{aligned} x_c = x_d = x_f = x_{UE} + (a - h \tan(\Psi_c - \Theta_{PD})) \\ = x_{UE} + \frac{h \sin(2\Theta_{PD})}{\cos(2\Psi_c) + \cos(2\Theta_{PD})}. \end{aligned} \quad (3.21)$$

From Fig. 3.2 (b), we know that  $x_e = h \tan(\Theta_{PD}) + x_{UE}$ . Based on the parameters above, **OE** and **OC** are given by:

$$\mathbf{OE} = (h \tan(\Theta_{PD}), 0, h) \quad (3.22a)$$

$$\mathbf{OC} = \left( \frac{h \sin(2\Theta_{PD})}{\cos(2\Psi_c) + \cos(2\Theta_{PD})}, b, h \right) \quad (3.22b)$$

Since  $\cos(\Psi_c) = \frac{\mathbf{OE} \cdot \mathbf{OC}}{|\mathbf{OE}| |\mathbf{OC}|}$ ,  $b$  can be obtained as:

$$b = \frac{\sqrt{2} h \sin(\Psi_c)}{\sqrt{\cos(2\Psi_c) + \cos(2\Theta_{PD})}}. \quad (3.23)$$

Hence, the projection area of the 1-st PD, where  $\theta_{PD,1} = \Theta_{PD}$  and  $\omega_{PD,1} = 0$ , is given by:

$$\frac{(x_{\text{ellipse},1} - x_{\text{center}})^2}{a^2} + \frac{(y_{\text{ellipse},1} - y_{\text{center}})^2}{b^2} = 1, \quad (3.24)$$

where the center of the ellipse is given by  $(x_{\text{center}} = x_f, y_{\text{center}} = y_f)$ . Fig. 3.3 depicts that the shape of the projection area of the  $p$ -th PD can be obtained by rotating the 1-st PD around  $(x_{UE}, y_{UE})$  with an angle of  $\omega_{PD,p}$ , which can be represented as:

$$\begin{aligned} \begin{bmatrix} x_{\text{ellipse},p} - x_{UE} \\ y_{\text{ellipse},p} - y_{UE} \end{bmatrix} &= R_{xy}(\omega_{PD,p}) \begin{bmatrix} x_{\text{ellipse},1} - x_{UE} \\ y_{\text{ellipse},1} - y_{UE} \end{bmatrix} \\ &= \begin{bmatrix} \cos \omega_{PD,p} & -\sin \omega_{PD,p} \\ \sin \omega_{PD,p} & \cos \omega_{PD,p} \end{bmatrix} \begin{bmatrix} x_{\text{ellipse},1} - x_{UE} \\ y_{\text{ellipse},1} - y_{UE} \end{bmatrix}. \end{aligned} \quad (3.25)$$

The TPR can be seen as the combination of a PR, where  $N_{PR} = N_{TPR} - 1$ , and a central

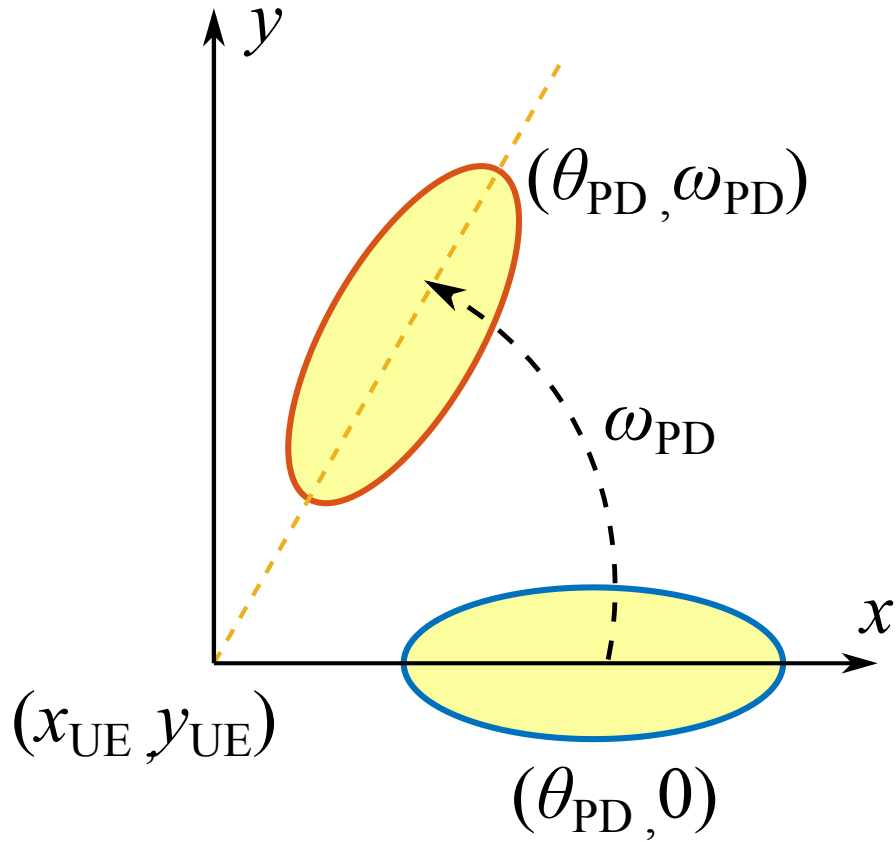


**Figure 3.3:** Projection area of PD on the  $xy$ -plane

PD. When the UE is facing vertically upward, the projection area of the central PD is a circle. Therefore, the shape of the projection area of the  $p$ -th PD on a TPR is given by:

$$\begin{bmatrix} x_{\text{ellipse},p} \\ y_{\text{ellipse},p} \end{bmatrix} = \begin{cases} \begin{bmatrix} \cos \omega_{PD,p} & -\sin \omega_{PD,p} \\ \sin \omega_{PD,p} & \cos \omega_{PD,p} \end{bmatrix} \begin{bmatrix} x_{\text{ellipse},1} - x_{UE} \\ y_{\text{ellipse},1} - y_{UE} \end{bmatrix} + \begin{bmatrix} x_{UE} \\ y_{UE} \end{bmatrix}, & \text{if } 1 \leq p < N_{\text{TPR}} \\ \begin{bmatrix} x_{\text{circle}} \\ y_{\text{circle}} \end{bmatrix}, & \text{if } p = N_{\text{TPR}} \end{cases}, \quad (3.26)$$

where  $x_{\text{circle}}^2 + y_{\text{circle}}^2 = (h \tan \Psi_c)^2$ .

### 3.4.3 Lower Bound of Field of View

For a fixed UE location, the ADR has the smallest projection area on the ceiling when vertically orientated. In other words, we will investigate the worst condition, i.e., the situation that an ADR is positioned vertically upward which provides the smallest projection area on the ceiling. Under other orientation scenarios, the projection area is larger. Based on (3.25) and (3.26), Fig. 3.4 illustrates the projection area of 4 different types of ADRs when the UE is at the cell corner, that is to say, the cross-point of four LiFi cells. The blue curve is the outer boundary of the projection area. On the outer boundary, the points that have the shortest distance to the



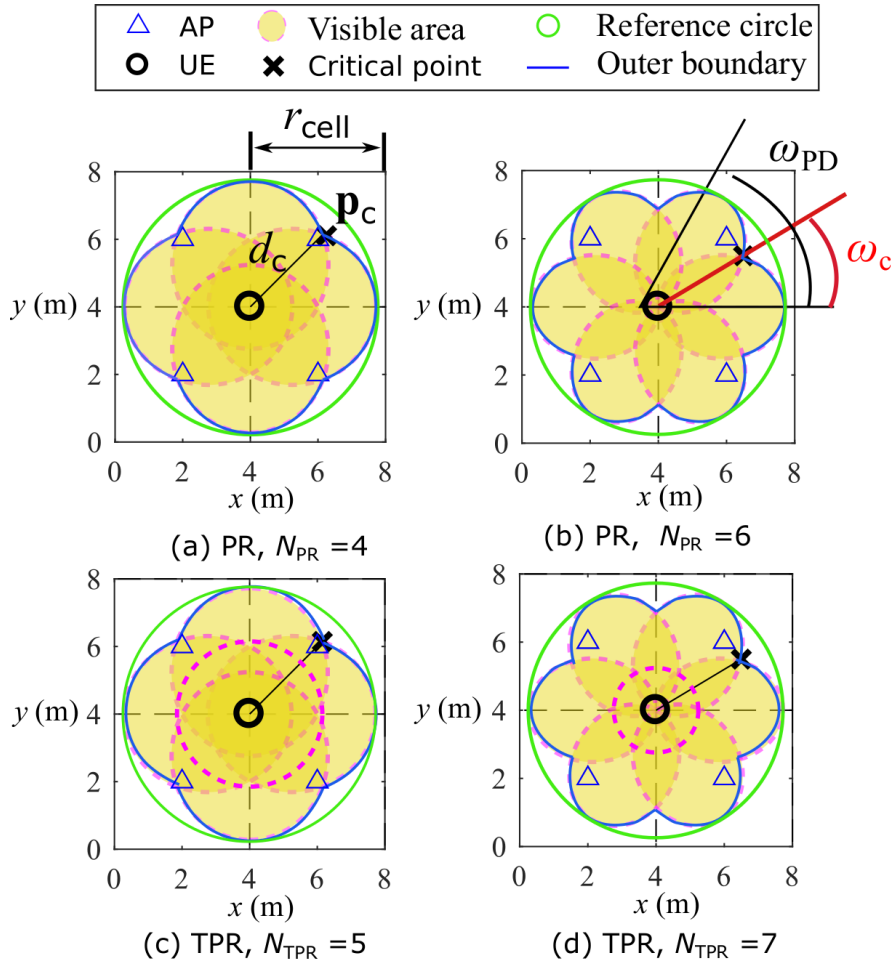


**Figure 3.4:** Projection area of PR and TPR with different number of PDs.

UE are defined as critical points,  $\mathbf{p}_c$ . Also,  $d_c$  denotes the horizontal distance between  $\mathbf{p}_c$  and the UE. To ensure that  $p_v = 1$ , there are two constraints. The detailed explanation of these constraints are given as follows:

### 3.4.3.1 Constraint I: The central area above the ADR should be visible to the ADR.

As shown in Fig. 3.5 (a), the total FOV of an ADR is represented as  $\Psi_{\text{total}}$ , which can be written as:

$$\Psi_{\text{total}} = \Psi_c + \Theta_{PD}. \quad (3.27)$$

In terms of PRs, if  $\Theta_{PD} \geq \Psi_c$ , then the central part is not covered by the projection area of the ADR as demonstrated in Fig. 3.5 (a). If the UE is in the cell center, then no APs will be visible to the ADR. Hence, the condition  $\Theta_{PD} \leq \Psi_c$  should be satisfied so that the area directly above the UE is covered by the projection area of the ADR. Based on this constraint and (3.27), the lower bound of  $\Psi_c$  can be obtained as:

$$\Psi_{c1,\min} = \frac{\Psi_{\text{total}}}{2}. \quad (3.28)$$

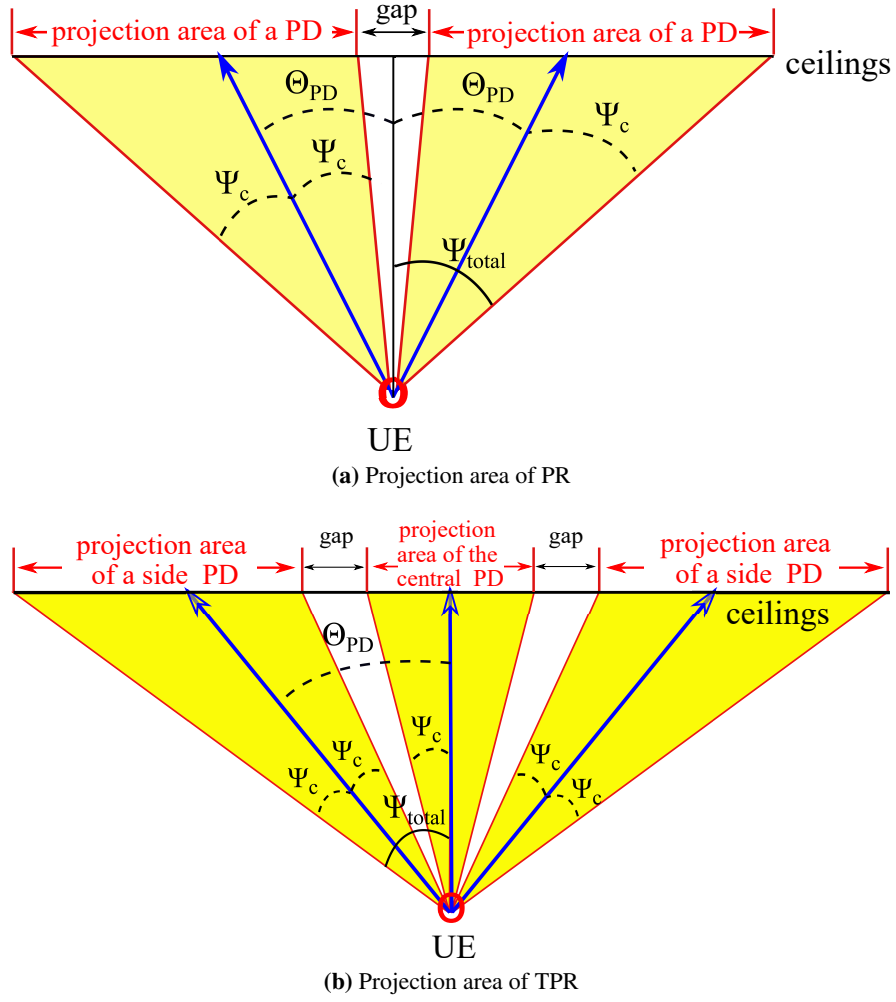


**Figure 3.5:** Projection area of ADR in  $xz$ -plane.

With respect to the TPR, the area directly above the UE is covered by the central PD orientating vertically upwards as illustrated in Fig. 3.5 (b). The concern should be the gap between projection area of the central PD and the side PD as shown in Fig. 3.5 (b). Therefore,  $\Theta_{PD} \leq 2\Psi_c$  is required to ensure there is no gap between them. By substituting this constraint into (3.27), it can be derived that:

$$\Psi_{c1,\min} = \frac{\Psi_{\text{total}}}{3}. \quad (3.29)$$

#### 3.4.3.2 Constraint II: The outer boundary of the projection area should be large enough.

The side length of a square cell is denoted as  $r_{\text{cell}}$  as shown in Fig. 3.4. The horizontal distance between the UE and the  $\alpha$ -th AP is denoted as  $d_{h,\alpha}$ . When the UE is at the cell corner,  $d_{h,\alpha} = \frac{\sqrt{2}}{2}r_{\text{cell}}$  for any  $\alpha \in \mathcal{A}$ . With the decrease of  $\Psi_c$ , the outer boundary of the projection

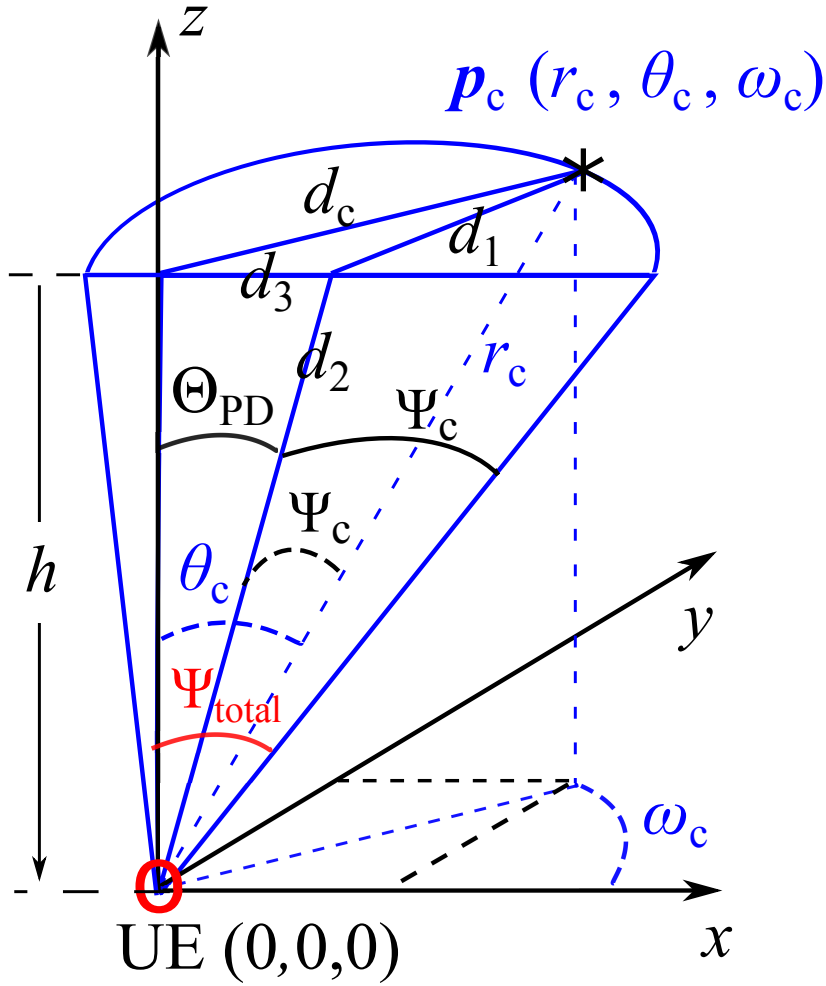


**Figure 3.6:** The geometrical representation of  $\Psi_c$ ,  $\Theta_{PD}$ ,  $\Psi_{total}$  and  $d_c$  in the spherical coordinate system.

area will decrease, which means  $d_c$  will decrease. If  $d_c$  is smaller than the horizontal distance from the AP to the cell corner, which is  $\frac{\sqrt{2}}{2}r_{cell}$ , there will be no APs within the projection area of the ADR for cell-corner users. Therefore, to ensure that at least one AP is visible to the cell-corner UE,  $d_c$  should be larger than the horizontal distance from the AP to the cell corner. By moving towards any direction, due to the symmetry, the cell-corner UE will get closer to at least one AP. In other words,

$$d_{c,min} = \max_{x_{UE}, y_{UE}} \left( \min_{\alpha} (d_{h,\alpha}) \right) = \frac{\sqrt{2}}{2}r_{cell}, \quad \text{subject to } \alpha \in \mathcal{A}. \quad (3.30)$$

That is to say, if there is at least one AP inside the outer boundary of the projection area for the cell-corner UE, then, when the UE moves to other locations, the AP will still be inside the outer boundary of the projection area. Hence, to meet the condition  $p_v = 1$ , it is required that  $d_c \geq \frac{\sqrt{2}}{2}r_{cell}$ . Also, it can be seen from Fig. 3.4 that  $\mathbf{p}_c$  is always inside the green reference circle, which has a radius of  $h \tan(\Psi_{total})$ . Hence,  $d_{c,min} \leq d_c \leq h \tan(\Psi_{total})$ , where

$d_{c,\min} = \frac{\sqrt{2}}{2}r_{\text{cell}}$ . Fig. 3.6 presents the geometrical relationship in a spherical coordinate system. The coordinate of  $\mathbf{p}_c$  is represented as  $(r_c, \theta_c, \omega_c)$  and  $\omega_c = \frac{\omega_{\text{PD},p}}{2}|_{p=2}$  for both PRs and TPRs. The geometrical relationships among  $d_1, d_2$  and  $d_3$ , illustrated in Fig. 3.6, can be represented as:

$$d_1^2 = d_2^2 + r_c^2 - 2d_2r_c \cos(\Psi_c), \quad (3.31)$$

$$d_1^2 = d_3^2 + d_c^2 - 2d_3d_c \cos(\omega_c), \quad (3.32)$$

$$d_2^2 = h^2 + d_3^2, \quad r_c^2 = h^2 + d_c^2, \quad d_3 = h \tan(\Theta_{\text{PD}}). \quad (3.33)$$

Substituting (3.32) and (3.33) into (3.31), we can get:

$$-d_c \cos \omega_c \tan(\Theta_{\text{PD}}) = h - \frac{\sqrt{h^2 + d_c^2} \cos(\Psi_c)}{\cos(\Theta_{\text{PD}})}. \quad (3.34)$$

Substituting (3.27) into (3.34), the elevation angle of each PD,  $\Theta_{\text{PD}}$ , on PRs is derived as:

$$\Theta_{\text{PD}} = F_1(d_c) = \tan^{-1} \frac{f_1(d_c)}{f_2(d_c)}, \quad (3.35)$$

where

$$\begin{aligned} f_1(d_c) &= \sqrt{h^2 + d_c^2} \cos(\Psi_{\text{total}}) - h, \\ f_2(d_c) &= d_c \cos(\omega_c) - \sqrt{h^2 + d_c^2} \sin(\Psi_{\text{total}}). \end{aligned} \quad (3.36)$$

The function  $F_1$  has one zero at  $z_1 = h \tan(\Psi_{\text{total}})$  and one pole at  $p_1 = \frac{h \sin(\Psi_{\text{total}})}{\sqrt{\cos^2(\Psi_{\text{total}}) - \sin^2(\omega_c)}}$ .

The derivative of  $F_1(d_c)$  is given by:

$$\frac{\partial F_1}{\partial d_c} = - \frac{h^2 \cos(\omega_c) \cos(\Psi_{\text{total}}) - h \sqrt{h^2 + d_c^2} \cos(\omega_c) + h d_c \sin(\Psi_{\text{total}})}{(f_1^2(d_c) + f_2^2(d_c)) \sqrt{h^2 + d_c^2}}. \quad (3.37)$$

By calculating the  $d_c$  satisfying  $\frac{\partial F_1}{\partial d_c} = 0$ , the two roots are denoted as:

$$d_{c1} = \frac{h \cos(\omega_c) \sin(\Psi_{\text{total}})}{\cos(\Psi_{\text{total}}) - \sin(\omega_c)}, \quad (3.38a)$$

$$d_{c2} = \frac{h \cos(\omega_c) \sin(\Psi_{\text{total}})}{\cos(\Psi_{\text{total}}) + \sin(\omega_c)}. \quad (3.38b)$$

When  $\sin(\omega_c) < \cos(\Psi_{\text{total}})$ , it can be proven that  $0 < d_{c2} < z_1 = h \tan(\Psi_{\text{total}}) < d_{c1}$  and  $z_1 \leq p_1$ . In addition,  $\frac{\partial^2 F_1(d_{c2})}{\partial^2 d_c} < 0$ . Therefore, for  $d_c \in (0, h \tan(\Psi_{\text{total}})]$ ,  $F_1$  has a local maximum at  $d_{c2}$ . When  $\sin(\omega_c) \geq \cos(\Psi_{\text{total}})$ ,  $p_1$  and  $d_{c1}$  do not have real value. It can also be proved that  $0 < d_{c2} < z_1$  and  $\frac{\partial^2 F_1(d_{c2})}{\partial^2 d_c} < 0$ . Similarly, for  $d_c \in (0, h \tan(\Psi_{\text{total}})]$ , there is a local maximum at  $d_{c2}$ . In summary, the upper bound of  $F_1$  is thus given by:

$$F_{1,\max} = \begin{cases} F_1(d_{c2}), & \text{if } d_{c,\min} \leq d_{c2} \\ F_1(d_{c,\min}), & \text{otherwise.} \end{cases} \quad (3.39)$$

According to (3.27),  $\Psi_c$  is given by:

$$\Psi_c = \Psi_{\text{total}} - \Theta_{\text{PD}} = \Psi_{\text{total}} - F_1(d_c). \quad (3.40)$$

Hence, the lower bound of  $\Psi_c$  set by Constraint II is denoted as:

$$\Psi_{c2,\min} = \begin{cases} F_2(d_{c2}), & \text{if } d_{c,\min} \leq d_{c2} \\ F_2(d_{c,\min}), & \text{otherwise.} \end{cases} \quad (3.41)$$

where

$$F_2(d_c) = \Psi_{\text{total}} - \tan^{-1} \frac{\sqrt{h^2 + d_c^2} \cos(\Psi_{\text{total}}) - h}{d_c \cos(\omega_c) - \sqrt{h^2 + d_c^2} \sin(\Psi_{\text{total}})}, \quad (3.42)$$

and

$$d_{c2} = \frac{h \cos(\omega_c) \sin(\Psi_{\text{total}})}{\cos(\Psi_{\text{total}}) + \sin(\omega_c)}. \quad (3.43)$$

### 3.4.3.3 Summary

Based on (3.28), (3.29) and (3.41), the lower bound of  $\Psi_c$  can be expressed as:

$$\Psi_{c,\min} = \max(\Psi_{c1,\min}, \Psi_{c2,\min}). \quad (3.44)$$

Therefore, the solution set  $\mathbb{R}$  is  $\Psi_{c,\min} \leq \Psi_c \leq \Psi_{\text{total}}$ . The channel gain and received signal power increases as  $\Psi_c$  decreases. Therefore, the optimum FOV is  $\Psi_{c,\min}$ .

## 3.5 Double Source Cell Configuration

In the conventional single source (SS) cell configuration, each cell is equipped with a single AP in the cell center. The double source (DS) cell configuration is proposed to further exploit the spatial diversity of the ADR in [20]. As demonstrated in Fig. 3.7, each LiFi AP consists of two sources which transmit the same information signals but with opposite polarity. These two sources are termed as the positive source and the negative source, which transmit the time domain signal  $s_{\text{pos}}(t)$  and  $s_{\text{neg}}(t)$  respectively. The dynamic range of them is from 0 to  $S_H$ . The relationship between  $s_{\text{pos}}(t)$  and  $s_{\text{neg}}(t)$  is represented as  $s_{\text{neg}}(t) = S_H - s_{\text{pos}}(t)$  [20]. The distance between the positive source and negative source is  $d_{\text{source}}$  as shown in Fig. 3.7. In terms of illumination, when the  $d_{\text{source}}$  is small, the illumination condition of DS cell configuration is similar to that of SS cell configuration. However, when  $d_{\text{source}}$  is large, illumination condition will be different and might not meet the indoor illumination requirement. In this case, extra dummy light source can be added in the system to compensate the illumination. In a single optical cell, the received optical signal at a PD is denoted as [20]:

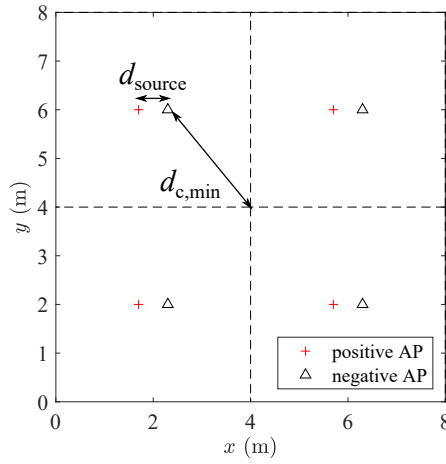
$$s_{\text{sum}}(t) = s_{\text{pos}}(t)H_{\text{pos}} + s_{\text{neg}}(t)H_{\text{neg}}, \quad (3.45)$$

where  $H_{\text{pos}}$  is the channel gain between the positive source and the PD;  $H_{\text{neg}}$  is the channel gain between the negative source and the PD. For a fair comparison, the total transmitting power for the SS system and DS system should be the same. Hence, the transmit power of each source

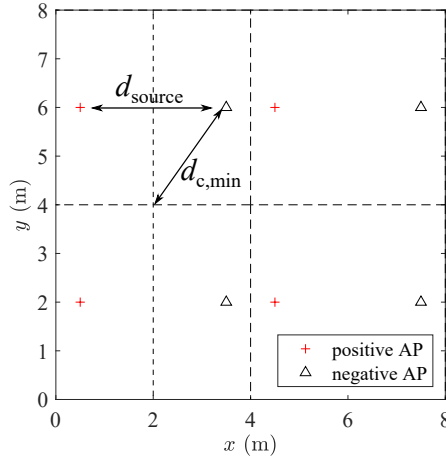
is halved when the DS configuration is applied and the received optical power at the PD can be written as [20]:

$$P_{\text{rx}} = \frac{P_{\text{tx}}}{2} |H_{\text{pos}} - H_{\text{neg}}| = \frac{P_{\text{tx}} \Delta H}{2}. \quad (3.46)$$

Generally, the Rx is closer to the desired AP than the interfering AP. For the desired AP, due to the narrow FOV of ADRs, one PD can hardly receive LOS signals from both the positive source and negative source simultaneously, and only one appears as the LOS channel gain. In respect



(a)  $d_{\text{source}} \leq \frac{r_{\text{cell}}}{2}$



(b)  $d_{\text{source}} > \frac{r_{\text{cell}}}{2}$

**Figure 3.7: DS cell configuration.**

of the interfering AP, the channel gains  $H_{\text{pos}}$  and  $H_{\text{neg}}$  are both NLOS. Hence, the difference between  $H_{\text{pos}}$  and  $H_{\text{neg}}$  is small and the interference is attenuated accordingly. Therefore, the DS cell configuration can suppress the signal power from interfering APs [20]. As the LOS interference can be mitigated by the narrow FOV of the ADR and the NLOS interference can be mitigated due to the adoption of the DS configuration, the SINR of user  $\mu$  on subcarrier  $m$

can be approximated by:

$$\tilde{\gamma}_{\mu,m} \approx \frac{(\sum_{p=1}^{N_{PD}} w_p \tau \frac{P_{tx}}{2} \Delta H_{\alpha_s, \mu, p})^2}{\sum_{p=1}^{N_{PD}} w_p^2 \kappa^2 N_0 B_L (M-2)/M}. \quad (3.47)$$

where  $\Delta H_{\alpha_s, \mu, p}$  is the overall DC channel gain between the PD  $p$  of user  $\mu$  and the serving AP  $\alpha_s$  in the DS system. As shown in Fig. 3.7,  $d_{c, \min}$  will vary according to the distance between the positive and negative sources, which can be represented as:

$$d_{c, \min} = \max_{x_{UE}, y_{UE}} \left( \min_{\alpha} (d_{h, \alpha}) \right) = \begin{cases} \sqrt{\left(\frac{r_{cell}}{2} - \frac{d_{source}}{2}\right)^2 + \left(\frac{r_{cell}}{2}\right)^2}, & \text{if } d_{source} \leq \frac{r_{cell}}{2} \\ \sqrt{\left(\frac{r_{cell}}{2}\right)^2 + \left(\frac{d_{source}}{2}\right)^2}, & \text{otherwise} \end{cases}, \quad \text{subject to } \alpha \in \mathcal{A}. \quad (3.48)$$

Therefore, the lower bound of  $\Psi_c$  for the DS cell system can be calculated based on (3.41) - (3.44).

### 3.6 Results and Discussions

Parameter	Symbol	Value
Transmitted optical power per AP	$P_{tx}$	10 W
Modulated bandwidth for LED	$B$	20 MHz
Physical area of the single PD	$A_p$	1 cm <sup>2</sup>
FOV of the single PD	$\Psi_c$	60°
The total FOV of an ADR	$\Psi_{total}$	60°
Half-intensity radiation angle	$\Phi_{1/2}$	60°
PD responsivity	$\tau$	0.5 A/W
Noise power spectral density	$N_0$	10 <sup>-21</sup> A <sup>2</sup> /Hz
Vertical distance between APs and UEs	$h$	2.15 m
Wall reflectivity	$\rho_{wall}$	0.8
Ceiling reflectivity	$\rho_{ceiling}$	0.8
Floor reflectivity	$\rho_{floor}$	0.3
Refractive index	$n_{ref}$	1.5
Optical filter gain	$G$	1
Permittivity of vacuum	$\epsilon_0$	8.854 × 10 <sup>-12</sup> F·m <sup>-1</sup>
Relative permittivity of silicon	$\epsilon_r$	11.68
Hole velocity	$v_p$	4.8 × 10 <sup>4</sup> m/s

**Table 3.1:** Parameters Lists [1]

### 3.6.1 Simulation Setups

The simulation setup is shown in Fig. 3.1. An indoor office scenario with a size of an  $8 \text{ m} \times 8 \text{ m} \times 3 \text{ m}$  is considered in this study, where 4 LiFi APs are deployed following a square topology as illustrated in Fig. 3.4. All of the users are uniformly distributed in the room and move randomly following the random waypoint (RWP) [83]. The other parameters used in the simulations are listed in Table 3.1.

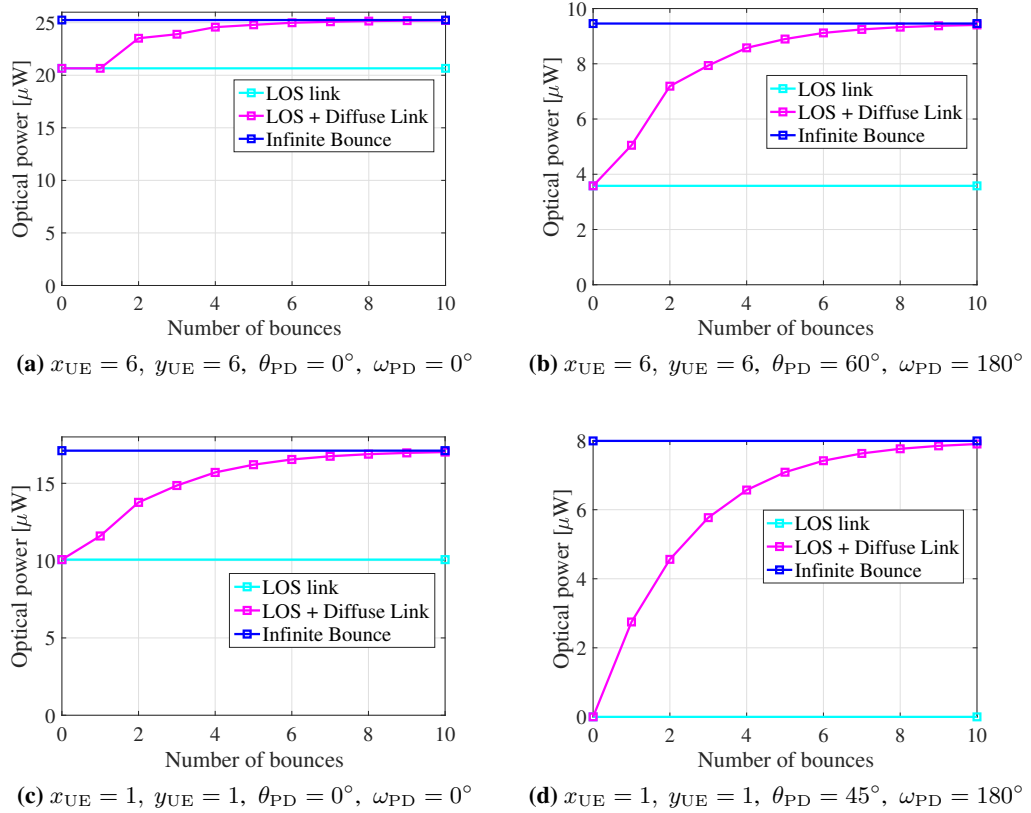


**Figure 3.8:** Comparisons among received optical power for LOS link, LOS + diffuse link up to order  $L$  and infinite reflections in 2 different positions with different orientations.

### 3.6.2 Importance of Reflection and Orientation

Fig. 3.8 shows the received optical power in two different locations with different orientations. The room setup and the SS deployment is as shown in Fig. 3.1 and the transmitted optical power  $P_{\text{tx}}$  is 1 W. Here, to evaluate the importance of reflection and device orientation, we first consider the Rx as a single PD with a FOV of  $60^\circ$ . The received optical power from the LOS and NLOS link can be calculated based on (2.34) and (2.41), respectively. The ratio of the received optical power from the LOS signal link to the total received optical power is represented as  $p_{\text{los}}$ . In Fig. 3.8 (a) and 3.8 (b), the  $p_{\text{los}}$  of cell-center UEs at  $(x_{\text{UE}} = 6, y_{\text{UE}} = 6)$  degrades substantially when the orientation of the PD changes from  $(\theta_{\text{PD}} = 0^\circ, \omega_{\text{PD}} = 0^\circ)$  to  $(\theta_{\text{PD}} = 60^\circ, \omega_{\text{PD}} = 180^\circ)$ . In Fig. 3.8 (c), the optical power from the diffuse link occupies



more than 40% of the total optical power when the UE is at  $(x_{\text{UE}} = 1, y_{\text{UE}} = 1)$  with a PD orientation of  $(\theta_{\text{PD}} = 0^\circ, \omega_{\text{PD}} = 0^\circ)$ . Nevertheless, in Fig. 3.8 (d), by changing the device orientation to  $(\theta_{\text{PD}} = 45^\circ, \omega_{\text{PD}} = 180^\circ)$ , there is no LOS signal and only the signal from the diffuse links can be received. Therefore, the device orientation has a great impact on the received single power and thus cannot be ignored. In addition, both the LOS link and diffuse link should be considered to analyze the performance of a multi-cell VLC system. Fig. 3.8 demonstrates that when the number of bounces is more than 5, the sum of the optical power of these paths occupies less than 10% of the total received optical power. Hence, to reduce the computational complexity while maintaining high channel estimation accuracy, a light reflection order of  $L = 5$  and the orientation model proposed in [83] are considered for the following simulations.

### 3.6.3 Performance Analysis for Single Source cells

The simulation environment for the SS system is shown in Fig. 3.1 and the AP deployment is shown in Fig. 3.4. Other parameters are listed in Table 3.1.

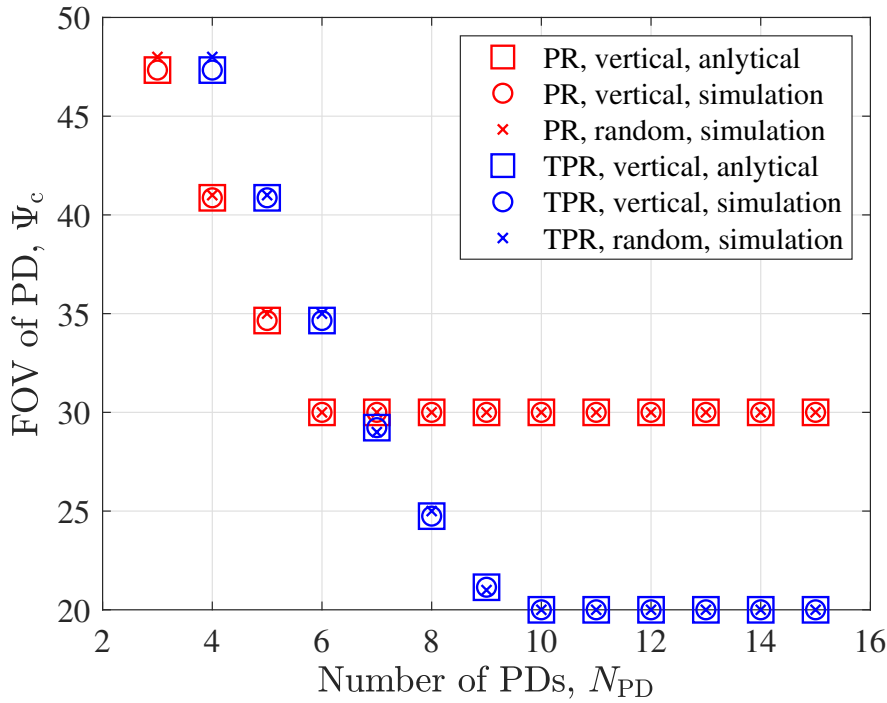


**Figure 3.9:** The relationship between  $\Psi_{c,\min}$  and the number of PD,  $N_{\text{PD}}$ , on an ADR for the SS system.

1) *Lower bound of FOV:* Fig. 3.9 shows the relationship between the lower bound of the FOV,  $\Psi_{c,\min}$ , and the number of PDs. Based on the lower bound given in (3.44), the analytical results are calculated for with different number of PDs. The lower bound of the FOV,  $\Psi_{c,\min}$ , for both PRs and TPRs are analyzed. Then, the Monte-Carlo simulations for UEs with a vertical orientation are carried out by finding the minimum value of  $\Psi_c$  that satisfies  $p_v = 1$  where  $p_v$  is

denoted in (3.16). 100,000 locations are chosen randomly following uniform distribution. The lowest value of  $\Psi_c$  that could ensure  $V(x_{UE}, y_{UE}, \theta_{UE}, \omega_{UE}, \Psi_c)$ , denoted in (3.15), equal 1 for all locations is  $\Psi_{c,min}$ . It can be seen that the analytical results exactly match the simulation results. When  $N_{PD} \leq 6$ , with the increase of  $N_{PD}$ ,  $\Psi_{c,min}$  decreases and the PR achieves smaller  $\Psi_{c,min}$  than the TPR. With the further increase of  $N_{PD}$  from 6 to 10, the lower bound of FOV,  $\Psi_{c,min}$ , for the PR becomes fixed due to (3.28) while the  $\Psi_{c,min}$  for the TPR still decreases and is lower than the  $\Psi_{c,min}$  for the PR. For  $N_{PD} > 10$ ,  $\Psi_{c,min}$  does not change anymore for the TPR as well due to (3.29). Secondly, the Monte-Carlo simulations are also performed following (3.16) for UEs with random orientation. Similarly, 100,000 locations are chosen. For each location, 10,000 orientations are generated based on the orientation model introduced in Chapter 2.7.1. The lowest value of  $\Psi_c$  that could ensure  $V(x_{UE}, y_{UE}, \theta_{UE}, \omega_{UE}, \Psi_c) = 1$  for all locations and orientations is  $\Psi_{c,min}$ . The results are matched with the analytical derivation for vertical-orientated UEs as well.

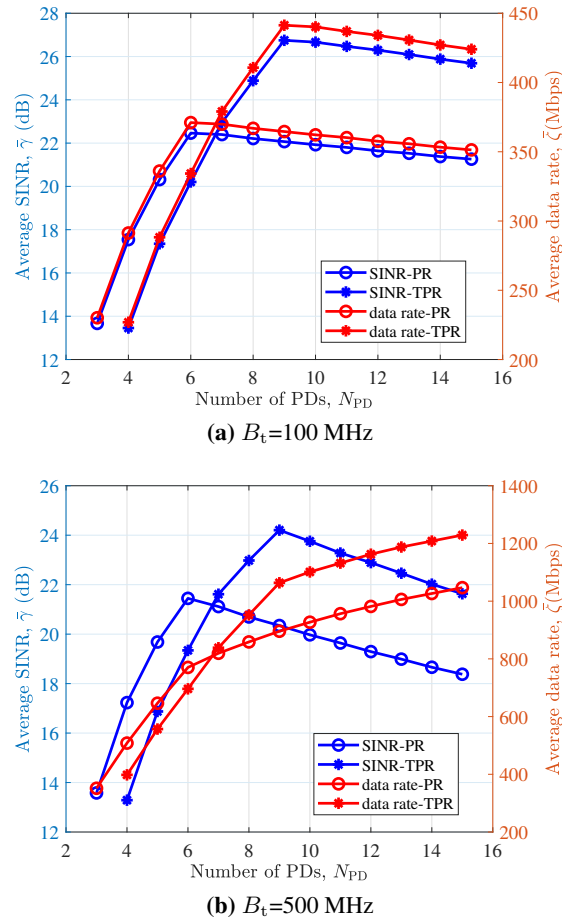


**Figure 3.10:** The performance comparison between PR and TPR configurations considering different Tx bandwidth in the SS system (MRC,  $N_0 = 10^{-21}$  A<sup>2</sup>/Hz).

2) *PR vs. TPR*: Fig. 3.10 manifests how the number of PDs  $N_{PD}$  affects the system performance for both PR and TPR configurations. Monte-Carlo simulations are carried out and it is assumed that the users follow the orientation-based random waypoint (ORWP) model introduced in

Chapter 2.7.3. The average SINR in Fig. 3.10 (a) and Fig. 3.10 (b) exhibit the same trend. For fair comparisons, it is assumed that the total physical area,  $A_t = N_{PD}A_p$ , of the ADRs should be the same. Hence, the increase in  $N_{PD}$  will lead to the decrease in the physical area  $A_p$  on each PD, which means less received power. Nevertheless, when  $N_{PD}$  increases from 3 to 6, the average SINR for the PR and TPR both increase. The increase is caused by the decrease in  $\Psi_{c,min}$  as displayed in Fig. 3.9, which leads to a higher channel gain and compensates for the power loss due to the decrease in  $A_p$ . In terms of the PR, the further growth of  $N_{PD}$  leads to the decline in the average SINR since  $\Psi_{c,min}$  does not change anymore. In comparison, the average SINR for the TPR increases until  $N_{PD} = 9$  as  $\Psi_{c,min}$  is still decreasing. When  $N_{PD}$  increases from 9 to 10 for the TPR,  $\Psi_{c,min}$  decreases slightly from  $21^\circ$  to  $20^\circ$  as demonstrated in Fig. 3.9. However, the power loss caused by the reduction in  $A_p$  exceeds the increase of received power gained from the small decrease in  $\Psi_{c,min}$ , and thus the average SINR drops. Considering  $N_{PD} \geq 10$ ,  $\Psi_{c,min}$  is fixed and the average SINR declines as  $A_p$  reduces. Hence, in terms of the average SINR, the optimum values of  $N_{PD}$  are 6 and 9 for PR and TPR, respectively. It can also be observed that the PR outperforms the TPR with regard to both the average SINR and average data rate when  $N_{PD} \leq 6$  since the PR has smaller  $\Psi_{c,min}$ . On the other hand, when  $N_{PD} > 6$ , the TPR has smaller  $\Psi_{c,min}$  than the PR and hence achieves better performance.

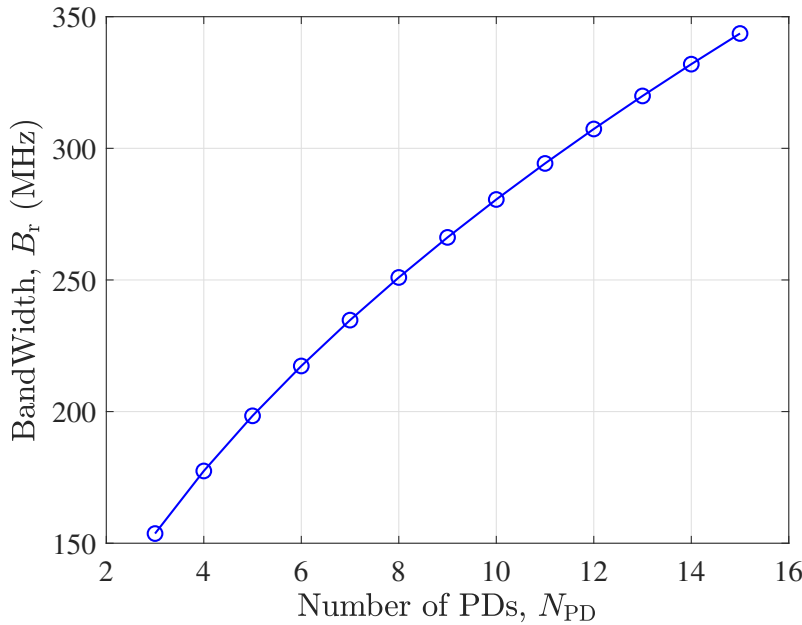


**Figure 3.11:** Rx bandwidth versus the number of PD,  $N_{PD}$ .

3) *Rx bandwidth vs. Tx bandwidth:* The user data rate is determined by the SINR and the communication bandwidth. Hence, it is important to know the maximum achievable communication bandwidth of the system. The communication bandwidth  $B_L$  is the minimum value between the Rx bandwidth and the transmitter (Tx) bandwidth, which is denoted as  $B_L = \min(B_r, B_t)$ . The Rx bandwidth increase as the physical area of the PD decrease. Based on (2.25), the relationship between the Rx bandwidth,  $B_r$ , and the number of PDs,  $N_{PD}$ , is demonstrated in Fig. 3.11. When  $N_{PD}$  increases from 3 to 15, the bandwidth increases from 150 MHz to around 350 MHz due to the decrease in the physical area of each PD. When the Tx

bandwidth  $B_t$  is 100 MHz, which is less than  $B_r$  for all values of  $N_{PD}$  as shown in Fig. 3.11, the communication bandwidth is limited by the Tx and thus  $B_L = 100$  MHz. As  $B_L$  does not vary according to  $N_{PD}$ , the average data rate follows the same trend as the average SINR in Fig. 3.10 (a). By increasing the Tx bandwidth  $B_t$  to 500 MHz,  $B_r \leq B_t$  for all  $N_{PD}$  and the communication bandwidth is limited by the Rx side. Hence, the communication bandwidth  $B_L = B_r$ . In Fig. 3.10 (b), with the increase of  $N_{PD}$ , the average SINR first increases and then decreases, which peaks at  $N_{PD} = 6$  and  $N_{PD} = 9$  for the PR and TPR, respectively. In contrast, when  $N_{PD}$  grows, the average data rate increases even when the SINR degrades, which is due to the greater bandwidth. To sum up, the PR with  $N_{PD} = 6$  and TPR with  $N_{PD} = 9$  achieve the highest average data rate for Tx-bandwidth-limited systems whereas the average data rate peaks at  $N_{PD} = 15$  in a Rx-bandwidth-limited system for both PR and TPR.

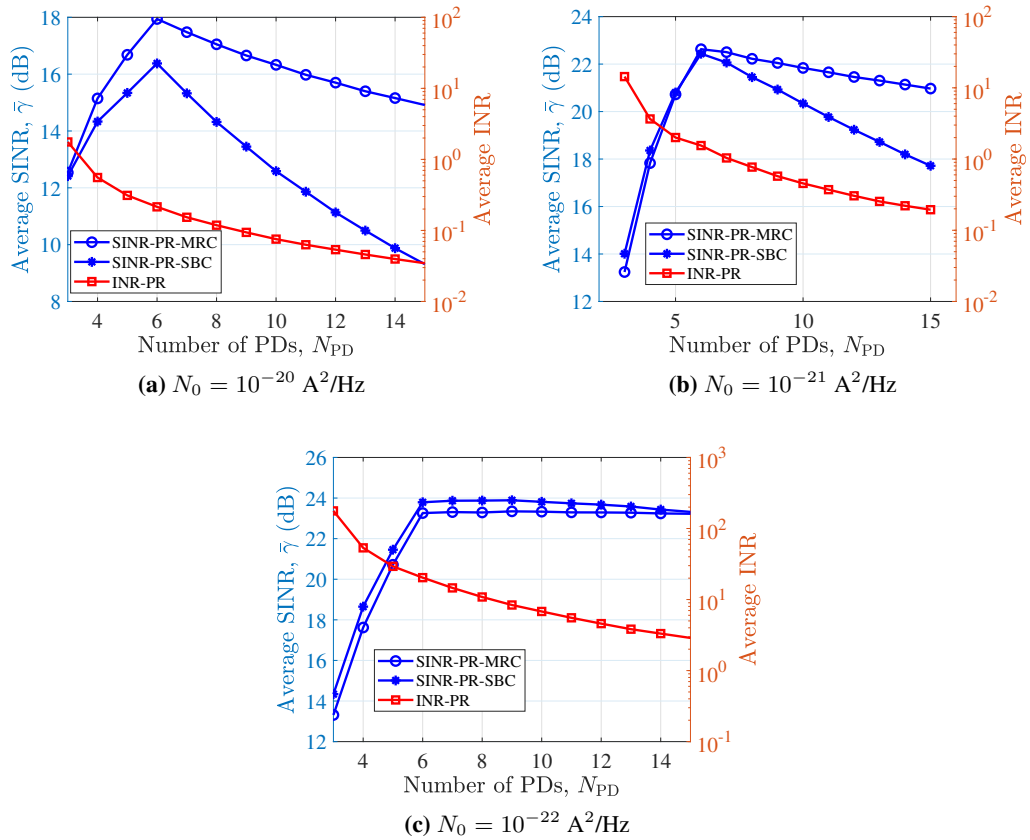


**Figure 3.12:** The performance comparison between MRC and SBC for the SS (PR,  $B_t=100$  MHz).

4) *MRC* vs. *SBC*: The MRC scheme is known to achieve better performance than the SBC scheme when there is no interference in the system. However, this may not be true when the interference is taken into consideration. To demonstrate the performance comparison between the MRC and SBC scheme, Monte-Carlo simulations are carried out for different noise levels. It is assumed that the users follow the ORWP model introduced in Chapter 2.7.3. In Fig. 3.12 (a), the noise power spectrum density level  $N_0$  is  $10^{-20} \text{ A}^2/\text{Hz}$ . When  $N_{PD} = 3$ , the level of interference is slightly higher than the noise, and the MRC schemes achieves similar average

SINR as the SBC scheme. With the increase of  $N_{PD}$ , the noise level becomes higher than the interference level and the system gradually becomes noise dominated. It can be seen that in a noise-limited system, MRC outperforms SBC in terms of average SINR. The noise power spectrum density level  $N_0$  is  $10^{-21}$  A<sup>2</sup>/Hz in Fig. 3.12 (b). When  $N_{PD} \leq 6$ , the interference level is higher than the noise level and SBC performs slightly better than MRC. However, the noise starts to rise above the interference level with the further increase of  $N_{PD}$  and thus MRC outperforms SBC. For a noise power spectrum density level of  $10^{-22}$  A<sup>2</sup>/Hz, Fig. 3.12 (c) depicts an interference-limited system and the SBC scheme achieves a higher average SINR than the MRC scheme for all values of  $N_{PD}$ . In brief, when the system is interference dominated, SBC is a better combining scheme. Otherwise, MRC outperforms SBC when considering the average SINR.

### 3.6.4 Performance Analysis for Double Source cells

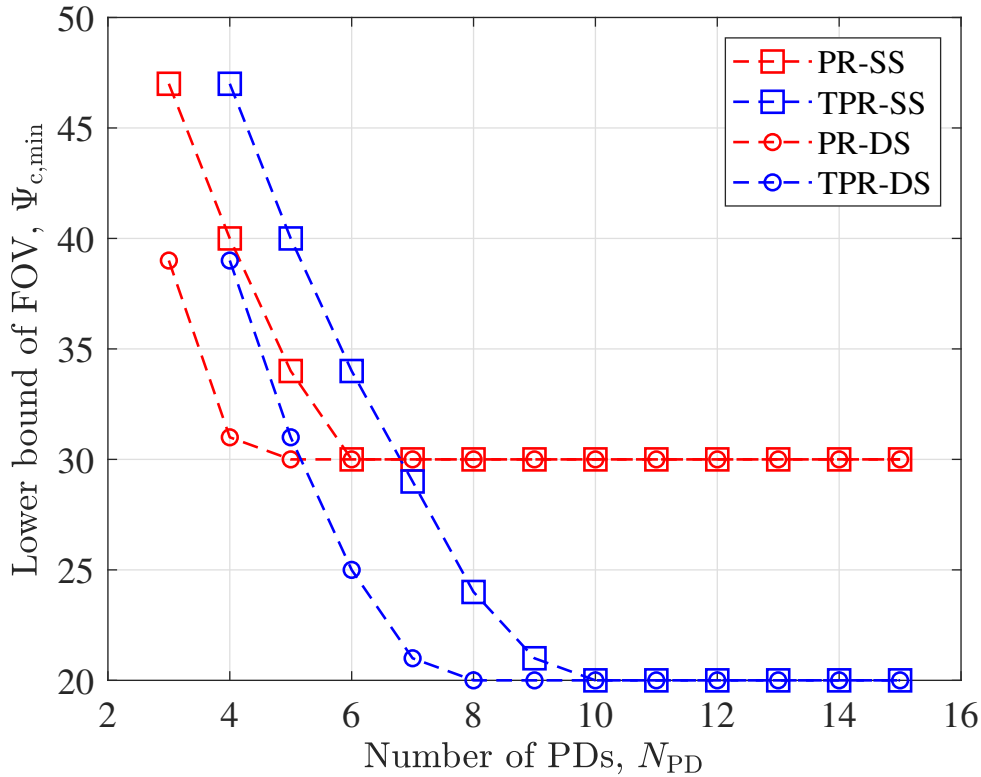


**Figure 3.13:** The relationship between  $\Psi_{c,min}$  and the number of PD,  $N_{PD}$ , on an ADR for the DS system.

The simulation environment for the DS system is shown in Fig. 3.1 but the AP deployment is shown in Fig. 3.7. The distance between the positive and negative AP  $d_{source}$  is set to be 1 m. Other parameters are given in Table. 3.1

1) *Lower bound of FOV*: Fig. 3.13 demonstrates the change in the minimum FOV against the number of PDs for the DS configuration. As shown for the PR, with the increase in  $N_{PD}$ , the

lower bound of FOV  $\Psi_{c,\min}$  for the DS cells decreases and converges to  $30^\circ$  at  $N_{PD} = 5$ , which is earlier than the SS configuration. When  $N_{PD} \leq 5$ , the  $\Psi_{c,\min}$  for the DS configuration is lower than the counterpart in the SS configuration. In terms of the TPR, the minimum FOV for DS converges to  $20^\circ$  at  $N_{PD} = 8$  and has smaller  $\Psi_{c,\min}$  than the SS when  $N_{PD} \leq 9$ . When  $N_{PD} \leq 10$ , the  $\Psi_{c,\min}$  for the DS configuration is lower than the counterpart in the SS configuration.

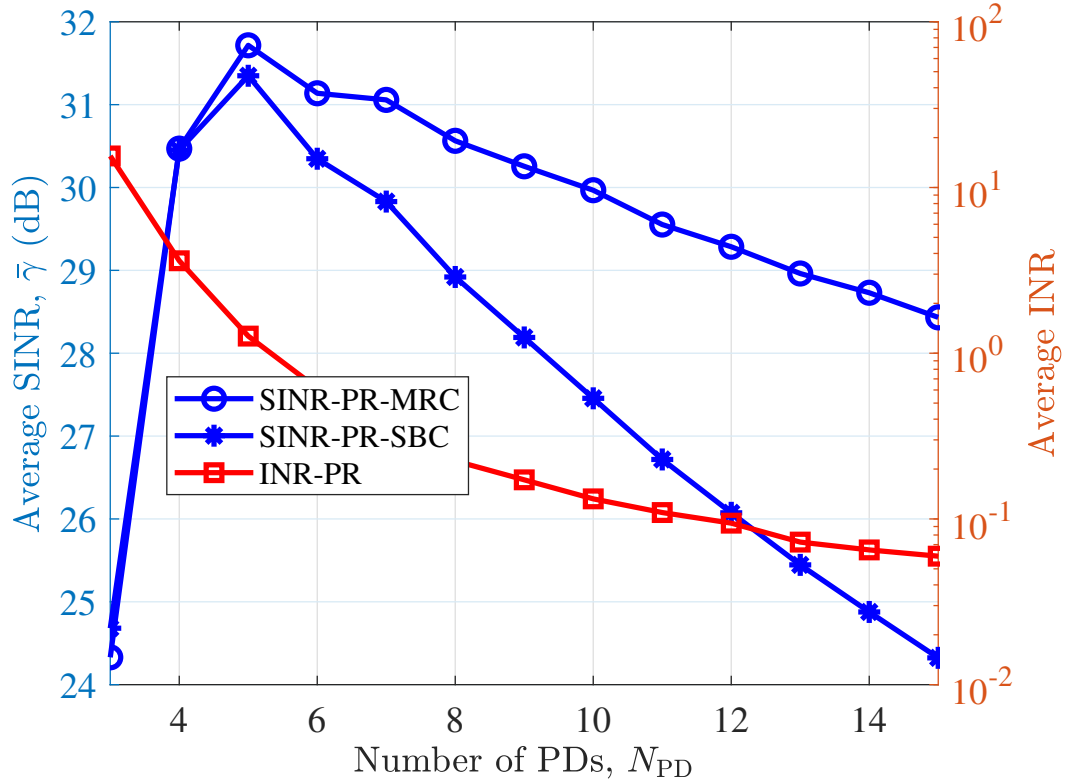


**Figure 3.14:** The performance comparison between MRC and SBC in DS cells (PR,  $N_0 = 10^{-22} \text{ A}^2/\text{Hz}$ ,  $B_t = 100 \text{ MHz}$ ).

2) *MRC vs. SBC*: Previously, in Fig. 3.12 (c), we have shown the performance comparison between the MRC and SBC for the SS system with  $N_0 = 10^{-22} \text{ A}^2/\text{Hz}$ . Due to the low level of noise power spectral density, the system is mostly interference-limited and SBC outperforms MRC for all given values of  $N_{PD}$ . By adopting the DS configuration, as shown in Fig. 3.14, the average interference to noise ratio (INR) is larger than 1 only when there are 3 or 4 PDs on the PR. Whereas for  $N_{PD} \geq 5$ , the noise plays a similar or more important role than the interference. Therefore, compared with the SS system, for the same level of noise power spectral density, the average INR of the DS system degrades substantially. This indicates that the DS system can mitigate interference. With regards to the average SINR, MRC and SBC have similar performance when  $N_{PD} \leq 4$  whereas MRC outperforms SBC for  $N_{PD} > 4$ . From the above analysis, it can be deduced that MRC is a better combining scheme for the DS system with respect to the three different levels of  $N_0$  given previously in this study.

3) *PR vs. TPR*: Fig. 3.15 illustrates the performance comparison between PR and TPR

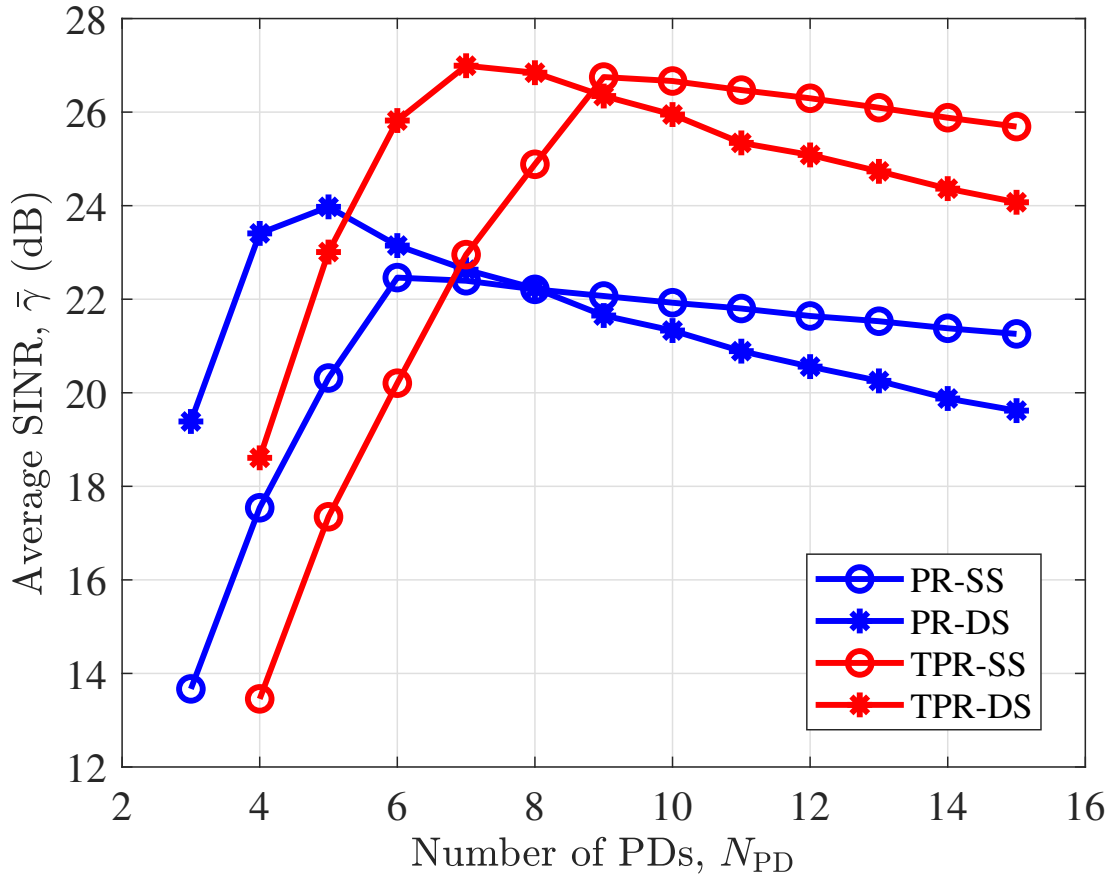


**Figure 3.15:** The performance comparison between PR and TPR in DS cells (MRC,  $N_0 = 10^{-21} \text{ A}^2/\text{Hz}$ ).

configurations. With respect to the PR, when  $N_{PD}$  rises from 3 to 5, the average SINR increases from 19.3 dB to 24 dB, where the increment comes from the decline in  $\Psi_{c,\min}$ . For the same reason, with regards to the TPR, the average SINR grows from 18.5 dB to 27 dB when  $N_{PD}$  increases from 4 to 7. The PR and TPR achieves the peak at  $N_{PD} = 5$  and  $N_{PD} = 7$  respectively. For both PR and TPR configurations, after the peak points, the average SINR drops due to the reduction in the area  $A_p$  of each PD, which leads to less physical power. With regard to TPR, changing  $N_{PD}$  from 7 to 8 results in the decrease in  $\Psi_{c,\min}$ , which leads to a channel gain boost. However, the gain cannot compensate for the power loss that stems from the reduction in  $A_p$  and thus the system performance degrades. When  $N_{PD} \leq 5$ , the PR outperforms the TPR, otherwise, the TPR is a preferred structure. In conclusion, the optimum number of PDs is 5 and 7 for PRs and TPRs, respectively. In addition, the TPR with  $N_{PD} = 7$  outperforms the PR with  $N_{PD} = 5$  in terms of the average SINR.

4) *DS vs. SS*: Fig. 3.16 demonstrates the performance comparison between the DS system and the SS system with respect to different levels of noise power spectrum density,  $N_0$ . The typical value of  $N_0$  for a PD is  $10^{-21} \text{ A}^2/\text{Hz}$ , at which the DS system achieves a slightly higher average SINR than the SS system for both PRs and TPRs. By reducing the noise power spectrum density level to  $10^{-22} \text{ A}^2/\text{Hz}$ , the system becomes interference-limited. With the aid of the DS configuration, the ADR can suppress the signal power from interfering APs by attenuating the

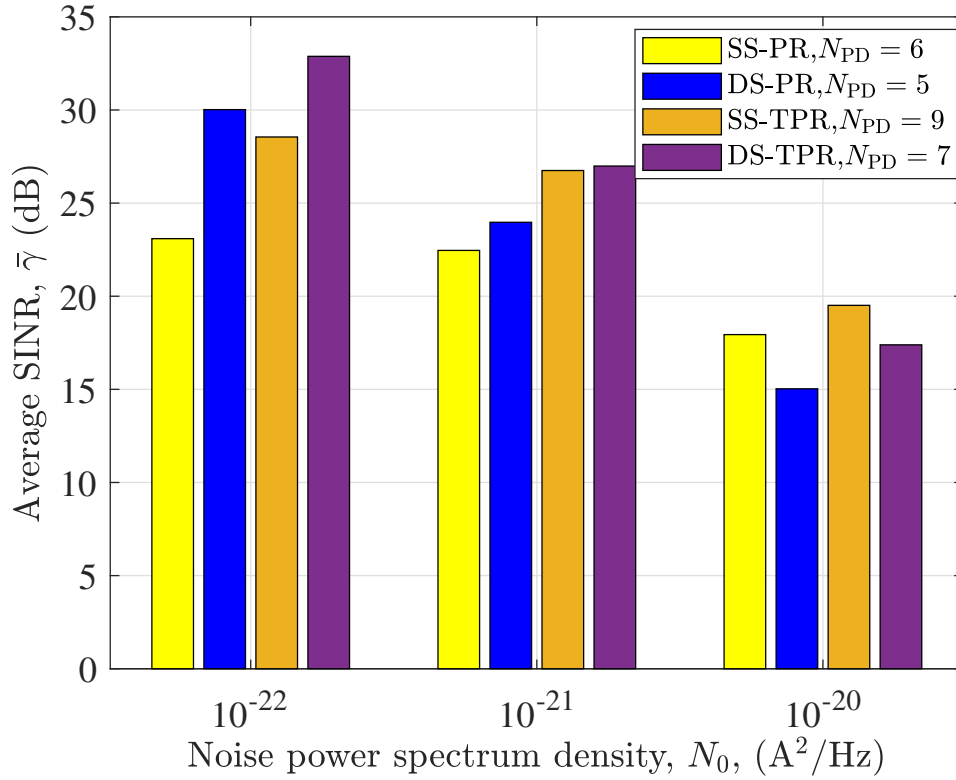


**Figure 3.16:** The performance comparison between the DS and SS systems.

NLOS path. Hence, when  $N_0 = 10^{-22} A^2/Hz$ , the average SINR of DS cells is 7 dB and 5 dB higher than the average SINR of SS cells for PRs and TPRs, respectively. For a noise spectrum density level of  $10^{-20} A^2/Hz$ , the system becomes noise limited, in which the DS could not improve system performance by reducing the power of interference signal. In addition, the received power is halved when the DS configuration is applied, and thus the SS outperforms the DS in terms of the average SINR.

### 3.7 Summary

This chapter have investigated the ICI mitigation in LiFi networks using ADRs. The impact of the diffuse link considering random UE orientation has been studied and it has been shown that both LOS and diffuse links have a significant effect on the system performance. The projection area of the ADRs has been defined to differentiate from the coverage area of APs. Analytical expressions for the projection area of both PRs and TPRs have been given. Based on the constraint set by the projection area of ADRs, the lower bound of the FOV for the PD on an ADR has been given for the SS system. A performance comparison has been conducted between the PRs and TPRs, and optimized ADR structures have been proposed to fully exploit the performance gain of ADRs. In addition, the joint effect of the Rx and Tx bandwidth on the average data rate have been analyzed. The performance comparison between the SBC and



MRC have been given regarding different levels of noise power spectral density. It is the first time shown that under certain circumstances, the SBC can outperform the MRC. The DS cell system has been considered to further mitigate the NLOS interference. The lower bound of FOV for PD on an ADR has been derived and the optimized ADR structures were proposed for the DS system. By comparing the average SINR between the DS system and the SS system under different levels of noise power spectral density, we showed that, in a noise-dominated scenario, the SS system should be applied, otherwise, the DS system is preferred.

---

Chapter 4

**Realistic Indoor Hybrid WiFi and  
OFDMA-Based LiFi Networks**

---

## 4.1 Introduction

Despite a wide variety of advantages provided by light-fidelity (LiFi), the limitations of this technology should also be considered to develop feasible solutions. Link blockage is one factor that can affect LiFi performance significantly. Inter-cell interference (ICI) is another factor that can significantly restrict the spectrum efficiency, especially for the cell-edge users. An effective solution is to combine LiFi with existing radio frequency (RF) networks, e.g. wireless fidelity (WiFi), to form a hybrid LiFi/WiFi network (HLWN) [26, 27, 92]. When the signal to interference-plus-noise ratio (SINR) of the LiFi link degrades greatly due to either high ICI or severe blockage, WiFi should be selected for signal transmission. Such a network cannot only achieve high data rates through LiFi, but can also provide ubiquitous coverage through WiFi in case of any link blockage within the optical channels or severe ICI. As LiFi uses a different spectrum from WiFi, there is no interference between LiFi and WiFi systems. Thus, the HLWN is able to offer a total system throughput greater than that of a stand-alone LiFi or WiFi network [27].

In HLWNs, efficient load balancing (LB) can significantly improve the overall quality of service (QoS). When user mobility is involved, the LB consists of AP assignment (APA), resource allocation (RA) and also handover management. Several studies on the topic of HLWNs have been undertaken [93–97]. In [93], the hybrid visible light communication (VLC) and RF network are studied for the purpose of system throughput enhancement. In that work, APA and RA are performed in a static system without the consideration of user mobility and random device orientation. In [94], a practical hybrid VLC/WiFi network is studied, which only uses VLC for downlink and WiFi for uplink communications. The hybrid network proposed in that paper is different from the HLWNs where LiFi and WiFi can be used for both downlink and uplink communications. The majority of subsequent research focuses on system LB optimization in HLWNs so as to improve the performance of data rate and user fairness [95–97]. Most papers consider a static and simple network setup where user movement and receiver (Rx) orientation are ignored, which can affect the performance of LiFi systems [98] and, consequently, HLWNs. In addition, the proposed optimization schemes in [95–97] are of high computational complexity, which renders them difficult to implement. In recent literature, game theory has been extensively applied to network selection and interference management problems in heterogeneous wireless networks [99, 100]. In the evolutionary game theory (EGT) model, each user will adapt their strategy to achieve a better payoff until each user's payoff cannot be increased unilaterally. In [101], an EGT-based LB scheme for hybrid LiFi and RF networks is proposed, where random device orientation in LiFi systems is considered. The proposed EGT scheme in [101] is able to achieve a better user satisfaction performance at a low computational complexity. However, in order to attain a more accurate evaluation of the system performance, there are three factors that should be considered:

1) *RA Enhancement*: In most of the research studies on hybrid LiFi and RF networks, the RA in both LiFi and RF (e.g. WiFi) systems is considered as an optimization of users' resource portions, which are fractional numbers between 0 and 1 [95–97, 102]. This is suitable for the time division multiple access (TDMA) scheme. However, an efficient multiple access scheme can help to avoid intra-cell interference and achieve multi-user diversity gains in multi-user LiFi systems,. Due to the flexibility in RA, orthogonal frequency division multiple access (OFDMA) has been widely adopted in RF networks [80]. By means of the OFDMA scheme, resources

can be allocated in both time and frequency domains, where the minimum and indivisible time-frequency slots are known as resource units (RUs). A resource block (RB) is composed of a number of RUs. It is evident that allocating those RUs to different users is more efficient and flexible than only allocating subcarriers or time slots. Moreover, by considering the low pass effect of front-end elements, an adaptive user-to-RU assignment is able to substantially enhance the overall system spectral efficiency compared to TDMA schemes. In [103, 104], OFDMA in LiFi systems has been studied, however, OFDMA and TDMA achieve the same throughput performance as equal channel gains are assumed for all subcarriers. Hence, it is important to consider the channel response with the effect of front-end elements in the RA of LiFi OFDMA systems.

2) *Handover*: In order to ensure seamless connectivity as well as to fulfill the data rate requirement of mobile users in cellular networks, the ongoing connection may require to be transferred from one access point (AP) to another. This process is called handover. Many current research studies on hybrid LiFi and RF networks consider a static network and handover is not taken into account [95–97]. However, when a handover occurs in dynamic HLWNs, signaling information (referred to as handover overhead) would have to be exchanged. This process causes transmission losses of desired data, leading to a reduction in the data rate. Thus, handover overhead must be considered in LB for such hybrid networks. In a heterogeneous hybrid network, a handover may result in subsequent handovers. For example, when a user switches from LiFi to WiFi, due to the increased load and reduced user data rate in the corresponding WiFi cell, users allocated to this WiFi AP may have to be reallocated to other WiFi or LiFi APs. Moreover, the load decrease of the LiFi attocell may lead to the increase in the data rate of existing users served by this AP. During each of these handovers, the overhead may affect the achievable user data rate. Therefore, LB should be designed with handover considered.

3) *Device Orientation*: Due to the directionality of the LiFi transmitter (Tx) and Rx, the change of device orientation will lead to variations in the channel conditions, which may further result in a new APA. To the best of our knowledge, all the previous studies about the HLWN assume that the orientation of the user device is fixed or follows a uniform distribution model, which is not practical. The device orientation model has been proposed recently in [29, 83] through experimental measurements. To evaluate the performance of HLWN in a more realistic scenario, the orientation-based random waypoint (ORWP) mobility model in Chapter 2.7.3 is considered in this study.

## 4.2 Hybrid LiFi/WiFi Network Model

### 4.2.1 System Setup

As shown in Fig. 4.1 (a), an indoor HLWN is considered in this study, where one WiFi AP and  $N_L$  LiFi APs are deployed. All LiFi APs and the WiFi AP are connected to the central unit (CU) through optical fibers with the CU controlling and managing them. In this study, it is assumed that the user can only be served by one technology, either WiFi or LiFi, at a time.

In the LiFi system, the visible light spectrum is used for the downlink transmission and illumination simultaneously. Regarding the uplink transmission, the infrared (IR) spectrum

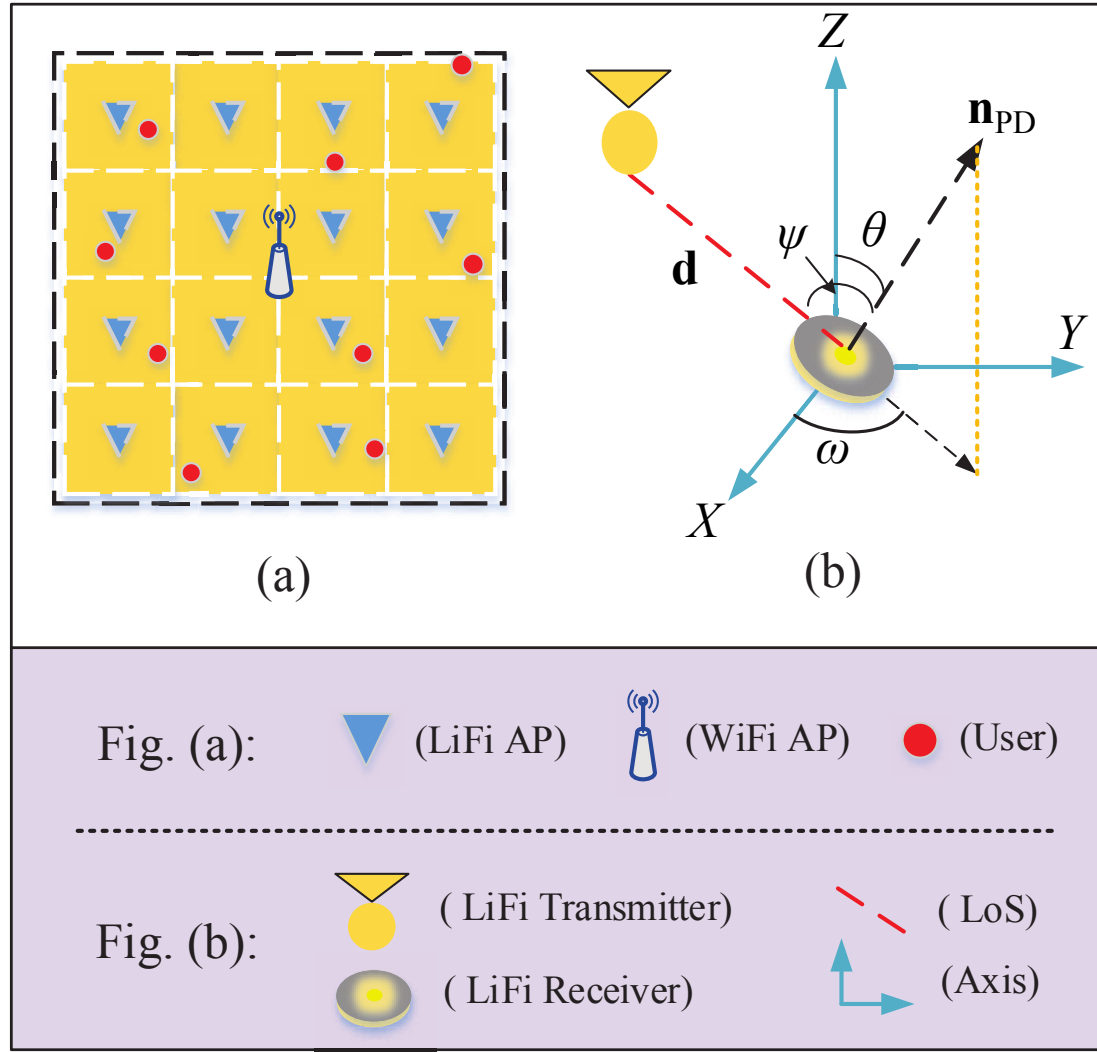


**Figure 4.1:** (a) Illustration of AP deployment in HLWN and (b) polar and azimuth orientation angle of LiFi Rx.

is adopted in this study since it does not affect the illumination and adds no interference to the LiFi downlink communication and the existing RF networks [105, 106]. It should be noted that the downlink communication in LiFi systems is the primary focus of this study. Each LiFi AP is composed of multiple light-emitting diodes (LEDs) to transmit optical power and an IR Rx to detect the uplink signals. The user terminals are equipped with photodiodes (PDs) to receive visible light signals and IR TxS to serve the uplink. In each LiFi cell, optical OFDMA is employed as the multiple access scheme.

For the WiFi system, it is assumed that the WiFi AP follows the IEEE 802.11ad standard [25]. According to this standard, each station (STA) can communicate with the AP (uplink and downlink) or with other STAs (direct link). Particularly, we only consider the uplink and downlink in WiFi systems in this study while direct user to user communication is not taken into account. The main medium access control (MAC) of IEEE 802.11 is carrier sense multiple

access with collision detection (CSMA/CA), which is therefore also considered in this study [82]. All the nodes in the WiFi system including the WiFi AP are allowed to access the channel using the available bandwidth during data transmission. This means that the uplink transmission of WiFi will affect the downlink communication. For example, when increasing the uplink throughput, the downlink network will have fewer chances to get access to the channel. This can lead to a drastic decrease in downlink throughput. Therefore, in this work, the effect of the WiFi uplink data rate requirement on the downlink resource allocation is considered.

In the HLWNs, the set of users is denoted as  $\mathcal{U} = \{\mu | \mu \in [1, N_{UE}], \mu \in \mathbb{N}\}$ , where  $\mathbb{N}$  is the set of natural numbers. Assume the total number of users and LiFi APs are  $N_{UE}$  and  $N_L$ , respectively. The set of LiFi APs is denoted by  $\mathcal{A} = \{\alpha | \alpha \in [1, N_L], \alpha \in \mathbb{N}\}$  and the WiFi AP is denoted by  $W_{AP}$ . The RA algorithms which use the historical data and future-state prediction have been studied in [107–109]. However, random device orientation is considered in this study and, to the best of our knowledge, no previous study has shown that the device orientation can be predictable. Since the future state cannot be predicted, it may not be practical to optimize the long-term performance of the system. Hence, the system performance in a single quasi-static state is considered instead. A quasi-static period is a short duration where the channel state information (CSI) can be assumed to be constant [41]. In the indoor scenario, for both LiFi and WiFi channels, the CSI can be assumed to be constant for a short time period, commonly known as the coherence time [110]. The coherence time for LiFi networks is in the order of tens of milliseconds [83], which encompasses several RBs. During each quasi-static period, the CSI of channels in HLWNs is fixed for the duration of  $T_p$ , which is the minimum value between the coherence time of LiFi channels,  $T_L$ , and the coherence time of WiFi channels,  $T_W$ . So that,  $T_p = \min\{T_L, T_W\}$ . The evaluation of the coherence time of both LiFi and WiFi channels is not the focus of this study and will be considered in future work. The dynamic HLWN system can be divided into many quasi-static periods and each period is referred to as a 'state'. Each user will be served by either a LiFi AP or a WiFi AP in each state and the sequence numbers of the state are denoted by  $\{1, 2, \dots, n | n \in \mathbb{N}\}$ . The CU performs the APA and allocates the available resources to each individual more efficiently compared to a distributed case in which each AP allocates its own resources to the users. In this study, the proposed EGT algorithm is realized in a centralized manner within the CU. By monitoring the network continuously, the CU obtains knowledge of the CSI. Based on the collected CSI, the CU undertakes the AP selection and RA at each state.

#### 4.2.2 LiFi System

In LiFi systems, optical-OFDM (O-OFDM) is developed to ensure real and positive signals. direct current biased optical orthogonal frequency division multiplex (DCO-OFDM) and asymmetrically clipped optical orthogonal frequency division multiplex (ACO-OFDM) are two of the most well-known and commonly used O-OFDM schemes. The spectrum efficient DCO-OFDM described in Chapter 2.4.1 is used in this study to achieve high data rates. More spectrum efficient techniques have been developed such as spectral and energy efficient (SEE)-OFDM [111] and enhanced unipolar (eU)-OFDM [112], but they use the same subcarrier structures as in DCO-OFDM. Therefore, using these more advanced modulation techniques will not alter the main contributions of this work. The analysis can be applied to other types of orthogonal frequency division multiplex (OFDM) systems in a similar manner.

The SINR between user  $\mu$  and the serving LiFi AP  $\alpha$  can be expressed as [101]:

$$\gamma_{\mu,\alpha}(f) = \frac{(\tau P_{\text{tx}} H_{\mu,\alpha}(f))^2}{\kappa^2 N_0 B_L + \sum_{i \in \mathcal{A} \setminus \{\alpha\}} (\tau P_{\text{tx}} H_{\mu,i}(f))^2}, \quad (4.1)$$

where  $\tau$  is the Rx's optical to electrical conversion efficiency;  $P_{\text{tx}}$  is the transmitted optical power of a LiFi AP;  $H_{\mu,\alpha}(f)$  is the channel gain between user  $\mu$  and the serving LiFi AP  $\alpha$  based on (2.42);  $\kappa$  is the ratio of direct current (DC) optical power to the square root of electric signal power. Furthermore,  $N_0$  and  $B_L$  denote the noise power spectral density and the baseband modulation bandwidth in the LiFi system, respectively. The channel gain between user  $\mu$  and the interfering LiFi AP  $i$  at frequency  $f$  is denoted as  $H_{\mu,i}(f)$ . It is noted that when other OFDM techniques, which has closed form SINR expressions, are applied, (4.1) should be replaced with the corresponding expression.

min. SINR [dB]	Modulation	Code rate	Spectral efficiency [bit/s/Hz]
-	-	-	0
1	QPSK	0.44	0.8770
3	QPSK	0.59	1.1758
5	16QAM	0.37	1.4766
8	16QAM	0.48	1.9141
9	16QAM	0.60	2.4063
11	64QAM	0.45	2.7305
12	64QAM	0.55	3.3223
14	64QAM	0.65	3.9023
16	64QAM	0.75	4.5234
18	64QAM	0.85	5.1152
20	64QAM	0.93	5.5547

**Table 4.1:** Modulation and Coding Table [2].

In the LiFi system, adaptive  $M$ -quadrature amplitude modulation ( $M$ -QAM) is used on different OFDM subcarriers. The number of OFDM subcarriers is denoted by  $M$ , which is an even and positive integer. The sequence number of OFDM subcarriers is denoted by  $m \in [1, M]$ ,  $m \in \mathbb{N}$ . The effective subcarrier set (referring to the subcarriers bearing information data) is defined as  $\mathcal{M}_e$ . It is assumed that there are several RBs in a quasi-static period, and each RB contains  $M_e K$  RUs, where  $K$  is the number of subframes in the time domain. The frequency of the subcarrier  $m$  is denoted as  $f_m$ . As the channel is assumed to be constant during a quasi-static period, the spectral efficiency of the RU on the  $m$ -th subcarrier is identical for each subframe. According to the modulation and coding scheme given in Table 4.1 [2], for user  $\mu$  served by the LiFi AP  $\alpha$ , the spectral efficiency of subcarrier  $m$ ,  $q_{\mu,\alpha,m}$ , can be determined based on  $\gamma_{\mu,\alpha}(f_m)$  obtained from (4.1). Therefore, for user  $\mu$  served by the LiFi AP  $\alpha$ , the communication link data rate of the RU on subcarrier  $m$  for each subframe can be written as:

$$r_{\mu,\alpha,m}^{\text{Link}} = \frac{2B_L q_{\mu,\alpha,m}}{MK}. \quad (4.2)$$

Therefore, the total LiFi link data rate of user  $\mu$  served by the LiFi AP  $\alpha$  is expressed as:

$$\zeta_{\mu,\alpha}^{\text{Link}} = K \sum_{m \in \mathcal{M}_e} r_{\mu,\alpha,m}^{\text{Link}}. \quad (4.3)$$

### 4.2.3 WiFi System Model

It is assumed that the WiFi AP follows the IEEE 802.11ad standard [25]. According to this standard, each STA can communicate with the AP (uplink and downlink) or with other STAs (direct link). Particularly, we only consider the uplink and downlink in WiFi systems in this study while direct user to user communication is not taken into account. The main MAC of IEEE 802.11 is CSMA/CA, therefore it is considered in this study [82]. All the nodes in the WiFi system including the WiFi AP are allowed to access the channel using the available bandwidth during data transmission. This means that the uplink transmission of WiFi will affect the downlink communication. For example, when increasing the uplink throughput, the downlink network will have fewer chances to get access to the channel. This can lead to a drastic decrease in downlink throughput.

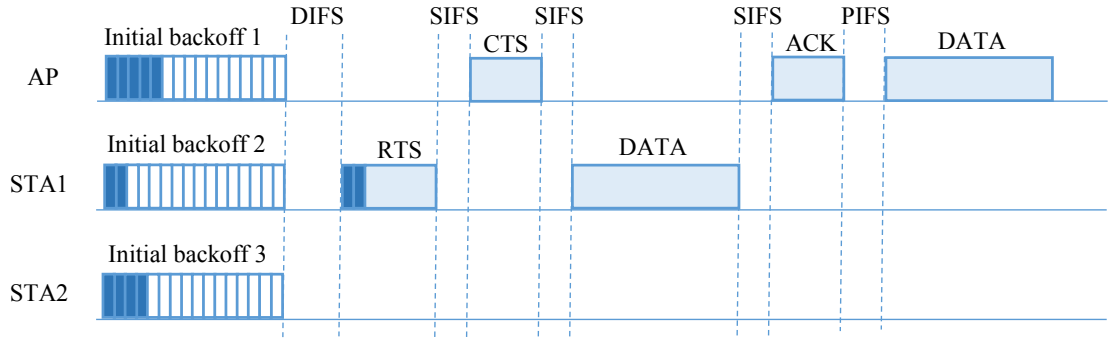


**Figure 4.2:** Illustration of CSMA/CA with DCA mechanism.

In a WiFi system, users and the WiFi AP use the CSMA/CA with request to send (RTS) and clear to send (CTS) hand-shaking mechanism, as shown in Fig. 4.2. In CSMA/CA, the STAs listen to the channel for an interval called distributed inter-frame space (DIFS). If the channel is sensed to be idle after DIFS, they initiate their backoff time. Both the users and the AP have a random backoff number and the one with the lowest backoff number has the priority to transmit the information. Before data transmission, the STA sends the RTS packet. If the RTS packet is received successfully by the AP, a CTS packet will be sent by the AP after a short inter-frame space (SIFS). After the two-way handshaking of RTS/CTS, the data frame will be transmitted. Also, an acknowledgment (ACK) frame will be sent by the AP if the data frame is successfully received. In [82], a detailed explanation and performance analysis of the CSMA/CA with RTS/CTS mechanism is provided. The time duration used for successful data transmission on the uplink (downlink) is called the uplink (downlink) utilization. The ratio of the uplink (downlink) utilization and the total transmission time is defined as uplink (downlink) utilization efficiency [113]. We denote this ratio by  $U_{\text{up}}$  ( $U_{\text{down}}$ ), which is a fractional number



between 0 and 1. In addition, the utilization ratio of  $U_{\text{down}}$  and  $U_{\text{up}}$  is defined as:

$$\epsilon = \frac{U_{\text{down}}}{U_{\text{up}}}. \quad (4.4)$$

In this work, the full buffer model is considered. This means that there are always packets to send in the buffers of the WiFi AP and user equipments (UEs). Since the WiFi AP and each user have the same probability to access the channel, the utilization ratio  $\epsilon$  is naturally equal to  $\frac{1}{N_W+1}$ , where  $N_W$  is the number of users served by the WiFi AP. In order to flexibly allocate the available spectrum between uplink and downlink transmission, a mechanism called downlink compensation access (DCA) is considered [113]. By using DCA,  $\epsilon$  can be any required utilization ratio greater than or equal to  $\frac{1}{N_W+1}$ . In the DCA mechanism, the AP can transmit data frames after point inter-frame space (PIFS) following the previous ACK packet until the utilization ratio reaches the requirement, as shown in Fig. 4.2. Assume that  $\epsilon_0$  is the required utilization ratio. Initially, the utilization ratio  $\epsilon = 1/(N_W + 1)$  is less than  $\epsilon_0$ . In this case, the DCA is used and the handshake mechanism of RTS and CTS is not necessary. The AP can transmit multiple data frames while  $\epsilon < \epsilon_0$ . Note that the AP accesses the channel without collision during the DCA because PIFS is used as the frame gap, which is shorter than DIFS. When  $\epsilon \geq \epsilon_0$  is achieved, the RTS/CTS handshake instead of DCA will be used for the WiFi AP transmission. In this way, the required utilization ratio is maintained. The uplink and downlink utilization efficiency can be expressed as:

$$U_{\text{up}} = U \frac{1}{1 + \epsilon}, \quad (4.5a)$$

$$U_{\text{down}} = U \frac{\epsilon}{1 + \epsilon}, \quad (4.5b)$$

where  $U$  is the system utilization efficiency given by [113]:

$$U = \frac{p_s p_t t_p}{(1 - p_t)t_f + p_t p_s (1 - p_d)t_s + p_t p_s p_d t_d + p_t (1 - p_s)t_c}, \quad (4.6)$$

where  $p_s$  is the probability of successful transmission;  $p_t$  is the probability that there is at least one transmission in a backoff unit time;  $p_d$  is the probability that a data frame is transmitted by the DCA under the condition that the previous transmission was successful;  $t_f$  is the duration of an empty slot time;  $t_p$  is the average transmission time of the frame payload;  $t_c$  is the average time that the channel is sensed to be busy because of a collision;  $t_s$  is the average time that the channel is sensed as busy because of a successful transmission; and  $t_d$  is the time duration for DCA. Specifically,  $p_s$ ,  $p_t$ ,  $p_d$  can be presented with the number of users served by the WiFi AP as the primary variable, which has been given in [113]:

$$p_t(N_W) = 1 - (1 - p_c)^{N_W+1}, \quad (4.7a)$$

$$p_s(N_W) = \frac{(N_W + 1)p_c(1 - p_c)^{N_W}}{p_t}, \quad (4.7b)$$

$$p_d(N_W) = \frac{N_W - 1}{2N_W p_s}, \quad (4.7c)$$

where  $p_c = 2/(C_{\max} + 1)$  is the probability that a user transmits a data frame in a backoff counter time;  $C_{\max}$  is the maximum backoff stage. Also,  $t_c$ ,  $t_s$  and  $t_d$  are expressed as follows:

$$t_c = t_{\text{RTS}} + t_{\text{DIFS}}, \quad (4.8)$$

$$t_s = t_{\text{RTS}} + t_{\text{CTS}} + t_{\text{H}} + t_{\text{p}} + t_{\text{ACK}} + 3t_{\text{SIFS}} + t_{\text{DIFS}}, \quad (4.9)$$

$$t_d = t_{\text{H}} + t_{\text{p}} + t_{\text{ACK}} + t_{\text{SIFS}} + t_{\text{PIFS}}, \quad (4.10)$$

where  $t_{\text{RTS}}$ ,  $t_{\text{CTS}}$ ,  $t_{\text{H}}$ ,  $t_{\text{ACK}}$ ,  $t_{\text{SIFS}}$ ,  $t_{\text{DIFS}}$ , and  $t_{\text{PIFS}}$  are the time duration of RTS, CTS, frame header, ACK, SIFS, DIFS and PIFS. In this way, the utilization function in (4.6) can be written as a function corresponding to the number of users served by the WiFi AP, denoted by  $U(N_{\text{W}})$ . Similarly, the uplink and downlink utilization efficiency can be rewritten as  $U_{\text{up}}(N_{\text{W}})$  and  $U_{\text{down}}(N_{\text{W}})$ .

The channel bit rate in the WiFi system is denoted by  $R_c$ . The downlink data rates for user  $\mu$  in the WiFi cell can be expressed as:

$$R_{\mu, \text{wifi}} = \frac{R_c U_{\text{down}}(N_{\text{W}})}{N_{\text{W}}}, \quad (4.11)$$

and the uplink data rate for a WiFi user can be expressed as:

$$\Upsilon_{\mu, \text{wifi}} = \frac{R_c U_{\text{up}}(N_{\text{W}})}{N_{\text{W}}}. \quad (4.12)$$

#### 4.2.4 Handover

The handover overhead causes a reduction in the average data rate of the users who have to be handed off to new APs. The definition of handover efficiency was first introduced in [27] and was later used in [114] and [107]. Generally, in an indoor scenario, the handover overhead is in the order of milliseconds and the overhead time is considered as a random variable [115]. Hence, the exact overhead time is unknown at the beginning of each state, which means the exact handover efficiency cannot be calculated. Therefore, the average handover efficiency will be used to estimate the negative effect of handover on user's data rate [107]. The average handover efficiency is assumed to range from 0 to 1. There are two types of handover in a hybrid network, horizontal handover (HHO) and vertical handover (VHO). HHO occurs between APs of the same access technology. VHO refers to the change of connectivity between different wireless access technologies. The average handover efficiency for HHO and VHO are denoted by  $\eta_{0, \text{HHO}}$  and  $\eta_{0, \text{VHO}}$ , respectively. Hence, the estimated handover efficiency between two consecutive states can be written as follows:

1) HHO: Since a single WiFi AP is considered in this study, HHO only occurs between two LiFi APs. Assuming that user  $\mu$  is served by a LiFi AP  $\alpha_{\mu}^{(n-1)}$  in the state  $(n-1)$ , the estimated HHO efficiency between state  $(n-1)$  and state  $n$  can be expressed as:

$$\eta_{\text{H}}(i) = \begin{cases} \eta_{0, \text{HHO}}, & i \neq \alpha_{\mu}^{(n-1)} \\ 1, & i = \alpha_{\mu}^{(n-1)} \end{cases}, \quad i \in \mathcal{A}, \quad (4.13)$$

where the operation  $[\cdot]^+$  denotes  $\max(\cdot, 0)$ .

2) VHO: VHO occurs when the host AP of user  $\mu$  is transferred from a LiFi AP to the WiFi AP or vice versa. Assume that user  $\mu$  is served by AP  $\alpha_\mu^{(n-1)}$  in state  $(n-1)$ , where  $\alpha_\mu^{(n-1)}$  can be either a LiFi AP or the WiFi AP. The estimated VHO efficiency can be defined as follows:

$$\eta_V(j) = \begin{cases} \eta_{0,VHO}, & j \neq \alpha_\mu^{(n-1)} \\ 1, & j = \alpha_\mu^{(n-1)} \end{cases}, j \in \{\mathcal{A}, W_{AP}\}. \quad (4.14)$$

We note that the CSI feedback can be notably reduced by means of limited-feedback mechanisms [41, 116, 117]. Hence, the overhead due to handover is dominant compared to the overhead due to CSI feedback, however, the handover efficiency can include both overheads, and this does not change the generality of our model.

### 4.3 Dynamic Load Balancing Scheme in Hybrid LiFi/WiFi Networks

Two algorithms are discussed in this section. The low-complexity OFDMA RA scheme for LiFi systems is summarized in Algorithm 1. The EGT-based LB scheme of the HLWNs is presented in Algorithm 2. The RA scheme in Algorithm 1 is part of the LB scheme in Algorithm 2. Hence, in the following, the detailed explanations of Algorithm 1 will be given first in Section 4.3.1 and then, Algorithm 2 is described in Section 4.3.2.

#### 4.3.1 Resource Allocation in OFDMA LiFi Systems

In this section, the RA in a single LiFi cell in a quasi-static state is investigated. As a single cell  $\alpha$  is considered in this section, for the simplicity of notation, the communication link data rate of the RU on subcarrier  $m$  for each subframe,  $r_{\mu,\alpha,m}^{\text{Link}}$ , will be written as  $\zeta_{\mu,m}$ . The  $\beta$ -proportional fairness is a generic fairness function which includes a number of well-known fairness concepts such as proportional fairness, max-min fairness and throughput maximization. Hence, it has been widely adopted in studies dealing with RA problem [95, 96, 101, 118]. The  $\beta$ -proportional fairness function considering both user data rate and fairness is used as the utility function in this study, which is defined as [119]:

$$\psi_\beta(x) = \begin{cases} \ln(x), & \beta = 1 \\ \frac{x^{1-\beta}}{1-\beta}, & \beta \geq 0, \beta \neq 1 \end{cases}, \quad (4.15)$$

where  $\beta$  denotes the fairness coefficient and  $x$  is the user data rate. The well-known proportional fairness and the max-min fairness can be realized using this utility function by setting  $\beta = 1$  and  $\beta \rightarrow +\infty$ , respectively [96]. In order to solve the RA problem, the

optimization problem can be formulated as follows:

$$\begin{aligned} \max_{k_{\mu,m}} \quad & \sum_{\mu \in \mathcal{U}_\alpha} \psi_\beta \left( \sum_{m \in \mathcal{M}_e} k_{\mu,m} \zeta_{\mu,m} \right) \\ \text{s.t.} \quad & \sum_{\mu \in \mathcal{U}_\alpha} k_{\mu,m} = K, \quad m \in \mathcal{M}_e. \end{aligned} \quad (4.16)$$

where  $k_{\mu,m}$  denotes the number of RUs allocated to user  $\mu$  on subcarrier  $m$  in each RB and  $\mathcal{U}_\alpha$  denotes the set of users served by the AP  $\alpha$ . By using the Lagrangian multiplier method, an iterative algorithm is proposed to find the optimum of (4.16) in [78]. However, this method is of high computational complexity due to the iterative algorithm. In order to reduce the complexity, a novel RA scheme in LiFi OFDMA systems is proposed in this section.

Since the LiFi channel gain in the frequency domain is inversely proportional to the frequency [73], only users with high SINR are able to utilize the high frequency resources. In other words, the number of users who can utilize high-frequency resources is much less than the number of users who can use low-frequency resources. Therefore, the low-complexity RA scheme is proposed to be carried out from the high-frequency to the low-frequency subcarriers in sequence. For user  $\mu$ , the aggregate data rate from subcarriers  $m$  to  $M/2$ ,  $Z_{\mu,m}$ , can be calculated by adding the data rate achieved on subcarrier  $m$ ,  $k_{\mu,m} \zeta_{\mu,m}$ , and the aggregate data rate from subcarriers  $m+1$  to  $M/2$ ,  $Z_{\mu,m+1}$ . This can be expressed as:

$$Z_{\mu,m} = \begin{cases} k_{\mu,m} \zeta_{\mu,m} + Z_{\mu,m+1}, & 2 \leq m \leq M/2 \\ 0, & M/2 < m \end{cases}. \quad (4.17)$$

It should be noted that the sum of  $k_{\mu,m} \zeta_{\mu,m}$  and  $Z_{\mu,m+1}$  is less than  $\sum_{m \in \mathcal{M}_e} k_{\mu,m} \zeta_{\mu,m}$ . Hence, the sub-optimization problem can be formulated as follows:

$$\begin{aligned} \max_{k_{\mu,m}} \quad & \sum_{\mu \in \mathcal{U}_\alpha} \psi_\beta (k_{\mu,m} \zeta_{\mu,m} + Z_{\mu,m+1}) \\ \text{s.t.} \quad & \sum_{\mu \in \mathcal{U}_\alpha} k_{\mu,m} = K, \quad m \in \mathcal{M}_e. \end{aligned} \quad (4.18)$$

To solve the sub-optimization problem in (4.18), the Lagrangian multiplier method is used and the Lagrangian function can be expressed as:

$$F(k_{\mu,m}, \lambda_m) = \sum_{\mu \in \mathcal{U}_\alpha} \psi_\beta (k_{\mu,m} \zeta_{\mu,m} + Z_{\mu,m+1}) + \lambda_m \left( K - \sum_{\mu \in \mathcal{U}_\alpha} k_{\mu,m} \right), \quad (4.19)$$

where  $\lambda_m$  is the Lagrangian multiplier for the  $m$ -th constraint in (4.18). To obtain the optimal  $k_{\mu,m}$ , the gradient of the Lagrangian function in (4.19) is set to be equal to 0, which is written as:

$$\frac{\partial F(k_{\mu,m}, \lambda_m)}{\partial k_{\mu,m}} = \zeta_{\mu,m} (k_{\mu,m} \zeta_{\mu,m} + Z_{\mu,m+1})^{-\beta} - \lambda_m = 0. \quad (4.20)$$

It can be obtained from (4.20) that:

$$k_{\mu,m} = \frac{1}{\zeta_{\mu,m}} \left( \frac{\zeta_{\mu,m}}{\lambda_m} \right)^{\frac{1}{\beta}} - \frac{Z_{\mu,m+1}}{\zeta_{\mu,m}}. \quad (4.21)$$

Based on the constraint in (4.18), (4.21) can be solved as:

$$\lambda_m^{-\frac{1}{\beta}} = \left( K + \sum_{\mu \in \mathcal{U}_\alpha} \frac{Z_{\mu,m+1}}{\zeta_{\mu,m}} \right) / \sum_{\mu \in \mathcal{U}_\alpha} (\zeta_{\mu,m})^{\frac{1}{\beta}-1}. \quad (4.22)$$

By inserting (4.22) into (4.21), the number of RUs allocated to user  $\mu \in \mathcal{U}_\alpha$  on subcarrier  $m$  in each RB is given by:

$$k_{\mu,m} = \frac{\zeta_{\mu,m}^{\frac{1}{\beta}-1}}{\sum_{\mu \in \mathcal{U}_\alpha} \zeta_{\mu,m}^{\frac{1}{\beta}-1}} \left( K + \sum_{\mu \in \mathcal{U}_\alpha} \frac{Z_{\mu,m+1}}{\zeta_{\mu,m}} \right) - \frac{Z_{\mu,m+1}}{\zeta_{\mu,m}}. \quad (4.23)$$

It can be noted that the iterative computation is not required in (4.23). A closed-form solution is obtained for  $k_{\mu,m}$  in (4.23) which reduces the computational complexity substantially. Algorithm 1 summarizes the low-complexity RA scheme. The LiFi data rate of user  $\mu$  can be expressed as:

$$D_{\mu,\alpha} = \sum_{m \in \mathcal{M}_e} k_{\mu,m} \zeta_{\mu,m}, \quad \mu \in \mathcal{U}_\alpha. \quad (4.24)$$

---

**Algorithm 1** : Low-complexity RA algorithm in the cell  $\alpha$  for LiFi OFDMA systems

---

- 1: Initialization: Subcarrier  $m = \frac{M}{2}$ ; For all user  $\mu \in \mathcal{U}_\alpha$ ,  $Z_{\mu, \frac{M}{2}+1} = 0$ .
  - 2: **while** Subcarrier  $m \geq 2$  **do**
  - 3:   **for** Each user  $\mu \in \mathcal{U}_\alpha$  **do**
  - 4:     Calculate the link data rate,  $\zeta_{\mu,m}$ .
  - 5:     Calculate  $Z_{\mu,m+1}$  based on (4.17).
  - 6:   **end for**
  - 7:   Calculate  $k_{\mu,m}$  for each user on subcarrier  $m$  according to (4.23).
  - 8:    $m = m - 1$ .
  - 9: **end while**
- 

### 4.3.2 Proposed Evolutionary-game-theory-based Load Balancing Scheme

The global optimum of the system LB problem can be determined using the exhaustive search method. However, the exhaustive search is very computational expensive. In this section, an EGT-based LB scheme, which reduces the computational complexity and achieves sub-optimum performance, is proposed for the APA. At the beginning of each state, the EGT-based scheme is performed and each user will be assigned to an AP. If a handover occurs, users cannot transfer any data during the handover association time. The setup of evolutionary game for LB in each state are described as follows:

1. *Players Set ( $\mathcal{U}$ ):* The players in the game are the users in the hybrid network. The set of players is  $\mathcal{U}$  and the total number of players is  $N_{\text{UE}}$ .

2. *Strategy Set ( $\mathcal{S}_\mu$ ):* Each user can be potentially served by one of the LiFi APs or the WiFi APs. In order to efficiently utilize the LiFi resources, each user will be allocated to its best LiFi AP if it must be served by LiFi. The best LiFi AP is defined as the one which can offer the highest link data rate with handover efficiency taken into account. The best LiFi AP for user  $\mu$  can be defined as:

$$A_\mu = \arg \max_{i \in \mathcal{A}} \eta_H(i) r_{\mu,i}^{\text{Link}}. \quad (4.25)$$

To reduce the complexity of the AP selection scheme, user  $\mu$  will be assigned to the AP from the strategy set  $\mathcal{S}_\mu$ . This set contains the best LiFi AP and the WiFi AP, denoted as  $\mathcal{S}_\mu = \{A_\mu, W_{\text{AP}}\}$ .

3. *Payoff Function:* The payoff of a player is defined by the user data rate, which is achieved by either a LiFi or the WiFi AP. The payoff function of user  $\mu$  served by the AP  $\alpha$  can be written as:

$$\pi_{\mu,\alpha} = \begin{cases} D_{\mu,\alpha}, & \alpha = A_\mu \\ R_{\mu,\text{wifi}}, & \alpha = W_{\text{AP}} \end{cases}, \quad (4.26)$$

where  $D_{\mu,\alpha}$  is the achievable data rate when user  $\mu$  is served by the LiFi AP  $\alpha$ , given in (4.24); and  $R_{\mu,\text{wifi}}$  is the achievable data rate if user  $\mu$  is connected to WiFi AP, expressed in (4.11).

In the EGT-based LB scheme, the players can achieve a better payoff by adapting their strategy iteratively. The adaptation of the AP selection strategy and the evolution of the population is based on the ‘mutation and selection mechanism’ in EGT [100]. For each player, the strategy shift occurs randomly. The players experiencing a lower value of payoff are more likely to adapt their strategy. Following the rule, in the  $t$ -th iteration, the probability of mutation for user  $\mu$  can be expressed as:

$$p_\mu^{<t>} = \begin{cases} 1 - \frac{\pi_{\mu,\alpha}^{<t-1>}}{\bar{\pi}^{<t-1>}}, & \pi_{\mu,\alpha}^{<t-1>} < \bar{\pi}^{<t-1>} \\ 0, & \pi_{\mu,\alpha}^{<t-1>} \geq \bar{\pi}^{<t-1>} \end{cases}. \quad (4.27)$$

where  $\pi_{\mu,\alpha}^{<t-1>}$  denotes the player’s payoff in the previous iteration;  $\bar{\pi}^{<t-1>}$  represents the average payoff of all players in the previous iteration. The average payoff of all players in the  $t$ -th iteration is given by:

$$\bar{\pi}^{<t>} = \frac{1}{N_{\text{UE}}} \sum_{\mu \in \mathcal{U}} \pi_{\mu,\alpha}^{<t>}, \quad (4.28)$$

where  $\pi_{\mu,\alpha}^{<t>}$  is the payoff of user  $\mu$  in the  $t$ -th iteration, given in (4.26). When a mutation occurs, the user may be assigned to a new AP to maximize the estimated payoff in the current iteration. The new serving AP can be determined as:

$$\alpha_\mu^{<t>} = \arg \max_{i \in \mathcal{S}_\mu} \hat{\pi}_{\mu,i}^{<t>} \quad (4.29)$$

and

$$\hat{\pi}_{\mu,i}^{<t>} = \begin{cases} \pi_{\mu,i}^{<t-1>}, & i = \alpha_\mu^{<t-1>} \\ \eta_V(i) \pi_{\mu,i}^{<t>}, & i \neq \alpha_\mu^{<t-1>} \end{cases},$$

---

**Algorithm 2** : EGT-based centralized LB algorithm executed in the CU.
 

---

- 1: Initialization: The users are randomly allocated to an AP from  $\mathcal{S}_\mu$ ; based on OFDMA (for LiFi) or CSMA/CA (for WiFi), each AP allocates the available resources to the players of the corresponding cell; the CU calculates the payoff of each player  $\pi_{\mu,\alpha}^{<0>}$  and the average payoff  $\bar{\pi}^{<0>}$ ; and  $t \leftarrow 1$ .
  - 2: **for** each player  $\mu \in \mathcal{U}$  **do**
  - 3:   Calculate the probability of mutation,  $p_\mu^{<t>}$ , based on (4.27) and generate a random number  $\delta$ , which is uniformly distributed between 0 and 1.
  - 4:   **if**  $\delta < p_\mu^{<t>}$  **then**
  - 5:     **if**  $\alpha_\mu^{<t-1>}$  is a WiFi AP **then**
  - 6:       Calculate the estimated payoff if connected to the best LiFi AP,  $\hat{\pi}_{\mu,v}^{<t>}$ , based on (4.30) and Algorithm 1.
  - 7:     **else**
  - 8:       Compute the estimated payoff if connected to the WiFi AP,  $\hat{\pi}_{\mu,v}^{<t>}$ , based on (4.31) and CSMA/CA scheme.
  - 9:     **end if**
  - 10:   Based on (4.29), check whether the potential AP will be overloaded first and then decide to stay with the previous AP or switch to a new AP.
  - 11: **else**
  - 12:   No mutation occurs, the player  $\mu$  remains with the previous AP.
  - 13: **end if**
  - 14: **end for**
  - 15: **for** each AP  $\alpha \in \mathcal{A} \cup \{W_{AP}\}$  **do**
  - 16:   According to Algorithm 1 and (4.11), the available resources are allocated by the CU to players in each cell.
  - 17: **end for**
  - 18:  $t \leftarrow t + 1$  and repeat from Step 2 until no AP switch occurs.
- 

where  $\alpha_\mu^{<t>}$  is the AP assigned to player  $\mu$  at the  $t$ -th iteration;  $\hat{\pi}_{\mu,i}^{<t>}$  is the estimated payoff when the player is allocated to a new AP  $v$  other than  $\alpha_\mu^{<t-1>}$ . The estimated payoff  $\hat{\pi}_{\mu,v}^{<t>}$  is greatly related to the RA scheme in different networks:

i) *LiFi network* ( $v = A_\mu$ ): In this case,  $\alpha_\mu^{<t-1>}$  is the WiFi AP and user  $\mu$  may experience a handover from WiFi to LiFi in the  $t$ -th iteration. The estimated payoff can be calculated by using the data rate result in LiFi OFDMA systems, shown in (4.24). Assume that the set of users allocated to LiFi AP  $v$  in  $(t-1)$ -th iteration is denoted by  $\mathcal{U}_v^{<t-1>}$ . After the user is handed off from the WiFi AP to LiFi AP  $v$ , the set of users served by the LiFi AP  $v$  becomes  $\mathcal{U}_v^{<t>} = \mathcal{U}_v^{<t-1>} \cup \{\mu\}$ . According to (4.24), the estimated payoff of user  $\mu$  if connected to LiFi AP  $v$  can be obtained as:

$$\hat{\pi}_{\mu,v}^{<t>} = \sum_{m \in \mathcal{M}_e} \dot{k}_{\mu,m} \zeta_{\mu,m}, \quad \mu \in \mathcal{U}_v^{<t>}, \quad v = A_\mu, \quad (4.30)$$

where  $\dot{k}_{\mu,m}$  is the estimated number of RUs that is allocated to user  $\mu$  on subcarrier  $m$  of each RB, which can be calculated according to Algorithm 1.

ii) *WiFi network* ( $v = W_{AP}$ ): It is assumed that the number of users served by the WiFi AP at

the  $(t-1)$ -th iteration is denoted by  $N_w^{<t-1>}$ . In the case of  $v = W_{AP}$ , user  $\mu$  would experience handover from a LiFi AP to the WiFi AP. According to (4.11), the estimated payoff of user  $\mu$  is expressed as:

$$\hat{\pi}_{\mu,v}^{<t>} = \frac{R_c U_{\text{down}}}{N_w^{<t-1>} + 1}, \quad v = W_{AP}, \quad (4.31)$$

where  $R_c$  is the channel bit rate in the WiFi system; and  $U_{\text{down}}$  is the downlink utilization efficiency which is given in (4.5b). Note that  $U_{\text{down}}$  should be computed based on  $N_w^{<t>} = N_w^{<t-1>} + 1$ .

The proposed EGT-based LB algorithm can be summarized in three steps: i) in the APA step, each user adapts their AP selection strategy unilaterally to improve the payoff; 2) in the RA step, based on the RA schemes, e.g. OFDMA or CSMA/CA, the available resources are allocated to users; 3) repeat step 1 and 2 until no user can adjust the AP selection unilaterally to increase their payoff. The EGT-based LB algorithm is given in Algorithm 2.

### 4.3.3 Convergence Analysis of Proposed Scheme

The EGT-based LB scheme can converge after several iterations, which has been proved in [101]. Typically, when a convergence is reached, an evolutionary equilibrium (EE), referred to as the Nash Equilibrium in the evolutionary game [100], can be achieved.

**Definition 1** A strategy profile  $\mathcal{E} = \{\alpha_\mu | \mu \in \mathcal{U}\}$  reaches an EE when no user can change the strategy unilaterally to improve their payoff, i.e. [100]:

$$\pi_{\mu, \alpha_\mu} \geq \pi_{\mu, \alpha'_\mu}, \quad \alpha_\mu \neq \alpha'_\mu, \quad \alpha_\mu, \alpha'_\mu \in \mathcal{S}_\mu, \quad (4.32)$$

where the payoff of the user  $\mu$  connected to the AP  $\alpha$  is denoted as  $\pi_{\mu, \alpha}$ .

In this section, the numerical simulations are used to evaluate the iteration numbers required in the proposed LB scheme. The simulation setup is described in Section 4.4 and simulation parameters are listed in Table 4.2. The users are moving randomly in an indoor scenario for 1000 quasi-static states. In each state, the EGT-based LB scheme is executed to find the EE, which provides the APA and RA results. At the first state, users randomly choose an AP from their strategy sets as an initial host AP. After the first state, the allocated APs in the previous state are considered as the initialization of host APs. The iteration number of the proposed EGT-based LB scheme is evaluated and shown in Fig. 4.3. In the legend, ‘PF’ represents proportional fairness ( $\beta = 1$ ) while ‘MF’ means max-min fairness ( $\beta \rightarrow +\infty$ ). It can be seen that in order to achieve an EE, 7 iterations are needed at the first state while only 4-5 iterations are required from state 2 to state 1000. This means that when considering a dynamic network, the proposed EGT-based LB scheme achieves a quick convergence by using an average of less than 5 iterations.



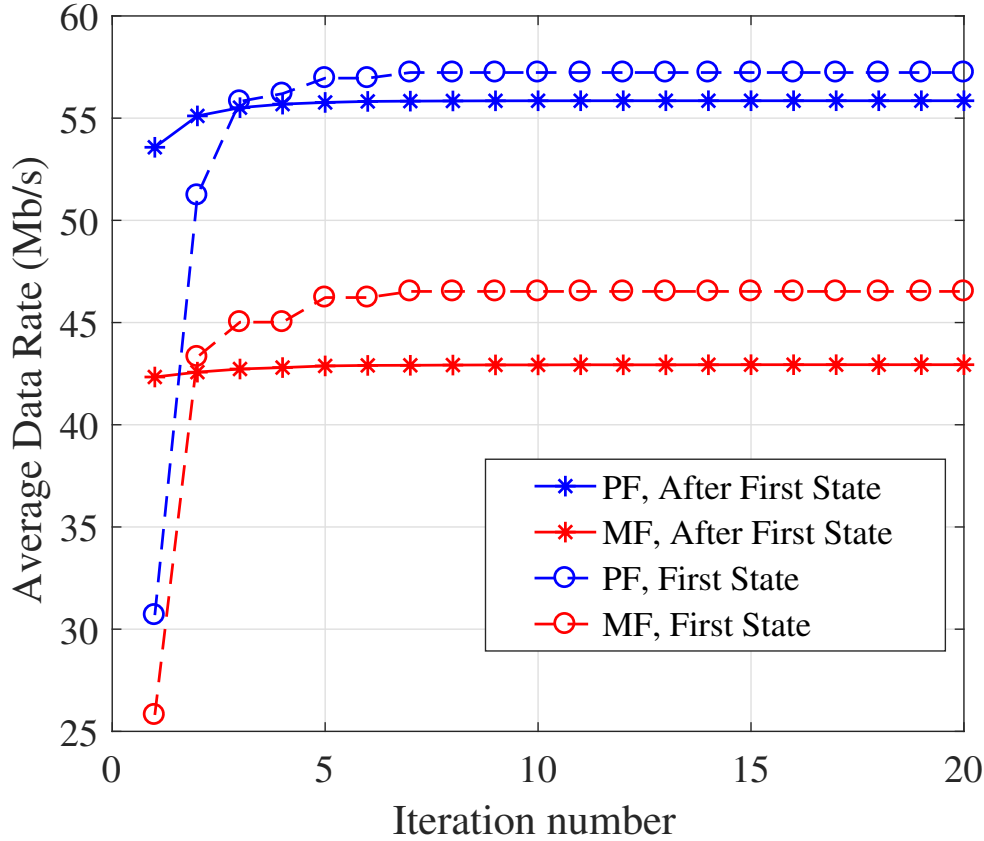


**Figure 4.3:** Average user data rate versus the iteration number.

## 4.4 Performance Evaluation

### 4.4.1 Simulation Setups

As shown in Fig. 4.1 (a), a  $16 \text{ m} \times 16 \text{ m}$  indoor office scenario is considered for the numerical simulations. The network consists of 16 LiFi APs which are deployed following a square topology on the ceiling. A WiFi AP is located at the center of the room to provide ubiquitous wireless coverage. The users are initially distributed uniformly in the  $XY$ -plane of the room and they hold a device in their hands. In our simulations, the users move randomly following an ORWP model described in Section 2.7.3 to realize a real-life scenario. We use (2.46) to calculate the  $k$ -th sample of autoregressive (AR)(1). The mean and variance of the random process (RP),  $\theta$ , are  $\mathbb{E}[\theta] = 30^\circ$  and  $\sigma_\theta = 7.78^\circ$ , which are compatible with the experimental measurements. Moreover, the sampling time and the coherence time of  $\theta$  are  $T_s = 13 \text{ ms}$  and  $T_{c,\theta} = 130 \text{ ms}$  [83]. The  $k$ -th sample of  $\theta$  along with  $\omega$  can be used in (2.6) to calculate the normal vector at the Rx. Note that we used  $\omega = \Omega - \pi$  similar to [83], where  $\Omega$  defines the movement direction of users.

To evaluate user fairness, the fairness index,  $I$ , will be used as the metric which can be expressed

Name of Parameters	Symbol	Value
Height of the AP	$z_{AP}$	3.5 m
Height of the user device	$z_{UE}$	1.5 m
Optical transmit power in LiFi system	$P_{tx}$	9 W
Noise power spectral density of LiFi	$N_0$	$10^{-19} A^2/Hz$
The physical area of a PD	$A_p$	1 cm <sup>2</sup>
Half-intensity radiation angle	$\Phi_{1/2}$	60 deg.
Half angle of the Rx field of view (FOV)	$\Psi_c$	90 deg.
Gain of optical filter	$T_s(\psi)$	1.0
Refractive index	$n_{ref}$	1.5
Optical to electric conversion efficiency	$\tau$	0.53 A/W
Maximum backoff stage	$C_{max}$	1024
Time duration of RTS	$t_{RTS}$	0.16 $\mu s$
Time duration of CTS	$t_{CTS}$	0.14 $\mu s$
Time duration of frame header	$t_H$	0.23 $\mu s$
Time duration of ACK	$t_{ACK}$	0.14 $\mu s$
Time duration of SIFS	$t_{SIFS}$	28 $\mu s$
Time duration of DIFS	$t_{DIFS}$	80 $\mu s$
Time duration of PIFS	$t_{PIFS}$	128 $\mu s$
Propagation delay	$t_p$	1 $\mu s$
Channel bit rate in the WiFi system	$R_c$	1.732 Gbit/s
Average user movement speed	$v_s$	1 m/s

**Table 4.2:** *Simulation Parameters*

as [27]:

$$I_F = \frac{(\sum_{i=1}^{N_{UE}} x_i)^2}{N_{UE} \sum_{i=1}^{N_{UE}} x_i^2}. \quad (4.33)$$

where  $x_i$  is the achievable data rate of user  $i$ . The fairness index ranges from 0 to 1, where 1 means all users achieve the same data rate. The parameters in the simulation are summarized in Table 4.2. Each simulation contains 1000 quasi-static states. The results shown in the following plots are averaged over 1000 independent tests.

#### 4.4.2 Performance Analysis

In this section, the data rate performance of OFDMA and TDMA RA schemes in LiFi systems is first evaluated. Following this, the HLWN is considered and the evaluation of the proposed EGT-based LB scheme on both user data rate and fairness is undertaken. Finally, the impact of the average handover efficiency and user speed on the system throughput is analyzed.

1) *OFDMA vs. TDMA*: Initially, a stand-alone LiFi OFDMA network with 16 LiFi APs is considered. In LiFi, due to the low pass effect of the front-end elements, the available channel bandwidth depends on the actual devices. Therefore, the impact of cutoff frequency is studied. Fig. 4.4 presents the average user data rate achieved by the proposed low complexity OFDMA RA scheme versus the 3 dB bandwidth,  $f_0$ . It can be seen that the user data rate increases with

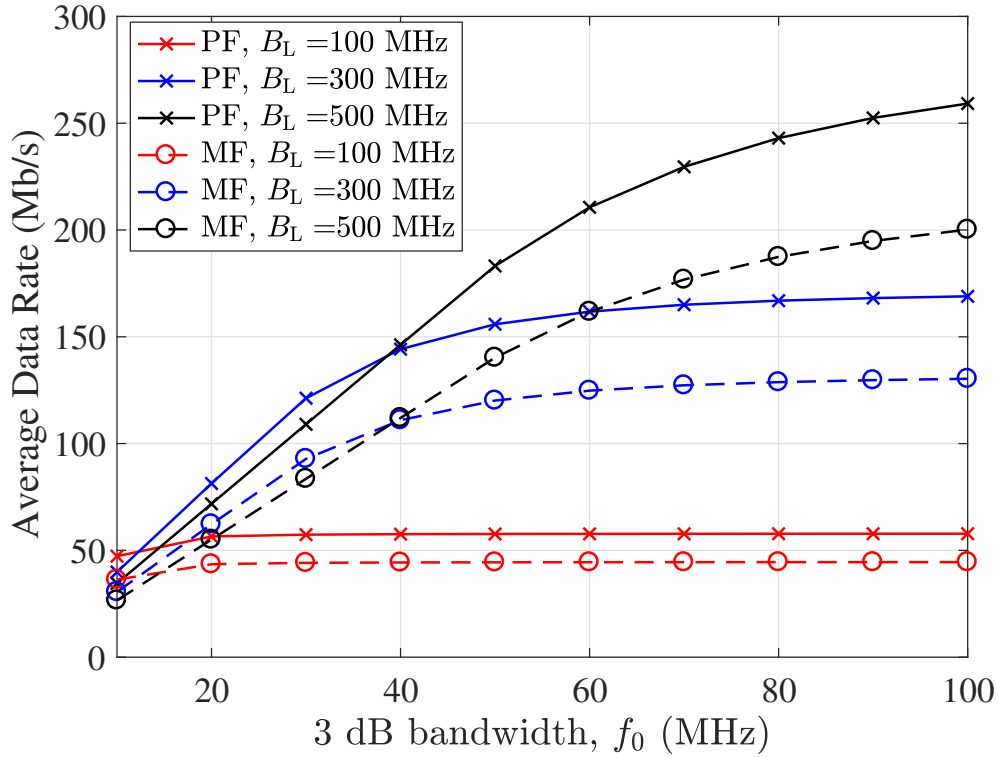


**Figure 4.4:** Evaluation of average data rate with different 3 dB bandwidth in LiFi OFDMA network. A comparison between proportional fairness (PF) and max-min fairness (MF). ( $N_{\text{UE}} = 80$ , 16 LiFi APs and no WiFi AP considered)

$f_0$ , but the gradient decreases. This is because when 3 dB bandwidth is large enough and the modulation bandwidth is fixed, the LiFi channel gain tends to be flat and the achievable data rate is maximized. In addition, Fig. 4.4 shows that ‘PF’ can achieve a better data rate performance than ‘MF’ due to the sacrifice of user fairness. The gap between these two curves increases along with the modulation bandwidth  $B_L$ . For the typical 3 dB bandwidth of 30 MHz, the data rate differences between ‘PF’ and ‘MF’ are 9.6, 41.2, 57.7 Mb/s, respectively when  $B_L$  equals to 100, 300 and 500 MHz.

Considering a HLWN, the data rate performance achieved by an EGT-based LB scheme is presented in Fig. 4.5 (a), where OFDMA and TDMA RA methods are used in the LiFi network, respectively. In the TDMA RA scheme, resources are partitioned only in the time domain [101]. The user fairness is evaluated and shown in Fig. 4.5b, where the fairness index is used as the criteria. As shown in Figs. 4.5 (a) and Figs. 4.5 (b), when using the proposed EGT-based LB scheme, the OFDMA RA method outperforms the TDMA RA method in terms of both user data rate and fairness index. This is because the OFDMA scheme can utilize the high-frequency RUs more efficiently than the TDMA RA method when the low-pass effect of the front-end devices are considered. As shown in (2.43), the LiFi channel response in the frequency domain is inversely proportional to the frequency. This means that users with high SINRs are able to use a large modulation bandwidth, while the users with low SINRs may not be able to transmit signals on high-frequency subcarriers. The OFDMA RA scheme is able to carefully allocate

high-frequency RUs to users with high SINRs while allocating low-frequency RUs to users with low SINRs. By this method, the overall user data rate can be enhanced in LiFi systems.

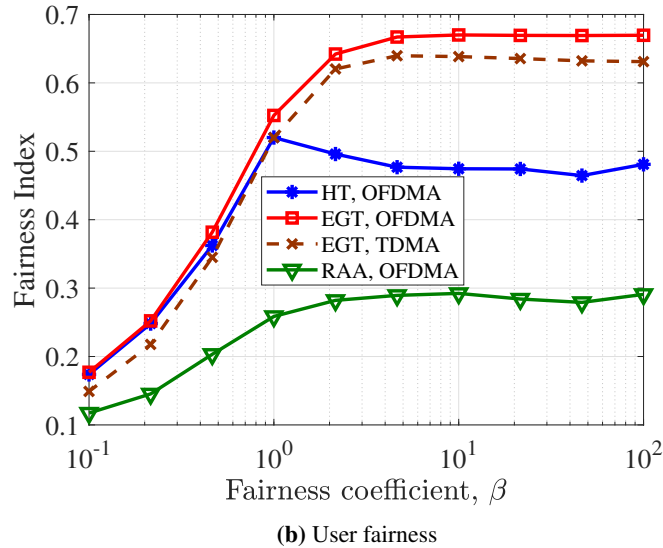
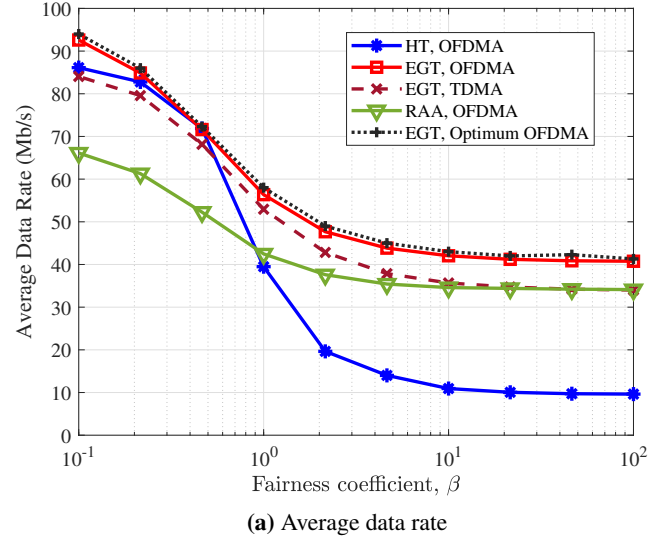


**Figure 4.5:** Evaluation of the system performance by using different LB and RA schemes in HLWN. ( $B_L = 300$  MHz,  $f_0 = 30$  MHz,  $\epsilon = 2$ ,  $\eta_{0,\text{HHO}} = 0.9$ ,  $\eta_{0,\text{VHO}} = 0.6$  and  $N_{\text{UE}} = 200$ )

2) *EGT vs. Benchmark LB schemes:* In Figs. 4.5 (a) and 4.5 (b), two benchmark LB algorithms for HLWNs are evaluated and compared with the proposed EGT-based LB scheme. Specifically, ‘HT’ represents that the APA of users is determined by using a hard threshold while ‘RAA’ means that each user randomly chooses the host AP from their strategy set  $S_\mu$  [101]. The handover efficiency is considered in the AP selection in the benchmark algorithms. After the AP allocation, the proposed OFDMA resource allocation scheme is used in both ‘HT’ and ‘RAA’ schemes. It can be seen that the EGT-based LB scheme achieves a better

performance in terms of user data rate and fairness index. Particularly, the achievable data rate by EGT is notably 20 Mb/s and 30 Mb/s more than RAA and HT, respectively. Regarding the fairness index, the EGT-based LB scheme offers a significant improvement compared to the two benchmark schemes. This is because in the EGT scheme, there is a high probability that users with low payoff will switch to better APs, which makes the network well load-balanced. It can be seen from Fig. 4.5b that the proposed low-complexity OFDMA scheme achieves data-rate performance closed to the optimum scheme. Another interesting observation from Fig. 4.5b is with regard to the HT with OFDMA in the downlink. As can be seen, the fairness index increases initially with the increase of  $\beta$  due to the fairness among LiFi users increase. However, after  $\beta > 1$ , it starts to decrease. The reason for this is that when the HT is applied, the number of users connected to the WiFi AP will increase as the increase of  $\beta$ , which leads to a degradation in the throughput of WiFi users. On the other hand, the LiFi users benefit from more released resources and their data rate increases. Therefore, the load between WiFi and LiFi is not well balanced, which leads to a slight decrease in the fairness index.

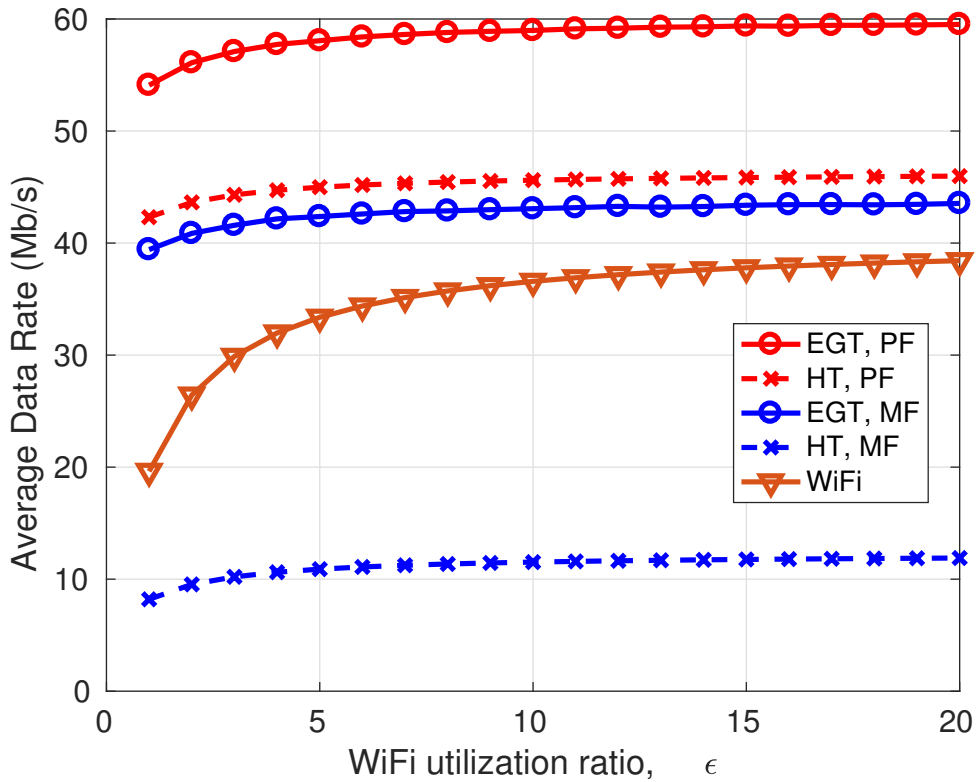


**Figure 4.6:** Evaluation of the effects of WiFi utilization ratio on the user data rate in HLWN ( $B_L = 300$  MHz,  $f_0 = 30$  MHz,  $\eta_{0,\text{HHO}} = 0.9$ ,  $\eta_{0,\text{VHO}} = 0.6$  and  $N_{\text{UE}} = 200$ ) and a stand-alone WiFi network ( $N_{\text{UE}} = 40$ ).

3) *WiFi utilization*: In Fig. 4.6, the effect of the WiFi utilization ratio,  $\epsilon$ , on the user data rate is evaluated. As shown in (4.5a),  $\epsilon = 1$  means that the uplink and downlink have the same probability to access the WiFi channel. When  $\epsilon$  is large enough (e.g.  $\epsilon = 20$ ), the downlink can utilize more than 95% of the WiFi resources. As shown in Fig. 4.6, by decreasing  $\epsilon$  from 20 to 1, the average user data rate will reduce by approximately 50% from 40 Mb/s to 20 Mb/s.

In comparison, users in HLWNs only have a 8% decrease in the achievable data rate. This is because, in HLWNs, some of the users in WiFi can be transferred to LiFi layers when WiFi provides less resources for downlink. It should be noted that in the simulation, it is assumed that HLWN has 200 users while the stand-alone WiFi network has only 40 users. Although the HLWN has 5 times users, when proposed EGT method is applied, the users can still achieve much higher data rate than users in the stand-alone WiFi network for all  $\epsilon$ . Hence, the HLWNs can maintain a good downlink performance regardless of the WiFi utilization ratio. Also, it can be seen in Fig. 4.6 that the proposed EGT-based LB scheme can always achieve a higher user data rate than the HT scheme regardless of the WiFi utilization ratio.

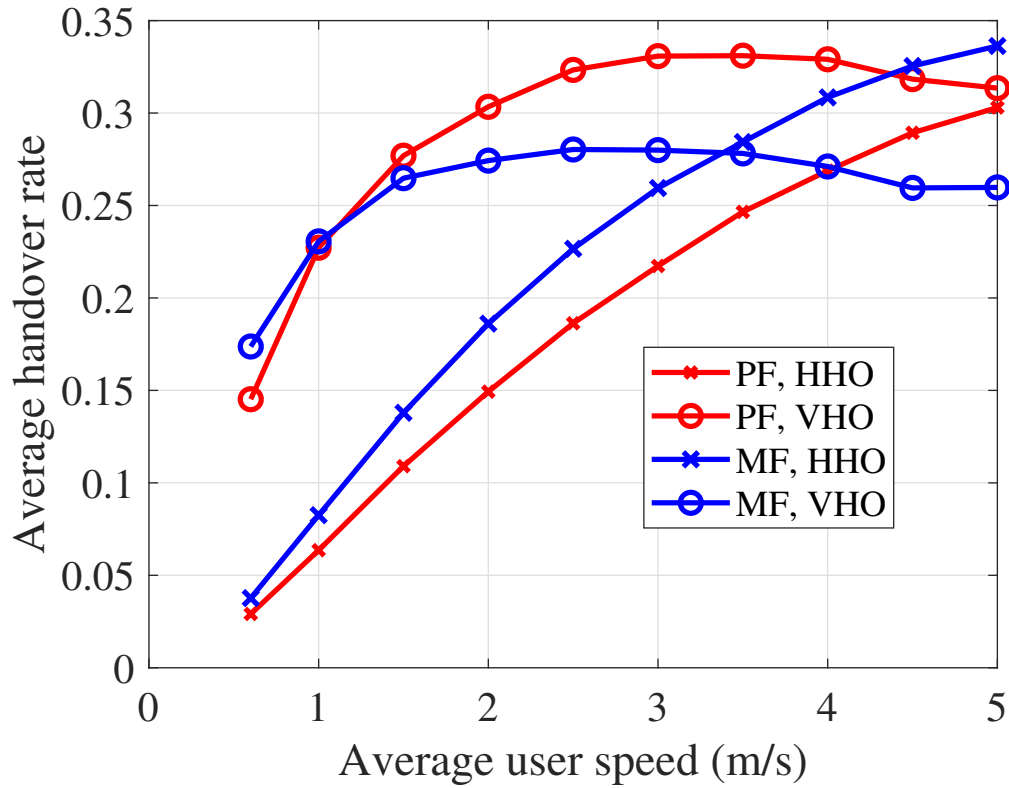


**Figure 4.7:** Evaluation of average handover rate corresponding to user speed. (The EGT-based LB scheme is applied,  $B_L = 300$  MHz,  $f_0 = 30$  MHz,  $\epsilon = 2$ ,  $\eta_{0,HHO} = 0.9$ ,  $\eta_{0,VHO} = 0.6$  and  $N_{UE} = 200$ )

4) *User Speed:* The effect of user speed on the handover rate is evaluated and presented in Fig. 4.7. Handover rate is defined as the ratio of the total number of handovers and the total simulation time. It appears that when the user speed is less than 3 m/s, the handover rate of VHO is higher than the handover rate of HHO and they both increase along with user speed. If the user speed is greater than 3 m/s, the handover rate of HHO still increases with user velocity while the VHO performs oppositely. This can be explained as follows. Due to the ICI in LiFi systems, when a user moves from one cell center to another cell center, the SINR will first decrease and then increase. In this case, for low speeds, the LiFi-connected user will be handed off to WiFi when approaching the cell edge, then, they will connect to another LiFi AP when entering the cell-center region. Accordingly, the number of VHOs is higher than the HHO. For

high speeds, the users may pass the cell-edge regions quickly without being connected to the WiFi AP. Therefore, the number of VHOs decreases while the number of HHOs still increases. It can be seen that by using the proposed EGT scheme, the number of handovers in the fast movement case (e.g. 4 m/s) is still more than twice that in the low movement case (e.g. 1 m/s). Work is ongoing to try and reduce the number of VHOs and achieve a high throughput for high-speed users in HLWNs.

5) *Average Handover Efficiency*: In Fig. 4.8, the impact of the average horizontal and vertical handover efficiency,  $\eta_{0,\text{HHO}}$  and  $\eta_{0,\text{VHO}}$ , on the user data rate is evaluated. It can be seen that with an increase in  $\eta_{0,\text{VHO}}$ , the user data rate achieved by EGT is almost constant. However, the user data rate achieved by HT significantly increases with an increase in  $\eta_{0,\text{VHO}}$ . This is because a hard threshold,  $T$ , is used for the APA in the HT scheme and the vertical handover from a LiFi AP to a WiFi AP will only occur when  $\eta_{0,\text{VHO}} \times D_{\mu,A\mu} < T$  and vice versa. Hence, for a low  $\eta_{0,\text{VHO}}$ , it is more likely for the user to switch from a LiFi AP to the WiFi AP and less likely to switch back. Therefore, when considering a low value for  $\eta_{0,\text{VHO}}$ , the majority of users in the HT scheme are served by WiFi. In comparison, in the EGT-based LB scheme, the AP allocation is determined based on the achievable data rate in both WiFi and LiFi cells. If the WiFi cell is overloaded, the user data rate achieved by WiFi is low. This may result in users transferring from the WiFi layer to the LiFi layer despite a high vertical handover overhead. In this case, users will be assigned to the LiFi or WiFi APs in a more balanced way. Thus, it can be concluded that the proposed EGT-based LB scheme can achieve a better user data rate than the HT scheme when the average vertical handover efficiency,  $\eta_{0,\text{VHO}}$ , is low. It should

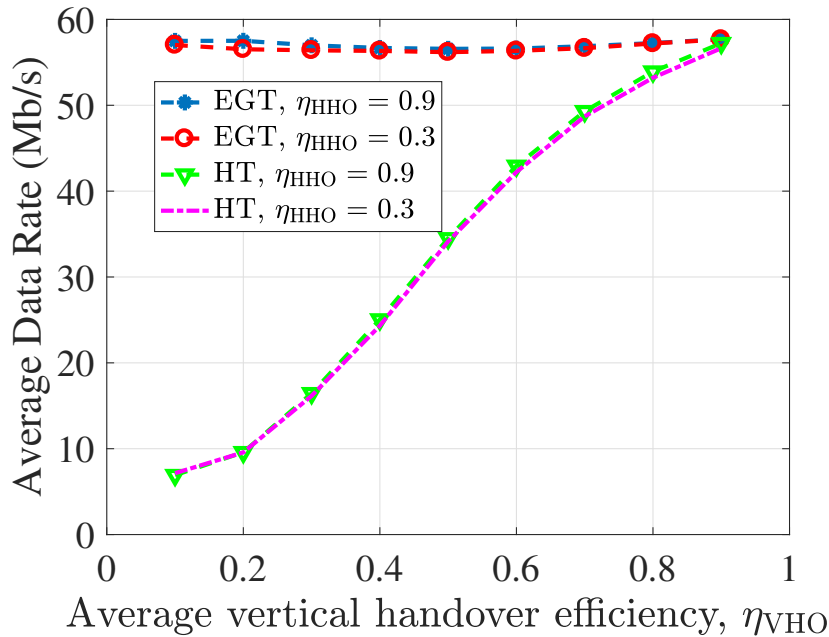


**Figure 4.8:** Evaluation of the effects of  $\eta_{\text{HHO}}$  and  $\eta_{\text{VHO}}$  on the user data rate. ( $B_L = 300$  MHz,  $f_0 = 30$  MHz,  $\epsilon = 2$  and  $N_{\text{UE}} = 200$ )

also be noted that for both EGT and HT schemes, increasing the average horizontal handover efficiency,  $\eta_{0,\text{HHO}}$ , from 0.3 to 0.9 only increases the average data rate slightly. Hence,  $\eta_{0,\text{HHO}}$

has little impact on the system performance. This can be explained by two factors. First, with an average user speed of 1 m/s, the average horizontal handover rate is very small as shown in Fig. 4.7. This means the likelihood of horizontal handover is low. Second, considering  $\eta_{0,HHO}$  in (4.25) has little effect on the best LiFi AP selection. As a result, in a system suffering ICI, only the AP with the best received signal strength can provide efficient data to the UE. If a UE is assigned to APs other than the one that provides the best signal strength, then the signal from the AP providing the best signal strength will become interference. This will cause the signal power to be less than the interference power and the SINR to be less than 0 dB, which does not yield high data rates.

## 4.5 Summary

In this chapter, the joint effect of random orientation and mobility has been considered to evaluate the performance of HLWN in a more realistic scenario by using the ORWP mobility model. The handover management takes into account the effect of the handover overhead. The impact of vertical and horizontal handover on the average throughput of a HLWN has been evaluated. A low-complexity OFDMA RA scheme in LiFi systems has been proposed for HLWNs. The performance of user data rate and fairness has been evaluated compared to the HLWN system where TDMA is used in LiFi. An enhanced EGT-based dynamic LB scheme for HLWNs has been proposed. In the proposed HLWN, the LiFi system adopts the OFDMA scheme while the WiFi system applies the CSMA/CA which benefits from a utilization ratio to fairly allocate WiFi resources between the uplink and downlink. Then, LB has been achieved based on these two schemes and the EGT algorithm. Also, the impact of the WiFi utilization ratio on the average data rate of a HLWN has been assessed in this chapter.





---

Chapter 5

**A VCSEL Array Transmission System  
with Novel Beam Activation  
Mechanisms**

---

## **5.1 Introduction**

Instead of using wide-spread beams emerging from illumination systems, the beam-steered infrared light communication (BS-ILC) systems use narrow well-directed beams emerging from a dedicated source. The deployment of narrow infrared (IR) beams in BS-ILC systems leads to small cell coverage, which implies that it is more likely that each beam only serves a single user equipment (UE). Therefore, capacity sharing among multiple UEs as well as traffic congestion can be avoided. By only activating beams that point towards the UEs, the BS-ILC systems provide better energy-efficiency as narrow beams with high directivity can send a greater portion of the transmitted power to the corresponding UE. Therefore, a higher signal-to-noise ratio (SNR) can be achieved. Moreover, due to the high bandwidth of narrow beam sources, such as fiber-coupled source, laser diode and vertical-cavity surface-emitting laser (VCSEL), the link can support higher capacity. In addition, compared with wide-spread beams, the narrow beams provide better privacy as UEs outside the coverage area cannot receive the transmitted signals. The BS-ILC systems have been explored in [28, 42–44]. Wavelength-controlled 2D beam-steered systems based on fully-passive crossed-grating devices are introduced and 1D beam steering has been demonstrated in [42], which shows a multi-beam system with a capacity of 2.5 Gbit/s. The 2D steering of the multi-beam system has been first demonstrated in [43] and with adaptive discrete multitone modulation (DMT) using 512 tones, a gross bit rate of 42.8 Gbit/s has been achieved. In addition, by using 60 GHz radio signal in the uplink, upstream delivery of 10 Gbit/s per upstream has been presented. In [44], the authors proposed a novel optical wireless communication (OWC) receiver (Rx) concept, which can enlarge the Rx aperture without reducing the bandwidth. Also, a multi-beam system with downstream capacities of up to 112 Gbit/s per IR beam was demonstrated. In [28], an alternative approach, which is based on a high port count arrayed waveguide grating router (AWGR) and a high-speed lens, is proposed. With pulse amplitude modulation (PAM)-4 modulation, a total system throughput beyond 8.9 Gbit/s over 2.5 m can be achieved by using 80-ports C-band AWGR. Moreover, the localization and tracking of the UE are achieved based on a 60 GHz ultra-wideband (UWB) radio link. However, all these studies consider fixed user location without mobility and the latency is high in these systems. When a mobile UE is considered, due to the small confined coverage area of the narrow beam, the beam that serves a UE may vary fast and frequently. Therefore, a high-accuracy and low-latency beam activation system or user tracking system is required to achieve a seamless connection.

Ordinary radio based indoor positioning techniques based on wireless fidelity (WiFi), Bluetooth, UWB and radio frequency identification (RFID) are not suitable candidates in this study due to their low accuracy, high latency and high hardware cost [120]. In recent years, visible light positioning (VLP) systems have emerged and various algorithms for VLP systems have been proposed, which include received signal strength (RSS), time differential of arrival (TDOA) and angle of arrival (AOA) methods. Due to being able to achieve high positioning accuracy and low cost, VLP is attracting more and more attention. Some studies have shown that the VLP technologies can achieve centimeter-level accuracy [120–123], which is way more accurate than Bluetooth (2-5 m), WiFi (1-7 m) and other technologies [124]. The VLP systems can be divided into two categories based on the receiving device: photodiode (PD) based VLP or image sensor (IS) based VLP. The PD-based VLP system has low latency but is sensitive to the device rotation, and hence cannot achieve high positioning accuracy for UEs without fixed orientation. The IS-based VLP systems are more robust to device rotation.

However, due to the high computational latency of image processing or the communication latency of transmitting image data for server-assisted computation, the real-time performance of these systems is limited [120].

Also, when VLP is adopted, the UE is required to autonomously transmit location information to the access points (APs) owing to the lack of a real-time backward channel from UE to APs. This adds an unnecessary burden on the UE and leads to the inevitable latency in real-time tracking. As the VLP system requires illumination devices and real-time backward channels, it may not be suitable for the VCSEL array system proposed in this study. To address the issue of power consumption and latency caused by UE localization, two beam activation schemes are proposed in this study. The first method is a passive beam activation scheme using a corner-cube retroreflector (CCR). The CCR is a light-weight small device, which can reflect light back to its source with minimal scattering. By using CCR, immediate feedback can be obtained for beam activation which minimizes the latency and leads to almost zero delay. The CCR has been proposed for the VLP system in [125]. Compared to the method in [125], no illumination equipment is required in our method and the power consumption for the localization system is almost zero. The second method utilizes the omnidirectional transmitter (ODTx) in the uplink communication. By using the uplink RSS matrix, this method does not require any extra signal power for localization. Compared with the PD-based VLP system, the beam activation system with ODTx is robust to the device orientation, that is to say the user can be located accurately without concerning the random orientation of the UE. Compared with the IS-based system, IS is not required, which reduces the cost. And the computation latency is reduced as the positioning algorithm is based on the RSS, which is the simplest and most cost effective schemes.

Among different types of laser diodes, VCSELs are one of the promising candidates to ensure high-data rate communications due to several outstanding features such as [52]: high-speed modulation (bandwidths of larger than 10 GHz), high power conversion efficiency, low cost and compact in size. These attributes make VCSELs appealing to many applications, particularly for high-speed indoor networks [53]. In this study, a VCSEL array system with novel beam activation methods is proposed. Compared with the wavelength-controlled BS-ILC systems, the proposed VCSEL array system removes the requirement of wavelength-tuning, spatial light modulation (SLM), microelectromechanical systems (MEMS) and coherence of beams and fiber connection to the AP End-point devices may include virtual reality devices, smartphones, televisions, computers and internet of things (IoT) applications.

## 5.2 Multi-beam System Setup

A VCSEL array system is presented in Fig. 5.1. The APs of the system is composed of  $N_{\text{beam}}$  narrow-beam transmitters (Tx) and each Tx is a VCSEL with a beam divergence of  $\theta_{\text{beam}}$ . The position of the  $\hat{n}$ -th Tx is denoted as  $\mathbf{p}_{\text{tx},\hat{n}}$ . The  $\hat{n}$ -th Tx is slightly tilted so that it is directed towards the center of its corresponding cell,  $\mathbf{p}_{\text{cell},\hat{n}}$ . Hence, the normal vector of the  $\hat{n}$ -th Tx is denoted as  $\mathbf{n}_{\text{tx},\hat{n}} = (\mathbf{p}_{\text{cell},\hat{n}} - \mathbf{p}_{\text{tx},\hat{n}}) / \|\mathbf{p}_{\text{cell},\hat{n}} - \mathbf{p}_{\text{tx},\hat{n}}\|$ , where  $\|\cdot\|$  denotes the norm operator. The side length of each cell is denoted as  $d_{\text{cell}}$ . The location of the UE is denoted as  $\mathbf{p}_{\text{UE}}$  and for the downlink communication, an avalanche photodiode (APD) is used as the Rx at the UE side.



rate for the UE can be expressed as [91]:

$$\zeta = \sum_{m=1}^{M/2-1} \frac{B_L}{M} \log_2(1 + \gamma_m) = \frac{(M/2-1)}{M} B_L \log_2 \left( 1 + \frac{(R_{\text{APD}} P_{\text{rx,opt}})^2}{(M-2)\kappa^2 \sigma_n^2} \right), \quad (5.3)$$

At the Rx, we utilize a high-bandwidth indium gallium arsenide (InGaAs) APD (G8931-10), where it works in the spectral range of 950 nm to 1700 nm. The peak sensitivity wavelength is 1550 nm. The parameters of this APD are given in Table 5.1 [126]. It is noted that the Rx bandwidth inversely depends on the capacitance of the APD, i.e.,  $B_r = 1/(2\pi R_F C_T)$ , where  $C_T$  is the capacitance of the APD and  $R_F$  is the feedback resistor of the transimpedance amplifier (TIA). Therefore, small-area APDs are required to achieve wide bandwidth at the Rx. However, for small-area APDs, a lens is required at the Rx to collect enough power and consequently enhance the SNR.

Parameter	Symbol	Value
Bandwidth	$B_L$	1.5 GHz
Spectral response range	-	950 to 1700 nm
Peak sensitivity wavelength	-	1550 nm
Effective Area of APD	$A_{\text{eff}}$	$\pi \times 0.25 \times 0.25 \times 10^{-4} \text{ m}^2$
Rx FOV	$\Psi_c$	60°
Gain of APD	$G_{\text{APD}}$	30
Responsivity	$R_{\text{APD}}$	0.9 A/W
Refractive index	$n_{\text{ref}}$	1
Laser noise	RIN	-155 dB/Hz

**Table 5.1:** APD parameters. [3]

### 5.3 Beam Activation

For a VCSEL array system, it is important to determine which beam should be activated to optimize the system performance. The beam selection strategy considered in this study is the signal strength strategy (SSS), which only selects the beam providing the highest received power. Other beam selection strategies can be applied to activate two or more beams simultaneously to achieve better performance. However, two or more beams consume more power, which may not be energy efficient. The trade of between spectrum and energy efficiency will be considered in our future work. Therefore, the index of the serving beam for the user is expressed as:

$$I = \arg \max_{\hat{n} \in \mathcal{N}} P_{\text{rx,UE},\hat{n}}, \quad (5.4)$$

where  $\mathcal{N}$  is the set of beams and  $P_{\text{rx,UE},\hat{n}}$  is the received optical power of the user from the  $\hat{n}$ -th beam. To solve (5.4), the knowledge of user location is required. The cell size is very small in the VCSEL array system, therefore, an accurate localization technique is needed. For the mobile UE, the user tracking system is required to update the location of the UE quickly and frequently. The VLP can easily achieve sub-meter accuracy. However, most VLP localization technologies utilize the downlink transmission of the visible light communication

(VLC) system [28], which requires extra light setting for the proposed system. In addition, the location information needs to be processed and sent back to the server, which causes extra delays to the real-time beam activation system. Two beam activation schemes are proposed in this study to address the power consumption and delay issue. The first method is a passive beam activation scheme, which uses a CCR to obtain a power matrix and then find the serving beam. The second method uses the ODTx in the uplink communication. The details of these two schemes are presented in the following subsections.

### 5.3.1 Systems with a Corner-cube Retroreflector

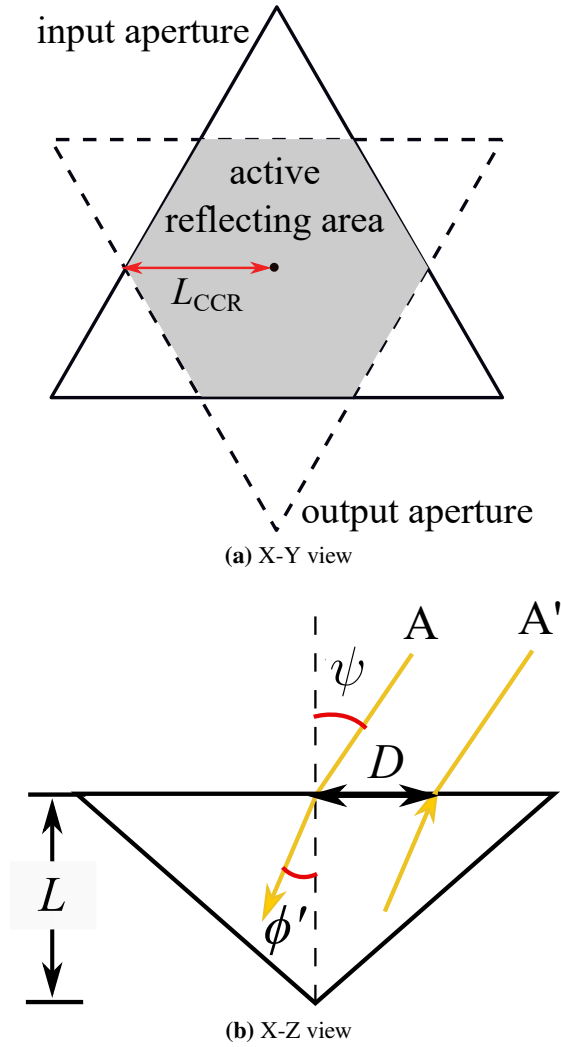


**Figure 5.2:** Corner-Cube retroreflector.

A retroreflector can reflect part of the incident beam back to the direction it came from. The retroreflector can be realized by a CCR, retroreflective sheeting or even retroreflective spray paint [127]. The CCR is a light-weight small device, which can reflect light back to its source with minimal scattering. By using CCR, immediate feedback can be obtained for beam

activation which minimizes the latency and leads to almost zero delay. The CCR has been proposed for the VLP system in [125]. In this thesis, the CCR is considered. As the distance between the Tx and the CCR,  $d$ , is much larger than the size of a CCR, all the incident rays can be considered to be parallel with an incident angle of  $\psi$ . According to Snell's law, the refracted angle  $\phi' = \sin^{-1} \frac{\sin \psi}{n_{re}}$ , where  $n_{re}$  is the refractive index of the retroreflector. Fig. 5.2 (a) shows the result for a triangular corner-cube reflector at normal incidence. The solid line is the input aperture, which is the shape of the CCR face, and the dotted line is the output aperture which is the outline of the retroreflected beam. The overlap area of the input and output aperture is the active reflecting area, and the incident rays outside this area will not be retroreflected. Fig. 5.2 (b) shows the result for a triangular corner-cube reflector at oblique incidence. The displacement of input and output apertures,  $D$ , can be obtained as:

$$D = 2L \tan \phi', \quad (5.5)$$

where  $L$  is the length of the CCR. The size of the active reflecting area mainly depends on  $L_{CCR}$ , which is shown in Fig. 5.2 (a) .

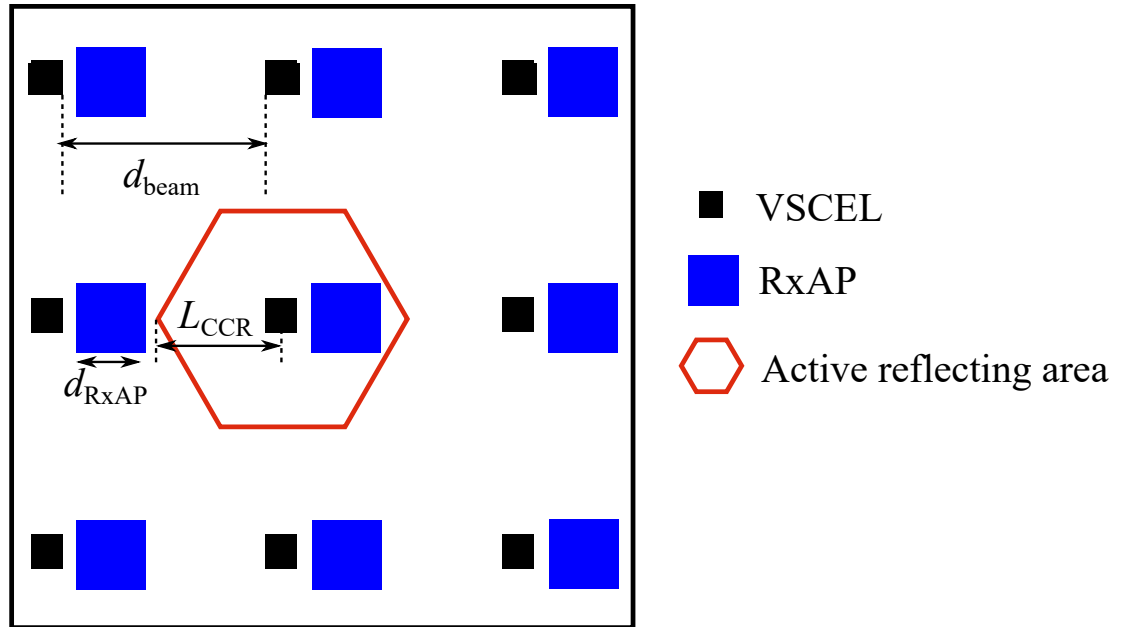


**Figure 5.3:** The setup of the AP in the VCSEL array system using a CCR ( $N_{beam} = 9$ ).

A CCR can reflect part of the incident light to the opposite direction. Based on this property, a passive beam activation is proposed to reduce the power consumption of the battery-operated UE and the latency. A CCR will be mounted next to the Rx of a UE and will reflect part of the transmitting light back to the source beam. As shown in Fig. 5.3, a PD, which is referred to as RxAP, is mounted next to each source beam to detect the light reflected by the CCR. The area bounded by the red line in Fig. 5.3 is the active reflecting area, which is the area hit by the retroreflected light. As discussed previously, the size of the active reflecting area



is determined by  $L_{CCR}$ , which mainly depends on the size of the retroreflector as shown in Fig. 5.2. The side length of the RxAP is denoted as  $d_{RxAP}$ . To make sure the light transmitted by the source beam, after being reflected by the CCR, will only be received by the RxAP next to this source beam, the source beams need to be separated from each other with a distance of  $d_{beam} \geq L_{CCR} + d_{RxAP}$ . In this chapter, the orientation of the Rx and CCR are assumed to be fixed and vertically upward. However, it should be noted that due to the limitation of the maximum incident angle of the CCR and the rotation of the UE, a single Rx may not always receive the signal and a single CCR may not always reflect the light back to the reversed direction. As a result, when a UE's orientation is considered, multiple Rxs and CCRs should be mounted in different directions to solve the issue. The structure of multiple Rxs and CCRs, which ensures that the system is robust against random orientation, will be a subject for future studies. In terms of beam activation mechanism, before transmitting the data packet, all the beams will send test signals simultaneously. By monitoring the power matrix, which is the power received by the array of RxAPs, the beam corresponds to the RxAP receiving the maximum reflected power will be activated to transmit the data packet. Therefore, the index of the source beam for the UE in (5.4) can be reformulated as:

$$I = \arg \max_{\hat{n} \in \mathcal{N}} P_{RxAP, \hat{n}}, \quad (5.6)$$

where  $P_{RxAP, \hat{n}}$  is the received power, reflected by the UE's CCR, of the  $\hat{n}$ -th RxAP. By covering the front face of the CCR with a liquid crystal display (LCD) which produces unique signal frequency, the retroreflected light can be modulated. By transitioning between transparent and opaque states, LCD shutter can approximate a square wave signal at low modulation frequency [125]. In addition, the power consumption of the LCD with its driver circuit is only in the order of tens of  $\mu W$ . The use of the LCD serves multiple purposes. First, it can be used to determine whether a UE is active and requires data communication. Second, it helps to distinguish the active UE from mirrors or CCRs in the environment. Finally, for a multi-user scenario, the active UEs can be distinguished among each other through modulating the retroreflected light differently.

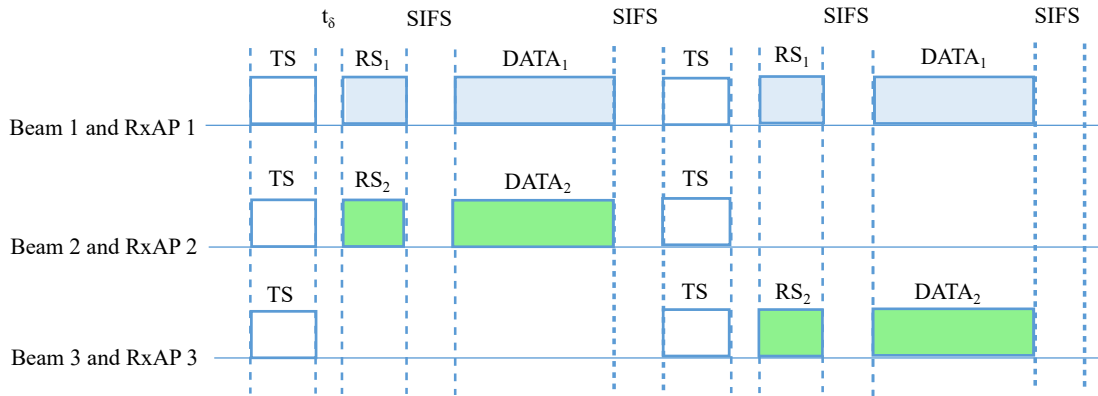


**Figure 5.4:** Beam activation mechanism.

The beam activation mechanism is shown in Fig. 5.4. At the beginning, all the beams send test signal (TS) simultaneously. It is noted that the TS can be unmodulated light. The UE will retroreflect and modulate the TS into the reflected signal (RS), and the RS will be received by the corresponding RxAP after a mean propagation delay of  $t_\delta$ . The beam will be activated based

on (5.6). Then, the data frame will be transmitted by the serving beam after a short inter-frame space (SIFS). In Fig. 5.4, firstly, beams 1, 2, and 3 send TS simultaneously. Then, the RxAP 1 and 2 receive RS retroreflected by the UE 1 and UE 2, respectively, while the RxAP 3 does not receive any reflected signal. Therefore, beams 1 and 2 are activated to transmit data frames to UE 1 and UE 2, respectively. After the SIFS, all the beams send TS again. Here, the RxAP 3 receives RS retroreflected by the UE 2, which means that UE 2 moved to the cell served by the beam 3. Hence, the beam 3 is activated to transmit data to the UE 2 while the beam 2 is deactivated. As a consequence, real-time tracking of UEs and real-time beam activation can be executed with almost zero-delay for a UE with ultra-low power and no computational capability. In addition, the proposed system with CCR does not first require the estimation of the position of UEs.

### 5.3.1.1 Signaling Cost Analysis

The effective throughput can be obtained based on the ratio of the time allocated for data transmission and the total time, including that used for the signaling. Accordingly, we have:

$$\begin{aligned} t_{\text{Data}} &= \frac{L_{\text{Data}}}{\zeta_{\text{down}}}, \quad t_{\text{tot}} = t_{\text{Data}} + t_{\text{delay}}, \\ t_{\text{delay}} &= t_{\text{TS}} + t_{\delta} + t_{\text{RS}} + t_{\text{SIFS}} + t_{\text{SIFS}}, \end{aligned} \quad (5.7)$$

where  $t_{\text{Data}}$  is the average data transmission time;  $L_{\text{Data}}$  is the average data packet length;  $\zeta_{\text{down}}$  is the average downlink data rate which can be obtained based on (5.3); the  $t_{\text{delay}}$  is the total delay time; and  $t_{\text{tot}}$  is the total time required to complete the transmission of a packet;  $t_{\text{TS}}$  and  $t_{\text{RS}}$  are the signaling periods;  $t_{\text{SIFS}}$  is the time required for the SIFS. Assuming there is no collision, the effective throughput can be obtained as:

$$\mathcal{T}_{\text{eff}} = \frac{t_{\text{Data}}}{t_{\text{tot}}} \zeta_{\text{down}}. \quad (5.8)$$

Parameter	Symbol	Value
Test signal time	$t_{\text{TS}}$	0.3 micro-seconds
Reflected signal time	$t_{\text{RS}}$	0.3 micro-seconds
Average length of data packet [128]	$L_{\text{Data}}$	64 Kbytes
Mean propagation delay [129]	$t_{\delta}$	3 ns
SIFS [128]	SIFS	2 micro-seconds

**Table 5.2:** Parameters of beam activation mechanism.

### 5.3.2 Systems with Omnidirectional Transmitter on the User Equipment

In this study, an alternative scheme is proposed for beam activation by using ODTx for the wireless IR uplink transmission. An ODTx, which achieves omnidirectional transmission characteristics by using multiple transmitting elements, is first proposed for light-fidelity (LiFi) systems in [106]. The ODTx is chosen as it is very robust against random device orientation.

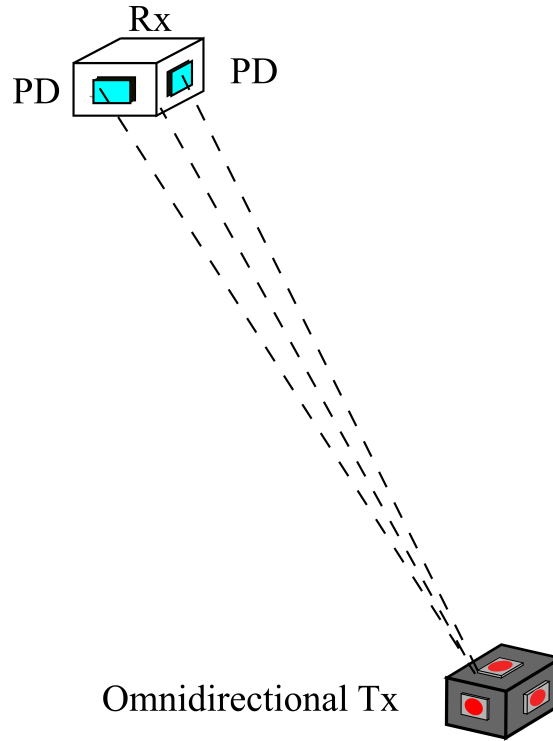


**Figure 5.5:** Localization using the ODTx.

The structure of this ODTx is shown in Fig. 5.5. There is one IR light-emitting diode (LED) located on each side of the UE. It is assumed that the IR LED follows Lambertian radiation and  $m$  is the Lambertian order which is given as  $m = 2$ . The received optical power of a PD from the ODTx can be written as [106]:

$$P_{rx,OD} = \begin{cases} \frac{(m+1)P_{tx,OD}A_P n_{ref}^2 \cos(\psi)}{2\pi d^2 \sin^2(\Psi_c)}, & \psi \leq \Psi_c \\ 0, & \text{otherwise} \end{cases}, \quad (5.9)$$

where  $P_{tx,OD}$  is the transmitted optical power of a single IR LED in the ODTx;  $A_P$  represents the physical area of the PD;  $n_{ref}$  denotes the internal refractive index; the incidence angle of the PD is  $\psi$  and the FOV of the PD is  $\Psi_c$ . Based on (5.9), it can be observed that the received optical power is independent of the irradiance angle of the ODTx, which means that the rotation of the UE will not change  $P_{tx,OD}$ . Consequently, the received optical power only depends on the position of the UE,  $\mathbf{p}_{UE}$ .

By mounting multiple PDs in different orientations on the ceiling, multiple RSS values,  $P_{rx,OD}$ , can be collected. In indoor positioning systems, RSS-based methods have been widely adopted since RSS values are easy to obtain [124]. In this study, the artificial neural network (ANN) algorithm is used to estimate the user position. The ANN is only one of the algorithms used to estimate the user position, and it is used in this study to help the comparisons between the performance of different beam activation schemes. Other positioning algorithms such as fingerprinting, proximity and trilateration can be adopted as well. The main motivation of using ANN is that it can estimate the beam activation directly without estimating the UE location,

which reduces the latency. Other methods require the prediction of the user position first and

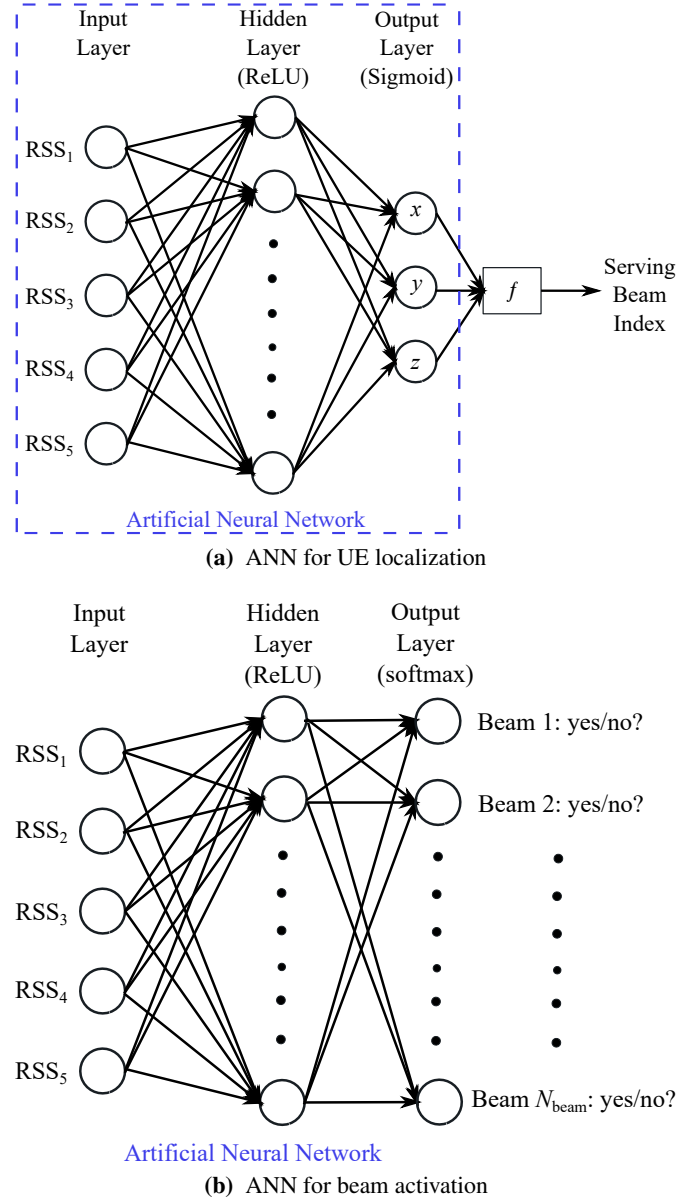


**Figure 5.6:** The ANN structures

then complete the beam activation. Conventionally, the ANN is adopted to estimate the user position first. After finding the position of the UE,  $\mathbf{p}_{\text{UE}}$ , the beam that needs to be activated can be obtained based on (5.4). Fig. 5.6 (a) shows the layout of the ANN for the UE localization. The input of the ANN is the RSS from 5 receiving PDs facing in different directions. There are  $N_{\text{hidden}}$  neurons in the hidden layer and the activation function is a rectified linear unit (ReLU). In the output layer, the sigmoid activation function is adopted and the output is the position of the UE  $\mathbf{p}_{\text{UE}}$ , which should be normalized. Then, the index of the serving beam can be calculated based on (5.4). In this study, the proposed ANN predicts the index of serving beam directly without the need of positioning first. The layout of the ANN for beam activation is

shown in Fig. 5.6 (b). The input and hidden layer is the same as the counterpart in the ANN for UE localization, while the output layer uses the softmax activation function and the number of output neurons equals the number of beams  $N_{\text{beam}}$ . The value of each output neuron represents the probability of activating the corresponding beam. As the SSS is adopted here, the beam with the highest probability should be selected as the serving beam for the UE. The beam activation can be executed in two steps: the offline training of ANN and then the online activating of beams. The RSS data in this study can be generated based on the ideal channel model in (5.9). However, the Lambertian irradiation model is not exactly accurate in real applications. To ensure the accuracy of the beam activation, the ANN can be pre-trained using the data from the ideal model and then trained with the on-site data [130].

Users can access the uplink and receive the data on the downlink simultaneously since the uplink and downlink are operating on different wavelengths and, hence, there would be no interference between them. It is assumed that the uplink is always active for data or TS transmission. By using the collected uplink RSS values, the index of the serving beam can be predicted. However, the delay time,  $t_{\text{delay}}$ , of the system is caused by the signal propagation from the ODTx to the APs and the ANN processing time to estimate the active beam index. The signal propagation time, which is in the order of tens of ns, can be ignored when compared with the ANN processing time. Hence, the  $t_{\text{delay}}$  is mainly determined by the ANN processing. For a static user, the effect of  $t_{\text{delay}}$  can be ignored. If the user is moving,  $t_{\text{delay}}$  should be taken into account when evaluating the system performance. It is noted that this method can be still applied to mobile users with low speed, however, for those users with high speed, the delay due to ANN mechanism can cause the location information to be outdated and a wrong beam might be activated. When there are multiple UEs, multiple access schemes, such as time division multiple access (TDMA), frequency division multiple access (FDMA), or carrier sense multiple access with collision detection (CSMA/CA) should be adopted.

## 5.4 System Level Analysis

### 5.4.1 System with Single User

In a VCSEL array system, the total number of beams is denoted as  $N_{\text{beam}}$  and the beams are pointing in different directions. Therefore, the channel gain distribution is different for each beam. The central beam, which points vertically downward, provides the best channel as it has the shortest distance to the UE. Hence, initially, we start with the central beam and then we extend the analysis to the whole system. In a single user system, the SNR and average data rate of the  $\hat{n}$ -th beam are represented as  $\gamma_{\text{single},\hat{n}}$  and  $\bar{\zeta}_{\text{single},\hat{n}}$ , respectively. The central beam is assumed to be the 1<sup>st</sup> beam and its SNR and average data rate are denoted as  $\gamma_{\text{single},\hat{n}=1}$  and  $\bar{\zeta}_{\text{single},\hat{n}=1}$ , respectively. For the central beam, the horizontal distance between an active user and the cell center is denoted as  $r$ . It is assumed that UEs are uniformly distributed and the probability density function (PDF) of  $r$  can therefore be given as:

$$f_r(r) = \frac{2r}{R^2}, \quad r \leq R, \quad (5.10)$$

where  $R$  is the radius of the service region of the central beam and  $R = \sqrt{d_{\text{cell}}^2/\pi}$ . The vertical distance between the Tx and the UE is denoted as  $h$ . As the central beam is pointing vertically downward,  $\cos \phi = \cos \psi = h/\sqrt{h^2 + r^2}$ ,  $\sin \phi = r/\sqrt{h^2 + r^2}$  and  $d = \sqrt{h^2 + r^2}$ . Hence, for UEs served by the central beam, (5.1) can be reformulated as:

$$P_{\text{rx,UE}}(r) = \frac{2P_{\text{tx,opt}}A_{\text{eff}}G_{\text{APD}}}{\pi W^2(h)} \frac{h}{\sqrt{h^2 + r^2}} \exp\left(-\frac{2r^2}{W^2(h)}\right). \quad (5.11)$$

For a single user case, the system is noise-limited and there is no interference. Therefore, the SNR given in (5.2) for the user served by the central beam can be obtained as:

$$\begin{aligned} \gamma_{\text{single},\hat{n}=1}(r) &= \frac{(R_{\text{APD}}P_{\text{rx,UE}}(r))^2}{(M-2)\kappa^2\sigma_n^2} \\ &= \frac{\gamma_0}{h^2 + r^2} \exp\left(-\frac{4r^2}{W^2(h)}\right). \end{aligned} \quad (5.12)$$

where  $\gamma_0 = \left(\frac{2R_{\text{APD}}P_{\text{tx,opt}}A_{\text{eff}}G_{\text{APD}}h}{\pi W^2(h)\sqrt{M-2}\kappa\sigma_n}\right)^2$ . The SNR in decibel (dB) can be expressed as:

$$\gamma_{\text{db},\hat{n}=1}(r) = 10 \log_{10}(\gamma_{\text{single},\hat{n}=1}(r)). \quad (5.13)$$

Recalling from the fundamental theorem of a function of a random variable [131], the PDF of  $\gamma_{\text{db},\hat{n}=1}$  can be written as:

$$\begin{aligned} f_\gamma(\gamma) &= \frac{f_r(r_0)}{\left|\frac{d}{dr}\gamma_{\text{db},\hat{n}=1}(r)\right|_{r=r_0}} \\ &= \frac{2r_0/R^2}{\left|\frac{d}{dr}10 \log_{10}\left(\frac{\gamma_0}{h^2+r^2} \exp\left(-\frac{4r^2}{W^2(h)}\right)\right)\right|_{r=r_0}} \\ &= \frac{\log(10)(h^2 + r_0^2)W^2(h)}{10R^2(4h^2 + 4r_0^2 + W^2(h))}, \end{aligned} \quad (5.14)$$

where

$$\begin{aligned} r_0 &= f_r^{-1}(\gamma) \\ &= \frac{1}{2} \sqrt{W^2(h)W_k\left(\frac{4\gamma_0 \exp\left(4h^2/W^2(h) - y \ln(10)/10\right)}{W^2(h)}\right) - 4h^2}, \quad \gamma_{\text{db},\hat{n}=1}(R) \leq \gamma \leq \gamma_{\text{db},\hat{n}=1}(0), \end{aligned} \quad (5.15)$$

where  $W_k(\cdot)$  is the Lambert W function, also called as the omega function or product logarithm;  $\ln(\cdot)$  denotes the natural logarithm. As  $0 \leq r_0 \leq R \ll h$ , the PDF of  $\gamma_{\text{db},\hat{n}=1}$  in (5.14) can be approximated as:

$$f_\gamma(\gamma) \approx \frac{\ln(10)(h^2)W^2(h)}{10R^2(4h^2 + W^2(h))}, \quad \gamma_{\text{db},\hat{n}=1}(R) \leq \gamma \leq \gamma_{\text{db},\hat{n}=1}(0), \quad (5.16)$$

Therefore, the approximated PDF of  $\gamma_{\text{db},\hat{n}=1}$  is a uniform distribution function between  $\gamma_{\text{db},\hat{n}=1}(R)$  and  $\gamma_{\text{db},\hat{n}=1}(0)$ , where  $\gamma_{\text{db},\hat{n}=1}(R)$  and  $\gamma_{\text{db},\hat{n}=1}(0)$  can be obtained from (5.13).

Based on (5.3) and (5.12), the data rate of the central beam at radius  $r$  can be represented as:

$$\zeta_{\text{single},\hat{n}=1}(r) = \frac{M/2-1}{M} B \log_2 \left( 1 + \frac{\gamma_0}{h^2+r^2} \exp \left( -\frac{4r^2}{W^2(h)} \right) \right). \quad (5.17)$$

Therefore, the average data rate of the central beam can be written as:

$$\begin{aligned} \bar{\zeta}_{\text{single},\hat{n}=1} &= \mathbb{E}[\zeta_{\text{single},\hat{n}=1}(r)] \\ &= \int_0^R \frac{M/2-1}{M} B \log_2 \left( 1 + \frac{\gamma_0}{h^2+r^2} \exp \left( -\frac{4r^2}{W^2(h)} \right) \right) f_r(r) dr \\ &= \frac{M-2}{2M} B \int_0^R \log_2 \left( 1 + \frac{\gamma_0}{h^2+r^2} \exp \left( -\frac{4r^2}{W^2(h)} \right) \right) \frac{2r}{R^2} dr \\ &\approx \frac{M-2}{2 \ln(2) M R^2} B \int_0^R 2r \ln \left( \frac{\gamma_0}{h^2+r^2} \exp \left( -\frac{4r^2}{W^2(h)} \right) \right) dr \\ &= \frac{M-2}{2 \ln(2) M R^2} B \left[ (h^2 + R^2) \ln \left( \frac{\gamma_0}{h^2 + R^2} \right) + R^2 - h^2 \ln \left( \frac{\gamma_0}{h^2} \right) - \frac{2R^4}{W^2(h)} \right]. \end{aligned} \quad (5.18)$$

The approximation is made as is the SNR,  $\gamma_{\text{single},\hat{n}=1}(r) = \frac{\gamma_0}{h^2+r^2} \exp \left( -\frac{4r^2}{W^2(h)} \right)$ , is much larger than 1. For a single-user case, the average data rate of the VCSEL array system,  $\bar{\zeta}_{\text{single}}^{\text{sys}}$ , is the mean of the average data rate of all beams, which can be expressed as:

$$\bar{\zeta}_{\text{single}}^{\text{sys}} = \frac{1}{N_{\text{beam}}} \sum_n^{N_{\text{beam}}} \bar{\zeta}_{\text{single},\hat{n}} \leq \frac{1}{N_{\text{beam}}} \sum_n^{N_{\text{beam}}} \bar{\zeta}_{\text{single},\hat{n}=1} = \bar{\zeta}_{\text{single},\hat{n}=1} = \bar{\zeta}_{\text{single}}^{\text{UB}}, \quad (5.19)$$

where  $\bar{\zeta}_{\text{single}}^{\text{UB}}$  denotes the upper bound of the system average data rate in a single-user scenario. According to (5.19), the upper bound is the average data rate of the central beam,  $\bar{\zeta}_{\text{single},\hat{n}=1}$ .

## 5.4.2 System with Multiple Users

The performance of a multi-user system is limited by two factors: noise and inter-cell interference (ICI). When multiple UEs are served by the same beam, due to the high-directionality of each Tx in the VCSEL array system, space division multiple access scheme (SDMA) proposed in [13] will be adopted. Based on (5.4), the UEs served by the same beam are grouped together. Multiple beams can serve corresponding UEs simultaneously within the same time slot as the interference between these narrow beams can be significantly mitigated. Active UEs served by the same beam share the bandwidth resource equally. Hence, the data rate of the optical SDMA system can be expressed as:

$$\zeta_{\text{multi}}^{\text{sys}} = \sum_{\hat{n}=1}^{N_{\text{beam}}} \sum_{\mu=1}^{N_{\text{UE},\hat{n}}} \zeta_{\text{multi},\mu,\hat{n}} = \sum_{\hat{n}=1}^{N_{\text{beam}}} \sum_{\mu=1}^{N_{\text{UE},\hat{n}}} \frac{1}{N_{\text{UE},\hat{n}}} \zeta_{\text{single},\mu,\hat{n}} \quad (5.20)$$

where  $\zeta_{\text{multi},\mu,\hat{n}}$  is the data rate of user  $\mu$  served by  $\hat{n}$ -th beam in the multi-user scenario;  $N_{\text{UE},\hat{n}}$  is the number of active UEs served by the  $\hat{n}$ -th beam; and  $\zeta_{\text{single},\mu,\hat{n}}$  is data rate of user  $\mu$  served by  $\hat{n}$ -th beam in a single-user scenario. For the best-case scenario, it is assumed that all

the beams are utilizing different wavelengths, which should be perfectly distinguished by the optical Rx. Therefore, the system is noise limited as ICI is completely avoided and the signal to interference-plus-noise ratio (SINR) is represented as shown in (5.12). Hence, the average data rate of the central beam can be written as:

$$\bar{\zeta}_{\text{multi},\hat{n}=1} = \mathbb{E}\left[\sum_{\mu=1}^{N_{\text{UE},\hat{n}=1}} \zeta_{\text{multi},\mu,\hat{n}=1}\right] = \sum_{\mu=1}^{N_{\text{UE},\hat{n}=1}} \frac{1}{N_{\text{UE},\hat{n}=1}} \mathbb{E}\left[\zeta_{\text{single},\hat{n}=1}(r_{\mu})\right] = \bar{\zeta}_{\text{single},\hat{n}=1}, \quad (5.21)$$

where  $\zeta_{\text{multi},\mu,\hat{n}=1}$  is the data rate of user  $\mu$  served by the central beam, and  $r_{\mu}$  is the horizontal distance between the user  $\mu$  and the center of central cell. We can see that the average data rate of the central beam for the multi-user scenario is the same as the one for the single-user scenario. It should be noted that the average data rate of other beams is less than the average data rate of the central beam. Hence, the average data rate of the entire system for multi-user scenario will be upper bounded as follows:

$$\bar{\zeta}_{\text{multi}}^{\text{sys}} = \sum_{n=1}^{N_{\text{beam}}} \bar{\zeta}_{\text{multi},\hat{n}} \leq \bar{N}_{\text{a}} \bar{\zeta}_{\text{multi},\hat{n}=1} = \bar{\zeta}_{\text{multi}}^{\text{UB}}, \quad (5.22)$$

where  $\bar{N}_{\text{a}}$  denotes the average number of active beams and  $\bar{\zeta}_{\text{multi}}^{\text{UB}}$  denotes the upper bound of the average data rate in the VCSEL array system. The value of  $\bar{N}_{\text{a}}$  depends on the total number of active UEs,  $N_{\text{UE}}$ , in the system as well as the total number of beams,  $N_{\text{beam}}$ , on the Tx, and it can be calculated as follows [132]:

$$\bar{N}_{\text{a}} = N_{\text{beam}} - N_{\text{beam}}(1 - 1/N_{\text{beam}})^{N_{\text{UE}}}. \quad (5.23)$$

If the number of active UEs are infinite,  $N_{\text{UE}} = \infty$ , the average number of active beams,  $\bar{N}_{\text{a}}$ , is equal to the total number of beams on the Tx. On the other hand, when there is only one active UE,  $\bar{N}_{\text{a}} = 1$ .

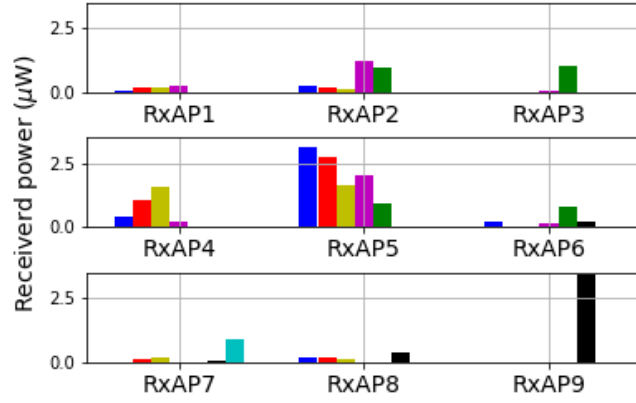
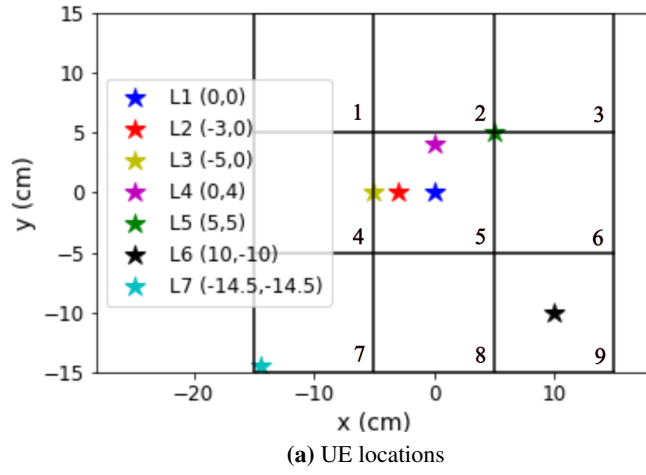
## 5.5 Simulation Results

$d_{\text{beam}}$	$L_{\text{CCR}}$	$d_{\text{RxAP}}$	APs height	UE height	$\theta_{\text{FWHM}}$
12 mm	5 mm	5 mm	3.5 m	1.5 m	4°

**Table 5.3:** Parameters in Zemax simulation

First of all, it should be noted that for all simulations in this chapter, the corresponding transmit power of the beams for different values of  $\theta_{\text{FWHM}}$  are based on the eye safety regulations given in Appendix A. Hence, the transmit power for  $\theta_{\text{FWHM}}$  of 2°, 4° and 6° are 19, 60 and 129 mW, respectively. To test the accuracy of the beam activation using CCR, simulations with a beam number of  $N_{\text{beam}} = 9$  are carried out in Zemax and the setup of the AP in the VCSEL array system is presented in Fig. 5.3. Each beam is pointed to the center of each square cell and the cell size is 10 cm × 10 cm. The configuration of cells is shown in Fig. 5.7 (a) and different UE positions are considered. The parameters are listed in Table 5.3. The simulation result is presented in Fig. 5.7 (b). The received power of each PD in the array of RxAPs is analyzed. When the UE is in L1, L2 or L4, which are inside cell 5, it can be seen that the

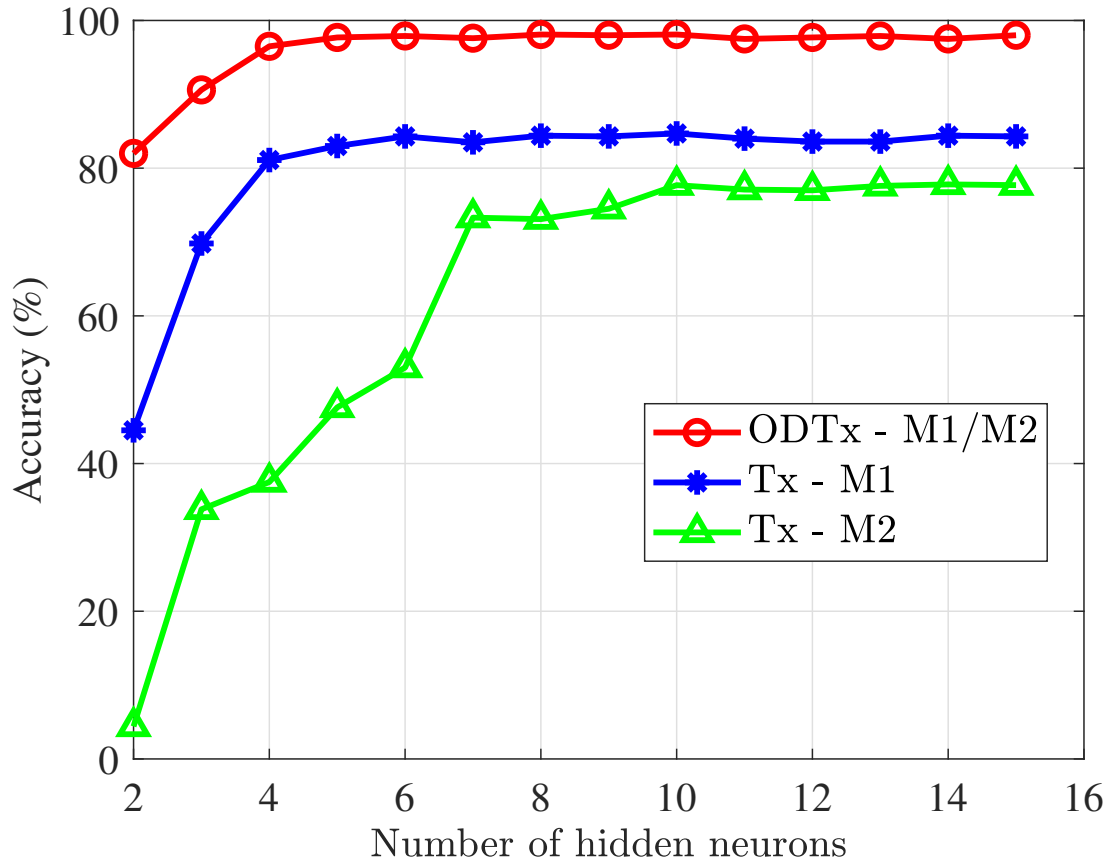




**Figure 5.7:** The UE locations and received power matrix,  $N_{\text{beam}} = 9$ .

RxAP 5 receives much higher power than other RxAPs and thus beam 5 should be activated. When the UE is at L3, which is in the boundary of cell 4 and 5, the RxAP 4 and RxAP 5 receives similar power. Therefore, based on the beam activation algorithm, either beam 4 or beam 5 or both of them should be activated. When the UE is inside cell 9 such as L6, RxAP 9 has the highest power and beam 9 will be activated. L7 is located in the corner of cell 7, for this case, only the RxAP 7 collects power from the retroreflected light. These simulation results show that by using the CCR, the system can activate the corresponding beam for the UE accurately. The IS-based VLP system proposed in [120], is selected as the benchmark scheme. According to (5.7) and Table 5.2, the average latency, caused by the system can be calculated. Therefore, the average latency of the system using CCR is in the order of a few micro-seconds, which is significantly lower than the average positioning time, 44.3 ms, of the IS-based VLP system proposed in [120]. Hence, real-time fast tracking can be enabled by using the retroreflector. In the traditional VLP systems, if the position estimation is completed in the

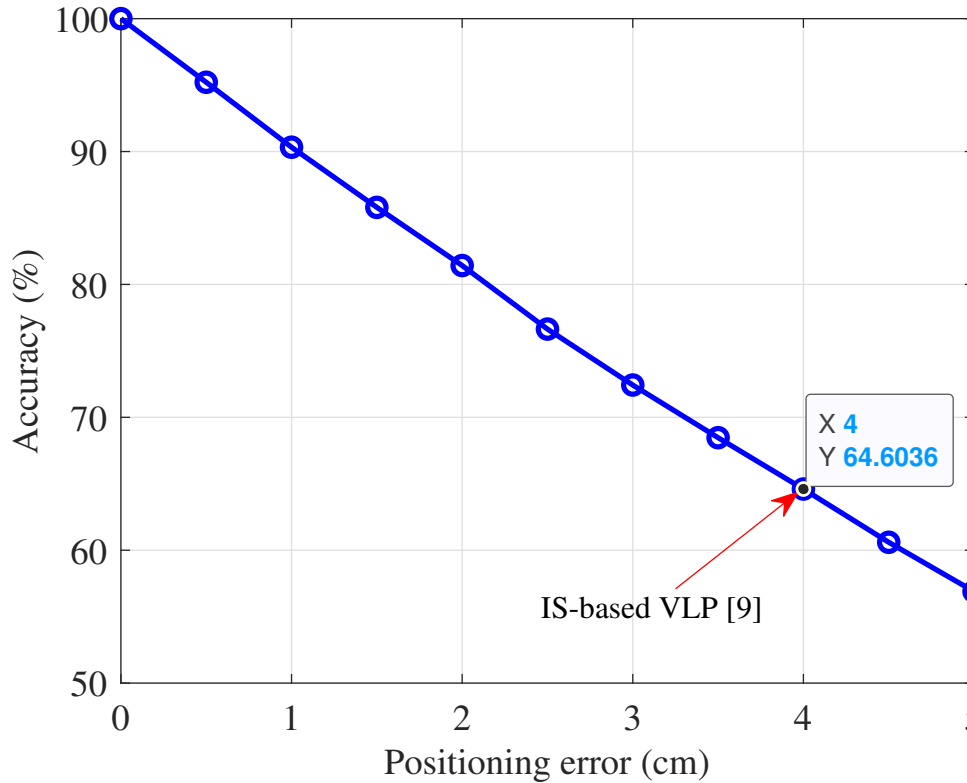
UE, the computation will add a high power burden to the UE. Also, in order to activate the best beam, it requires the autonomous transmission of users' location information from UE to APs. If the position estimation is done at the AP side, the UE needs to transmit data collected by the ISs or PDs to the AP for server-assisted computation. In conclusion, when the traditional VLP system is applied for the beam activation, it always requires a real-time backward channel from UE to APs. However, with the utilization of a retroreflector, the backward channels can be replaced by the RS reflected by the retroreflector. In addition, no additional illumination devices are required as the TS is transmitted by the VCSEL array system, which severs the dual functionality of communication and positioning. Hence, the proposed beam activation method based on a retroreflector has the advantage of low latency, low power consumption and low cost.



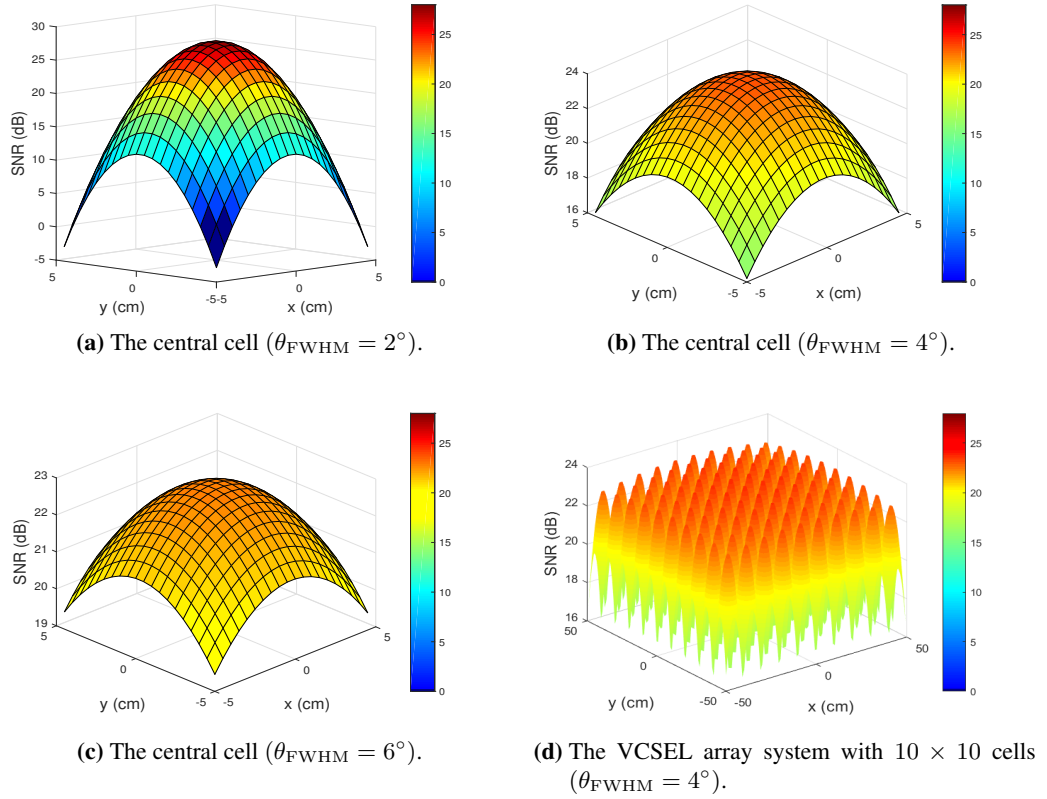
**Figure 5.8:** The comparison of beam activation accuracy between the ODTx and the single-PD Tx for both orientation models (M1 and M2) with different number of hidden neurons.

The accuracy of the beam activation is analyzed in this part. In order to train the ANN shown in Fig. 5.6, which has one hidden layer, we first generate 100,000 UEs with different positions and orientations. For each location and orientation, the corresponding RSS matrix are generated based on (5.9) and the serving beam index is calculated according to (5.1) and (5.4). The RSS values are treated as the input of the ANN while the serving beam index is the output. After generating these samples, 80% of the data is used for the training set and 20% of the data is used for the test set. In a real scenario, the accuracy can be further increased by training the on-site

data. The effect of device orientation is studied and two orientation models are considered here. The first orientation model (M1) is the Gaussian model introduced in Chapter 2.7.1 for elevation angle of the UE and the second orientation model (M2) is the uniform model, which assumes uniform distribution in all movement directions. The selected benchmarks for comparison include: a) a single IR LED for uplink transmission and beam activation (which is called a single Tx in the rest of this chapter), b) the IS-based VLP [120]. As shown in Fig. 5.8, the system with ODTx achieves 98% accuracy when  $N_{\text{hidden}} = 5$ . Systems with a single Tx can only achieve an accuracy of 82% and 78% for orientation models M1 and M2, respectively. The position error of the IS-based VLP system is around 4 cm [120], which leads to a poor activation accuracy of 64.6%, as shown in Fig. 5.8. To achieve an accuracy of more than 90%, the positioning error is required to be less than 1 cm according to Fig. 5.9. In terms of the beam activation latency for the system using ODTx, the delay time,  $t_{\text{delay}}$ , is mainly caused by the ANN processing time. In a laptop with Intel(R) Core(TM) i7-7700HQ CPU @ 2.8 GHz, the processing time of ANN with  $N_{\text{hidden}} = 5$  for user positioning is 29.7 ms, which is lower than the 44.3 ms of the IS-based VLP systems. In addition, no additional illumination device is required for the ODTx as it serves the purpose of uplink communication and beam activation simultaneously. In conclusion, the ODTx is much more robust against random device orientation compared with the single Tx system, while it has the advantage of higher accuracy, lower latency, lower power consumption and lower cost compared with the IS-based VLP.

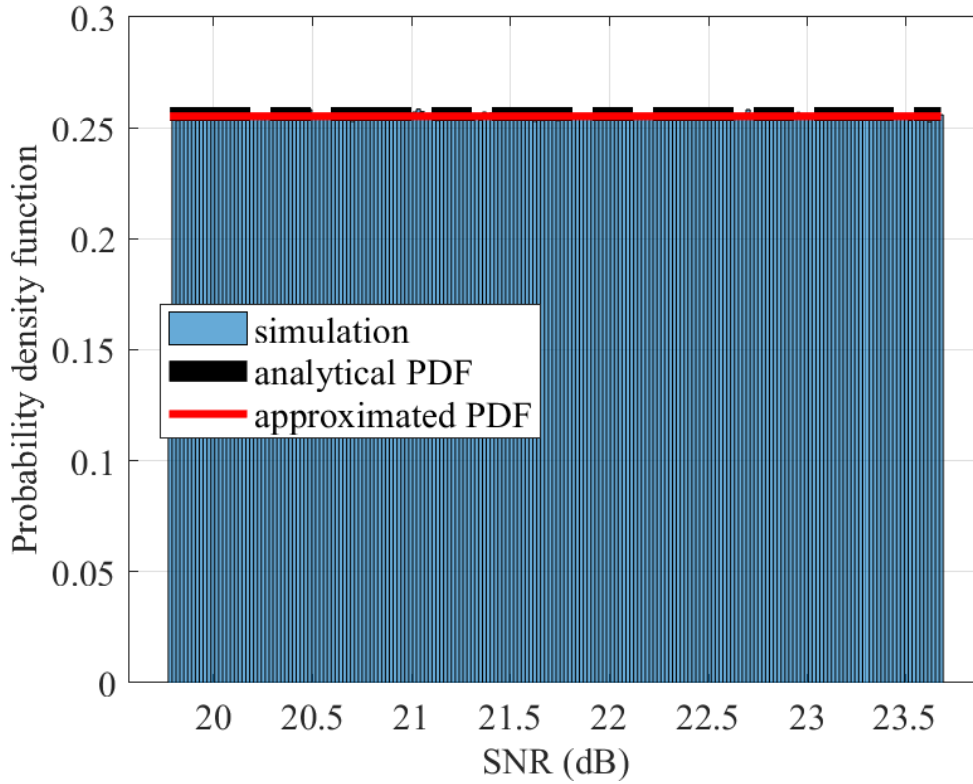


**Figure 5.9:** The comparison of beam activation accuracy between the ODTx and the IS-based VLP system for different positioning error.



**Figure 5.10:** SNR distribution in a single user system.

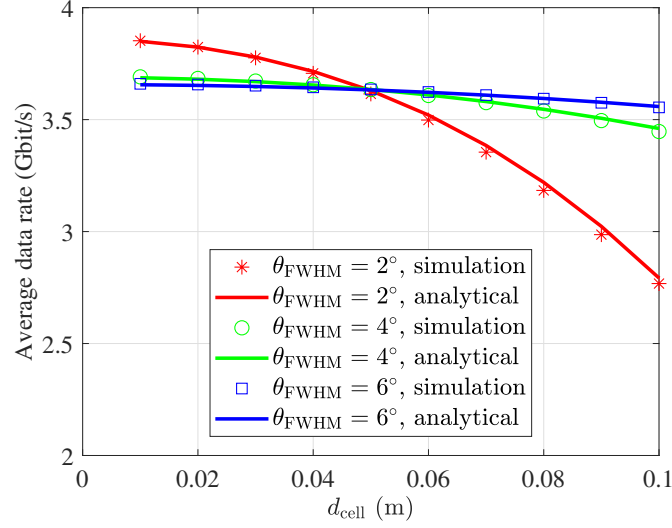
The simulation results for systems with a single user scenario are shown in Fig. 5.10-5.12. In the central cell with a size of  $10 \text{ cm} \times 10 \text{ cm}$ , the SNR distribution is illustrated in Fig. 5.10 (a)-(c) for different values of  $\theta_{FWHM}$ . When  $\theta_{FWHM} = 2^\circ$ , the UE achieves the highest SNR, 27.7 dB, in the cell center. However the SNR at the cell corner is almost 0 dB. This is because the beam divergence angle is small and thus most of the power is focused around the beam center. By increasing  $\theta_{FWHM}$  from  $2^\circ$  to  $4^\circ$ , although the transmit power increases from 19 mW to 60 mW, the peak SNR decreases to 23.7 dB since the beam is more diverged. However, the wider divergence angle leads to a great increase, 16 dB, in the SNR for the UE at the cell corner. With the further increase of  $\theta_{FWHM}$  to  $6^\circ$ , the transmit power doubles to 120 mW but the SNR slightly decreases to 22.7 dB. The advantage is that the UE at the cell corner can achieve a SNR of 19.4 dB. The SNR distribution of the VCSEL array system with  $10 \times 10$  beams is plotted in Fig. 5.10 (d). It can be seen that the distributions of all other cells have similar distributions to the central cell with a slight decrease in the SNR values. To verify the PDF of the SNR derived for the central beam in (5.14), Monte-Carlo simulations are carried out and the histogram of SNR are plotted by the blue bars in Fig. 5.11. The analytical PDF in (5.14) is plotted by the black dash-dot line while the approximated PDF in (5.16) is plotted by the red line. As the red line, black dash-dot line and the histogram are well matched, the PDF of the SNR for the central beam can be well approximated by the uniform distribution expressed in (5.16).



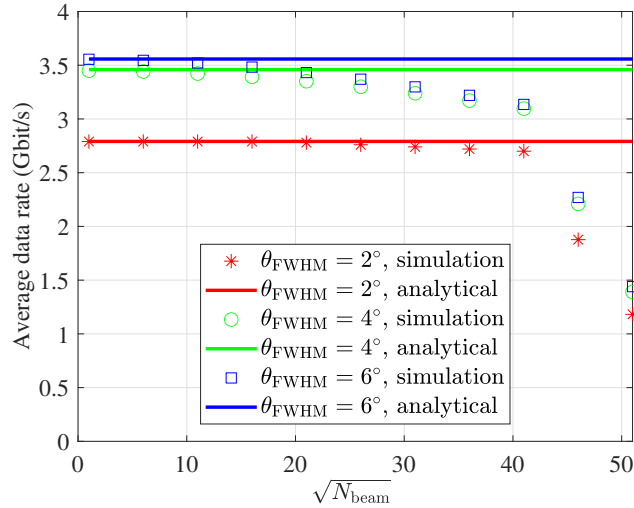
**Figure 5.11:** Probability density function of the SNR for the central beam ( $\theta_{\text{FWHM}} = 4^\circ$ ).

Fig. 5.12 (a) shows the average data rate for the central cell with different cell size. It can be seen that for different values of  $\theta_{\text{FWHM}}$ , the analytical derivation in (5.18) matched the Monte-Carlo simulation results. When the cell size is small, the central beam with  $\theta_{\text{FWHM}} = 2^\circ$  provides higher average data rate. However, with the increase in cell size, its average data rate decreases faster than the others. This is because, with a smaller  $\theta_{\text{FWHM}}$ , the beam power is more focused on the center, which leads to high power in the cell center and low power in the edge, as shown in Fig. 5.10 (a). By increasing  $\theta_{\text{FWHM}}$ , the beam power is less focused. Therefore, the decrease in the average data rate is slower when the cell size increases. When the cell size  $d_{\text{cell}}$  is 5 cm, the beam with  $\theta_{\text{FWHM}} = 2^\circ$  provides the highest data rate, 3.8 Gbit/s. However, when the cell size  $d_{\text{cell}}$  is 10 cm, the average data rate for  $\theta_{\text{FWHM}} = 4^\circ$  and  $\theta_{\text{FWHM}} = 6^\circ$  are 3.4 Gbit/s and 3.5 Gbit/s, respectively, which are higher than the average data rate for  $\theta_{\text{FWHM}} = 2^\circ$ , 2.7 Gbit/s. Fig. 5.12 (b) demonstrates the average data rate for the VCSEL array system with  $N_{\text{beam}}$  beams and  $d_{\text{cell}} = 10$  cm. The number of beams along one axis is denoted as  $\sqrt{N_{\text{beam}}}$ . It can be seen from Fig. 5.12 (b) that by varying the number of beams along one axis, the value of average data rate for the simulation results will be upper bounded by  $\bar{\zeta}_{\text{single}}^{\text{UB}}$  in (5.19). The result indicates that, in a VCSEL array system,  $\bar{\zeta}_{\text{single}}^{\text{UB}}$  is actually a good approximation of the average data rate when the number of cells is small. This occurs because the distance between the central cell and the edge cell is small, the SNR distribution of other cells will be similar to the SNR distribution of the central cell as shown in Fig. 5.10 (d). However, with the further increase of  $\sqrt{N_{\text{beam}}}$ , the distance between

the central cell and the edge cell increases, which will lead to higher path loss and a decrease in the average data rate. In such cases,  $\bar{\zeta}_{\text{single}}^{\text{UB}}$  can only be considered as the upper bound instead of a well-approximation. It should be noted that for a single UE scenario with  $d_{\text{cell}} = 10$  cm, a VCSEL array system with  $\theta_{\text{FWHM}} = 4^\circ$  and  $6^\circ$  can provide similar performance, which is better than the system with  $\theta_{\text{FWHM}} = 2^\circ$ .



(a) Average data rate for the central cell with different cell size.



(b) Average data rate for the VCSEL array system with  $\sqrt{N_{\text{beam}}} \times \sqrt{N_{\text{beam}}}$  cells. ( $d_{\text{cell}} = 10$  cm)

**Figure 5.12:** Average data rate in a single user system.

Simulations for systems with multiple users are carried out. The relationship between the number of UEs,  $N_{\text{UE}}$ , and the average data rate of the VCSEL array system ( $N_{\text{beam}} = 100$  and  $d_{\text{cell}} = 10$  cm) is shown in Fig. 5.13. For the ideal case without ICI, where each beam uses a different wavelength, the analytical derivation in (5.22) matches with the simulations without ICI for both  $\theta_{\text{FWHM}} = 4^\circ$  and  $6^\circ$ . This also gives the upper bound of the average data rate,

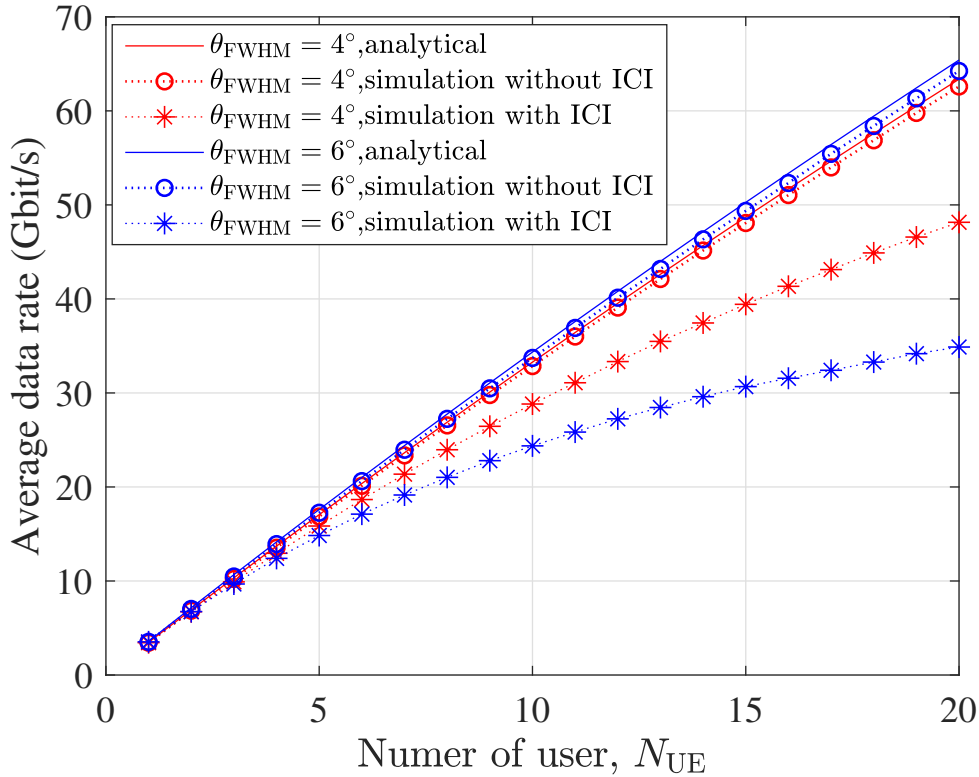


**Figure 5.13:** Average data rate for the VCSEL array system with multiple users. ( $N_{\text{beam}} = 10 \times 10$ ,  $d_{\text{cell}} = 10 \text{ cm}$ ).

$\bar{\zeta}_{\text{multi}}^{\text{UB}}$ , for the VCSEL array system with multiple UEs. When all the beams are using the same wavelength, the ICI needs to be taken into consideration as the ICI will degrade the system performance. When the number of UEs,  $N_{\text{UE}}$ , is less than 6, we can see the average data rate of the system with ICI is very close to the average data rate of the system without ICI, and thus the average data rate of the system with ICI can be well approximated by (5.22) for small value of  $N_{\text{UE}}$ . With the increase of  $N_{\text{UE}}$  from 6 to 20, the chance of having ICI rises, which widens the gap between the average data rate of simulations with ICI and the average data rate of a system without ICI. Further increases in  $N_{\text{UE}}$  from 20 will lead to a larger gap between systems with and without ICI. It should be noted that in a VCSEL array system with multiple UEs, the system with  $\theta_{\text{FWHM}} = 4^\circ$  achieves a higher data rate than the system with  $\theta_{\text{FWHM}} = 6^\circ$ . When the cell size is fixed, a larger divergence angle means more power will reach the adjacent cells and will be treated as interference noise by UEs in the adjacent cells. Therefore, a small divergence angle can alleviate the ICI and increase the average data rate. When  $N_{\text{UE}} = 20$ , a throughput of around 50 Gbit/s can be achieved by systems with  $\theta_{\text{FWHM}} = 4^\circ$ , while only 33 Gbit/s can be achieved for a systems with  $\theta_{\text{FWHM}} = 6^\circ$ .

To calculate the system throughput, the user mobility should be considered and, hence, the effect of the delay caused by the beam activation should be evaluated. It is assumed that all of the users are moving randomly following the random waypoint model [133]. In terms of the mechanism using CCR, the effective throughput,  $\mathcal{T}_{\text{eff}}$ , can be obtained based on (5.8).

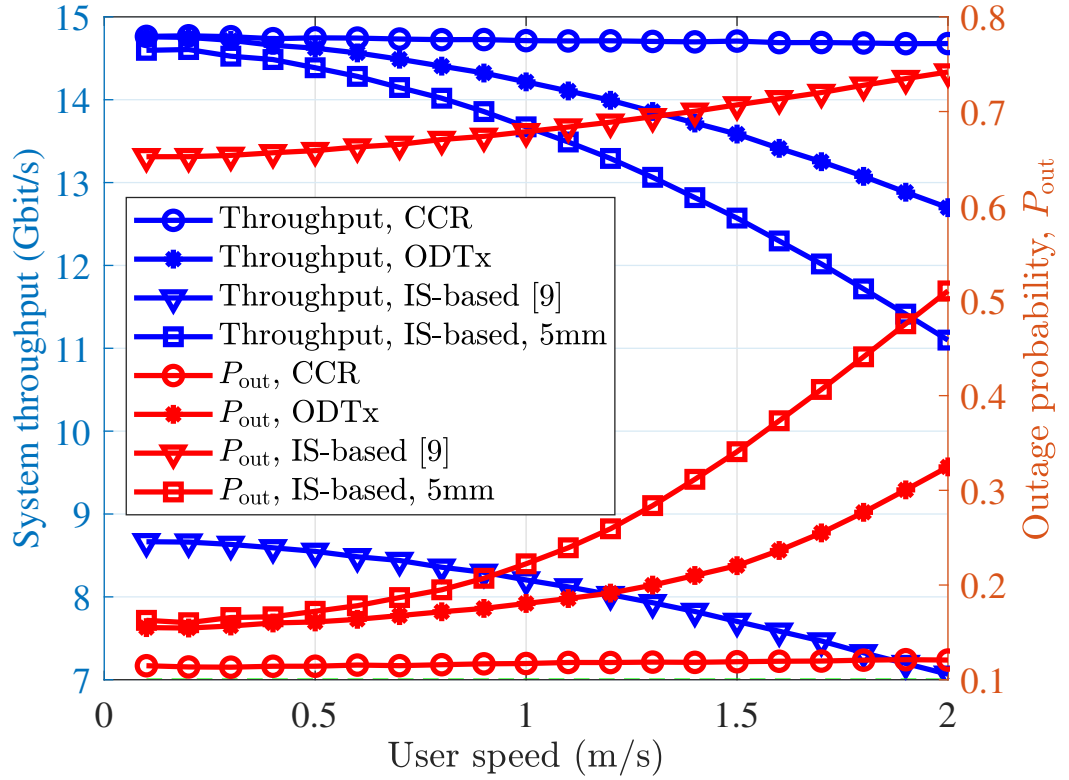


**Figure 5.14:** Evaluation of system throughput and outage probability corresponding to user speed. ( $N_{\text{beam}} = 10 \times 10$ ,  $d_{\text{cell}} = 10$  cm,  $\theta_{\text{FWHM}} = 4^\circ$ ),  $N_{\text{UE}} = 5$ .

According to the parameters in Table 5.2, it can be obtained that  $\mathcal{T}_{\text{eff}} = 0.98 \times \zeta_{\text{down}}$ . For the mechanism using ODTx, the latency,  $t_{\text{delay}}$ , is majorly caused by the ANN processing time. Hence, the beam activated at current time will be based on the user location in  $t_{\text{delay}}$  ms ago. In a laptop with Intel(R) Core(TM) i7-7700HQ CPU @ 2.8 GHz, the processing time of ANN with  $N_{\text{hidden}} = 5$  is 30 ms. The selected benchmarks for comparison include: a) the IS-based VLP proposed [120], b) the IS-based VLP system in which the position error is assumed to be 5 mm. The evaluation of system throughput and outage probability corresponding to the user speed is presented in Fig. 5.14. The outage probability,  $P_{\text{out}}$ , is defined as the probability that the user throughput is less than the required threshold data rate,  $R_T$ , where  $R_T$  is assumed to be 2.5 Gbit/s. When the IS-based VLP [120] is adopted for positioning and beam activation, due to the high positioning error and high latency, the effective system throughput is much lower than the other schemes while the outage probability is more than 60%. When the user speed is 0.1 m/s, by decreasing the positioning error of the IS-based scheme from 3.97 cm to 5 mm, the system throughput increases substantially from 8.7 Gbit/s to 14.5 Gbit/s, which achieves similar performance as the system with CCR and the system with ODTx. However, for high-speed users, the latency, caused by beam activation and positioning, can lead to outdated location information, and the wrong beam may be activated. Therefore, when the user speed increases to 2 m/s, the system throughput of the IS-based scheme (5 mm positioning error) decreases rapidly to 11 Gbit/s. In comparison, due to the lower latency, the system throughput of the ODTx-based scheme only decreases to 12.8 Gbit/s. In terms of the CCR-based scheme,



the system throughput and outage probability is independent of the user speed, which indicates the CCR mechanism has a extremely low latency and thus the effect of delay can be ignored. Hence, the system with CCR mechanism can be used for scenario which required extremely high data rate and low latency such as virtual reality and augmented reality. In comparison, the system with ODTx can be used for low-speed scenario which requires robustness against orientation such as smartphones and tablets.

## **5.6 Summary**

In this chapter, we have proposed a VCSEL array system which can support high data rate, low latency and multiple UEs without the requirement of expensive/complex hardware, such as SLM, MEMS, fiber and so on. Two beam activation methods have been proposed based on the small cell property of the VCSEL array system. The beam activation based on the CCR can achieve low power consumption and almost-zero delay, allowing real-time beam activation for high-speed users. The other beam activation is based on the ODTx, which serves the purpose of the uplink transmission and beam activation simultaneously. This method is robust against random device orientation and is suitable for low-speed users. The effects of the cell size and beam divergence angle have been considered in this study. By evaluating the system performance, the choices of cell size and beam divergence angle have been proposed for the VCSEL array system.

---

Chapter 6

**Conclusions, Limitations and Future  
Research**

---

## **6.1 Summary and Conclusions**

Similar to other cellular systems, inter-cell interference (ICI) significantly degrades the system performance of light-fidelity (LiFi) attocell networks. In this thesis, to deal with ICI in LiFi attocell networks, different methods have been proposed. The structures of angle diversity receivers (ADRs) have been studied to fully exploit the potential of LiFi networks. To overcome the disadvantages due to ICI, blockage and random device orientation, the hybrid LiFi/WiFi network (HLWN) is a potential solution to future wireless communications where LiFi augments wireless fidelity (WiFi) in providing ultra-high speed and low latency wireless connectivity. In addition, a vertical-cavity surface-emitting laser (VCSEL) array transmission system with proper beam activation mechanisms has been proposed to mitigate ICI as well due to high directivity of the narrow beams.

In the third chapter of this thesis, we have investigated the ICI mitigation in LiFi networks using ADRs. The impact of the diffuse link considering random user equipment (UE) orientation has been studied and it has been shown that both line-of-sight (LOS) and non-line-of-sight (NLOS) links have an important influence on the system performance. The performance of different ADR structures have been compared and the optimized ADR structures have been proposed for the considered scenario. This method can be extended to other scenarios easily. By studying systems with different levels of noise power spectrum density, we have shown that when the system is noise-limited, maximum ratio combining (MRC) outperforms select best combining (SBC), otherwise, SBC is the preferred combining scheme. In an interference-limited system or noise-plus-interference limited system, the adoption of the double source (DS) cell configuration can further mitigate the NLOS interference and thus improve the system performance. This study contributes to guiding the designs of ADRs, the choice of signal combining schemes and the adoption of the AP configurations.

In chapter 4, a hybrid LiFi/WiFi network with user movement and random device orientation has been considered. A low complexity orthogonal frequency division multiple access (OFDMA) resource allocation (RA) scheme for LiFi systems and an evolutionary game theory (EGT) scheme for load balancing (LB) considering the handover effect in HLWNs have been proposed. The proposed RA scheme for LiFi OFDMA systems outperforms that in time division multiple access (TDMA) systems in terms of both data rate and user fairness because of an efficient use of high-frequency resources. For both proportional fairness (PF) and max-min fairness (MF) schemes, the proposed EGT-based LB scheme can achieve a better data rate and fairness performance than benchmark LB schemes. The HLWNs can maintain a good downlink performance regardless of the uplink requirements in WiFi. The average horizontal handover efficiency has little impact on the system performance while the average vertical handover efficiency affects the system performance greatly. In the case of low average vertical handover efficiency, the EGT-based LB scheme achieves a better user data rate than the hard threshold (HT) scheme by balancing the user load between LiFi and WiFi more efficiently.

In the fifth chapter, a novel VCSEL array system, which supports high data rate, low latency and multiple user access without the requirement of expensive/complex hardware, is proposed. In addition, the choices of cell size and beam divergence angles are recommended. In order to support mobile users, two beam activation methods are proposed. Beam activation based on the corner-cube retroreflector (CCR) can achieve low power consumption and almost-zero

delay, allowing real-time beam activation for high-speed users. The mechanism based on the omnidirectional transmitter (ODTx) is suitable for low-speed users and very robust to random orientation. The proposed methods exhibits significantly superior data rate and outage probability performance than the benchmark schemes. For a single UE scenario, regarding the central beam, the probability density function (PDF) of the signal-to-noise ratio (SNR) in dB can be considered as a uniform distribution. In addition, the analytical derivations for the average data rate of the central beam and its upper bound are presented and proven by simulations. This study may have great potential in guiding the designs in future experiment studies and performance analysis on the VCSEL array system.

## **6.2 Limitations and Future Research**

In chapter 3, it is assumed that all ADRs are equipped with compound parabolic concentrators (CPCs) to achieve high concentration gain and narrow field of view (FOV) of photodiodes (PDs). This characteristic of CPC is very beneficial for interference mitigation in LiFi attocell networks. The narrower the FOV of a CPC, the higher the concentrator gain, but the longer a concentrator will be. The number of PDs on an ADR is limited by the size requirement. In further work, the system performance of ADRs with other types of concentrators can be evaluated. Moreover, when the DS cell configuration is adopted, the transmit power is equally split to the positive and negative sources, which degrades the performance of the noise-limited system. Also, when no LOS link exists, the NLOS paths from the desired positive and negative sources will cancel each other out, which leads to poor SNR performance. Upgrading the design of the DS cell to overcome the aforementioned problems could be a topic for future studies. In addition, the impact of blockage, which could substantially affect the system performance, is not considered. Therefore, another topic for future research is evaluating the effect of link blockage on LiFi systems with ADRs. Besides, experimental works which validate the use of ADR in a real scenario should be carried out in the future. By using adaptive signal combining schemes or adaptive single source and double source configuration, the system performance may be improved, which could also be subjects for future study.

In chapter 4, the most significant problem is that the proposed LB algorithm for the HLWN system only considers the average throughput within each coherent time slot and makes decisions based on this. If only the immediate reward is taken into account, the algorithm will end up with overlooking the long term benefits of performing handover. For a long-term system performance assessment, user behavior prediction is required. In LiFi systems, the mobility-aware resource allocation algorithms, which use the historical data and future-state prediction, have been studied in [107–109]. In these studies, the mobility-aware algorithm is a feasible solution as it has been previously shown that human mobility is relatively predictable [134]. However, device orientation is considered in this study as it will affect both positioning and handover. To the best of our knowledge, no study has shown that the device orientation can be predictable. If the device orientation cannot be predicted, then the channel state information (CSI) in the next state also cannot be estimated as well. Hence, finding a model which predicts the position and orientation of UE and performing handover considering the long-term effect could be a potential future direction. Furthermore, the effect of the uplink load balancing on downlink LiFi communications is not considered in this study and will be considered in future work.

In chapter 5, we only consider a VCSEL array system which covers a small open space area. The reflection from other objects is ignored and only the LOS is considered. In future studies, we may consider a network of VCSEL arrays to cover the entire indoor scenario, in that case, the NLOS components should be taken into consideration. Furthermore, the beam selection strategy considered in this study is the signal strength strategy (SSS), which only selects one serving beam at a time. Other beam selection strategies can be applied to activate two or more beams simultaneously to achieve better performance. However, two or more beams consume more power, which may not be energy efficient. The trade of between spectrum and energy efficiency will be considered in our future work. The research area is still broadly open for research and could be extended in many interesting directions, such as utilizing the spatial and multiplexing gain, designing the omnidirectional CCR and optimizing the resource management in a multi-VCSEL-array network.

Another interesting area to explore is combining different interference mitigation techniques into one system. For example, a hybrid LiFi/WiFi network system where the LiFi systems use the VCSEL array as transmitters and ADRs as the receivers. Besides, device to device communication can be taken into consideration in such systems.

---

# Appendix A

## Maximum Transmit Power Considering Eye Safety

---

When laser diodes or VCSEIs are deployed, it is necessary to consider eye safety, which will limit the value of the transmit power,  $P_{\text{tx,opt}}$ . In this section, the maximum allowable transmit optical power  $P_{\text{tx,max}}$  will be calculated based on regulations in the eye safety standard [135]. The Gaussian beam intensity at the distance  $z$  is:

$$I(r, z) = \frac{2P_{\text{tx,opt}}}{\pi W^2(z)} \exp\left(-\frac{2r^2}{W^2(z)}\right). \quad (\text{A.1})$$

The aperture diameter of cornea is denoted as  $d_a$ . The exposure level of the cornea at distance  $z$  can be calculated as:

$$\begin{aligned} E_{\text{exp}}(z) &= \frac{1}{\pi(d_a/2)^2} \int_0^{d_a/2} I(r, z) 2\pi r \, dr \\ &= \frac{1}{\pi(d_a/2)^2} \int_0^{d_a/2} \frac{2P_{\text{tx,opt}}}{\pi W^2(z)} \exp\left(-\frac{2r^2}{W^2(z)}\right) 2\pi r \, dr. \\ &= \frac{P_{\text{tx,opt}}}{\pi(d_a/2)^2} \left(1 - \exp\left(-\frac{d_a^2}{2W^2(z)}\right)\right) \end{aligned} \quad (\text{A.2})$$

The level of radiation to which persons may be exposed without suffering adverse effects is called the maximum permissible exposure (MPE). Exposures above the MPE will lead to eye injuries. Instead of actually performing an MPE analysis for all locations along the beam, the exposure level at the most hazardous position (MHP),  $z_{\text{mph}}$ , can be calculated and compared with the MPE. If the exposure level at the MHP,  $E_{\text{exp}}(z_{\text{mph}})$ , is less than the MPE, then the MPE is not exceeded anywhere else in the beam [136]. Hence, when considering eye safety,  $E_{\text{exp}}(z_{\text{mph}}) \leq E_{\text{mpe}}(t_{\text{exp}})$ , where  $t_{\text{exp}}$  represents the exposure duration and  $E_{\text{mpe}}(t_{\text{exp}})$  represents the MPE value corresponding to  $t_{\text{exp}}$ . Therefore, the maximum allowable transmit optical power  $P_{\text{tx,max}}$  can be written as:

$$P_{\text{tx,max}}(t_{\text{exp}}) = \frac{\pi d_a^2 E_{\text{mpe}}(t_{\text{exp}})}{4 \left(1 - \exp\left(-\frac{d_a^2}{2W^2(z_{\text{mph}})}\right)\right)}. \quad (\text{A.3})$$

When the angular subtense of the apparent source is less than 1.5 mrad, the MPH,  $z_{\text{mph}}$ , is 10 cm. The MPE value  $E_{\text{mpe}}(t_{\text{exp}})$  can be calculated based on parameters in Table A.1 [135]. The maximum allowable transmit optical power,  $P_{\text{tx,max}}$  is plotted against the exposure duration  $t_{\text{exp}}$  in Fig. A.1 for different wavelengths and different  $\theta_{\text{FWHM}}$ . The  $P_{\text{tx,max}}$  for  $\lambda = 1550$  nm is much larger than the  $P_{\text{tx,max}}$  for  $\lambda = 850$  nm so that  $\lambda = 1550$  nm is chosen

in this study for higher data rate communication. The maximum allowable transmitted power,  $P_{tx,max}$ , for  $\theta_{FWHM} = 2^\circ, 4^\circ, 6^\circ$  are 20 mW, 60 mW, and 130 mW, respectively.

	$\lambda = 1550 \text{ nm}$		$\lambda = 850 \text{ nm}$	
Exposure duration, $t_{exp}$ (s)	0.35 to 10	10 to $10^3$	$10^{-3}$ to 10	10 to $10^3$
MPE, $E_{mpe}$ ( $\text{W} \cdot \text{m}^{-2}$ )	$10^4/t_{exp}$	1000	$18t_{exp}^{0.75}C_4/t_{exp}$	$10C_4C_7$
Aperture stop (mm) $d_a$	$1.5t_{exp}^{3/8}$	3.5	7	7
$C_4$	-	-	$10^{0.002(\lambda-700)}$	$10^{0.002(\lambda-700)}$
$C_7$	-	-	1	1

**Table A.1:** Parameters for eye safety

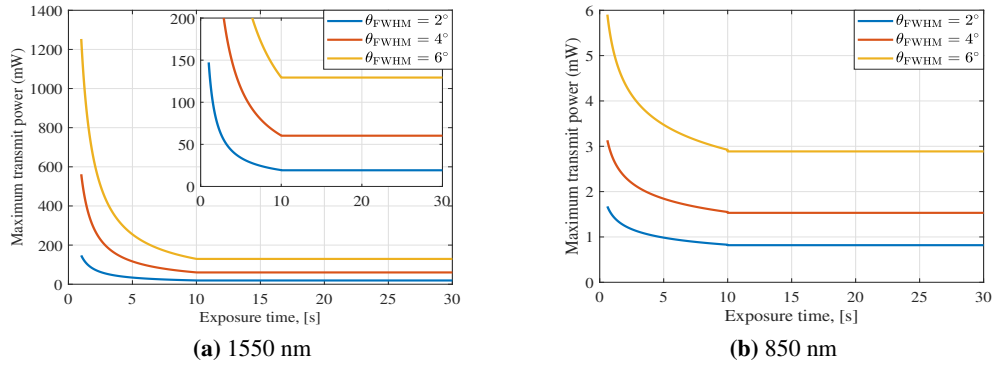


**Figure A.1:** Maximum transmit power considering eye safety

---

# Appendix B

## Publications

---

The list of published papers are included here.

### B.1 Journal Papers

Z. Zeng, M. Dehghani Soltani, Y. Wang, X. Wu, and H. Haas, "Realistic Indoor Hybrid WiFi and OFDMA-based LiFi Networks," *IEEE Transactions on Communications*, vol. 68, no. 5, pp. 29782991, 2020.

Z. Zeng, M. Dehghani Soltani, M. Safari, and H. Haas, "Interference Mitigation using Optimized Angle Diversity Receiver in LiFi Cellular network," Submitted to *IEEE Transaction on Communications*, July. 2021.

Z. Zeng, M. Dehghani Soltani, C. Chen, M. Safari, and H. Haas, "A VCSEL Array Transmission System with Novel Beam Activation Mechanisms," Submitted to *IEEE Transaction on Communications*, July. 2021.

M. D. Soltani, A. A. Purwita, Z. Zeng, H. Haas, and M. Safari, "Modeling the Random Orientation of Mobile Devices: Measurement, Analysis and LiFi Use Case," *IEEE Transactions on Communications*, 2018.

### B.2 Conference Papers

Z. Zeng, M. D. Soltani, H. Haas, and M. Safari, "Orientation Model of Mobile Device for Indoor VLC and Millimetre Wave Systems," in *IEEE Veh. Technol. Conf. (VTC Fall)*, Chicago, USA, August 2018.

Z. Zeng, M. D. Soltani, M. Safari, and H. Haas, "Angle Diversity Receiver in LiFi Cellular Networks," in *ICC 2019 - 2019 IEEE International Conference on Communications (ICC)*, May 2019, pp. 16.

Z. Zeng, M. D. Soltani, X. Wu, and H. Haas, "Access Point Selection Scheme for LiFi Cellular Networks using Angle Diversity Receivers," in *2019 IEEE Wireless Communications and Networking Conference (WCNC)*, 2019, pp. 16.



# Realistic Indoor Hybrid WiFi and OFDMA-Based LiFi Networks

Zhihong Zeng<sup>✉</sup>, *Student Member, IEEE*, Mohammad Dehghani Soltani<sup>✉</sup>, *Student Member, IEEE*,  
Yunlu Wang<sup>✉</sup>, *Student Member, IEEE*, Xiping Wu<sup>✉</sup>, *Member, IEEE*,  
and Harald Haas<sup>✉</sup>, *Fellow, IEEE*

**Abstract**—The increasing number of mobile devices challenges the current radio frequency (RF) networks, e.g. wireless fidelity (WiFi) networks. Light Fidelity (LiFi) is considered as a promising complementary technology, which operates within the visible light spectrum and infrared spectrum. In an indoor scenario, a hybrid LiFi/WiFi network (HLWN) provides a potential solution to future wireless communications where LiFi augments WiFi in providing ultra-high speed and low latency wireless connectivity. In this paper, dynamic load balancing (LB) with handover in HLWNs is studied. The orientation-based random waypoint (ORWP) mobility model is considered to provide a more realistic framework to evaluate the performance of HLWNs. Based on the low-pass filtering effect of the LiFi channel, we firstly propose an orthogonal frequency division multiplexing access (OFDMA)-based resource allocation (RA) method in LiFi systems. Also, an enhanced evolutionary game theory (EGT)-based LB scheme with handover in HLWNs is proposed. In the EGT scheme, each user adapts their strategy to improve the payoff until LB is achieved across LiFi and WiFi. Then, the LiFi system uses the proposed OFDMA-based RA method while the WiFi system applies the carrier sense multiple access with collision detection (CSMA/CA). Simulation results show that in the LiFi system the OFDMA-based RA scheme outperforms the time division multiple access (TDMA) scheme in terms of both user data rate and fairness. Regarding LB in HLWNs, the proposed EGT scheme can achieve a remarkable enhancement in throughput compared to benchmark schemes, such as hard threshold (HT) scheme and random access point assignment (RAA) scheme.

**Index Terms**—Evolutionary game theory, hybrid network, LiFi, load balancing, WiFi, handover overhead, OFDMA.

## I. INTRODUCTION

**D**UE to rapid growth in the number of mobile devices as well as their ever increasing communication speeds, which are expected to surpass 20 Mbps by 2021 [1], the traditional radio frequency (RF) wireless networks face challenges

to fulfill the future demands. It is reported that the entire RF spectrum will not be sufficient to provide the demanded traffic by 2035 [2]. Light-fidelity (LiFi) is a novel, bidirectional and fully networked wireless communication technology that can support the next-generation high-speed requirement [3]. LiFi can potentially utilize more than 300 THz of the visible light spectrum, which is approximately 139,000 times greater than the 2.16 GHz wireless gigabit alliance (WiGig) channel in the IEEE 802.11ad standard [4]. It has been shown that a single light-emitting diode (LED) can achieve a data rate of 10 Gbit/s using orthogonal frequency division multiplexing [5]. In addition, by using wavelength division multiplexing (WDM), LiFi is able to provide data rates of 14 Gbit/s [6].

Despite a wide variety of advantages provided by LiFi, limitations of this technology should also be considered to develop feasible solutions. Link blockage is one factor that can affect LiFi performance significantly. Inter-cell interference (ICI) can significantly restrict the spectrum efficiency, especially for the cell-edge users. An effective solution is to combine LiFi with existing RF networks, e.g. wireless fidelity (WiFi), to form a hybrid LiFi and WiFi network (HLWN) [7], [8]. Such a network cannot only achieve high data rates through LiFi, but can also provide ubiquitous coverage through WiFi in case of any link blockage within the optical channels or severe ICI. As LiFi uses a different spectrum from WiFi, there is no interference between LiFi and WiFi systems. Thus, the HLWN is able to offer a total system throughput greater than that of a stand-alone LiFi or WiFi network [8].

In HLWNs, efficient load balancing (LB) can significantly improve the overall quality of service (QoS). When user mobility is involved, the LB consists of access point (AP) assignment (APA), resource allocation (RA) and also handover management. Several studies on the topic of HLWNs have been undertaken [9]–[13]. In [9], the hybrid visible light communication (VLC) and RF network are studied for the purpose of system throughput enhancement. In that work, APA and RA are performed in a static system without consideration of user mobility and random device orientation. In [10], a practical hybrid VLC/WiFi network is studied, which uses VLC only for downlink and WiFi just for uplink communications. The hybrid network proposed in that paper is different from the HLWNs where LiFi and WiFi can be used for both downlink and uplink communications. The majority of subsequent research focused on system LB optimization in HLWNs so

Manuscript received February 23, 2019; revised July 10, 2019, October 12, 2019, and January 18, 2020; accepted February 4, 2020. Date of publication February 17, 2020; date of current version May 15, 2020. This publication was made possible by the funding from PureLiFi Ltd. The statements made herein are solely the responsibility of the author(s). Harald also acknowledges the financial support of his research by the Wolfson Foundation and the Royal Society. The associate editor coordinating the review of this article and approving it for publication was A. Chaaban. (*Corresponding author: Zhihong Zeng.*)

The authors are with LiFi R&D Centre, The University of Edinburgh, Edinburgh EH9 3JL, U.K. (e-mail: zhihong.zeng@ed.ac.uk; m.dehghani@ed.ac.uk; yunlu.wang@ed.ac.uk; xiping.wu@ed.ac.uk; h.haas@ed.ac.uk).

Color versions of one or more of the figures in this article are available online at <http://ieeexplore.ieee.org>.

Digital Object Identifier 10.1109/TCOMM.2020.2974458

0090-6778 © 2020 IEEE. Personal use is permitted, but republication/redistribution requires IEEE permission.

See <https://www.ieee.org/publications/rights/index.html> for more information.

as to improve the performance of data rate and user fairness [11]–[13]. Most papers consider a static and simple network setup where user movement and receiver orientation are ignored, which can affect the performance of LiFi systems [14] and consequently HLWNs. In addition, the proposed optimization schemes in [11]–[13] are of high computational complexity, which are difficult to implement. In recent literature, game theory has been extensively applied to network selection and interference management problems in heterogeneous wireless networks [15], [16]. In the evolutionary game theory (EGT) model, each user will adapt their strategy to achieve a better payoff until each user's payoff cannot be increased unilaterally. In our previous work, an EGT-based LB scheme for hybrid LiFi and RF networks is proposed [17], where random device orientation in LiFi systems is considered. The proposed EGT scheme in our previous work is able to achieve a better user satisfaction performance at low computational complexity. However, in order to attain a more accurate evaluation of the system performance, there are three factors that should be considered:

1) *RA Enhancement*: In most of the research studies on hybrid LiFi and RF networks, the RA in both LiFi and RF (e.g. WiFi) systems is considered as an optimization of users' resource portions, which are fractional numbers between 0 and 1 [11]–[13], [18]. This is suitable for a time division multiple access (TDMA) scheme. In multi-user LiFi systems, an efficient multiple access scheme can help to avoid intra-cell interference and achieve multi-user diversity gains. Due to the flexibility in RA, orthogonal frequency division multiplexing access (OFDMA) has been widely adopted in RF networks [19]. By means of the OFDMA scheme, resources can be allocated in both time and frequency domains, where the minimum and indivisible time-frequency slots are known as resource units (RUs). A resource block (RB) is composed of a number of RUs. It is evident that allocating those RUs to different users is more efficient and flexible than allocating subcarriers or time slots only. Moreover, by considering the low pass effect of front-end elements, an adaptive user-to-RU assignment is able to substantially enhance the overall system spectral efficiency compared to TDMA schemes. In [20], [21], OFDMA in LiFi systems has been studied, however, OFDMA and TDMA achieve the same throughput performance as equal channel gains are assumed for all subcarriers. Hence, it is important to consider the channel response with the effect of front-end elements in the RA of LiFi OFDMA systems. In addition, WiFi is the most widely used local area network where carrier sense multiple access with collision avoidance (CSMA/CA) is implemented for allocating transmission resources in a multiuser system. To the best of our knowledge, all previous studies on HLWNs consider TDMA or OFDMA for WiFi, which is not realistic. Hence, in this study, we consider the realistic/practical RA scheme, CSMA/CA, for WiFi.

2) *Handover*: In order to ensure seamless connectivity as well as to fulfill the data rate requirement of mobile users in cellular networks, the ongoing connection may require to be transferred from one AP to another. This process is called handover. Many current research studies on hybrid LiFi

and RF networks consider a static network and handover is not taken into account [11]–[13]. However, when a handover occurs in dynamic HLWNs, signalling information (referred to as handover overhead) would have to be exchanged. This process causes transmission losses of desired data, leading to a reduction in data rate. Thus, handover overhead must be considered in LB for such hybrid networks. In a heterogeneous hybrid network, a handover may result in subsequent handovers. For example, when a user switches from LiFi to WiFi, due to the increased load and reduced user data rate in the corresponding WiFi cell, users allocated to this WiFi AP may have to be reallocated to other WiFi or LiFi APs. Moreover, the load decrease of the LiFi attocell may lead to the increase in the data rate of existing users served by this AP. During each of these handovers, the overhead may affect the achievable user data rate. Therefore, LB should be designed with handover considered.

3) *Device Orientation*: Due to the directionality of the LiFi transmitter and receiver, the change of device orientation will lead to the variation of the channel condition, which may further result in the new AP assignment. To the best of our knowledge, all the previous studies about the HLWN assume that the orientation of the user device is fixed or with a uniform distribution model, which is not practical. The device orientation model has been proposed recently in [22], [23] through experimental measurements. By considering the random orientation of the UE during the user's movement, an orientation-based random waypoint (ORWP) mobility model has been proposed in [23]. To evaluate the performance of HLWN in a more realistic scenario, the ORWP mobility model is considered in this study.

It should be noted that compared to our previous study in [17], we first considered OFDMA in LiFi and CSMA/CA in WiFi systems in this study. Secondly, the joint effect of random orientation and mobility has been considered in a more realistic framework which has been ignored in [17]. Thirdly, both horizontal and vertical handover efficiencies have been included in our analysis. All these can affect the AP selection as well as the RA scheme, which pose new challenges regarding RA and LB in a hybrid LiFi/WiFi network. To address these challenges, an enhanced EGT-based algorithm is proposed, which is intrinsically different from the one presented in [17]. The detailed description of the EGT-based algorithm is given in Section III-B. In summary, the main contributions of this work are listed as follows:

- The joint effect of random orientation and mobility are considered to evaluate the performance of HLWN in a more realistic scenario by using the ORWP mobility model.
- The handover management takes into account the effect of the handover overhead. The impact of vertical and horizontal handover on the average throughput of a HLWN is evaluated.
- A low-complexity OFDMA RA scheme in LiFi systems is proposed for HLWNs. The performance of user data rate and fairness is evaluated compared to the HLWN system where TDMA is used in LiFi.

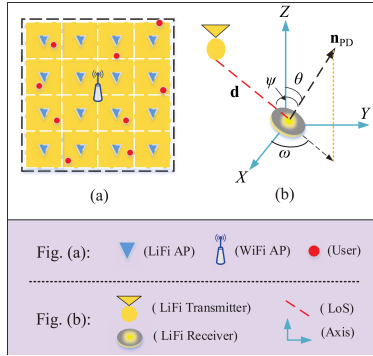


Fig. 1. (a) Illustration of AP deployment in HLWNs and (b) polar and azimuth orientation angle of LiFi receivers.

- An enhanced EGT-based dynamic LB scheme for HLWNs is proposed. In the proposed HLWN, the LiFi system adopts the OFDMA scheme while the WiFi system applies the CSMA/CA which benefits from a utilization ratio to fairly allocate WiFi resources between the uplink and downlink. Then, LB is achieved based on these two schemes and the EGT algorithm. Also, the impact of the WiFi utilization ratio on the average data rate of a HLWN is assessed in this study.

The rest of the paper is organized as follows. The hybrid LiFi and WiFi system model is introduced in Section II. In Section III, the low complexity OFDMA RA scheme for LiFi systems and the EGT-based LB scheme including handover for HLWNs are proposed. The performance evaluation and discussion are presented in Section IV. Conclusions are drawn in Section V.

## II. HYBRID LiFi/WiFi NETWORK MODEL

### A. System Setup

As shown in Fig. 1(a), an indoor hybrid LiFi/WiFi network is considered in this study, where one WiFi AP and  $N_L$  LiFi APs are deployed. All LiFi APs and the WiFi AP are connected to the central unit (CU) through optical fibres with the CU controlling and managing them. In this study, it is assumed that the user can only be served by one technology, either WiFi or LiFi, at a time.

In the LiFi system, the visible light spectrum is used for the downlink transmission. Regarding the uplink transmission, the infrared (IR) spectrum is adopted in this study since it does not affect the illumination and adds no interference to the LiFi downlink communication and the existing RF networks [24], [25]. It should be noted that the downlink communication in LiFi systems is the primary focus of this study. Each LiFi AP is composed of multiple LEDs to transmit optical power and an infrared receiver to detect the uplink signals. The user terminals are equipped with photodiodes (PDs) to

receive visible light signals and infrared transmitters to serve the uplink. In each LiFi cell, optical OFDMA is employed as the multiple access scheme.

For the WiFi system, it is assumed that the WiFi AP follows the IEEE 802.11ad standard [4]. According to this standard, each station (STA) can communicate with the AP (uplink and downlink) or with other STAs (direct link). Particularly, we only consider the uplink and downlink in WiFi systems in this study while direct user to user communication is not taken into account. The main medium access control (MAC) of IEEE 802.11 is CSMA/CA, which is therefore also considered in this study [26]. All the nodes in the WiFi system including the WiFi AP are allowed to access the channel using the available bandwidth during data transmission. This means that the uplink transmission of WiFi will affect the downlink communication. For example, when increasing the uplink throughput, the downlink network will have fewer chances to get access to the channel. This can lead to a drastic decrease in downlink throughput. Therefore, in this work, the effect of the WiFi uplink data rate requirement on the downlink resource allocation is considered.

In the HLWNs, the set of users is denoted as  $\mathcal{U} = \{\mu | \mu \in [1, N_{UE}], \mu \in \mathbb{N}\}$ , where  $\mathbb{N}$  is the set of natural numbers. Assume the total number of users and LiFi APs are  $N_{UE}$  and  $N_L$ , respectively. The set of LiFi APs is denoted by  $\mathcal{A} = \{\alpha | \alpha \in [1, N_L], \alpha \in \mathbb{N}\}$  and the WiFi AP is denoted by  $W$ . The mobility-aware resource allocation algorithms which use the historical data and future-state prediction have been studied in [27]–[29]. However, random device orientation is considered in this study and to the best of our knowledge, no previous study has shown that the device orientation can be predictable. Since the future state cannot be predicted, it may not be practical to optimize the long-term performance of the system. Hence, the system performance in a single quasi-static state is considered instead. A quasi-static period is a short duration where the channel state information (CSI) can be assumed to be constant [30]. In the indoor scenario, for both LiFi and WiFi channels, the CSI can be assumed to be constant for a short time period, commonly known as the coherence time. The coherence time for LiFi networks is in the order of tens of milliseconds [23], which encompasses several RBs. During each quasi-static period, the CSI of channels in HLWNs is fixed for the duration of  $T_p$ , which is the minimum value between the coherence time of LiFi channels,  $T_L$ , and the coherence time of WiFi channels,  $T_W$ . So that,  $T_p = \min\{T_L, T_W\}$ . The evaluation of the coherence time of both LiFi and WiFi channels is not the focus of this study and will be considered in future work. The dynamic HLWN system can be divided into many quasi-static periods and each period is referred to as a ‘state’. Each user will be served by either a LiFi AP or a WiFi AP in each state and the sequence numbers of the state are denoted by  $\{1, 2, \dots, n | n \in \mathbb{N}\}$ . The CU performs the AP assignment and allocates the available resources to each individual more efficiently compared to a distributed case in which each AP allocates its own resources to the users. In this study, the proposed EGT algorithm is realized in a centralized manner within the CU. By monitoring the network continuously, the CU obtains knowledge of the CSI. Based on

the collected CSI, the CU undertakes the AP selection and resource allocation at each state. In the following, the LiFi and WiFi system models are described.

### B. LiFi System Model

According to [31], the LiFi channel impulse response between the transmitter (Tx) and the receiver (Rx) in the frequency domain can be modelled as:

$$H(f) = H_{\text{LOS}} H_{\text{F}}(f), \quad (1)$$

where  $H_{\text{LOS}}$  denotes the path loss of a line-of-sight (LOS) channel and  $H_{\text{F}}(f)$  represents the front-end device frequency response. The LOS channel fading gain between the Tx and Rx can be modelled as follows [32]:

$$H_{\text{LOS}} = \begin{cases} \frac{(m+1)A_{\text{p}}n_{\text{ref}}^2 T_s(\psi) \cos^m(\phi) \cos(\psi)}{2\pi d^2 \sin^2 \Psi_c}, & \psi \leq \Psi_c \\ 0, & \psi > \Psi_c, \end{cases} \quad (2)$$

where  $A_{\text{p}}$  is the physical area of the PD;  $n_{\text{ref}}$  is the internal refractive index of the concentrator;  $d$  is the distance between the Tx and Rx;  $\Psi_c$  denotes the field of view (FOV) of the PD;  $\psi$  is the incidence angle of the receiving PD;  $T_s(\psi)$  represents the gain of the optical filter;  $\phi$  denotes the irradiance angle of the Tx. The Lambertian order is denoted as  $m = -1/\log_2(\cos(\Phi_{1/2}))$ , where  $\Phi_{1/2}$  is the half-intensity radiation angle. The distance vector between the LiFi AP and the user equipment (UE) is denoted as  $\mathbf{d}$ . As shown in Fig. 1(b), the random device orientation can be described by two angles: the polar angle  $\theta$  and azimuth angle  $\omega$  [33]. In the Cartesian coordinate system, the normal vector of the user device can be written as [23]:

$$\mathbf{n}_{\text{PD}} = (\cos(\omega) \sin(\theta), \sin(\omega) \sin(\theta), \cos(\theta)). \quad (3)$$

Accordingly, the angle of incidence to the PDs is denoted as  $\psi = \arccos < \mathbf{d}, \mathbf{n}_{\text{PD}} >$ , where  $< \cdot, \cdot >$  is the inner product operator.

The front-end frequency response can be modelled by a first order low pass filter as [34]–[36]:

$$H_{\text{F}}(f) = \exp\left(-\frac{f}{v_e f_0}\right), \quad (4)$$

where  $f_0$  is the 3 dB cut-off frequency of the front-end filtering effect;  $v_e$  is the fitting coefficient and  $|H_{\text{F}}(f_0)|^2 = -3$  dB when  $v_e = 2.88$  [35].

In LiFi systems, the Tx and Rx use intensity modulation (IM) and direct detection (DD), respectively. Due to the baseband IM/DD communication, the transmit signals are required to be positive and real. Modulation techniques such as direct current biased optical (DCO)-OFDM and asymmetrically clipped optical (ACO)-OFDM are developed to ensure real and positive signals [36]. The spectrum efficient DCO-OFDM is used in this study to achieve high data rates. More spectrum efficient techniques have been developed such as spectral and energy efficient (SEE)-OFDM [37] and enhanced unipolar (eU)-OFDM [38], but they use the same subcarrier structures as in DCO-OFDM. Therefore, using these

more advanced modulation techniques will not alter the main contributions of this work. The analysis can be applied to other types of OFDM systems in a similar manner. The SINR between user  $\mu$  and the serving LiFi AP  $\alpha$  can be expressed as [17]:

$$\gamma_{\mu,\alpha}(f) = \frac{(\tau P_{\text{tx}} H_{\mu,\alpha}(f))^2}{\kappa^2 N_0 B_{\text{L}} + \sum_{i \in \mathcal{A} \setminus \{\alpha\}} (\tau P_{\text{tx}} H_{\mu,i}(f))^2}, \quad (5)$$

where  $\tau$  is the receiver's optical to electrical conversion efficiency;  $P_{\text{tx}}$  is the transmitted optical power of a LiFi AP;  $H_{\mu,\alpha}(f)$  is the channel gain between user  $\mu$  and the serving LiFi AP  $\alpha$  based on (1);  $\kappa$  is the ratio of DC optical power to the square root of electric signal power. When  $\kappa = 3$ , it can be guaranteed that 0.3% of the signals are clipped and the clipping noise is neglectable [39]. Furthermore,  $N_0$  and  $B_{\text{L}}$  denote the noise power spectral density and the baseband modulation bandwidth in the LiFi system, respectively. The channel gain between user  $\mu$  and the interfering LiFi AP  $i$  at frequency  $f$  is denoted as  $H_{\mu,i}(f)$ . It is noted that when other OFDM techniques, which has closed form SINR expressions, are applied, (5) should be replaced with the corresponding expression.

In the LiFi system, adaptive M-quadrature amplitude modulation (M-QAM) is used on different OFDM subcarriers. The number of OFDM subcarriers is denoted by  $M$ , which is an even and positive integer. The sequence number of OFDM subcarriers is denoted by  $m \in [1, M]$ ,  $m \in \mathbb{N}$ . In order to ensure that the OFDM signal is real, Hermitian symmetry is applied. As a result, only half of all available subcarriers can be used for information transmission, i.e., subcarriers  $m > M/2$  do not carry any information. As DCO-OFDM is used in this study, the effective subcarrier set (referring to the subcarriers bearing information data) is defined as  $\mathcal{M}_e = \{m | m \in [2, M/2], m \in \mathbb{N}\}$ . The number of effective subcarriers [36] is denoted by  $M_e = M/2 - 1$ . In this study, it is assumed that there are several RBs in a quasi-static period, and each RB contains  $M_e K$  RUs, where  $K$  is the number of subframes in the time domain. The frequency of the subcarrier  $m$  is denoted as  $f_m$ . As the channel is assumed to be constant during a quasi-static period, the spectral efficiency of the RU on the  $m$ -th subcarrier is identical for each subframe. According to the modulation and coding scheme given in Table I [40], for user  $\mu$  served by the LiFi AP  $\alpha$ , the spectral efficiency of subcarrier  $m$ ,  $q_{\mu,\alpha,m}$ , can be determined based on  $\gamma_{\mu,\alpha}(f_m)$  obtained from (5). Therefore, for user  $\mu$  served by the LiFi AP  $\alpha$ , the communication link data rate of the RU on subcarrier  $m$  for each subframe can be written as:

$$r_{\mu,\alpha,m}^{\text{Link}} = \frac{2B_{\text{L}} q_{\mu,\alpha,m}}{MK}. \quad (6)$$

Therefore, the total LiFi link data rate of user  $\mu$  served by the LiFi AP  $\alpha$  is expressed as:

$$r_{\mu,\alpha}^{\text{Link}} = K \sum_{m \in \mathcal{M}_e} r_{\mu,\alpha,m}^{\text{Link}}. \quad (7)$$

### C. WiFi System Model

In a WiFi system, users and the WiFi AP use the CSMA/CA with request to send/ clear to send (RTS/CTS) hand-shaking

TABLE I  
MODULATION AND CODING TABLE [40]

min. SINR [dB]	Modulation	Code rate	Spectral efficiency [bit/s/Hz]
-	-	-	0
1	QPSK	0.44	0.8770
3	QPSK	0.59	1.1758
5	16QAM	0.37	1.4766
8	16QAM	0.48	1.9141
9	16QAM	0.60	2.4063
11	64QAM	0.45	2.7305
12	64QAM	0.55	3.3223
14	64QAM	0.65	3.9023
16	64QAM	0.75	4.5234
18	64QAM	0.85	5.1152
20	64QAM	0.93	5.5547

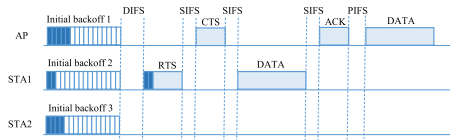


Fig. 2. Illustration of CSMA/CA with DCA mechanism.

mechanism, as shown in Fig. 2. In CSMA/CA, the STAs listen to the channel for an interval called distributed inter-frame space (DIFS). If the channel is sensed to be idle after DIFS, they initiate their backoff time. Both users and the AP have a random backoff number and the one with the lowest backoff number has the priority to transmit the information. Before data transmission, the STA sends the RTS packet. If the RTS packet is received successfully by the AP, a CTS packet will be sent by the AP after a short inter-frame space (SIFS). After the two-way handshaking of RTS/CTS, the data frame will be transmitted. Also, an acknowledgement (ACK) frame will be sent by the AP if the data frame is successfully received. In [26], a detailed explanation and performance analysis of the CSMA/CA with RTS/CTS mechanism is provided. The time duration used for successful data transmission on the uplink (downlink) is called the uplink (downlink) utilization. The ratio of the uplink (downlink) utilization and the total transmission time is defined as uplink (downlink) utilization efficiency [41]. We denote this ratio by  $U_{up}$  ( $U_{down}$ ), which is a fractional number between 0 and 1. In addition, the utilization ratio of  $U_{down}$  and  $U_{up}$  is defined as:

$$\epsilon = \frac{U_{down}}{U_{up}}. \quad (8)$$

In this work, the full buffer model is considered. This means that there are always packets to send in the buffers of the WiFi AP and UEs. Since the WiFi AP and each user have the same probability to access the channel, the utilization ratio  $\epsilon$  is naturally equal to  $\frac{1}{N_w+1}$ , where  $N_w$  is the number of users served by the WiFi AP. In order to flexibly allocate the

available spectrum between uplink and downlink transmission, a mechanism called downlink compensation access (DCA) is considered [41]. By using DCA,  $\epsilon$  can be any required utilization ratio greater than or equal to  $\frac{1}{N_w+1}$ . In the DCA mechanism, the AP can transmit data frames after point inter-frame space (PIFS) following the previous ACK packet until the utilization ratio reaches the requirement, as shown in Fig. 2. Assume that  $\epsilon_0$  is the required utilization ratio. Initially, the utilization ratio  $\epsilon = 1/(N_w + 1)$  is less than  $\epsilon_0$ . In this case, the DCA is used and the handshake mechanism of RTS and CTS is not necessary. The AP can transmit multiple data frames while  $\epsilon < \epsilon_0$ . Note that the AP accesses the channel without collision during the DCA because PIFS is used as the frame gap, which is shorter than DIFS. When  $\epsilon \geq \epsilon_0$  is achieved, the RTS/CTS handshake instead of DCA will be used for the WiFi AP transmission. In this way, the required utilization ratio is maintained.

The uplink and downlink utilization efficiency can be expressed as:

$$U_{up} = U \frac{1}{1 + \epsilon}, \quad (9)$$

$$U_{down} = U \frac{\epsilon}{1 + \epsilon}, \quad (10)$$

where  $U$  is the system utilization efficiency given by [41]:

$$U = \frac{p_s p_t t_p}{(1 - p_t) t_f + p_t p_s (1 - p_d) t_s + p_t p_s p_d t_d + p_t (1 - p_s) t_c}, \quad (11)$$

where  $p_s$  is the probability of successful transmission;  $p_t$  is the probability that there is at least one transmission in a backoff unit time;  $p_d$  is the probability that a data frame is transmitted by the DCA under the condition that the previous transmission was successful;  $t_f$  is the duration of an empty slot time;  $t_p$  is the average transmission time of the frame payload;  $t_c$  is the average time that the channel is sensed to be busy because of a collision;  $t_s$  is the average time that the channel is sensed as busy because of a successful transmission; and  $t_d$  is the time duration for DCA. Specifically,  $p_s$ ,  $p_t$ ,  $p_d$  can be presented with the number of users served by the WiFi AP as the primary variable, which has been given in [41]:

$$p_t(N_w) = 1 - (1 - p_c)^{N_w+1}, \quad (12)$$

$$p_s(N_w) = \frac{(N_w + 1) p_c (1 - p_c)^{N_w}}{p_t}, \quad (13)$$

$$p_d(N_w) = \frac{N_w - 1}{2N_w p_s}, \quad (14)$$

where  $p_c = 2/(C_{max} + 1)$  is the probability that a user transmits a data frame in a backoff counter time;  $C_{max}$  is the maximum backoff stage. Also,  $t_c$ ,  $t_s$  and  $t_d$  are expressed as follows:

$$t_c = t_{RTS} + t_{DIFS}, \quad (15)$$

$$t_s = t_{RTS} + t_{CTS} + t_H + t_p + t_{ACK} + 3t_{SIFS} + t_{DIFS}, \quad (16)$$

$$t_d = t_H + t_p + t_{ACK} + t_{SIFS} + t_{PIFS}, \quad (17)$$

where  $t_{RTS}$ ,  $t_{CTS}$ ,  $t_H$ ,  $t_{ACK}$ ,  $t_{SIFS}$ ,  $t_{DIFS}$ , and  $t_{PIFS}$  are the time duration of RTS, CTS, frame header, ACK, SIFS,

DIFS and PIFS. In this way, the utilization function in (11) can be written as a function corresponding to the number of users served by the WiFi AP, denoted by  $U(N_w)$ . Similarly, the uplink and downlink utilization efficiency can be rewritten as  $U_{\text{up}}(N_w)$  and  $U_{\text{down}}(N_w)$ .

The channel bit rate in the WiFi system is denoted by  $R_c$ . The downlink data rates for user  $\mu$  in the WiFi cell can be expressed as:

$$R_{\mu,\text{wifi}} = \frac{R_c U_{\text{down}}(N_w)}{N_w}, \quad (18)$$

and the uplink data rate for a WiFi user can be expressed as:

$$\Upsilon_{\mu,\text{wifi}} = \frac{R_c U_{\text{up}}(N_w)}{N_w}. \quad (19)$$

#### D. Handover

The handover overhead causes a reduction in the average data rate of users who have to be handed off to new APs. The definition of handover efficiency was first introduced in [8] and was later used in [42] and [27]. Generally, in an indoor scenario, the handover overhead is in the order of milliseconds and the overhead time is considered as a random variable [43]. Hence, the exact overhead time is unknown at the beginning of each state, which means the exact handover efficiency cannot be calculated. Therefore, the average handover efficiency will be used to estimate the negative effect of handover on user's data rate [27]. The average handover efficiency is assumed to range from 0 to 1. There are two types of handover in a hybrid network, horizontal handover (HHO) and vertical handover (VHO). HHO occurs between APs of the same access technology. VHO refers to the change of connectivity between different wireless access technologies. The average handover efficiency for HHO and VHO are denoted by  $\eta_{0,\text{HHO}}$  and  $\eta_{0,\text{VHO}}$ , respectively. Hence, the estimated handover efficiency between two consecutive states can be written as follows:

1) HHO: Since a single WiFi AP is considered in this study, HHO only occurs between two LiFi APs. Assuming that user  $\mu$  is served by a LiFi AP  $\alpha_\mu^{(n-1)}$  in the state  $(n-1)$ , the estimated HHO efficiency between state  $(n-1)$  and state  $n$  can be expressed as:

$$\eta_{\text{H}}(i) = \begin{cases} \eta_{0,\text{HHO}}, & i \neq \alpha_\mu^{(n-1)} \\ 1, & i = \alpha_\mu^{(n-1)} \end{cases}, \quad i \in \mathcal{A}, \quad (20)$$

where the operation  $[\cdot]^+$  denotes  $\max(\cdot, 0)$ .

2) VHO: VHO occurs when the host AP of user  $\mu$  is transferred from a LiFi AP to the WiFi AP or vice versa. Assume that user  $\mu$  is served by AP  $\alpha_\mu^{(n-1)}$  in state  $(n-1)$ , where  $\alpha_\mu^{(n-1)}$  can be either a LiFi AP or the WiFi AP. The estimated VHO efficiency can be defined as follows:

$$\eta_{\text{V}}(j) = \begin{cases} \eta_{0,\text{VHO}}, & j \neq \alpha_\mu^{(n-1)} \\ 1, & j = \alpha_\mu^{(n-1)} \end{cases}, \quad j \in \{\mathcal{A}, \mathcal{W}\}. \quad (21)$$

We note that the CSI feedback can be notably reduced by means of limited-feedback mechanisms [30], [44], [45]. Hence, the overhead due to handover is dominant compared to the overhead due to CSI feedback, however, the handover

efficiency can include both overheads, and this does not change the generality of our model.

#### E. Orientation-Based RWP Mobility Model

In this section, we describe the ORWP which provides a more realistic framework for the analysis of system performance in a LiFi network [23]. In fact, the ORWP model incorporates the device orientation, which is modeled based on the experimental measurements, into the random waypoint mobility model. This method was later developed in [46]. It is shown that the random orientation for walking users can be modeled as a correlated Gaussian distribution with the mean of  $\mathbb{E}[\theta] = 30^\circ$  and variance of  $\sigma_\theta = 7.78^\circ$ . A first-order autoregressive (AR) model can be exploited to generate correlated random samples of device orientation. Therefore, the  $k$ -th sample of AR(1) can be obtained as [23]:

$$\theta[k] = c_0 + c_1 \theta[k-1] + w[k], \quad (22)$$

where  $w[k]$  is a white noise process with the variance of  $\sigma_w$ . To guarantee that the random process (RP),  $\theta$ , is wide-sense stationary, the condition  $|c_1| < 1$  should be met. The factors  $c_0$ ,  $c_1$  and the variance  $\sigma_w$  can be obtained based on the mean, variance and coherence time of the experimental measurements as follow:

$$c_0 = (1 - c_1) \mathbb{E}[\theta], \quad c_1 = 0.05 \frac{T_s}{T_{c,\theta}}, \quad \sigma_w^2 = (1 - c_1^2) \sigma_\theta^2, \quad (23)$$

where  $T_s$  is the sampling time and  $T_{c,\theta}$  is the coherence time of the RP,  $\theta$ . The coherence time is obtained based on the least-squares spectral analysis (LSSA) technique from the experimental measurements, which is described in detail in [33].

### III. DYNAMIC LB SCHEME IN HYBRID LiFi/WiFi NETWORKS

Two algorithms are discussed in this section. The low-complexity OFDMA RA scheme for LiFi systems is summarized in Algorithm 1. The EGT-based LB scheme of the HLWNs is presented in Algorithm 2. The RA scheme in Algorithm 1 is part of the LB scheme in Algorithm 2. Hence, in the following, the detailed explanations of Algorithm 1 will be given first in Section III-A and then, Algorithm 2 is described in Section III-B.

#### A. Resource Allocation in OFDMA LiFi Systems

In this section, the resource allocation in a single LiFi cell in a quasi-static state is investigated. As a single cell  $\alpha$  is considered in this section, for the simplicity of notation, the communication link data rate of the RU on subcarrier  $m$  for each subframe,  $r_{\mu,\alpha,m}^{\text{Link}}$ , will be written as  $r_{\mu,m}$ . The  $\beta$ -proportional fairness is a generic fairness function which includes a number of well-known fairness concepts such as proportional fairness, max-min fairness and throughput maximization. Hence, it has been widely adopted in studies dealing with resource allocation problem [11], [12], [17], [47]. The  $\beta$ -proportional fairness function considering both user data



**Algorithm 1** : Low-Complexity RA Algorithm in the Cell  $\alpha$  for LiFi OFDMA Systems

---

```

1: Initialization: Subcarrier  $m = \frac{M}{2}$ ; For all user  $\mu \in \mathcal{U}_\alpha$ ,
    $Z_{\mu, \frac{M}{2}+1} = 0$ .
2: while Subcarrier  $m \geq 2$  do
3:   for Each user  $\mu \in \mathcal{U}_\alpha$  do
4:     Calculate the link data rate,  $r_{\mu, m}$ .
5:     Calculate  $Z_{\mu, m+1}$  based on (26).
6:   end for
7:   Calculate  $k_{\mu, m}$  for each user on subcarrier  $m$  according
   to (33).
8:    $m = m - 1$ .
9: end while

```

---

rate and fairness is used as the utility function in this study, which is defined as [48]:

$$\psi_\beta(x) = \begin{cases} \ln(x), & \beta = 1 \\ \frac{x^{1-\beta}}{1-\beta}, & \beta \geq 0, \beta \neq 1, \end{cases} \quad (24)$$

where  $\beta$  denotes the fairness coefficient and  $x$  is the user data rate. The well known proportional fairness and the max-min fairness can be realized using this utility function by setting  $\beta = 1$  and  $\beta \rightarrow +\infty$ , respectively [12]. In order to solve the resource allocation problem, the optimization problem can be formulated as follows:

$$\begin{aligned} \max_{k_{\mu, m}} \quad & \sum_{\mu \in \mathcal{U}_\alpha} \psi_\beta \left( \sum_{m \in \mathcal{M}_e} k_{\mu, m} r_{\mu, m} \right) \\ \text{s.t.} \quad & \sum_{\mu \in \mathcal{U}_\alpha} k_{\mu, m} = K, \quad m \in \mathcal{M}_e. \end{aligned} \quad (25)$$

where  $k_{\mu, m}$  denotes the number of RUs allocated to user  $\mu$  on subcarrier  $m$  in each RB and  $\mathcal{U}_\alpha$  denotes the set of users served by the AP  $\alpha$ . By using the Lagrangian multiplier method, an iterative algorithm is proposed to find the optimum of (25) in [35]. However, this method is of high computational complexity due to the iterative algorithm. In order to reduce the complexity, a novel RA scheme in LiFi OFDMA systems is proposed in this section.

Since the LiFi channel gain in the frequency domain is inversely proportional to the frequency [36], only users with high SINR are able to utilize the high frequency resources. In other words, the number of users who can utilize high-frequency resources is much less than the number of users who can use low-frequency resources. Therefore, the low-complexity RA scheme is proposed to be carried out from high-frequency to low-frequency subcarriers in sequence. For user  $\mu$ , the aggregate data rate from subcarriers  $m$  to  $M/2$ ,  $Z_{\mu, m}$ , can be calculated by adding the data rate achieved on subcarrier  $m$ ,  $k_{\mu, m} r_{\mu, m}$ , and the aggregate data rate from subcarriers  $m+1$  to  $M/2$ ,  $Z_{\mu, m+1}$ . This can be expressed as:

$$Z_{\mu, m} = \begin{cases} k_{\mu, m} r_{\mu, m} + Z_{\mu, m+1}, & 2 \leq m \leq M/2 \\ 0, & M/2 < m. \end{cases} \quad (26)$$

**Algorithm 2** EGT-Based Centralized LB Algorithm Executed in the CU

---

```

1: Initialization: The users are randomly allocated to an AP
   from  $\mathcal{S}_\mu$ ; based on OFDMA (for LiFi) or CSMA/CA (for
   WiFi), each AP allocates the available resources to the
   players of the corresponding cell; the CU calculates the
   payoff of each player  $\pi_{\mu, \alpha}^{<0>}$  and the average payoff  $\bar{\pi}^{<0>}$ ;
   and  $t \leftarrow 1$ .
2: for each player  $\mu \in \mathcal{U}$  do
3:   Calculate the probability of mutation,  $p_\mu^{<t>}$ , based on
   (37) and generate a random number  $\delta$ , which is uniformly
   distributed between 0 and 1.
4:   if  $\delta < p_\mu^{<t>}$  then
5:     if  $\alpha_{\mu}^{<t-1>}$  is a WiFi AP then
6:       Calculate the estimated payoff if connected to the
       best LiFi AP,  $\hat{\pi}_{\mu, v}^{<t>}$ , based on (40) and Algorithm 1.
7:     else
8:       Compute the estimated payoff if connected to the
       WiFi AP,  $\hat{\pi}_{\mu, v}^{<t>}$ , based on (41) and CSMA/CA
       scheme.
9:     end if
10:    Based on (39), check whether the potential AP will
    be overloaded first and then decide to stay with the
    previous AP or switch to a new AP.
11:   else
12:    No mutation occurs, the player  $\mu$  remains with the
    previous AP.
13:   end if
14: end for
15: for each AP  $\alpha \in \mathcal{A} \cup \{W\}$  do
16:   According to Algorithm 1 and (18), the available
   resources are allocated by the CU to players in each cell.
17: end for
18:  $t \leftarrow t + 1$  and repeat from Step 2 until no AP switch
   occurs.

```

---

It should be noted that the sum of  $k_{\mu, m} r_{\mu, m}$  and  $Z_{\mu, m+1}$  is less than  $\sum_{m \in \mathcal{M}_e} k_{\mu, m} r_{\mu, m}$ . Hence, the sub-optimization problem can be formulated as follows:

$$\begin{aligned} \max_{k_{\mu, m}} \quad & \sum_{\mu \in \mathcal{U}_\alpha} \psi_\beta (k_{\mu, m} r_{\mu, m} + Z_{\mu, m+1}) \\ \text{s.t.} \quad & \sum_{\mu \in \mathcal{U}_\alpha} k_{\mu, m} = K, \quad m \in \mathcal{M}_e. \end{aligned} \quad (27)$$

To solve the sub-optimization problem in (27), the Lagrangian multiplier method is used and the Lagrangian function can be expressed as:

$$\begin{aligned} F(k_{\mu, m}, \lambda_m) = & \sum_{\mu \in \mathcal{U}_\alpha} \psi_\beta (k_{\mu, m} r_{\mu, m} + Z_{\mu, m+1}) \\ & + \lambda_m \left( K - \sum_{\mu \in \mathcal{U}_\alpha} k_{\mu, m} \right), \end{aligned} \quad (28)$$

where  $\lambda_m$  is the Lagrangian multiplier for the  $m$ -th constraint in (27). To obtain the optimal  $k_{\mu, m}$ , the gradient of the Lagrangian function in (29) is set to be equal to 0, which

is written as:

$$\frac{\partial F(k_{\mu,m}, \lambda_m)}{\partial k_{\mu,m}} = r_{\mu,m}(k_{\mu,m}r_{\mu,m} + Z_{\mu,m+1})^{-\beta} - \lambda_m = 0. \quad (30)$$

It can be obtained from (30) that:

$$k_{\mu,m} = \frac{1}{r_{\mu,m}} \left( \frac{r_{\mu,m}}{\lambda_m} \right)^{\frac{1}{\beta}} - \frac{Z_{\mu,m+1}}{r_{\mu,m}}. \quad (31)$$

Based on the constraint in (27), (31) can be solved as:

$$\lambda_m^{-\frac{1}{\beta}} = \left( K + \sum_{\mu \in \mathcal{U}_\alpha} \frac{Z_{\mu,m+1}}{r_{\mu,m}} \right) / \sum_{\mu \in \mathcal{U}_\alpha} (r_{\mu,m})^{\frac{1}{\beta}-1}. \quad (32)$$

By inserting (32) into (31), the number of RUs allocated to user  $\mu \in \mathcal{U}_\alpha$  on subcarrier  $m$  in each RB is given by:

$$k_{\mu,m} = \frac{r_{\mu,m}^{\frac{1}{\beta}-1}}{\sum_{\mu \in \mathcal{U}_\alpha} r_{\mu,m}^{\frac{1}{\beta}-1}} \left( K + \sum_{\mu \in \mathcal{U}_\alpha} \frac{Z_{\mu,m+1}}{r_{\mu,m}} \right) - \frac{Z_{\mu,m+1}}{r_{\mu,m}}. \quad (33)$$

It can be noted that iterative computation is not required in (33). A closed-form solution is obtained for  $k_{\mu,m}$  in (33) which reduces the computational complexity substantially. Algorithm 1 summarizes the low-complexity RA scheme. The LiFi data rate of user  $\mu$  can be expressed as:

$$D_{\mu,\alpha} = \sum_{m \in \mathcal{M}_\alpha} k_{\mu,m} r_{\mu,m}, \quad \mu \in \mathcal{U}_\alpha. \quad (34)$$

#### B. Proposed EGT-Based LB Scheme

The global optimum of the system LB problem can be determined using exhaustive search. However, exhaustive search is very computational expensive. In this section, an EGT-based LB scheme, which reduces the computational complexity and achieves sub-optimum performance, is proposed for the APA. At the beginning of each state, the EGT-based scheme is performed and each user will be assigned to an AP. If a handover occurs, users cannot transfer any data during the handover association time. The setup of evolutionary game for LB in each state are described as follows:

1. *Players Set* ( $\mathcal{U}$ ): The players in the game are the users in the hybrid network. The set of players is  $\mathcal{U}$  and the total number of players is  $N_{\text{UE}}$ .

2. *Strategy Set* ( $S_\mu$ ): Each user can be potentially served by one of LiFi APs or the WiFi AP. In order to efficiently utilize the LiFi resources, each user will be allocated to its best LiFi AP if it must be served by LiFi. The best LiFi AP is defined as the one which can offer the highest link data rate with handover efficiency taken into account. The best LiFi AP for user  $\mu$  can be defined as:

$$A_\mu = \arg \max_{i \in \mathcal{A}} \eta_{\text{H}}(i) r_{\mu,i}^{\text{Link}}. \quad (35)$$

To reduce the complexity of the AP selection scheme, user  $\mu$  will be assigned to the AP from the strategy set  $S_\mu$ . This set contains the best LiFi AP and the WiFi AP, denoted as  $S_\mu = \{A_\mu, W\}$ .

3. *Payoff Function*: The payoff of a player is defined by the user data rate, which is achieved by either a LiFi or the

WiFi AP. The payoff function of user  $\mu$  served by the AP  $\alpha$  can be written as:

$$\pi_{\mu,\alpha} = \begin{cases} D_{\mu,\alpha}, & \alpha = A_\mu \\ R_{\mu,\text{wifi}}, & \alpha = W, \end{cases} \quad (36)$$

where  $D_{\mu,\alpha}$  is the achievable data rate when user  $\mu$  is served by the LiFi AP  $\alpha$ , given in (34); and  $R_{\mu,\text{wifi}}$  is the achievable data rate if user  $\mu$  is connected to WiFi AP, expressed in (18).

In the EGT-based LB scheme, the players can achieve a better payoff by adapting their strategy iteratively. The adaptation of the AP selection strategy and the evolution of the population is based on the ‘mutation and selection mechanism’ in EGT [16]. For each player, the strategy shift occurs randomly. The players experiencing a lower value of payoff are more likely to adapt their strategy. Following the rule, in the  $t$ -th iteration, the probability of mutation for user  $\mu$  can be expressed as:

$$p_\mu^{<t>} = \begin{cases} 1 - \frac{\pi_{\mu,\alpha}^{<t-1>}}{\bar{\pi}^{<t-1>}}, & \pi_{\mu,\alpha}^{<t-1>} < \bar{\pi}^{<t-1>} \\ 0, & \pi_{\mu,\alpha}^{<t-1>} \geq \bar{\pi}^{<t-1>}. \end{cases} \quad (37)$$

where  $\pi_{\mu,\alpha}^{<t-1>}$  denotes the player’s payoff in the previous iteration;  $\bar{\pi}^{<t-1>}$  represents the average payoff of all players in the previous iteration. The average payoff of all players in the  $t$ -th iteration is given by:

$$\bar{\pi}^{<t>} = \frac{1}{N_{\text{UE}}} \sum_{\mu \in \mathcal{U}} \pi_{\mu,\alpha}^{<t>}, \quad (38)$$

where  $\pi_{\mu,\alpha}^{<t>}$  is the payoff of user  $\mu$  in the  $t$ -th iteration, given in (36).

When a mutation occurs, the user may be assigned to a new AP to maximize the estimated payoff in the current iteration. The new serving AP can be determined as:

$$\alpha_\mu^{<t>} = \arg \max_{i \in S_\mu} \hat{\pi}_{\mu,i}^{<t>} \quad (39)$$

$$\text{and } \hat{\pi}_{\mu,i}^{<t>} = \begin{cases} \pi_{\mu,i}^{<t-1>}, & i = \alpha_\mu^{<t-1>} \\ \eta_{\text{N}}(i) \pi_{\mu,i}^{<t>}, & i \neq \alpha_\mu^{<t-1>}, \end{cases}$$

where  $\alpha_\mu^{<t>}$  is the AP assigned to player  $\mu$  at the  $t$ -th iteration;  $\hat{\pi}_{\mu,i}^{<t>}$  is the estimated payoff when the player is allocated to a new AP  $v$  other than  $\alpha_\mu^{<t-1>}$ . The estimated payoff  $\hat{\pi}_{\mu,v}^{<t>}$  is greatly related to the resource allocation scheme in different networks:

i). *LiFi network* ( $v = A_\mu$ ): In this case,  $\alpha_\mu^{<t-1>}$  is the WiFi AP and user  $\mu$  may experience a handover from WiFi to LiFi in the  $t$ -th iteration. The estimated payoff can be calculated by using the data rate result in LiFi OFDMA systems, shown in (34). Assume that the set of users allocated to LiFi AP  $v$  in  $(t-1)$ -th iteration is denoted by  $\mathcal{U}_v^{<t-1>}$ . After the user is handed off from the WiFi AP to LiFi AP  $v$ , the set of users served by the LiFi AP  $v$  becomes  $\mathcal{U}_v^{<t>} = \mathcal{U}_v^{<t-1>} \cup \{\mu\}$ . According to (34), the estimated payoff of user  $\mu$  if connected to LiFi AP  $v$  can be obtained as:

$$\hat{\pi}_{\mu,v}^{<t>} = \sum_{m \in \mathcal{M}_v} k_{\mu,m} r_{\mu,m}, \quad \mu \in \mathcal{U}_v^{<t>}, v = A_\mu, \quad (40)$$



where  $k_{\mu,m}$  is the estimated number of RUs that is allocated to user  $\mu$  on subcarrier  $m$  of each RB, which can be calculated according to Algorithm 1.

ii). *WiFi network* ( $v = W$ ): It is assumed that the number of users served by the WiFi AP at the  $(t-1)$ -th iteration is denoted by  $N_w^{<t-1>}$ . In the case of  $v = W$ , user  $\mu$  would experience handover from a LiFi AP to the WiFi AP. According to (18), the estimated payoff of user  $\mu$  is expressed as:

$$\hat{\pi}_{\mu,v}^{<t>} = \frac{R_c U_{\text{down}}}{N_w^{<t-1>} + 1}, \quad v = W, \quad (41)$$

where  $R_c$  is the channel bit rate in the WiFi system; and  $U_{\text{down}}$  is the downlink utilization efficiency which is given in (10). Note that  $U_{\text{down}}$  should be computed based on  $N_w^{<t>} = N_w^{<t-1>} + 1$ .

The proposed EGT-based LB algorithm can be summarized into three steps: i) in the AP assignment step, each user adapts their AP selection strategy unilaterally to improve the payoff; 2) in the RA step, based on the RA schemes, e.g. OFDMA or CSMA, the available resources are allocated to users; 3) repeat step 1 and 2 until no user can adjust the AP selection unilaterally to increase their payoff. The EGT-based LB algorithm is given in Algorithm 2.

### C. Convergence Analysis of Proposed Scheme

The EGT-based LB scheme can converge after several iterations, which has been proved in [17]. Typically, when a convergence is reached, an evolutionary equilibrium (EE), referred to as the Nash Equilibrium in the evolutionary game [16], can be achieved.

*Definition 1:* A strategy profile  $\mathcal{E} = \{\alpha_\mu | \mu \in \mathcal{U}\}$  reaches an EE when no user can change the strategy unilaterally to improve their payoff, i.e. [16]:

$$\pi_{\mu,\alpha_\mu} \geq \pi_{\mu,\alpha'_\mu}, \quad \alpha_\mu \neq \alpha'_\mu, \quad \alpha_\mu, \alpha'_\mu \in \mathcal{S}_\mu, \quad (42)$$

where the payoff of the user  $\mu$  connected to the AP  $\alpha$  is denoted as  $\pi_{\mu,\alpha}$ .

In this section, the numerical simulation is used to evaluate the iteration numbers required in the proposed LB scheme. The simulation setup is described in Section IV and simulation parameters are listed in Table II. The users are moving randomly in an indoor scenario for 1000 quasi-static states. In each state, the EGT-based LB scheme is executed to find the EE, which provides the AP assignment and resource allocation results. At the first state, users randomly choose an AP from their strategy sets as an initial host AP. After the first state, the allocated APs in the previous state are considered as the initialization of host APs. The iteration number of the proposed EGT-based LB scheme is evaluated and shown in Fig. 3. In the legend, 'PF' represents proportional fairness ( $\beta = 1$ ) while 'MF' means max-min fairness ( $\beta \rightarrow +\infty$ ). It can be seen that in order to achieve an EE, 7 iterations are needed at the first state while only 4-5 iterations are required from state 2 to state 1000. This means that when considering a dynamic network, the proposed EGT-based LB scheme achieves a quick convergence by using an average of less than 5 iterations.

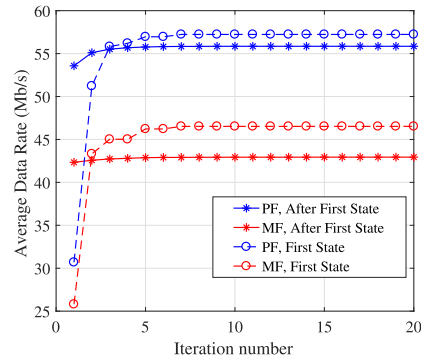


Fig. 3. Average user data rate versus the iteration number.

TABLE II  
SIMULATION PARAMETERS

Name of Parameters	Symbol	Value
Height of the AP	$z_{\text{AP}}$	3.5 m
Height of the user device	$z_{\text{UE}}$	1.5 m
Optical transmit power in LiFi system	$P_{\text{tx}}$	9 W
Noise power spectral density of LiFi	$N_0$	$10^{-19}$ A <sup>2</sup> /Hz
The physical area of a PD	$A_p$	1 cm <sup>2</sup>
Half-intensity radiation angle	$\Phi_{1/2}$	60 deg.
Half angle of the receiver FOV	$\Psi_c$	90 deg.
Gain of optical filter	$T_c(\psi)$	1.0
Refractive index	$n_{\text{ref}}$	1.5
Optical to electric conversion efficiency	$\tau$	0.53 A/W
Maximum backoff stage	$C_{\text{max}}$	1024
Time duration of RTS	$t_{\text{RTS}}$	0.16 $\mu$ s
Time duration of CTS	$t_{\text{CTS}}$	0.14 $\mu$ s
Time duration of frame header	$t_{\text{H}}$	0.23 $\mu$ s
Time duration of ACK	$t_{\text{ACK}}$	0.14 $\mu$ s
Time duration of SIFS	$t_{\text{SIFS}}$	28 $\mu$ s
Time duration of DIFS	$t_{\text{DIFS}}$	80 $\mu$ s
Time duration of PIFS	$t_{\text{PIFS}}$	128 $\mu$ s
Propagation delay	$t_p$	1 $\mu$ s
Channel bit rate in the WiFi system	$R_c$	1.732 Gbit/s
Average user movement speed	$v_s$	1 m/s

## IV. PERFORMANCE EVALUATION

### A. Simulation Setups

As shown in Fig. 1(a), a 16 m  $\times$  16 m indoor office scenario is considered for numerical simulation. The network consists of 16 LiFi APs which are deployed following a square topology over the ceiling. A WiFi AP is located at the centre of the room to provide ubiquitous wireless coverage. The users are initially distributed uniformly in the  $XY$ -plane of the room and they hold a device in their hands. In our simulations, the users move randomly following an ORWP model described in Section II-E to realize a real-life scenario. We use (22) to calculate the  $k$ -th sample of AR(1). The mean and variance of the RP,  $\theta$ , are  $\mathbb{E}[\theta] = 30^\circ$  and  $\sigma_\theta = 7.78^\circ$ , which are

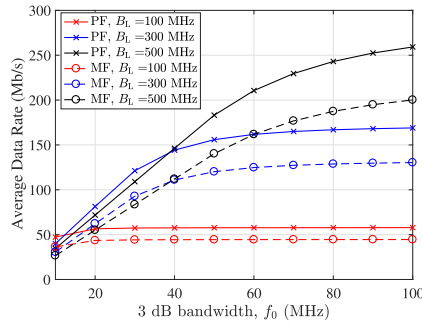


Fig. 4. Evaluation of average data rate with different 3 dB bandwidth in LiFi OFDMA network. A comparison between proportional fairness (PF) and max-min fairness (MF). ( $N_{UE} = 80$ , 16 LiFi AP and no WiFi AP considered).

compatible with the experimental measurements. Moreover, the sampling time and the coherence time of  $\theta$  are  $T_s = 13$  ms and  $T_{c,\theta} = 130$  ms [23]. The  $k$ -th sample of  $\theta$  along with  $\omega$  can be used in (3) to calculate the normal vector at the receiver. Note that we used  $\omega = \Omega - \pi$  similar to [23], where  $\Omega$  defines the movement direction of users.

To evaluate user fairness, the fairness index,  $I$ , will be used as the metric which can be expressed as [8]:

$$I = \frac{(\sum_{i=1}^{N_{UE}} x_i)^2}{N_{UE} \sum_{i=1}^{N_{UE}} x_i^2}. \quad (43)$$

where  $x_i$  is the achievable data rate of user  $i$ . The fairness index ranges from 0 to 1, where 1 means all users achieve the same data rate. The parameters in the simulation are summarized in Table II. Each simulation contains 1000 quasi-static states. The results shown in the following plots are averaged over 1000 independent tests.

#### B. Performance Analysis

In this section, the data rate performance of OFDMA and TDMA RA schemes in LiFi systems is first evaluated. Following that, the hybrid LiFi/WiFi network is considered and the evaluation of the proposed EGT-based LB scheme on both user data rate and fairness is undertaken. Finally, the impact of the average handover efficiency and user speed on the system throughput is analyzed.

1) *OFDMA vs. TDMA*: Initially, a stand-alone LiFi OFDMA network with 16 LiFi APs is considered. In LiFi, due to low pass effect of front-end elements, the available channel bandwidth depends on the actual devices. Therefore, the impact of cutoff frequency is studied. Fig. 4 presents the average user data rate achieved by the proposed low complexity OFDMA RA scheme versus the 3 dB bandwidth,  $f_0$ . It can be seen that the user data rate increases with  $f_0$ , but the gradient decreases. This is because when 3 dB bandwidth is large enough and the modulation bandwidth is fixed, the LiFi channel gain tends to be flat and the achievable data rate is

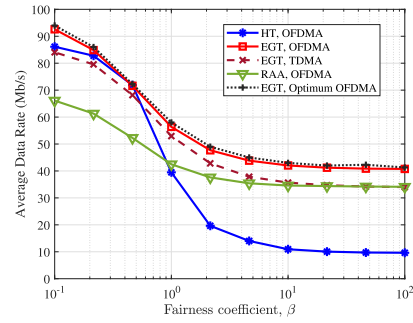


Fig. 5. Evaluation of average data rate by using different LB (resource allocation) schemes in HLWNs. ( $B_L = 300$  MHz,  $f_0 = 30$  MHz,  $\epsilon = 2$ ,  $\eta_{0,HFO} = 0.9$ ,  $\eta_{0,VHO} = 0.6$  and  $N_{UE} = 200$ ).

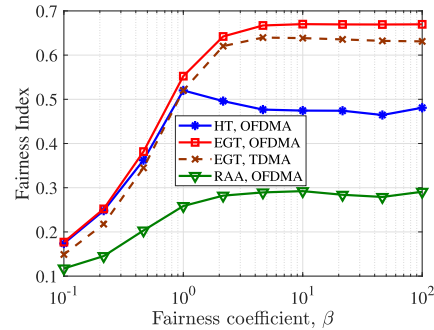


Fig. 6. Evaluation of user fairness by using different LB (resource allocation) schemes in HLWNs. ( $B_L = 300$  MHz,  $f_0 = 30$  MHz,  $\epsilon = 2$ ,  $\eta_{0,HFO} = 0.9$ ,  $\eta_{0,VHO} = 0.6$  and  $N_{UE} = 200$ ).

maximized. In addition, Fig. 4 shows that 'PF' can achieve a better data rate performance than 'MF' due to the sacrifice of user fairness. The gap between these two curves increases along with the modulation bandwidth  $B_L$ . For the typical 3 dB bandwidth of 30 MHz, the data rate differences between 'PF' and 'MF' are 9.6, 41.2, 57.7 Mb/s, respectively when  $B_L$  equals to 100, 300 and 500 MHz.

Considering a hybrid LiFi/WiFi network, the data rate performance by using an EGT-based LB scheme is presented in Fig. 5, where OFDMA and TDMA RA methods are used in the LiFi network, respectively. In the TDMA RA scheme, resources are partitioned only in the time domain [17]. The user fairness is evaluated and shown in Fig. 6, where the fairness index is used as the criteria. As shown in Figs. 5 and 6, when using the proposed EGT-based LB scheme, the OFDMA RA method outperforms the TDMA RA method in terms of both user data rate and fairness index. This is because the OFDMA scheme can utilize the high-frequency RUs more

efficiently than the TDMA RA method. As shown in (4), the LiFi channel response in the frequency domain is inversely proportional to the frequency. This means that users with high SINRs are able to use a large modulation bandwidth, while the users with low SINRs may not be able to transmit signals on high-frequency subcarriers. The OFDMA RA scheme is able to carefully allocate high-frequency RUs to users with high SINRs while allocate low-frequency RUs to users with low SINRs. In this way, the overall user data rate can be enhanced in LiFi systems.

2) *EGT vs. Benchmark LB Schemes*: In Figs. 5 and 6, two benchmark LB algorithms for HLWNs are evaluated and compared with the proposed EGT-based LB scheme. Specifically, ‘HT’ represents that the AP assignment of users is determined by a hard threshold while ‘RAA’ means that each user randomly chooses the host AP from their strategy set  $S_u$  [17]. The handover efficiency is considered in the AP selection in the benchmark algorithms. After the AP allocation, the proposed OFDMA resource allocation scheme is used in both ‘HT’ and ‘RAA’ schemes. It can be seen that the EGT-based LB scheme achieves a better performance in terms of user data rate and fairness index. Particularly, the achievable data rate by EGT is notably 20 Mb/s and 30 Mb/s more than RAA and HT, respectively. Regarding the fairness index, the EGT-based LB scheme has a significant improvement compared to the two benchmark schemes. This is because in the EGT scheme, there is a high probability that users with low payoff will switch to better APs, which makes the network well load-balanced. It can be seen from Fig. 6 that the proposed low-complexity OFDMA scheme achieve data-rate performance closed to the optimum scheme. Another interesting observation of Fig. 6 is with regard to the HT with OFDMA in the downlink. As can be seen, the fairness index increases initially with the increase of  $\beta$  due to the fairness among LiFi users increase. However, after  $\beta > 1$ , it starts to decrease. The reason for this is when the HT is applied, the number of users connected to the WiFi AP will increase as the increase of  $\beta$ , which leads to a degradation in the throughput of WiFi users. On the other hand, the LiFi users benefit from more released resources and their data rate increases. Therefore, the load between WiFi and LiFi is not well balanced which leads to a slight decrease in the fairness index.

3) *WiFi Utilization*: In Fig. 7, the effect of the WiFi utilization ratio,  $\epsilon$ , on the user data rate is evaluated. As shown in (9),  $\epsilon = 1$  means that the uplink and downlink have the same probability to access the WiFi channel. When  $\epsilon$  is large enough (e.g.  $\epsilon = 20$ ), the downlink can utilize more than 95% of the WiFi resources. As shown in Fig. 7, by decreasing  $\epsilon$  from 20 to 1, the average user data rate will reduce approximately 50% from 40 Mb/s to 20 Mb/s. In comparison, users in HLWNs only have a 8% decrease in the achievable data rate. This is because, in HLWNs, some of the users in WiFi can be transferred to LiFi layers when WiFi provides less resources for downlink. It should be noted that in the simulation, it is assumed that HLWN has 200 users while the stand-alone WiFi network has only 40 users. Although the HLWN has 5 times users, when proposed EGT method is applied, the users

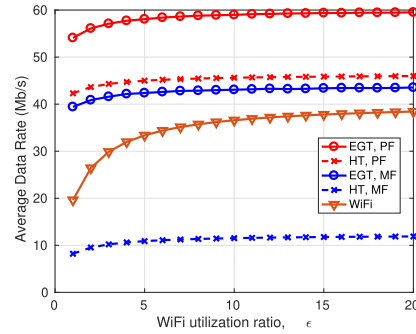


Fig. 7. Evaluation of the effects of WiFi utilization ratio on the user data rate in HLWNs ( $B_L = 300$  MHz,  $f_0 = 30$  MHz,  $\eta_{0,HHO} = 0.9$ ,  $\eta_{0,VHO} = 0.6$  and  $N_{UE} = 200$ ) and a stand-alone WiFi network ( $N_{UE} = 40$ ).

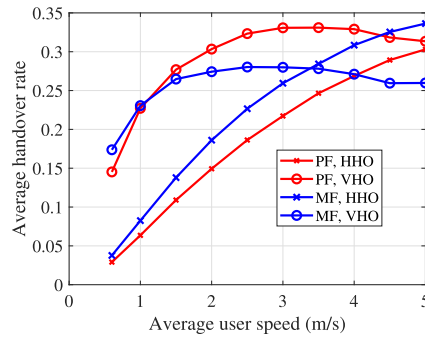


Fig. 8. Evaluation of average handover rate corresponding to user speed. (The EGT-based LB scheme is applied,  $B_L = 300$  MHz,  $f_0 = 30$  MHz,  $\epsilon = 2$ ,  $\eta_{0,HHO} = 0.9$ ,  $\eta_{0,VHO} = 0.6$  and  $N_{UE} = 200$ ).

can still achieve much higher data rate than users in the stand-alone WiFi network for all  $\epsilon$ . Hence, the HLWNs can maintain a good downlink performance regardless of the WiFi utilization ratio. Also, it can be seen in Fig. 7 that the proposed EGT-based LB scheme can always achieve a higher user data rate than the HT scheme regardless of the WiFi utilization ratio.

4) *User Speed*: The effect of user speed on the handover rate is evaluated and presented in Fig. 8. Handover rate is defined as the ratio of the total number of handovers and the total simulation time. It appears that when the user speed is less than 3 m/s, the handover rate of VHO is higher than the handover rate of HHO and they both increase along with user speed. If the user speed is greater than 3 m/s, the handover rate of HHO still increases with user velocity while the VHO performs oppositely. This can be explained as follows. Due to the ICI in LiFi systems, when a user moves from one cell

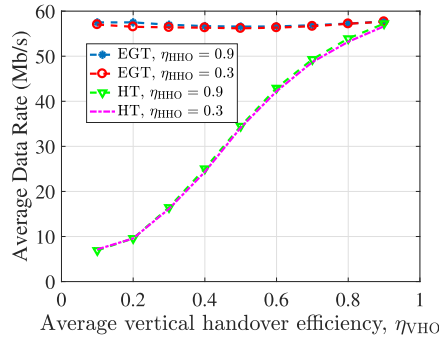


Fig. 9. Evaluation of the effects of  $\eta_{HHO}$  and  $\eta_{VHO}$  on the user data rate. ( $B_L = 300$  MHz,  $f_0 = 30$  MHz,  $\epsilon = 2$  and  $N_{UE} = 200$ ).

centre to another cell centre, the SINR will first decrease and then increase. In this case, for low speeds, the LiFi-connected user will be handed off to WiFi when approaching the cell edge, then, they will connect to another LiFi AP when entering the cell-centre region. Accordingly, the number of VHO is higher than the HHO. For high speeds, the users may pass the cell-edge regions quickly without being connected to the WiFi AP. Therefore, the number of VHO decreases while the number of HHO still increases.

It can be seen that by using the proposed EGT scheme, the number of handovers in the fast movement case (e.g. 4 m/s) is still more than twice that in the low movement case (e.g. 1 m/s). Work is ongoing to try and reduce the number of VHO and achieve a high throughput for high-speed users in HLWNs.

5) *Average Handover Efficiency*: In Fig. 9, the impact of the average horizontal and vertical handover efficiency,  $\eta_{HHO}$  and  $\eta_{VHO}$ , on the user data rate are evaluated. It can be seen that with an increase in  $\eta_{VHO}$ , the user data rate achieved by EGT is almost constant. However, the user data rate achieved by HT significantly increases with an increase in  $\eta_{VHO}$ . This is because a hard threshold,  $T$ , is used for AP assignment in the HT scheme and the vertical handover from a LiFi AP to a WiFi AP will only occur when  $\eta_{VHO} \times D_{\mu, A_{\mu}} < T$  and vice versa. Hence, for a low  $\eta_{VHO}$ , it is more likely for the user to switch from a LiFi AP to the WiFi AP and less likely to switch back. Therefore, when considering a low value for  $\eta_{VHO}$ , the majority of users in the HT scheme are served by WiFi. In comparison, in the EGT-based LB scheme, the AP allocation is determined based on the achievable data rate in both WiFi and LiFi cells. If the WiFi cell is overloaded, the user data rate achieved by WiFi is low. This may result in users transferring from the WiFi layer to the LiFi layer despite a high vertical handover overhead. In this case, users will be assigned to the LiFi or WiFi APs in a more balanced way. Thus, it can be concluded that the proposed EGT-based LB scheme can achieve a better user data rate than the HT scheme when the average vertical handover efficiency,  $\eta_{VHO}$ , is low.

It should also be noted that for both EGT and HT schemes, increasing the average horizontal handover efficiency,  $\eta_{HHO}$ , from 0.3 to 0.9 only increases the average data rate slightly. Hence,  $\eta_{HHO}$  has little impact on the system performance. This can be explained by two factors. First, with an average user speed of 1 m/s, the average horizontal handover rate is very small as shown in Fig. 8. This means the likelihood of horizontal handover is low. Second, considering  $\eta_{HHO}$  in (35) has little effect on the best LiFi AP selection. As a result, in a system suffering ICI, only the AP with the best received signal strength can provide efficient data to the UE. If a UE is assigned to APs other than the one that provides the best signal strength, then the signal from the AP providing the best signal strength will become interference. This will cause the signal power to be less than the interference power and the SINR to be less than 0 dB, which does not yield high data rates.

## V. CONCLUSION

In this study, a hybrid LiFi/WiFi network with user movement and a random orientation angle at LiFi receivers is considered. A low complexity OFDMA RA scheme for LiFi systems and an EGT scheme for LB considering the handover effect in HLWNs are proposed. Four conclusions are drawn based on the simulation results: (i). The proposed RA scheme for LiFi OFDMA systems outperforms that in TDMA systems in terms of both data rate and user fairness because of an efficient use of high-frequency resources. (ii). For both PF and MF schemes, the proposed EGT-based LB scheme can achieve a better data rate and fairness performance than benchmark LB schemes (HT & RAA). (iii) The HLWNs can maintain a good downlink performance regardless of the uplink requirements in WiFi. (iv). The average horizontal handover efficiency has little impact on the system performance while the average vertical handover efficiency affect the system performance greatly. In the case of a low average vertical handover efficiency, the EGT-based LB scheme achieves a better user data rate than the HT scheme by balancing the user load between LiFi and WiFi more efficiently.

## REFERENCES

- [1] Cisco. (Mar. 2017). *Cisco Visual Networking Index: Global Mobile Data Traffic Forecast Update, 2016–2021 White Paper*. [Online]. Available: <https://Cisco.com>
- [2] T. Cogalan and H. Haas, "Why would 5G need optical wireless communications?" in *Proc. IEEE 28th Annu. Int. Symp. Pers., Indoor, Mobile Radio Commun. (PIMRC)*, Oct. 2017, pp. 1–6.
- [3] H. Haas, L. Yin, Y. Wang, and C. Chen, "What is LiFi?" *J. Lightw. Technol.*, vol. 34, no. 6, pp. 1533–1544, Mar. 15, 2016.
- [4] W. Wu, Q. Shen, M. Wang, and X. Shen, "Performance analysis of IEEE 802.11ad downlink hybrid beamforming," in *Proc. IEEE Int. Conf. Commun. (ICC)*, May 2017, pp. 1–6.
- [5] M. S. Islim *et al.*, "Towards 10 Gb/s orthogonal frequency division multiplexing-based visible light communication using a GaN violet micro-LED," *Photon. Res.*, vol. 5, no. 2, pp. A35–A43, Apr. 2017.
- [6] D. Tsonev, S. Videv, and H. Haas, "Towards a 100 Gb/s visible light wireless access network," *Opt. Express*, vol. 23, no. 2, pp. 1627–1637, Jan. 2015.
- [7] Y. Wang, X. Wu, and H. Haas, "Distributed load balancing for Internet of Things by using Li-Fi and RF hybrid network," in *Proc. IEEE 26th Annu. Int. Symp. Pers., Indoor, Mobile Radio Commun. (PIMRC)*, HongKong, Aug. 2015, pp. 1289–1294.

- [8] Y. Wang and H. Haas, "Dynamic load balancing with handover in hybrid Li-Fi and Wi-Fi networks," *J. Lightw. Technol.*, vol. 33, no. 22, pp. 4671–4682, Nov. 15, 2015.
- [9] M. B. Rahaim, A. M. Vegni, and T. D. C. Little, "A hybrid radio frequency and broadcast visible light communication system," in *Proc. IEEE GLOBECOM Workshops (GC Wkshps)*, Dec. 2011, pp. 792–796.
- [10] S. Shao et al., "An indoor hybrid Wi-Fi-VLC Internet access system," in *Proc. IEEE 11th Int. Conf. Mobile Ad Hoc Sensor Syst.*, Oct. 2014, pp. 569–574.
- [11] X. Li, R. Zhang, and L. Hanzo, "Cooperative load balancing in hybrid visible light communications and WiFi," *IEEE Trans. Commun.*, vol. 63, no. 4, pp. 1319–1329, Apr. 2015.
- [12] F. Jin, R. Zhang, and L. Hanzo, "Resource allocation under delay-guarantee constraints for heterogeneous visible-light and RF femto-cell," *IEEE Trans. Wireless Commun.*, vol. 14, no. 2, pp. 1020–1034, Feb. 2015.
- [13] D. A. Basnayaka and H. Haas, "Hybrid RF and VLC systems: Improving user data rate performance of VLC systems," in *Proc. IEEE 81st Veh. Technol. Conf. (VTC Spring)*, Glasgow, U.K., May 2015, pp. 1–5.
- [14] M. Dehghani Soltani, A. A. Purwita, I. Tavakkolnia, H. Haas, and M. Safari, "Impact of device orientation on error performance of LiFi systems," *IEEE Access*, vol. 7, pp. 41690–41701, 2019.
- [15] M. Bennis, S. Guruacharya, and D. Niyato, "Distributed learning strategies for interference mitigation in femtocell networks," in *Proc. IEEE Global Telecommun. Conf. (GLOBECOM)*, Houston, TX, USA, Dec. 2011, pp. 1–5.
- [16] P. Semasinghe, E. Hossain, and K. Zhu, "An evolutionary game for distributed resource allocation in self-organizing small cells," *IEEE Trans. Mobile Comput.*, vol. 14, no. 2, pp. 274–287, Feb. 2015.
- [17] Y. Wang, X. Wu, and H. Haas, "Load balancing game with shadowing effect for indoor hybrid LiFi/RF networks," *IEEE Trans. Wireless Commun.*, vol. 16, no. 4, pp. 2366–2378, Apr. 2017.
- [18] X. Wu, M. Safari, and H. Haas, "Joint optimisation of load balancing and handover for hybrid LiFi and WiFi networks," in *Proc. IEEE Wireless Commun. Netw. Conf. (WCNC)*, Mar. 2017, pp. 1–5.
- [19] S. Sesia, I. Toufik, and M. Baker, *LTE—The UMTS Long Term Evolution: From Theory to Practice*. Hoboken, NJ, USA: Wiley, 2009.
- [20] F. Seguel, I. Soto, D. Iturralde, P. Adamne, and B. Nunez, "Enhancement of the QoS in an OFDMA/VLC system," in *Proc. 10th Int. Symp. Commun. Syst., Netw. Digit. Signal Process. (CSNDSP)*, Jul. 2016, pp. 1–5.
- [21] J. Fakidis, D. Tsonev, and H. Haas, "A comparison between DCO-OFDM and synchronous one-dimensional OCDMA for optical wireless communications," in *Proc. IEEE 24th Annu. Int. Symp. Pers., Indoor, Mobile Radio Commun. (PIMRC)*, Sep. 2013, pp. 3605–3609.
- [22] Z. Zeng, M. D. Soltani, H. Haas, and M. Safari, "Orientation model of mobile device for indoor VLC and millimetre wave systems," in *Proc. IEEE Veh. Technol. Conf. (VTC Fall)*, Chicago, IL, USA, Aug. 2018, pp. 1–6.
- [23] M. D. Soltani, A. A. Purwita, Z. Zeng, H. Haas, and M. Safari, "Modeling the random orientation of mobile devices: Measurement, analysis and LiFi use case," *IEEE Trans. Commun.*, vol. 67, no. 3, pp. 2157–2172, Mar. 2019.
- [24] G. Cossu, R. Corsini, and E. Ciaramella, "High-speed bi-directional optical wireless system in non-directed line-of-sight configuration," *J. Lightw. Technol.*, vol. 32, no. 10, pp. 2035–2040, May 15, 2014. [Online]. Available: <http://jlt.osa.org/abstract.cfm?URI=jlt-32-10-2035>
- [25] C. Chen, R. Bian, and H. Haas, "Omnidirectional transmitter and receiver design for wireless infrared uplink transmission in LiFi," in *Proc. IEEE Int. Conf. Commun. Workshops (ICC Workshops)*, May 2018, pp. 1–6.
- [26] G. Bianchi, "Performance analysis of the IEEE 802.11 distributed coordination function," *IEEE J. Sel. Areas Commun.*, vol. 18, no. 3, pp. 535–547, Mar. 2000.
- [27] M. A. Dastgheib, H. Beyranvand, J. A. Salehi, and M. Maier, "Mobility-aware resource allocation in VLC networks using T-step look-ahead policy," *J. Lightw. Technol.*, vol. 36, no. 23, pp. 5358–5370, Dec. 1, 2018.
- [28] L. Li, Y. Zhang, B. Fan, and H. Tian, "Mobility-aware load balancing scheme in hybrid VLC-LTE networks," *IEEE Commun. Lett.*, vol. 20, no. 11, pp. 2276–2279, Nov. 2016.
- [29] R. Wang, J. Zhang, S. H. Song, and K. B. Letaief, "Mobility-aware caching in D2D networks," *IEEE Trans. Wireless Commun.*, vol. 16, no. 8, pp. 5001–5015, Aug. 2017.
- [30] M. Dehghani Soltani, X. Wu, M. Safari, and H. Haas, "Bidirectional user throughput maximization based on feedback reduction in LiFi networks," *IEEE Trans. Commun.*, vol. 66, no. 7, pp. 3172–3186, Jul. 2018.
- [31] L. Wu, Z. Zhang, J. Dang, and H. Liu, "Adaptive modulation schemes for visible light communications," *J. Lightw. Technol.*, vol. 33, no. 1, pp. 117–125, Jan. 1, 2015.
- [32] J. Kahn and J. Barry, "Wireless infrared communications," *Proc. IEEE*, vol. 85, no. 2, pp. 265–298, Feb. 1997.
- [33] A. A. Purwita, M. D. Soltani, M. Safari, and H. Haas, "Terminal orientation in OFDM-based LiFi systems," *IEEE Trans. Wireless Commun.*, vol. 18, no. 8, pp. 4003–4016, Aug. 2019.
- [34] A. M. Khalid, G. Cossu, R. Corsini, P. Choudhury, and E. Ciaramella, "1-Gb/s transmission over a phosphorescent white LED by using rate-adaptive discrete multitone modulation," *IEEE Photon. J.*, vol. 4, no. 5, pp. 1465–1473, Oct. 2012.
- [35] Y. Wang, X. Wu, and H. Haas, "Resource allocation in LiFi OFDMA systems," in *Proc. IEEE Global Commun. Conf. (GLOBECOM)*, Dec. 2017, pp. 1–6.
- [36] C. Chen, D. A. Basnayaka, and H. Haas, "Downlink performance of optical attocell networks," *J. Lightw. Technol.*, vol. 34, no. 1, pp. 137–156, Jan. 1, 2016.
- [37] H. Elgala and T. D. C. Little, "SEE-OFDM: Spectral and energy efficient OFDM for optical IM/DD systems," in *Proc. IEEE 25th Annu. Int. Symp. Pers., Indoor, Mobile Radio Commun. (PIMRC)*, Sep. 2014, pp. 851–855.
- [38] D. Tsonev, S. Videv, and H. Haas, "Unlocking spectral efficiency in intensity modulation and direct detection systems," *IEEE J. Sel. Areas Commun.*, vol. 33, no. 9, pp. 1758–1770, Sep. 2015.
- [39] S. Dimitrov and H. Haas, *Principles of LED Light Communications: Towards Networked LiFi*. Cambridge, U.K.: Cambridge Univ. Press, Mar. 2015.
- [40] H. Burchardt, S. Sinanovic, Z. Bharucha, and H. Haas, "Distributed and autonomous resource and power allocation for wireless networks," *IEEE Trans. Commun.*, vol. 61, no. 7, pp. 2758–2771, Jul. 2013.
- [41] S. W. Kim, B.-S. Kim, and Y. Fang, "Downlink and uplink resource allocation in IEEE 802.11 wireless LANs," *IEEE Trans. Veh. Technol.*, vol. 54, no. 1, pp. 320–327, Jan. 2005.
- [42] Y. Wang, D. A. Basnayaka, X. Wu, and H. Haas, "Optimization of load balancing in hybrid LiFi/RF networks," *IEEE Trans. Commun.*, vol. 65, no. 4, pp. 1708–1720, Apr. 2017.
- [43] M. Kassab, J. M. Bonnin, and A. Belghith, "Fast and secure handover in WLANs: An evaluation of the signaling overhead," in *Proc. 5th IEEE Consum. Netw. Conf.*, Jan. 2008, pp. 770–775.
- [44] M. Dehghani Soltani, X. Wu, M. Safari, and H. Haas, "On limited feedback resource allocation for visible light communication networks," in *Proc. 2nd Int. Workshop Visible Light Commun. Syst.*, Paris, France, 2015, pp. 27–32.
- [45] D. J. Love, R. W. Heath, Jr., V. K. Lau, D. Gesbert, B. D. Rao, and M. Andrews, "An overview of limited feedback in wireless communication systems," *IEEE J. Sel. Areas Commun.*, vol. 26, no. 8, pp. 1341–1365, Oct. 2008.
- [46] M. D. Soltani et al., "Bidirectional optical spatial modulation for mobile users: Toward a practical design for LiFi systems," *IEEE J. Sel. Areas Commun.*, vol. 37, no. 9, pp. 2069–2086, Sep. 2019.
- [47] Q. Ye, B. Rong, Y. Chen, M. Al-Shalash, C. Caramanis, and J. G. Andrews, "User association for load balancing in heterogeneous cellular networks," *IEEE Trans. Wireless Commun.*, vol. 12, no. 6, pp. 2706–2716, Jun. 2013.
- [48] J. Mo and J. Walrand, "Fair end-to-end window-based congestion control," *IEEE/ACM Trans. Netw.*, vol. 8, no. 5, pp. 556–567, Oct. 2000.



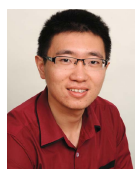
**Zhihong Zeng** (Student Member, IEEE) received the B.E. degree (Hons.) from The University of Edinburgh, U.K., in 2017, where he is currently pursuing the Ph.D. degree with the Institute for Digital Communications, funded by pureLiFi Ltd. His current research interests include co-channel interference mitigation and resource allocation in wireless cellular networks, visible light communications, and LiFi.



**Mohammad Dehghani Soltani** (Student Member, IEEE) received the M.Sc. degree from the Department of Electrical Engineering, Amirkabir University of Technology, Tehran, Iran, in 2012, and the Ph.D. degree in electrical engineering from The University of Edinburgh, Edinburgh, U.K., in 2019. During his M.Sc., he studied wireless communications, MIMO coding, and low complexity design of MIMO-OFDM systems. He worked for two years in the telecommunication industry in Iran. He is currently a Research Associate with the LiFi Research and Development Centre, The University of Edinburgh. His Ph.D. was funded by the British Engineering and Physical Sciences Research Council (EPSRC) Project TOUCAN.



**Xiping Wu** (Member, IEEE) received the Ph.D. degree from The University of Edinburgh, U.K., in 2015. From 2011 to 2014, he was a Marie-Curie Early-Stage Researcher, funded by the European Unions FP7 (Seventh Framework Program). From 2013 to 2014, he was on secondment to the Department of Electrical and Information Engineering, University of L'Aquila, Italy. From 2014 to 2018, he held a Post-Doctoral Fellowship with the LiFi Research and Development Centre, The University of Edinburgh, funded by the British Engineering and Physical Sciences Research Council (EPSRC). He is currently a Research Fellow with the University of Oxford. He has authored or coauthored more than 40 journal articles and conference papers. His main research interests are in the areas of information theory, optical wireless communications, hybrid network management, and the Internet of Things.



**Yunlu Wang** (Student Member, IEEE) received the B.Eng. degree in telecommunication engineering from the Beijing University of Post and Telecommunications, China, in 2011, the M.Sc. degree in digital communication and signal processing from The University of Edinburgh, U.K., in 2013, and the M.Sc. degree in electronic and electrical engineering from Beihang University, China, in 2014. He is currently pursuing the Ph.D. degree in electrical engineering with The University of Edinburgh. His research focus is on visible light communication and radio frequency and hybrid networking.



**Harald Haas** (Fellow, IEEE) received the Ph.D. degree from The University of Edinburgh in 2001. He is currently the Chair of mobile communications with The University of Edinburgh, the Initiator, the Co-Founder, and the Chief Scientific Officer of pureLiFi Ltd., and the Director of the LiFi Research and Development Centre, The University of Edinburgh. He has authored 500 conference papers and journal articles. His main research interests are in optical wireless communications, hybrid optical wireless and RF communications, spatial modulation, and interference coordination in wireless networks. He is a fellow of the Royal Academy of Engineering. He was a co-recipient of the EURASIP Best Paper Award for the *Journal on Wireless Communications and Networking* in 2015 and the Jack Neubauer Memorial Award of IEEE Vehicular Technology Society. In 2016, he received the Outstanding Achievement Award from the International Solid State Lighting Alliance. He was a co-recipient of recent best paper awards at VTC-Fall, 2013, VTC-Spring 2015, ICC 2016, ICC 2017, and ICC 2018. In 2019, he received the James Evans Avant Garde Award of IEEE Vehicular Technology Society. In 2012 and 2017, he was a recipient of the prestigious Established Career Fellowship from the Engineering and Physical Sciences Research Council (EPSRC), U.K. He is an Associate Editor of IEEE JOURNAL OF LIGHTWAVE TECHNOLOGIES. He gave two TED Global talks *Wireless Data From Every light Bulb* and *Forget Wi-Fi: Meet the New Li-Fi Internet* which together have been downloaded more than 5.5 million times. In 2014, he was selected by the EPSRC as one of ten Recognizing Inspirational Scientists and Engineers Leaders, U.K.

# Interference Mitigation using Optimized Angle Diversity Receiver in LiFi Cellular network

Zhihong Zeng, Mohammad Dehghani Soltani, Cheng Chen, Majid Safari and  
Harald Haas

## Abstract

Light-fidelity (LiFi) is an emerging technology for high-speed short-range mobile communications. Inter-cell interference (ICI) is an important issue that limits the system performance in an optical attocell network. Angle diversity receivers (ADRs) have been proposed to mitigate ICI. In this paper, the structure of pyramid receivers (PRs) and truncated pyramid receivers (TPRs) are studied. The coverage problems of PRs and TPRs are defined and investigated, and the lower bound of field of view (FOV) for each PD is given analytically. The impact of random device orientation and diffuse link signal propagation are taken into consideration. The performances of PRs and TPRs are compared and then optimized ADR structures are proposed. The performance comparison between the select best combining (SBC) and maximum ratio combining (MRC) is given under different noise levels. It is shown that SBC will outperform MRC in an interference limited system, otherwise, MRC is a preferred scheme. In addition, the double source system, where each LiFi AP consists of two sources transmitting the same information signals but with opposite polarity, is proved to outperform the single source (SS) system under certain conditions.

## I. INTRODUCTION

Due to the increasing demand for wireless data, the radio frequency (RF) spectrum has become a very limited resource. Alternative approaches are investigated to support future growth in data traffic and next-generation high-speed wireless communication systems. Techniques such as massive multiple-input multiple-output (MIMO), millimeter wave (mmWave) communications and Light-Fidelity (LiFi) are being explored. Among these technologies, LiFi is a novel bi-directional,

The authors are with the LiFi Research and Development Centre, Institute for Digital Communications, The University of Edinburgh, EH9 3JL, UK. (e-mail: {zhihong.zeng, m.dehghani, cheng.chen, majid.safari, h.haas}@ed.ac.uk).

July 21, 2021

DRAFT

IEEE Transactions on Communications



2

high-speed and fully networked wireless communication technology. A typical LiFi system uses off-the-shelf low-cost commercially available light emitting diodes (LEDs) and photodiodes (PDs) as front end devices [1]. Intensity modulation (IM) is used to encode the information in visible light communication (VLC) since the LED is an incoherent optical source. Direct detection (DD) is adopted at the receiver end. LiFi utilizes visible light as the propagation medium in the downlink for both illumination and communication purposes. It may use infrared light in the uplink in order to allow the illumination constraint of the room to be unaffected, and also to avoid interference with the visible light in the downlink [2]. The overall license-free bandwidth of visible light is more than 1000 times greater than the whole RF spectrum [2]. Also, LiFi can provide enhanced security as the light does not penetrate through opaque objects [3]. In many large indoor environments, multiple light fixtures are installed, these luminaries can act as VLC access points (APs). A network consisting of multiple VLC APs is referred to as a LiFi attocell network [2]. Given the widespread use of LED lighting, a LiFi attocell network can use the existing lighting infrastructures to offer fully networked wireless connectivity. Moreover, LiFi attocells can be regarded as an additional network layer within the existing wireless networks because there is no interference to the RF counterparts such as femtocell networks [2]. These benefits of LiFi have made it favorable for recent and future research.

By improving the spatial reuse of the spectrum resources, cellular networks can achieve a higher area spectral efficiency [4]. In comparison with RF femtocell networks, LiFi attocell networks use smaller cell sizes as the light beams from LEDs are intrinsically narrow [5]. Thus, with the densely deployed optical APs, the LiFi attocell network can achieve a better bandwidth reuse and a higher area spectral efficiency. However, similar to other cellular systems, inter-cell interference (ICI) in LiFi attocell networks limits the system performance. This is because the signal transmitted to a user will interfere with other users who are receiving signals from the same frequency resource. Particularly, cell-edge users suffer from severe ICI. Despite the dense deployment of APs, due to ICI, LiFi may not provide a uniform coverage concerning data rate. Interference coordination mechanisms have been extensively investigated for VLC systems [6]–[10]. The commonly used technique is static resource partitioning [6]. By separating any two cells that reuse the same frequency resource with a minimum reuse distance, ICI is effectively mitigated. However, there is a significant loss in spectral efficiency. A combined wavelength division and code division multiple access scheme was proposed in [7]. Although this approach enhances the system bandwidth, it requires separate filters for each color band and thus creates additional cost. In [8], the fractional

DRAFT

July 21, 2021

IEEE Transactions on Communications



frequency reuse (FFR) technique is proposed to mitigate ICI. The FFR scheme is a cost-effective approach to provide improvements both in cell-edge user performance and average spectral efficiency, but a low user-density will decrease the average spectral efficiency significantly. Joint transmission (JT) has been proven to improve signal quality for cell-edge users [9]. The downside of the JT systems is the extra signaling overhead. Moreover, the space division multiple access (SDMA) scheme using angle diversity transmitters proposed in [10] can mitigate ICI by generating concentrated beams to users at different locations.

The angle diversity reception, first proposed in [11], allows the receiver to achieve a wide field of view (FOV) and high optical gain simultaneously. An angle diversity receiver (ADR) is composed of multiple narrow-FOV PDs facing in different directions. In [12]–[19], the ADR is used to address the issue of ICI as well as frequency reuse in LiFi cellular systems, and different signal combining schemes are investigated. However, the proposed ADR structure is hard to implement and the optimum ADR design is not given. Moreover, the system is assumed to be interference limited instead of noise limited in [15], which is not always true as the ADR can mitigate most of ICI with noise being the dominated part. Recently, due to the lower channel correlation achieved from the angle diversity scheme, ADRs are introduced to improve the performance of indoor MIMO-VLC systems, and the pyramid receivers (PRs) are proposed [20]. The generalized structure of truncated pyramid receivers (TPRs) are given in [21] to reduce the signal to interference plus noise ratio (SINR) fluctuation. However, the optimum structures of the ADRs are not given and therefore the performance gain is not fully exploited. In addition, to obtain a more accurate evaluation of the system performance, the following three factors must be taken into consideration:

1) *User Device Orientation*: Most of the studies on ADRs assume that the receiving device is pointed vertically upward. However, it has been shown in our previous works that the random orientation of mobile devices can significantly affect the direct current (DC) channel gain and thus the system performance [22], [23]. Therefore, the random orientation of the user equipment (UE) needs to be considered. A random device orientation model has been proposed in [22]. This model will be applied in this study to evaluate the system more accurately.

2) *Diffuse Link Signal Propagation*: The non-line-of-sight (NLOS) link is neglected in most LiFi and VLC studies and only the line-of-sight (LOS) channel is considered [4]–[9]. In [24], it is shown that the LOS link is the dominate link and the effect of the reflected signal can be neglected. However, the UE is assumed to be positioned vertically upward, which is not realistic for mobile devices. In our study, we consider the effect of reflection when random device orientation is applied

4

and the results show that the diffuse link cannot be ignored. A microscopic frequency-domain method for the simulation of the indoor VLC channel is presented in [25]. A closed form for the transfer function that contains all reflection orders is formulated. The method can be extended to multi-spot transmission without a significant increase in the computational complexity. Therefore, in this study, we will use the frequency-domain method to simulate the impact of the diffuse link.

3) *Noise Power Spectral Density*: The noise power spectral density of the PD has a huge impact on the analyses of system performance. For different levels of noise power spectral density, the system could be noise-limited, interference-limited or noise-plus-interference limited, which could affect the choices of the signal combining schemes and the cell configurations.

The main contributions of this paper are summarized as follows:

- The coverage area of ADRs is defined to differentiate from the coverage area of APs. Analytical expressions for the coverage area of both PRs and TPRs are given.
- Based on the constraint set by the coverage area of ADRs, the lower bound of FOV of PDs on an ADR is given for the single source (SS) system. The performance of PRs and TPRs are compared, and optimized ADR structures are proposed to fully exploit the performance gain of ADRs. In addition, the joint effect of the receiver and transmitter bandwidth on the average data rate are analyzed.
- The performance comparison between the select best combining (SBC) and maximum ratio combining (MRC) are given regarding different levels of noise power spectral density. It is the first time shown that under certain circumstances, the SBC can outperform the MRC.
- The double source cell (DS) system is considered to further mitigate the NLOS interference. The lower bound of FOV of PDs on an ADR is derived and the optimized ADR structures are proposed for the DS system.
- By comparing the average SINR between the DS system and the SS system under different levels of noise power spectral density, we present that, in a noise-dominated scenario, the SS system should be applied, otherwise, the DS system is preferred.

The rest of this paper is organized as follows. The system model is introduced in Section II. The generalized structures of ADRs are given in Section III. Section IV presents the optimum FOV for PRs and TPRs. The concepts of the optical double-source cell are proposed in Section V. The simulation results and discussions are presented in Section VI. Finally, conclusions are drawn in Section VII.

DRAFT

July 21, 2021

IEEE Transactions on Communications

## II. SYSTEM MODEL

### A. Light Propagation Model

In indoor optical communications, the signal propagation consists of two components: the LOS link and the diffuse link. Therefore, the overall channel DC gain is the sum of the LOS and diffuse components:

$$H_{\text{total}} = H_{\text{LOS}} + H_{\text{diffuse}}, \quad (1)$$

where  $H_{\text{LOS}}$  represents the LOS DC channel gain between the transmitter (Tx) and receiver (Rx), and  $H_{\text{diffuse}}$  is the diffuse DC channel gain which is the superposition of all NLOS components that are caused by reflections from the surfaces of the walls.

1) *LOS link*: It is typically assumed that the LED follows the Lambertian radiation pattern[11]. The LOS DC gain is thus given by [25]:

$$H_{\text{LOS}} = \frac{(m+1)}{2\pi d^2} A_p T_s(\psi) \frac{n_{\text{ref}}^2}{\sin^2(\Psi_c)} \cos^m(\phi) \cos(\psi) v_{\text{Tx,Rx}}, \quad (2)$$

where  $m$  is the Lambertian order, which is given as  $m = -\ln(2)/\ln(\cos(\Phi_{1/2}))$ , and  $\Phi_{1/2}$  denotes the half-power semi-angle of the LED;  $d$  is the distance between the Tx and the Rx;  $A_p$  denotes the physical area of the PD;  $T_s(\psi)$  represents the signal transmission gain of the optical filter;  $n_{\text{ref}}$  represents the internal refractive index of the concentrator;  $\Psi_c$  denotes the FOV of the PD of the PD with concentrator; The irradiance angle of the transmitter is denoted as  $\phi$  and the incidence angle of the receiving PD is denoted as  $\psi$ . Note that  $\psi$  can be obtained by  $\cos(\psi) = \frac{\mathbf{n}_{\text{PD}} \cdot \mathbf{d}}{\|\mathbf{d}\|}$ , where  $\mathbf{d}$  defines the distance vector between the Tx and the Rx. The dot product is denoted as  $(\cdot)$  and  $\|\mathbf{d}\|$  denotes the Euclidean distance. Furthermore,  $\mathbf{n}_{\text{PD}}$  is the normal vector of the PD. The visibility factor is denoted as  $v_{\text{Tx,Rx}}$ , and  $v_{\text{Tx,Rx}} = 0$  if  $\phi > \pi/2$  or  $\psi > \Psi_c$  [25].

2) *NLOS link*: The diffuse link is due to the reflection from the walls. As mentioned earlier, the frequency-domain method in [25] is used to obtain the diffuse link DC channel gain. We assume that all the wall surfaces are purely diffuse Lambertian reflectors with  $m = 1$ . All of the surfaces are divided into a number of small surface elements numbered by  $k = 1, \dots, N_E$ , with areas  $A_k$  and reflective coefficients  $\rho_k$ . To calculate the diffuse link DC channel gain, the propagation of light is divided into the following three parts. The first part of the diffuse link propagation is the light path between the Tx and all the reflective surface elements of the room. The LOS DC channel gain between the Tx and the surface element  $k$  is defined as  $H_{\text{Tx},k}$ . The transmitter transfer vector,  $\mathbf{t}$ , is defined as  $\mathbf{t} = (H_{\text{Tx},1}, H_{\text{Tx},2}, \dots, H_{\text{Tx},N_E})^T$ , where  $(\cdot)^T$  defines the transpose of vectors. The second

6

part of the diffuse link is the LOS link from all the  $N_E$  surface elements to all the  $N_E$  surface elements. The LOS DC channel gain between the surface elements  $k$  and the surface element  $i$  is given as  $H_{k,i}$ . To describe the LOS links between all surfaces inside the room, the  $N_E \times N_E$  room-intrinsic transfer matrix,  $\mathbf{H}$ , is defined by its elements  $[\mathbf{H}]_{k,i} = H_{k,i}$ . In order to include the reflective coefficient  $\rho_k$  of the surface elements, the  $N_E \times N_E$  reflectivity matrix is defined as  $\mathbf{G}_\rho = \text{diag}(\rho_1, \rho_2, \dots, \rho_{N_E})$  [25]. In the third part of the diffuse link, the light propagates from all the surfaces of the room to the Rx. Similarly, we denote the LOS DC channel gain between the surface element  $k$  and the Rx as  $H_{k,Rx}$ . The LOS DC channel gain between all the reflective elements of the room and the receiver are grouped to give the receiver transfer vector  $\mathbf{r}$  which is defined by its transpose  $\mathbf{r}^T = (H_{1,Rx}, H_{2,Rx}, \dots, H_{N_E,Rx})$

3) *The total diffuse DC channel gain:* According to [25], the total diffuse DC channel gain with infinite reflection can be calculated by the matrix product:

$$H_{\text{diff}} = \mathbf{r}^T \mathbf{G}_\rho (\mathbf{I} - \mathbf{H} \mathbf{G}_\rho)^{-1} \mathbf{t}, \quad (3)$$

where  $\mathbf{I}$  denotes the unity matrix.

### B. Signal Combining Schemes for ADR

An indoor LiFi network is studied and it is assumed that the total number of UE and LiFi APs are  $N_{UE}$  and  $N_L$ , respectively. The set of APs is denoted by  $\mathcal{A} = \{a \mid a \in [1, N_L]\}$ . The set of users is denoted as  $\mathcal{U} = \{\mu \mid \mu \in [1, N_{UE}]\}$ . The ADR is used as the Rx and the set of PDs on an ADR is denoted as  $\mathcal{P} = \{p \mid p \in [1, N_{PD}]\}$ , where  $N_{PD}$  denotes the total number of PDs on the ADR. In order to achieve high data rates, the direct current biased optical (DCO)-OFDM is used in this study. The number of OFDM subcarriers is denoted as  $M$ , where  $M$  is an even and positive integer, and the sequence number of OFDM subcarriers is denoted by  $m \in \{0, 1, \dots, M-1\}$ . Two constraints should be satisfied to ensure real and positive signals: i)  $X(0) = X(M/2) = 0$ , and ii) the Hermitian symmetry constraint, i.e.,  $X(m) = X^*(M-m)$ , for  $m \neq 0$ , where  $(\cdot)^*$  denotes the complex conjugate operator [26]. Therefore, the effective subcarrier set bearing information data is defined as  $\mathcal{M}_e = \{m \mid m \in [1, M/2-1], m \in \mathbb{N}\}$ , where  $\mathbb{N}$  is the set of natural numbers.

For an ADR, multiple PDs are receiving signals simultaneously. Thus, attention should be paid to the selection of the signal combining schemes. There are different combining schemes such as equal gain combining (EGC), SBC and MRC. An important metric to evaluate the link quality and capacity is the SINR. The SINR of user  $\mu$  on subcarrier  $m$  can be obtained based on [15] and

[27]:

$$\gamma_{\mu,m} = \frac{(\sum_{p=1}^{N_{PD}} \tau P_{tx} w_p H_{a_s,\mu,p})^2 / (M-2)}{\sum_{p=1}^{N_{PD}} w_p^2 \kappa^2 N_0 B_L / M + \sum_{a_i \in \mathcal{A} \setminus \{a_s\}} (\tau P_{tx} \sum_{p=1}^{N_{PD}} w_p H_{a_i,\mu,p})^2 / (M-2)} \quad (4)$$

$$= \frac{(\sum_{p=1}^{N_{PD}} \tau P_{tx} w_p H_{a_s,\mu,p})^2}{\sum_{p=1}^{N_{PD}} w_p^2 \kappa^2 N_0 B_L (M-2) / M + \sum_{a_i \in \mathcal{A} \setminus \{a_s\}} (\tau P_{tx} \sum_{p=1}^{N_{PD}} w_p H_{a_i,\mu,p})^2}$$

where  $\tau$  is the optical-to-electrical conversion efficiency;  $P_{tx}$  is the transmitted optical power of the AP;  $w_p$  denotes the combining weight of PD  $p$ ;  $H_{a_s,\mu,p}$  is the overall DC channel gain between the PD  $p$  of user  $\mu$  and the serving AP  $a_s$ ;  $\kappa$  is the ratio of DC optical power to the square root of electrical signal power;  $N_0$  represents the noise power spectral density of the additive white Gaussian noise and  $B_L$  is the baseband modulation bandwidth;  $H_{a_i,\mu,p}$  is the overall DC channel gain between the PD  $p$  of user  $\mu$  and the interfering LiFi AP  $a_i$ . The serving AP  $a_s$  for user  $\mu$  is selected based on the signal strength strategy (SSS) where the UEs are connected to the APs providing the best received signal strength. Hence, the serving AP  $a_s$  for user  $\mu$  can be expressed as:

$$a_s = \arg \max_{a \in \mathcal{A}} \sum_{p=1}^{N_{PD}} |H_{a,\mu,p}|^2. \quad (5)$$

When the EGC scheme is adopted, the signals received by the PDs are simply combined with equal weights, which can be described as:

$$w_p = 1, \text{ for any } p \in \mathcal{P}. \quad (6)$$

In terms of the SBC scheme, a switch circuit is required to output the information from the PD with the highest SINR. Hence, the weight of each PD is given as:

$$w_p = \begin{cases} 1, & p = p_s \\ 0, & \text{otherwise} \end{cases}, \quad (7)$$

where  $p_s$  can be obtained by:

$$p_s = \arg \max_{p \in \mathcal{P}} \frac{(\tau P_{tx} H_{a_s,\mu,p})^2}{\kappa^2 N_0 B_L (M-2) / M + \sum_{a_i \in \mathcal{A} \setminus \{a_s\}} (\tau P_{tx} H_{a_i,\mu,p})^2}. \quad (8)$$

On the subject of the MRC schemes, the weight for each PD is denoted as [15]:

$$w_p = \frac{(\tau P_{tx} H_{a_s,\mu,p})^2}{\kappa^2 N_0 B_L (M-2) / M + \sum_{a_i \in \mathcal{A} \setminus \{a_s\}} (\tau P_{tx} H_{a_i,\mu,p})^2}. \quad (9)$$

8

Based on the Shannon capacity, assuming electrical signals after optical to electrical conversion, the data rate of the  $\mu$ -th UE on subcarrier  $m$  can be expressed as [28]:

$$\zeta_{\mu,m} = \begin{cases} \frac{B_L}{M} \log_2(1 + \gamma_{\mu,m}), & m \in [1, M/2 - 1] \\ 0, & \text{otherwise} \end{cases} \quad (10)$$

Hence, the data rate of the  $\mu$ -th UE can be obtained by  $\zeta_\mu = \sum_{m=1}^{M/2-1} \zeta_{\mu,m}$ .

### III. ADR STRUCTURE

The ADR is composed of multiple PDs facing in different directions. By using a PD in conjunction with a compound parabolic concentrator (CPC), a narrow FOV and high optical gain can be achieved [11]. However, the narrow FOV is achieved at the expense of the longer length of the CPC. Therefore, the number of PDs on the ADR should be limited due to the size limitation on the mobile devices and smartphones. In this study, the TPR [21] and the PR [20] are considered as they are both suitable for hand-held devices. The number of PDs on the TPR and PR are separately denoted as  $N_{\text{TPR}}$  and  $N_{\text{PR}}$ . The structure of the TPR with  $N_{\text{TPR}} = 9$  and the PR with  $N_{\text{PR}} = 8$  are presented in Fig. 1b and 1a, respectively. The ADR designs are analyzed in the following parts.

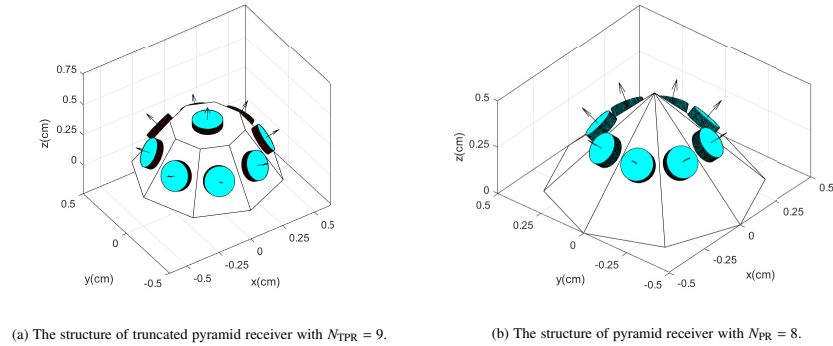


Fig. 1. ADR structures.

### A. TPR Design

The TPR is composed of a central PD and a ring of  $N_{\text{TPR}} - 1$  equally separated side PDs. Thus, the coordinate of the  $p$ -th PD on a TPR is represented as [19]:

$$(x_{\text{PD},p}, y_{\text{PD},p}, z_{\text{PD},p}) = \begin{cases} (x_{\text{UE}} + r \cos \frac{2(p-1)\pi}{N_{\text{TPR}} - 1}, y_{\text{UE}} + r \sin \frac{2(p-1)\pi}{N_{\text{TPR}} - 1}, z_{\text{UE}}), & \text{if } 1 \leq p < N_{\text{TPR}} \\ (x_{\text{UE}}, y_{\text{UE}}, z_{\text{UE}}), & \text{if } p = N_{\text{TPR}} \end{cases}, \quad (11)$$

where  $(x_{\text{UE}}, y_{\text{UE}}, z_{\text{UE}})$  is the UE position, denoted as  $\mathbf{p}_{\text{UE}}$ . As the distance between the AP and the UE is much larger than  $r$ , the distances between the AP and all PDs on a TPR are approximately the same. The normal vector of each PD can be described by two angles: the azimuth angle of a PD,  $\omega_{\text{PD}}$ , and the elevation angle of a PD,  $\theta_{\text{PD}}$  [18]. When the UE is pointing vertically upward, the TPR has one vertically orientated central PD and  $N - 1$  inclined side PDs with identical elevation angles  $\Theta_{\text{PD}}$ . In other words, the elevation angle of the  $p$ -th PD on a TPR can be expressed as:

$$\theta_{\text{PD,vert},p} = \begin{cases} \Theta_{\text{PD}}, & \text{if } 1 \leq p < N_{\text{TPR}} \\ 0, & \text{if } p = N_{\text{TPR}} \end{cases}. \quad (12)$$

The azimuth angle of the  $p$ -th PD is given by:

$$\omega_{\text{PD,vert},p} = \begin{cases} \frac{2(p-1)\pi}{N_{\text{TPR}} - 1}, & \text{if } 1 \leq p < N_{\text{TPR}} \\ 0, & \text{if } p = N_{\text{TPR}} \end{cases}. \quad (13)$$

### B. PR Design

The PR can be regarded as a TPR without the central PD. Therefore, the coordinate of the  $p$ -th PD on a PR is given by:

$$(x_{\text{PD},p}, y_{\text{PD},p}, z_{\text{PD},p}) = (x_{\text{UE}} + r \cos \frac{2(p-1)\pi}{N_{\text{PR}}}, y_{\text{UE}} + r \sin \frac{2(p-1)\pi}{N_{\text{PR}}}, z_{\text{UE}}). \quad (14)$$

When the UE is vertically orientated, the elevation angle and the azimuth angle of the  $p$ -th PD are separately expressed as:

$$\theta_{\text{PD,vert},p} = \Theta_{\text{PD}}, \quad \omega_{\text{PD,vert},p} = \frac{2(p-1)\pi}{N_{\text{PR}}}. \quad (15)$$

### C. Random Orientation Model

The orientation of a UE has a great impact on the channel DC gain according to (2). In [22], a model for the random orientation of mobile devices based on experiments is proposed so that

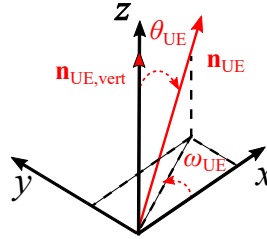


Fig. 2. Representation of random UE orientation.

the system performance of LiFi attocell networks can be evaluated more accurately. The random orientation model can be described by two angles: the elevation angle of a UE,  $\theta_{\text{UE}}$ , and the azimuth angle of a UE,  $\omega_{\text{UE}}$ . The geometrical representation of  $\theta_{\text{UE}}$  and  $\omega_{\text{UE}}$  is manifested in Fig. 2. The probability density function (PDF) of  $\theta_{\text{UE}}$  can be modeled as the truncated Laplace distribution and it can be simplified as [22]:

$$f_{\theta}(\theta_{\text{UE}}) \cong \frac{\exp(-\frac{|\theta_{\text{UE}} - \mu_{\theta}|}{b_{\theta}})}{2b_{\theta}}, \quad 0 \leq \theta \leq \frac{\pi}{2}, \quad (16)$$

where  $b_{\theta} = \sqrt{\sigma_{\theta}^2/2}$ . The mean and scale parameters are set as  $\mu_{\theta} = 41.39^{\circ}$  and  $\sigma_{\theta} = 7.68^{\circ}$  [22]. In addition, the PDF of the azimuth angle of a UE,  $\omega_{\text{UE}}$ , is modeled as a uniform distribution. It is assumed that the UE is initially pointing vertically upward and  $\mathbf{n}_{\text{UE,vert}} = [0, 0, 1]^T$ . The normal vector of the UE after rotation becomes  $\mathbf{n}_{\text{UE}}$ . The rotation can be simplified as rotating around the y-axis with  $\theta_{\text{UE}}$  and then rotating around z-axis with  $\omega_{\text{UE}}$ , which can be described by rotation matrices  $\mathbf{R}(\theta_{\text{UE}})$  and  $\mathbf{R}(\omega_{\text{UE}})$  separately [29]. Thus,  $\mathbf{n}_{\text{UE}}$  is given by:

$$\begin{aligned} \mathbf{n}_{\text{UE}} &= \mathbf{R}(\omega_{\text{UE}})\mathbf{R}(\theta_{\text{UE}})\mathbf{n}_{\text{UE,vert}} = \begin{bmatrix} \cos \omega_{\text{UE}} & -\sin \omega_{\text{UE}} & 0 \\ \sin \omega_{\text{UE}} & \cos \omega_{\text{UE}} & 0 \\ 0 & 0 & 1 \end{bmatrix} \begin{bmatrix} \cos \theta_{\text{UE}} & 0 & \sin \theta_{\text{UE}} \\ 0 & 1 & 0 \\ -\sin \theta_{\text{UE}} & 0 & \cos \theta_{\text{UE}} \end{bmatrix} \begin{bmatrix} 0 \\ 0 \\ 1 \end{bmatrix} \\ &= [\sin \theta_{\text{UE}} \cos \omega_{\text{UE}}, \sin \theta_{\text{UE}} \sin \omega_{\text{UE}}, \cos \theta_{\text{UE}}]^T \end{aligned} \quad (17)$$

#### D. Normal Vector of the ADR

When the UE is pointing vertically upward, for both PRs and TPRs, the normal vector of the  $p$ -th PD is obtained as:

$$\mathbf{n}_{\text{PD,vert},p} = [\sin(\theta_{\text{PD,vert},p}) \cos(\omega_{\text{PD,vert},p}), \sin(\theta_{\text{PD,vert},p}) \sin(\omega_{\text{PD,vert},p}), \cos(\theta_{\text{PD,vert},p})]^T. \quad (18)$$



However, the normal vector of the UE will change due to the random rotation. The random orientation model is described in Section III-C. Thus, the normal vector of the  $p$ -th PD after the random rotation is obtained by:

$$\mathbf{n}_{PD,p}(\theta_{UE}, \omega_{UE}) = \mathbf{R}(\omega_{UE})\mathbf{R}(\theta_{UE})\mathbf{n}_{PD,vert,p}$$

$$= \begin{bmatrix} C_1 \cos \omega_{UE} \cos \theta_{UE} - C_2 \sin \omega_{UE} + \sin \theta_{UE} \cos \omega_{UE} \cos(\theta_{PD,vert,p}) \\ C_1 \sin \omega_{UE} \cos \theta_{UE} + C_2 \cos \omega_{UE} + \sin \theta_{UE} \sin \omega_{UE} \cos(\theta_{PD,vert,p}) \\ -C_1 \sin \theta_{UE} + \cos \theta_{UE} \cos(\theta_{PD,vert,p}) \end{bmatrix}, \quad (19)$$

where  $C_1 = \sin(\theta_{PD,vert,p}) \cos(\omega_{PD,vert,p})$  and  $C_2 = \sin(\theta_{PD,vert,p}) \sin(\omega_{PD,vert,p})$ . Based on (19), after the random rotation, the elevation angle of the  $p$ -th PD can be obtained as:

$$\theta_{PD,p} = \cos^{-1}(-C_1 \sin \theta_{UE} + \cos \theta_{UE} \cos(\theta_{PD,vert,p})), \quad (20)$$

and the azimuth angle of the  $p$ -th PD can be expressed as:

$$\omega_{PD,p} = \tan^{-1} \left( \frac{C_1 \sin \omega_{UE} \cos \theta_{UE} + C_2 \cos \omega_{UE} + \sin \theta_{UE} \sin \omega_{UE} \cos(\theta_{PD,vert,p})}{C_1 \cos \omega_{UE} \cos \theta_{UE} - C_2 \sin \omega_{UE} + \sin \theta_{UE} \cos \omega_{UE} \cos(\theta_{PD,vert,p})} \right). \quad (21)$$

Therefore, the incidence angle of the  $p$ -th PD,  $\psi_p$ , can be obtained based on  $\theta_{PD,p}$  and  $\omega_{PD,p}$  as  $\psi_p = \cos^{-1}(\frac{\mathbf{n}_{PD} \cdot \mathbf{d}}{\|\mathbf{d}\|})$ .

#### E. Receiver Bandwidth vs PD Area

The bandwidth of a PD is affected by its physical area,  $A_p$ , and the PD thickness,  $L_p$ . The capacitance of the each PD is denoted as  $C_r = \epsilon_0 \epsilon_r \frac{A_p}{L_p}$ , where  $\epsilon_0$  and  $\epsilon_r$  are the permittivity of vacuum and the relative permittivity of silicon, respectively. The load resistance is defined as  $R_{load}$  while the hole velocity is denoted as  $v_p$ . Therefore, the receiver bandwidth can be written as [30]:

$$B_r = \frac{1}{\sqrt{(2\pi R_{load} C_r)^2 + \left(\frac{L_p}{0.443 v_p}\right)^2}}. \quad (22)$$

By solving  $\frac{\partial B_r}{\partial L_p} = 0$ , the optimum  $L_p$  can be denoted as  $L_{p,opt} = \sqrt{0.886\pi R_{load} \epsilon_0 \epsilon_r A_p v_p}$ .

#### F. Visibility of an ADR

The visibility of an ADR was first defined in [18]. An AP is visible to a PD when the AP is within the FOV of the PD. Hence, at the location  $\mathbf{p}_{UE}$  and the orientation  $(\theta_{UE}, \omega_{UE})$ , the visibility

12

factor between the  $p$ -th PD on the ADR and the  $a$ -th AP can be expressed as:

$$v_{a,p}(x_{\text{UE}}, y_{\text{UE}}, \theta_{\text{UE}}, \omega_{\text{UE}}, \Psi_c) = \begin{cases} 0, & \psi_{a,p} > \Psi_c \\ 1, & \text{otherwise} \end{cases}, \text{ and } \psi_{a,p} = \arccos\left(\frac{\mathbf{n}_{\text{PD},p}(\theta_{\text{UE}}, \omega_{\text{UE}}) \cdot \mathbf{d}_a}{\|\mathbf{d}_a\|}\right), \quad (23)$$

where  $\mathbf{d}_a = (x_a - x_{\text{UE}}, y_a - y_{\text{UE}}, z_a - z_{\text{UE}})$  is the distance vector between the AP  $a$  and the UE. The dot product is denoted as  $(\cdot)$  and  $\|\cdot\|$  is the norm operator. In terms of ADR, an AP is visible to an ADR if and only if the AP is visible to at least one of the PDs on the ADR. Hence, for a given UE position and orientation, the visibility of the ADR can be written as [18]:

$$V(x_{\text{UE}}, y_{\text{UE}}, \theta_{\text{UE}}, \omega_{\text{UE}}, \Psi_c) = \begin{cases} 1, & \text{if } \sum_{a \in \mathcal{A}} \sum_{p \in \mathcal{P}} v_{a,p} \neq 0 \\ 0, & \text{otherwise} \end{cases}. \quad (24)$$

It is assumed that both  $x_{\text{UE}}$  and  $y_{\text{UE}}$  follow a uniform distribution. The probability of visibility of an ADR is defined as the probability that there is at least one AP within the visible area of the ADR for all UE positions and orientations, and it can be expressed as follows:

$$\begin{aligned} P_v(\Psi_c) &= \int_{x_{\text{UE}}} \int_{y_{\text{UE}}} \int_{\theta_{\text{UE}}} \int_{\omega_{\text{UE}}} V(x_{\text{UE}}, y_{\text{UE}}, \theta_{\text{UE}}, \omega_{\text{UE}}, \Psi_c) \frac{1}{X_{\text{UE}}} \frac{1}{Y_{\text{UE}}} \frac{1}{\Omega_{\text{UE}}} f_{\theta}(\theta_{\text{UE}}) dx_{\text{UE}} dy_{\text{UE}} d\theta_{\text{UE}} d\omega_{\text{UE}} \\ &= \int_{x_{\text{UE}}} \int_{y_{\text{UE}}} \int_{\theta_{\text{UE}}} \int_{\omega_{\text{UE}}} \frac{V(x_{\text{UE}}, y_{\text{UE}}, \theta_{\text{UE}}, \omega_{\text{UE}}, \Psi_c)}{X_{\text{UE}} Y_{\text{UE}} \Omega_{\text{UE}}} f_{\theta}(\theta_{\text{UE}}) dx_{\text{UE}} dy_{\text{UE}} d\theta_{\text{UE}} d\omega_{\text{UE}} \end{aligned}, \quad (25)$$

where  $X_{\text{UE}}$ ,  $Y_{\text{UE}}$  and  $\Omega_{\text{UE}}$  are the range of  $x_{\text{UE}}$ ,  $y_{\text{UE}}$  and  $\omega_{\text{UE}}$ , respectively. Hence, it can be obtained that  $X_{\text{UE}} = \max(x_{\text{UE}}) - \min(x_{\text{UE}})$ ,  $Y_{\text{UE}} = \max(y_{\text{UE}}) - \min(y_{\text{UE}})$  and  $\Omega_{\text{UE}} = \max(\omega_{\text{UE}}) - \min(\omega_{\text{UE}})$ .

#### IV. THE OPTIMUM FIELD OF VIEW

##### A. Optimization Problem

In (2), the LOS channel gain  $H_{\text{LOS}}$  is a convex function of  $\Psi_c$  and decreases monotonically. Hence, the smaller the  $\Psi_c$ , the higher the channel gain. However, when the  $\Psi_c$  of the PD is too small, there is a high chance that no APs are visible to the ADR and the LOS link cannot be constructed. Thus, there is a trade off between the LOS channel gain and visibility. The optimization problem is formulated as maximizing the LOS channel gain based on the constraint that the ADR should provide visibility for all UE locations. Thus, the optimization function is written as:

$$\begin{aligned} &\arg \max_{\Psi_c} H_{\text{LOS}}(\Psi_c), \\ &\text{subject to } P_v(\Psi_c) = 1. \end{aligned} \quad (26)$$

DRAFT

July 21, 2021

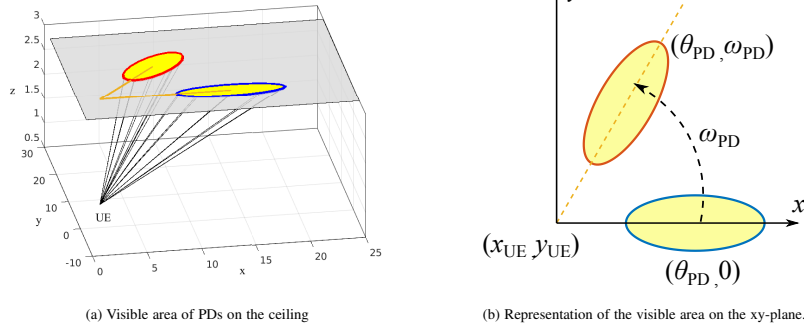


Fig. 3. Visible area of PDs

The solution set of  $P_v(\Psi_c) = 1$  is denoted as  $\mathbb{R}$  and  $\Psi_{c,\min}$  is the minimum value in  $\mathbb{R}$ . As  $H_{\text{LOS}}(\Psi_c)$  is a monotonically decreasing function, the maximum  $H_{\text{LOS}}(\Psi_c)$  is achieved when  $\Psi_c = \Psi_{c,\min}$ . Hence, the optimization problem can be solved by finding the minimum value of  $\Psi_c$ ,  $\Psi_{c,\min}$ , which satisfies  $P_v = 1$ . Based on (25),  $\Psi_{c,\min}$  cannot be solved in a closed form. Therefore, in the following parts, we will study the ADRs' visible area on the ceilings to solve the solution set  $\mathbb{R}$  and find a closed form for  $\Psi_{c,\min}$ .

#### B. Coverage Area of ADR on the Ceiling

The coverage area of a PR for a vertical-orientated UE is studied in [18]. Fig. 3a demonstrates that the visible area of the PD mounted on the PR is an ellipse on the ceiling. Hence, the visible area of the 1-st PD, where  $\theta_{\text{PD},1} = \Theta_{\text{PD}}$  and  $\omega_{\text{PD},1} = 0$ , is given by [18]:

$$\frac{(x_{\text{ellipse},1} - x_{\text{center}})^2}{a^2} + \frac{(y_{\text{ellipse},1} - y_{\text{center}})^2}{b^2} = 1, \quad (27)$$

where

$$a = \frac{h \sin(2\Psi_c)}{\cos(2\Psi_c) + \cos(2\Theta_{\text{PD}})}, \quad b = \frac{\sqrt{2}h \sin(\Psi_c)}{\sqrt{\cos(2\Psi_c) + \cos(2\Theta_{\text{PD}})}}, \quad (28)$$

and

$$x_{\text{center}} = x_{\text{UE}} + \frac{h \sin(2\Theta_{\text{PD}})}{\cos(2\Psi_c) + \cos(2\Theta_{\text{PD}})}, \quad y_{\text{center}} = y_{\text{UE}}, \quad (29)$$

where  $h$  is the vertical distance between the AP and UE. The detailed proof is given in Appendix A. Fig. 3b depicts that the shape of the visible area of the  $p$ -th PD can be obtained by rotating the

14

1-st PD around  $(x_{UE}, y_{UE})$  with an angle of  $\omega_{PD,p}$ , which can be represented as:

$$\begin{bmatrix} x_{\text{ellipse},p} - x_{UE} \\ y_{\text{ellipse},p} - y_{UE} \end{bmatrix} = R_{xy}(\omega_{PD,p}) \begin{bmatrix} x_{\text{ellipse},1} - x_{UE} \\ y_{\text{ellipse},1} - y_{UE} \end{bmatrix} = \begin{bmatrix} \cos \omega_{PD,p} & -\sin \omega_{PD,p} \\ \sin \omega_{PD,p} & \cos \omega_{PD,p} \end{bmatrix} \begin{bmatrix} x_{\text{ellipse},1} - x_{UE} \\ y_{\text{ellipse},1} - y_{UE} \end{bmatrix}. \quad (30)$$

The TPR can be seen as the combination of a PR, where  $N_{PR} = N_{TPR} - 1$ , and a central PD. When the UE is facing vertically upward, the visible area of the central PD is a circle. Therefore, the shape of the visible area of the  $p$ -th PD on a TPR is given by:

$$\begin{bmatrix} x_{\text{ellipse},p} \\ y_{\text{ellipse},p} \end{bmatrix} = \begin{cases} \begin{bmatrix} \cos \omega_{PD,p} & -\sin \omega_{PD,p} \\ \sin \omega_{PD,p} & \cos \omega_{PD,p} \end{bmatrix} \begin{bmatrix} x_{\text{ellipse},1} - x_{UE} \\ y_{\text{ellipse},1} - y_{UE} \end{bmatrix} + \begin{bmatrix} x_{UE} \\ y_{UE} \end{bmatrix}, & \text{if } 1 \leq p < N_{TPR} \\ \begin{bmatrix} x_{\text{circle}} \\ y_{\text{circle}} \end{bmatrix}, & \text{if } p = N_{TPR} \end{cases}, \quad (31)$$

where  $x_{\text{circle}}^2 + y_{\text{circle}}^2 = (h \tan \Psi_c)^2$ .

### C. Lower Bound of FOV

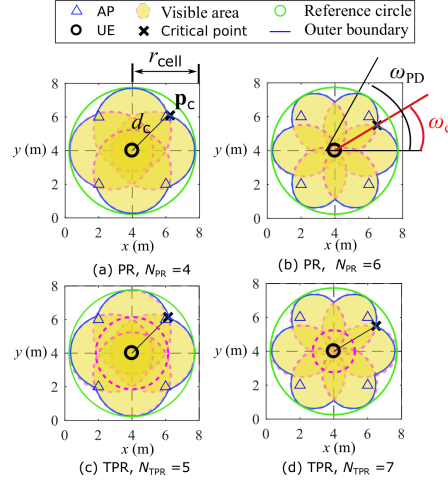
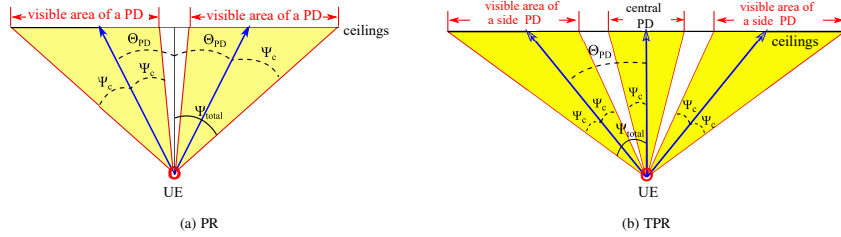


Fig. 4. Coverage area of PRs and TPRs with different number of PDs.

DRAFT

July 21, 2021

Fig. 5. Visible area of ADR in  $xz$ -plane.

For a fixed UE location, the ADR has the smallest coverage area on the ceiling when vertically orientated. In other words, we will investigate the worst condition, i.e. the situation that an ADR is positioned vertically upward which provides the smallest coverage area on the ceiling. Under other orientation scenarios, the coverage area is larger. Based on (30) and (31), Fig. 4 illustrates the visible area of 4 different types of ADRs when the UE is at the cell corner, that is to say, the cross-point of four LiFi cells. The blue curve is the outer boundary of the visible area. On the outer boundary, the points that have the shortest distance to the UE are defined as critical points,  $\mathbf{p}_c$ .  $d_c$  denotes the horizontal distance between  $\mathbf{p}_c$  and the UE. To ensure  $P_v = 1$ , there are two constraints and the detailed explanation of these constraints are given as follows:

1) *Constraint I: The central area above the ADR should be visible to the ADR.* As shown in Fig. 5a, the total FOV of an ADR is represented as  $\Psi_{\text{total}}$ , which can be written as:

$$\Psi_{\text{total}} = \Psi_c + \Theta_{\text{PD}}. \quad (32)$$

In terms of PRs, if  $\Theta_{\text{PD}} \geq \Psi_c$ , then the central part is not covered by the visible area of the ADR as manifested in Fig. 5a. If the UE is in the cell center, then no APs will be visible to the ADR. Hence, the condition  $\Theta_{\text{PD}} \leq \Psi_c$  should be satisfied so that the area directly above the UE is covered by the visible area of the ADR. Based on this constraint and (32), the lower bound of  $\Psi_c$  can be obtained as:

$$\Psi_{c1,\min} = \frac{\Psi_{\text{total}}}{2}. \quad (33)$$

With respect to the TPR, the area directly above the UE is covered by the central PD orientating vertically upwards as illustrated in Fig. 5b. The concern should be the central coverage gap between the central PD and the side PDs. Therefore,  $\Theta_{\text{PD}} \leq 2\Psi_c$  is required to ensure there is

16

no gap between them. By substituting this constraint into (32), it can be derived that:

$$\Psi_{c1,\min} = \frac{\Psi_{\text{total}}}{3}. \quad (34)$$

2) *Constraint II: The outer boundary of the visible area should be large enough.* The side length of a square cell is denoted as  $r_{\text{cell}}$  as shown in Fig. 4. The horizontal distance between the UE and the  $a$ -th AP is denoted as  $d_{h,a}$ . When the UE is at the cell corner,  $d_{h,a} = \frac{\sqrt{2}}{2}r_{\text{cell}}$  for any  $a \in \mathcal{A}$ . With the decrease of  $\Psi_c$ , the outer boundary of the visible area will decrease, which means  $d_c$  will decrease. If  $d_c$  is smaller than the horizontal distance from the AP to the cell corner, which is  $\frac{\sqrt{2}}{2}r_{\text{cell}}$ , there will be no APs within the visible area of the ADR for cell-corner users. Therefore, to ensure that at least one AP is visible to the cell-corner UE,  $d_c$  should be larger than the horizontal distance from the AP to the cell corner. By moving towards any direction, due to the symmetry, the cell-corner UE will get closer to at least one AP. In other words,

$$d_{c,\min} = \max_{x_{\text{UE}}, y_{\text{UE}}} \left( \min_a (d_{h,a}) \right) = \frac{\sqrt{2}}{2}r_{\text{cell}}, \quad \text{subject to } a \in \mathcal{A}. \quad (35)$$

That is to say, if there is at least one AP inside the outer boundary of the visible area for the cell-corner UE, then, when the UE moves to other locations, the AP will still be inside the outer boundary of the visible area. Hence, to meet the condition  $P_v = 1$ , it is required that  $d_c \geq \frac{\sqrt{2}}{2}r_{\text{cell}}$ . Also, it can be seen from Fig. 4 that  $\mathbf{p}_c$  is always inside the green reference circle, which has a radius of  $h \tan(\Psi_{\text{total}})$ . Hence,  $d_{c,\min} \leq d_c \leq h \tan(\Psi_{\text{total}})$ , where  $d_{c,\min} = \frac{\sqrt{2}}{2}r_{\text{cell}}$ .

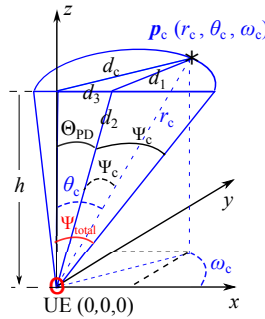


Fig. 6. The geometrical representation of  $\Psi_c$ ,  $\Theta_{\text{PD}}$ ,  $\Psi_{\text{total}}$  and  $d_c$  in the spherical coordinate system.

Fig. 6 presents the geometrical relationship in a spherical coordinate system. The coordinate of  $\mathbf{p}_c$  is represented as  $(r_c, \theta_c, \omega_c)$  and  $\omega_c = \frac{\omega_{\text{PD},p}}{2}|_{p=2}$  for both PRs and TPRs. The geometrical

relationships among  $d_1, d_2$  and  $d_3$ , illustrated in Fig. 6, can be represented as:

$$d_1^2 = d_2^2 + r_c^2 - 2d_2r_c \cos(\Psi_c), \quad (36)$$

$$d_1^2 = d_3^2 + d_c^2 - 2d_3d_c \cos(\omega_c), \quad (37)$$

$$d_2^2 = h^2 + d_3^2, \quad r_c^2 = h^2 + d_c^2, \quad d_3 = h \tan(\Theta_{PD}). \quad (38)$$

According to (37), (36) and (38), the lower bound of  $\Psi_c$  set by Constraint II is derived in Appendix B and is represented as:

$$\Psi_{c2,\min} = \begin{cases} F_2(d_{c2}), & \text{if } d_{c,\min} \leq d_{c2} \\ F_2(d_{c,\min}), & \text{otherwise} \end{cases}, \quad (39)$$

where

$$F_2(d_c) = \Psi_{\text{total}} - \tan^{-1} \frac{\sqrt{h^2 + d_c^2} \cos(\Psi_{\text{total}}) - h}{d_c \cos(\omega_c) - \sqrt{h^2 + d_c^2} \sin(\Psi_{\text{total}})}, \quad (40)$$

and

$$d_{c2} = \frac{h \cos(\omega_c) \sin(\Psi_{\text{total}})}{\cos(\Psi_{\text{total}}) + \sin(\omega_c)}. \quad (41)$$

3) *Summary*: Based on (33), (34) and (39), the lower bound of  $\Psi_c$  can be expressed as:

$$\Psi_{c,\min} = \max(\Psi_{c1,\min}, \Psi_{c2,\min}). \quad (42)$$

Therefore, the solution set  $\mathbb{R}$  is  $\Psi_{c,\min} \leq \Psi_c \leq \Psi_{\text{total}}$ . For different numbers of PDs on the PR, the optimum FOV is  $\Psi_{c,\min}$  as the FOV gets smaller, the higher the channel gain and received signal power.

## V. DOUBLE SOURCE CELL CONFIGURATION

In the conventional SS cell configuration, each cell is equipped with a single AP in the cell center. The double source (DS) cell configuration is proposed to further exploit the spatial diversity of the ADR in [17]. As demonstrated in Fig. 7, each LiFi AP consists of two sources which transmit the same information signals but with opposite polarity. These two sources are termed as the positive source and the negative source, which transmit the time domain signal  $s_{\text{pos}}(t)$  and  $s_{\text{neg}}(t)$  respectively. In a single optical cell, the received optical signal at a PD is denoted as [17]:

$$s_{\text{sum}}(t) = s_{\text{pos}}(t)H_{\text{pos}} + s_{\text{neg}}(t)H_{\text{neg}}, \quad (43)$$

where  $H_{\text{pos}}$  is the channel gain between the positive source and the PD;  $H_{\text{neg}}$  is the channel gain between the negative source and the PD. For a fair comparison, the total transmitting power for the

18

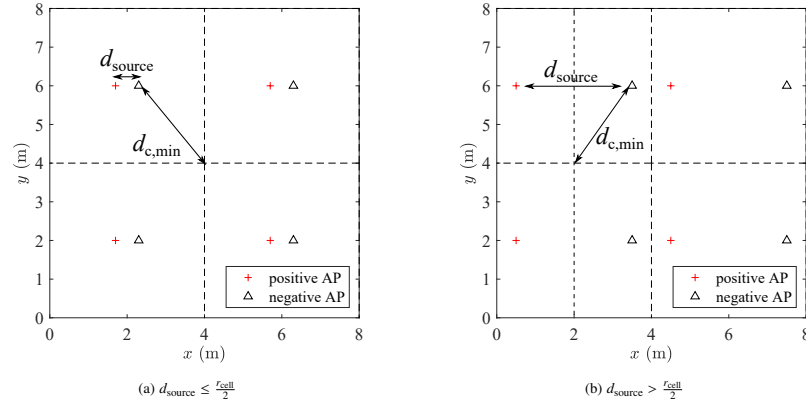


Fig. 7. Double source cell configuration.

SS system and DS system should be the same. Hence, the transmit power of each source is halved when the DS configuration is applied and the received optical power at the PD can be written as [17]:

$$P_{rx} = \frac{P_{tx}}{2} |H_{pos} - H_{neg}| = \frac{P_{tx} \Delta H}{2}. \quad (44)$$

Generally, the receiver is closer to the desired AP than the interfering AP. For the desired AP, due to the narrow FOV of ADRs, one PD can hardly receive LOS signals from both the positive source and negative source simultaneously, and only one appears as the LOS channel gain. In respect of the interfering AP, the channel gains  $H_{pos}$  and  $H_{neg}$  are both NLOS. Hence, the difference between  $H_{pos}$  and  $H_{neg}$  is small and the interference is attenuated accordingly. Therefore, the double source cell configuration can suppress the signal power from interfering APs [17]. As the LOS interference can be mitigated by the narrow FOV of the ADR and the NLOS interference can be mitigated due to the adoption of the DS configuration, the SINR of user  $\mu$  on subcarrier  $m$  can be approximated by:

$$\tilde{\gamma}_{\mu,m} \approx \frac{(\sum_{p=1}^{N_{PD}} w_p \tau \frac{P_{tx}}{2} \Delta H_{a_s \mu, p})^2}{\sum_{p=1}^{N_{PD}} w_p^2 \kappa^2 N_0 B_L (M-2)/M}. \quad (45)$$

where  $\Delta H_{a_s \mu, p}$  is the overall DC channel gain between the PD  $p$  of user  $\mu$  and the serving AP  $a_s$  in the DS system. As manifested in Fig. 7,  $d_{c,min}$  will vary according to the distance between the



positive and negative sources, which can be represented as:

$$d_{c,\min} = \max_{x_{UE}, y_{UE}} \left( \min_a (d_{h,a}) \right) = \begin{cases} \sqrt{\left(\frac{r_{\text{cell}}}{2} - \frac{d_{\text{source}}}{2}\right)^2 + \left(\frac{r_{\text{cell}}}{2}\right)^2}, & \text{if } d_{\text{source}} \leq \frac{r_{\text{cell}}}{2} \\ \sqrt{\left(\frac{r_{\text{cell}}}{2}\right)^2 + \left(\frac{d_{\text{source}}}{2}\right)^2}, & \text{otherwise} \end{cases}, \quad \text{subject to } a \in \mathcal{A}. \quad (46)$$

Therefore, the lower bound of  $\Psi_c$  for the double source cell system can be calculated based on (39) - (42).

Table I. Parameters Lists

Parameter	Symbol	Value
Transmitted optical power per AP	$P_{\text{tx}}$	10 W
Modulated bandwidth for LED	$B$	20 MHz
Physical are of the single PD receiver	$A_p$	1 cm <sup>2</sup>
FOV of the single PD receiver	$\Psi_c$	60°
The total FOV of an ADR	$\Psi_{\text{total}}$	60°
Half-intensity radiation angle	$\Phi_{1/2}$	60°
PD responsivity	$\tau$	0.5 A/W
Noise power spectral density	$N_0$	10 <sup>-21</sup> A <sup>2</sup> /Hz
Vertical distance between APs and UEs	$h$	2.15 m
Wall reflectivity	$\rho_{\text{wall}}$	0.8
Ceiling reflectivity	$\rho_{\text{ceiling}}$	0.8
Floor reflectivity	$\rho_{\text{floor}}$	0.3
Refractive index	$n_{\text{ref}}$	1.5
Optical filter gain	$G$	1
Permittivity of vacuum	$\epsilon_0$	8.854 × 10 <sup>-12</sup> F·m <sup>-1</sup>
Relative permittivity of silicon	$\epsilon_r$	11.68
Hole velocity	$v_p$	4.8 × 10 <sup>4</sup> m/s

## VI. RESULTS AND DISCUSSIONS

### A. Simulation Setups

As shown in Fig. 4, an 8 m × 8 m × 3 m indoor office scenario is considered in this study, where 4 LiFi APs are deployed following a square topology. All of the users are uniformly distributed in the room and move randomly following the random waypoint model [22]. To make a fair

20

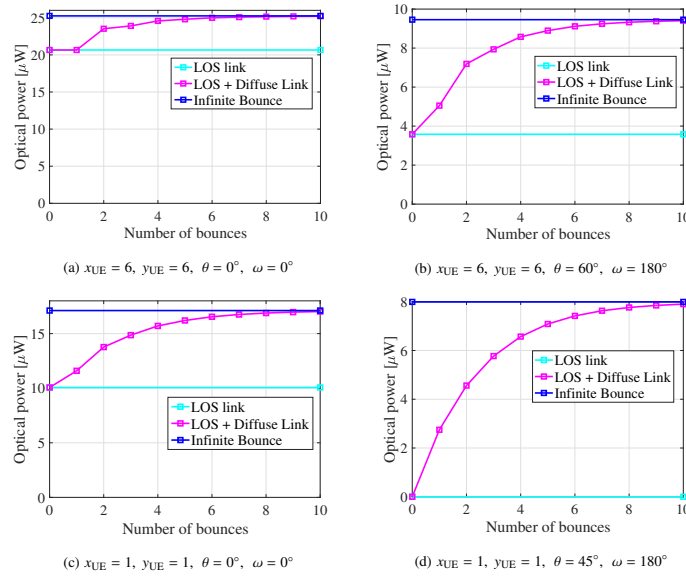


Fig. 8. Comparisons among received optical power for LOS link, LOS + diffuse link up to order  $L$  and infinite reflections in 2 different positions with different orientations.

comparison, the total physical area,  $A_t = N_{PD}A_p$ , of the ADRs should be the same. Hence, the physical area  $A_p$  on each PD decreases when the number of PDs increases. The other parameters used in the simulations are listed in Table I.

### B. Importance of Reflection and Orientation

Fig. 8 shows the received optical power in two different locations with different orientations. The room setup and the SS deployment is as shown in Fig. 5 and a single PD receiver with a FOV of  $60^\circ$  is used. The received optical power from the LOS and NLOS link can be calculated based on (2) and (3), respectively. The ratio of the received optical power from the LOS signal link to the total received optical power is represented as  $p_{los}$ . In Fig. 8a and 8b, the  $p_{los}$  of cell-center UEs at (6,6) degrades substantially when the orientation changes. In Fig. 8c, the optical power from the diffuse link occupies more than 40% of the total optical power when  $x_{UE} = 1, y_{UE} = 1$ . Nevertheless, in Fig. 8d, by changing the device orientation, there is no LOS signal and only the signal from the diffuse links can be received. Therefore, the device orientation has a great impact

DRAFT

July 21, 2021

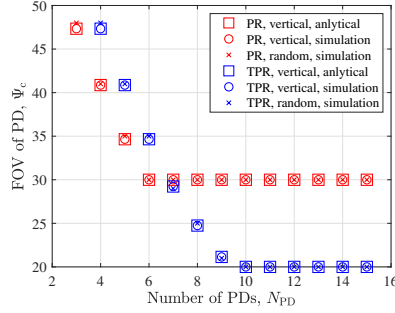


Fig. 9. The relationship between  $\Psi_{c,min}$  and the number of PDs,  $N_{PD}$ , on an ADR for the SS system.

on the received single power and thus cannot be ignored. In addition, both the LOS link and diffuse link should be considered to analyze the performance of a multi-cell visible light communication system. Fig. 8 demonstrates that when the number of bounces is more than 5, the corresponding paths make a minor contribution to the total optical power. Hence, to reduce the computational complexity while maintaining high channel estimation accuracy, a light reflection order of  $L = 5$  and the orientation model proposed in [22] are considered for the following simulations.

### C. Performance Analysis for SS cells

1) *Lower bound of FOV*: Fig. 9 manifests the relationship between the lower bound of the FOV,  $\Psi_{c,min}$ , and the numbers of PDs. The analytical results are calculated based on the lower bound given in (42). The Monte-Carlo simulations for UEs with a vertical orientation can be carried out based on (25), and the lowest value of  $\Psi_c$  satisfying  $P_v = 1$  is  $\Psi_{c,min}$ . It can be seen that the analytical results exactly match the simulation results. When  $N_{PD} \leq 6$ , with the increase of  $N_{PD}$ ,  $\Psi_{c,min}$  decreases and the PR achieves smaller  $\Psi_{c,min}$  than the TPR. With the further increase of  $N_{PD}$  from 6 to 10, the lower bound of FOV,  $\Psi_{c,min}$ , for the PR becomes fixed due to (33) while the  $\Psi_{c,min}$  for the TPR still decreases and is lower than the  $\Psi_{c,min}$  for the PR. For  $N_{PD} > 10$ ,  $\Psi_{c,min}$  does not change anymore for TPR as well due to (34). It is noted that the Monte-Carlo simulations are also performed for UEs with the random orientation model proposed in [22] and the results are matched with the analytical derivation for vertical-orientated UEs as well.

2) *MRC vs. SBC*: The MRC scheme is known to achieve better performance than the SBC

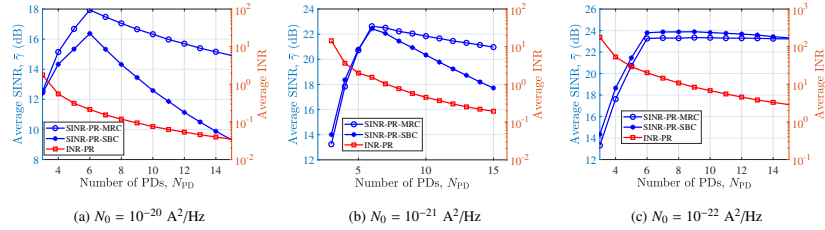


Fig. 10. The performance comparison between MRC and SBC for the SS (PR,  $B_t=100$  MHz).

scheme when there is no interference in the system. However, this may not be true when the interference is taken into consideration. To demonstrate the performance comparison between the MRC and SBC scheme, the simulation is carried out for different noise levels. In Fig. 10a, the noise power spectrum density level  $N_0$  is  $10^{-20}$  A<sup>2</sup>/Hz. When  $N_{PD} = 3$ , the level of interference is slightly higher than the noise, and the MRC schemes achieves similar average SINR as the SBC scheme. With the increase of  $N_{PD}$ , the noise level becomes higher than the interference level and the system gradually becomes noise dominated. It can be seen that in a noise-limited system, MRC outperforms SBC in terms of average SINR. The noise power spectrum density level  $N_0$  is  $10^{-21}$  A<sup>2</sup>/Hz in Fig. 10b. When  $N_{PD} \leq 6$ , the interference level is higher than the noise level and SBC performs slightly better than MRC. However, the noise starts to rise above the interference level with the further increase of  $N_{PD}$  and thus MRC outperforms SBC. For a noise power spectrum density level of  $10^{-22}$  A<sup>2</sup>/Hz, Fig. 10c depicts an interference-limited system and the SBC scheme achieves a higher average SINR than the MRC scheme for all values of  $N_{PD}$ . In brief, when the system is interference dominated, SBC is a better combining scheme. Otherwise, MRC outperforms SBC when considering the average SINR.

3) *PR* vs. *TPR*: Fig. 11 manifests how the number of PDs  $N_{PD}$  affects the system performance for both PR and TPR configurations. The average SINR in Fig. 11a and Fig. 11b exhibit the same tendency. For fair comparisons, it is assumed that the total physical area,  $A_t = N_{PD}A_p$ , of the ADRs should be the same. Hence, the increase in  $N_{PD}$  will lead to the decrease in the physical area  $A_p$  on each PD, which means less received power. Nevertheless, when  $N_{PD}$  increases from 3 to 6, the average SINR for the PR and TPR both increase. The increase is caused by the decrease in  $\Psi_{c,min}$  as displayed in Fig. 9, which leads to a higher channel gain and compensates for the power loss

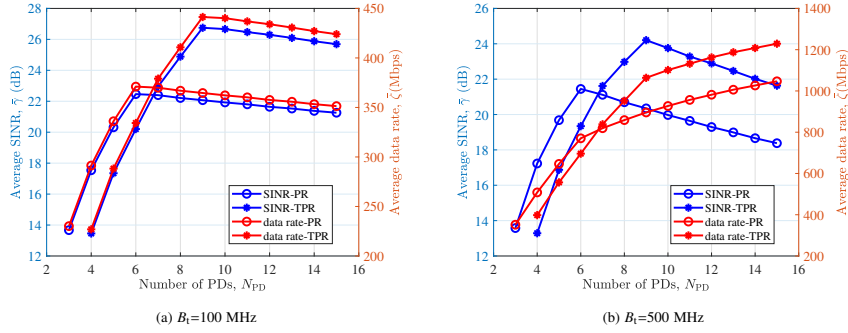
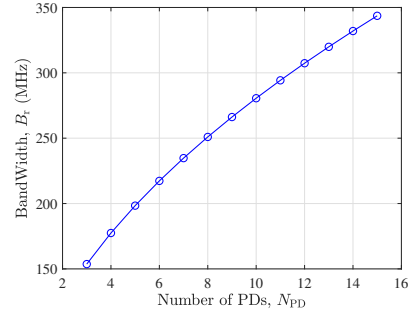


Fig. 11. The performance comparison between PR and TPR configurations considering different transmitter bandwidth in the SS system (MRC,  $N_0 = 10^{-21}$  A<sup>2</sup>/Hz).

due to the decrease in  $A_p$ . In terms of the PR, the further growth of  $N_{PD}$  leads to the decline in the average SINR since  $\Psi_{c,min}$  does not change anymore. In comparison, the average SINR for the TPR increases until  $N_{PD} = 9$  as  $\Psi_{c,min}$  is still decreasing. When  $N_{PD}$  increases from 9 to 10 for the TPR,  $\Psi_{c,min}$  decreases slightly from  $21^\circ$  to  $20^\circ$  as demonstrated in Fig. 9. However, the power loss caused by the reduction in  $A_p$  exceeds the increase of received power gained from the small decrease in  $\Psi_{c,min}$ , and thus the average SINR drops. Considering  $N_{PD} \geq 10$ ,  $\Psi_{c,min}$  is fixed and the average SINR declines as  $A_p$  reduces. Hence, in terms of the average SINR, the optimum values of  $N_{PD}$  are 6 and 9 for PR and TPR, respectively. It can also be observed that the PR outperforms the TPR with regard to both the average SINR and average data rate when  $N_{PD} \leq 6$  since the PR has smaller  $\Psi_{c,min}$ . On the other hand, when  $N_{PD} > 6$ , the TPR has smaller  $\Psi_{c,min}$  than the PR and hence achieves better performance.

4) *Receiver bandwidth vs. transmitter bandwidth*: Based on (22), the relationship between the receiver bandwidth,  $B_r$ , and the number of PDs,  $N_{PD}$ , is manifested in Fig. 12. When  $N_{PD}$  increases from 3 to 15, the bandwidth increases from 150 MHz to around 350 MHz due to the decrease in the physical area of each PD. The communication bandwidth  $B_L$  is the minimum value between the receiver bandwidth and the transmitter bandwidth, which is denoted as  $B_L = \min(B_r, B_t)$ . The user data rate is determined by the SINR and the communication bandwidth. When the transmitter bandwidth  $B_t$  is 100 MHz, which is less than  $B_r$  for all values of  $N_{PD}$  in Fig. 12, the communication bandwidth is limited by the transmitter and thus  $B_L = 100$  MHz. As  $B_L$  does not vary according to

Fig. 12. Receiver bandwidth versus the number of PDs,  $N_{PD}$ .

$N_{PD}$ , the average data rate follows the same trend as the average SINR in Fig. 11a. By increasing the transmitter bandwidth  $B_t$  to 500 MHz,  $B_r \leq B_t$  for all  $N_{PD}$  and the communication bandwidth is limited by the receiver side. Hence, the communication bandwidth  $B_L = B_r$ . In Fig. 11b, with the increase of  $N_{PD}$ , the average SINR first increases and then decreases, which peaks at  $N_{PD} = 6$  and  $N_{PD} = 9$  for the PR and TPR, respectively. In contrast, when  $N_{PD}$  grows, the average data rate increases even when the SINR degrades, which is due to the greater bandwidth. To sum up, the PR with  $N_{PD} = 6$  and TPR with  $N_{PD} = 9$  achieve the highest average data rate for transmitter-bandwidth-limited systems whereas the average data rate peaks at  $N_{PD} = 15$  in a receiver-bandwidth-limited system for both PR and TPR.

#### D. Performance Analysis for DS cells

1) *Lower bound of FOV*: Fig. 13 demonstrates the change in the minimum FOV against the number of PDs for the DS configuration. As shown for the PR, with the increase in  $N_{PD}$ , the lower bound of FOV  $\Psi_{c,min}$  for the DS cells decreases and converges to  $30^\circ$  at  $N_{PD} = 5$ , which is earlier than the SS configuration. When  $N_{PD} \leq 5$ , the  $\Psi_{c,min}$  for the DS configuration is lower than the counterpart in the SS configuration. In terms of the TPR, the minimum FOV for DS converges to  $20^\circ$  at  $N_{PD} = 8$  and has smaller  $\Psi_{c,min}$  than the SS when  $N_{PD} \leq 9$ .

2) *MRC vs. SBC*: Previously, in Fig. 10c, we have shown the performance comparison between the MRC and SBC for the SS system with  $N_0 = 10^{-22}$  A<sup>2</sup>/Hz. Due to the low level of noise power spectral density, the system is mostly interference-limited and SBC outperforms MRC for all given values of  $N_{PD}$ . By adopting the DS configuration, as shown in Fig. 14, the average interference to

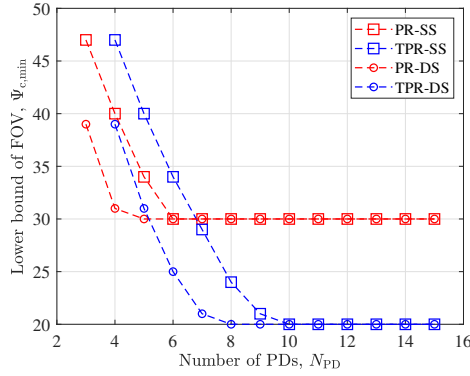


Fig. 13. The relationship between  $\Psi_{c,min}$  and the number of PDs,  $N_{PD}$ , on an ADR for the DS system.

noise ratio (INR) is larger than 1 only when there are 3 or 4 PDs on the PR. Whereas for  $N_{PD} \geq 5$ , the noise plays a similar or more important role than the interference. Therefore, compared with the SS system, for the same level of noise power spectral density, the average INR of the DS system degrades substantially. This indicates that the DS system can mitigate interference. With regards to the average SINR, MRC and SBC have similar performance when  $N_{PD} \leq 4$  whereas MRC outperforms SBC for  $N_{PD} > 4$ . From the above analyses, it can be deduced that MRC is a better combining scheme for the DS system with respect to the three different levels of  $N_0$  given

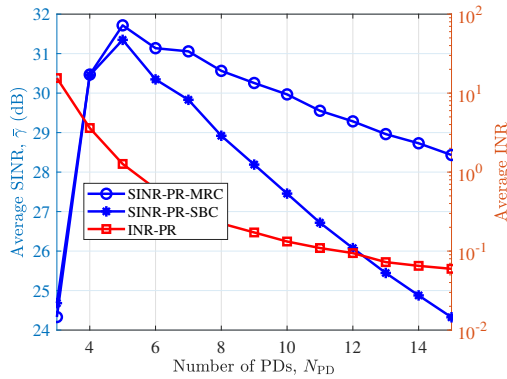


Fig. 14. The performance comparison between MRC and SBC in DS cells (PR,  $N_0 = 10^{-22}$  A<sup>2</sup>/Hz,  $B_i=100$  MHz).

26

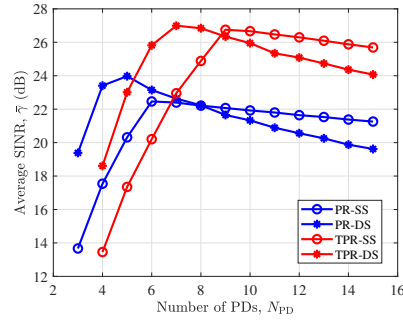


Fig. 15. The performance comparison between PRs and TPRs in DS cells (MRC,  $N_0 = 10^{-21}$  A<sup>2</sup>/Hz).

previously in this study.

3) *PR* vs. *TPR*: Fig. 15 illustrates the performance comparison between PR and TPR configurations. With respect to the PR, when  $N_{PD}$  rises from 3 to 5, the average SINR increases from 19.3 dB to 24 dB, where the increment comes from the decline in  $\Psi_{c,min}$ . For the same reason, with regards to the TPR, the average SINR grows from 18.5 dB to 27 dB when  $N_{PD}$  increases from 4 to 7. The PR and TPR achieves the peak at  $N_{PD} = 5$  and  $N_{PD} = 7$  respectively. For both PR and TPR configurations, after the peak points, the average SINR drops due to the reduction in the area  $A_p$  of each PD, which leads to less physical power. With regard to TPR, changing  $N_{PD}$  from 7 to 8 results in the decrease in  $\Psi_{c,min}$ , which leads to a channel gain boost. However, the gain cannot compensate for the power loss stems that from the reduction in  $A_p$  and thus the system performance degrades. When  $N_{PD} \leq 5$ , the PR outperforms the TPR, otherwise, the TPR is a preferred structure. In conclusion, the optimum number of PDs is 5 and 7 for PRs and TPRs, respectively. In addition, the TPR with  $N_{PD} = 7$  outperforms the PR with  $N_{PD} = 5$  in terms of the average SINR.

4) *DS* vs. *SS*: Fig. 16 demonstrates the performance comparison between the DS system and the SS system with respect to different levels of noise power spectrum density,  $N_0$ . The typical value of  $N_0$  for a PD is  $10^{-21}$  A<sup>2</sup>/Hz, at which the DS system achieves a slightly higher average SINR than the SS system for both PRs and TPRs. By reducing the noise power spectrum density level to  $10^{-22}$  A<sup>2</sup>/Hz, the system becomes interference-limited. With the aid of the DS configuration, the ADR can suppress the signal power from interfering APs by attenuating the NLOS path. Hence, when  $N_0 = 10^{-22}$  A<sup>2</sup>/Hz, the average SINR of DS cells is 7 dB and 5 dB higher than the average

DRAFT

July 21, 2021



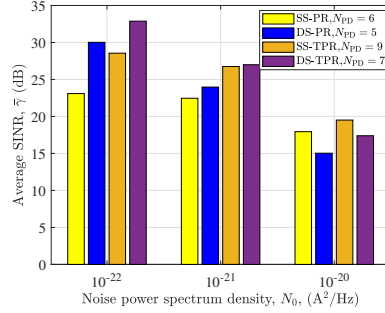


Fig. 16. The performance comparison between the DS and SS systems.

SINR of SS cells for PRs and TPRs, respectively. For a noise spectrum density level of  $10^{-20}$   $A^2/Hz$ , the system becomes noise limited, in which the DS could not improve system performance by reducing the power of interference signal. In addition, the received power is halved when the DS configuration is applied, and thus the SS outperforms the DS in terms of the average SINR.

## VII. CONCLUSIONS

This paper investigates the ICI mitigation in LiFi networks using ADRs. The impact of the diffuse link considering random UE orientation is studied and it is shown that both LOS and diffuse links have an important influence on the system performance. The performance of different ADR structures are compared and the optimized ADR structure is proposed for the considered scenario, where the method can be extended to other scenarios easily. By studying systems with different levels of noise power spectrum density, we showed that when the system is noise-limited, MRC outperforms SBC, otherwise, SBC is the preferred combining scheme. In an interference-limited system or noise-plus-interference limited system, the adoption of the DS cell configuration can further mitigate the NLOS interference and thus improve the system performance. However, the limitation of the DS cell is that the transmit power is equally split to the positive and negative sources, which degrades the performance of the noise-limited system.

## APPENDIX A

### PROOF OF (27)

The visible area of the 1-st PD with  $\omega_{PD}^1 = 0$  is illustrated in Fig. 6a. The point **O** represents the location of the UE, **p<sub>UE</sub>**, and **OE** represents the normal vector of the PD. The intersection point of

28

the normal vector with the ceiling is  $\mathbf{E}$ . The coordinate of  $\mathbf{E}$  is denoted as  $(x_e, y_e, z_e)$  and points  $\mathbf{A}$ ,  $\mathbf{B}$ ,  $\mathbf{C}$ ,  $\mathbf{D}$ ,  $\mathbf{F}$  are denoted in the same way. Points  $\mathbf{A}$  and  $\mathbf{B}$  are the vertices of the ellipse. Points  $\mathbf{C}$  and  $\mathbf{D}$  are the co-vertices of the ellipse. The centre point of the ellipse is denoted as  $\mathbf{F}$ . The angle between each of the four vectors,  $\mathbf{OA}$ ,  $\mathbf{OB}$ ,  $\mathbf{OC}$ ,  $\mathbf{OD}$  with  $\mathbf{OE}$  is  $\Psi_c$ . The length of the semi-major and semi-minor axes of the ellipse are represented by  $a$  and  $b$  separately. The length of semi-major axes  $a$  is denoted as:

$$a = \frac{|\mathbf{AB}|}{2} = \frac{h \tan(\Psi_c + \Theta_{PD}) + h \tan(\Psi_c - \Theta_{PD})}{2} = \frac{h \sin(2\Psi_c)}{\cos(2\Psi_c) + \cos(2\Theta_{PD})}. \quad (47)$$

As  $\mathbf{A}$ ,  $\mathbf{B}$ ,  $\mathbf{E}$ ,  $\mathbf{F}$  and  $\mathbf{O}$  are on the same  $xz$ -plane,  $y_a = y_b = y_e = y_f = y_{UE}$ . As  $\mathbf{A}$ ,  $\mathbf{B}$ ,  $\mathbf{C}$ ,  $\mathbf{D}$ ,  $\mathbf{E}$  and  $\mathbf{F}$  are on the ceiling,  $z_a = z_b = z_c = z_d = z_f = z_e = z_{AP}$ , where  $z_{AP}$  is the height of the AP. As  $\mathbf{C}$  and  $\mathbf{D}$  are on the same  $yz$ -plane with  $\mathbf{F}$ , the coordinates  $x$  of these points are represented by:

$$x_c = x_d = x_f = x_{UE} + (a - h \tan(\Psi_c - \Theta_{PD})) = x_{UE} + \frac{h \sin(2\Theta_{PD})}{\cos(2\Psi_c) + \cos(2\Theta_{PD})}. \quad (48)$$

From Fig. 6, we know that  $x_e = h \tan(\Theta_{PD}) + x_{UE}$ . Based on the parameters above, we have  $\mathbf{OE} = (h \tan(\Theta_{PD}), 0, h)$  and  $\mathbf{OC} = (\frac{h \sin(2\Theta_{PD})}{\cos(2\Psi_c) + \cos(2\Theta_{PD})}, b, h)$ . Since  $\cos(\Psi_c) = \frac{\mathbf{OE} \cdot \mathbf{OC}}{|\mathbf{OE}| |\mathbf{OC}|}$ ,  $b$  can be obtained as:

$$b = \frac{\sqrt{2} h \sin(\Psi_c)}{\sqrt{\cos(2\Psi_c) + \cos(2\Theta_{PD})}}. \quad (49)$$

Consequently, the equation of the ellipse is thus given by:

$$\frac{(x_{\text{ellipse}} - x_f)^2}{a^2} + \frac{(y_{\text{ellipse}} - y_f)^2}{b^2} = 1. \quad (50)$$

The visible area of  $p$ -th PD can be obtained by rotating the visible area of the 1-st PD around the line  $(x = x_{UE}, y = y_{UE})$  with an angle of  $\omega_{PD,p}$ .

## APPENDIX B

### PROOF OF (39)

Substituting (37) and (38) into (36), we can get:

$$-d_c \cos \omega_c \tan(\Theta_{PD}) = h - \frac{\sqrt{h^2 + d_c^2} \cos(\Psi_c)}{\cos(\Theta_{PD})}. \quad (51)$$

Substituting (32) into (51), the elevation angle of each PD,  $\Theta_{PD}$ , on PRs is derived as:

$$\Theta_{PD} = F_1(d_c) = \tan^{-1} \frac{f_1(d_c)}{f_2(d_c)}, \quad (52)$$

where

$$\begin{aligned} f_1(d_c) &= \sqrt{h^2 + d_c^2} \cos(\Psi_{\text{total}}) - h, \\ f_2(d_c) &= d_c \cos(\omega_c) - \sqrt{h^2 + d_c^2} \sin(\Psi_{\text{total}}). \end{aligned} \quad (53)$$

The function  $F_1$  has one zero at  $z_1 = h \tan(\Psi_{\text{total}})$  and one pole at  $p_1 = \frac{h \sin(\Psi_{\text{total}})}{\sqrt{\cos^2(\Psi_{\text{total}}) - \sin^2(\omega_c)}}$ . The derivative of  $F_1(d_c)$  is given by:

$$\frac{\partial F_1}{\partial d_c} = - \frac{h^2 \cos(\omega_c) \cos(\Psi_{\text{total}}) - h \sqrt{h^2 + d_c^2} \cos(\omega_c) + h d_c \sin(\Psi_{\text{total}})}{(f_1^2(d_c) + f_2^2(d_c)) \sqrt{h^2 + d_c^2}}. \quad (54)$$

By calculating the  $d_c$  satisfying  $\frac{\partial F_1}{\partial d_c} = 0$ , the two roots are denoted as:

$$d_{c1} = \frac{h \cos(\omega_c) \sin(\Psi_{\text{total}})}{\cos(\Psi_{\text{total}}) - \sin(\omega_c)}, \quad d_{c2} = \frac{h \cos(\omega_c) \sin(\Psi_{\text{total}})}{\cos(\Psi_{\text{total}}) + \sin(\omega_c)}. \quad (55)$$

When  $\sin(\omega_c) < \cos(\Psi_{\text{total}})$ , it can be proven that  $0 < d_{c2} < z_1 = h \tan(\Psi_{\text{total}}) < d_{c1}$  and  $z_1 \leq p_1$ . In addition,  $\frac{\partial^2 F_1(d_{c2})}{\partial^2 d_c} < 0$ . Therefore, for  $d_c \in (0, h \tan(\Psi_{\text{total}})]$ ,  $F_1$  has a local maximum at  $d_{c2}$ . When  $\sin(\omega_c) \geq \cos(\Psi_{\text{total}})$ ,  $p_1$  and  $d_{c1}$  do not have real value. It can also be proved that  $0 < d_{c2} < z_1$  and  $\frac{\partial^2 F_1(d_{c2})}{\partial^2 d_c} < 0$ . Similarly, for  $d_c \in (0, h \tan(\Psi_{\text{total}})]$ , there is a local maximum at  $d_{c2}$ . In summary, the upper bound of  $F_1$  is thus given by:

$$F_{1,\max} = \begin{cases} F_1(d_{c2}), & \text{if } d_{c,\min} \leq d_{c2} \\ F_1(d_{c,\min}), & \text{otherwise.} \end{cases} \quad (56)$$

According to (32),  $\Psi_c$  is given by:

$$\Psi_c = F_2(d_c) = \Psi_{\text{total}} - F_1(d_c). \quad (57)$$

Hence, the lower bound of  $F_2$  is denoted as:

$$F_{2,\min} = \begin{cases} F_2(d_{c2}), & \text{if } d_{c,\min} \leq d_{c2} \\ F_2(d_{c,\min}), & \text{otherwise.} \end{cases} \quad (58)$$

#### REFERENCES

- [1] D. C. O'Brien, "Visible Light Communications: Challenges and potential." *IEEE*, October 2011, pp. 365–366.
- [2] H. Haas, L. Yin, Y. Wang, and C. Chen, "What is LiFi?" *Journal of Lightwave Technology*, vol. 34, no. 6, pp. 1533–1544, March 2016.
- [3] S. Wu, H. Wang, and C. H. Youn, "Visible Light Communications for 5G Wireless Networking Systems: from Fixed to Mobile Communications," *IEEE Network*, vol. 28, no. 6, pp. 41–45, Nov 2014.
- [4] M. S. Alouini and A. J. Goldsmith, "Area Spectral Efficiency of Cellular Mobile Radio Systems," *Vehicular Technology, IEEE Transactions on*, vol. 48, no. 4, pp. 1047–1066, 1999.
- [5] T. Borogovac, M. Rahaim, and J. B. Carruthers, "Spotlighting for Visible Light Communications and Illumination," in *2010 IEEE Globecom Workshops*, Dec 2010, pp. 1077–1081.

30

- [6] G. W. Marsh and J. M. Kahn, "Channel Reuse Strategies for Indoor Infrared Wireless Communications," *Communications, IEEE Transactions on*, vol. 45, no. 10, pp. 1280–1290, 1997.
- [7] K. Cui, J. Quan, and Z. Xu, "Performance of Indoor Optical Femtocell by Visible Light Communication," *Optics Communications*, vol. 298–299, pp. 59–66, 2013.
- [8] C. Chen, S. Videv, D. Tsonev, and H. Haas, "Fractional Frequency Reuse in DCO- OFDM- Based Optical Attocell Networks," *Lightwave Technology, Journal of*, vol. 33, no. 19, pp. 3986–4000, 2015.
- [9] C. Chen, D. Tsonev, and H. Haas, "Joint Transmission in Indoor Visible Light Communication Downlink Cellular Networks," in *2013 IEEE Globecom Workshops (GC Wkshps)*, Dec 2013, pp. 1127–1132.
- [10] Z. Chen, D. A. Basnayaka, and H. Haas, "Space Division Multiple Access for Optical Attocell Network Using Angle Diversity Transmitters," *Journal of Lightwave Technology*, vol. 35, no. 11, pp. 2118–2131, June 2017.
- [11] J. M. Kahn and J. R. Barry, "Wireless Infrared Communications," *Proceedings of the IEEE*, vol. 85, no. 2, pp. 265–298, 1997.
- [12] J. Carruthers and J. Kahn, "Angle diversity for nondirected wireless infrared communication," in *ICC '98. 1998 IEEE International Conference on Communications. Conference Record. Affiliated with SUPERCOMM'98 (Cat. No.98CH36220)*, vol. 3, 1998, pp. 1665–1670 vol.3.
- [13] J. Carruthers and J. Kahn, "Angle diversity for nondirected wireless infrared communication," *IEEE Transactions on Communications*, vol. 48, no. 6, pp. 960–969, 2000.
- [14] G. Yun and M. Kavehrad, "Spot-diffusing and fly-eye receivers for indoor infrared wireless communications," in *1992 IEEE International Conference on Selected Topics in Wireless Communications*, 1992, pp. 262–265.
- [15] Z. Chen, D. Basnayaka, X. Wu, and H. Haas, "Interference Mitigation for Indoor Optical Attocell Networks using Angle Diversity Receiver," *Journal of Lightwave Technology*, pp. 1–1, 2018.
- [16] Z. Chen, N. Serafimovski, and H. Haas, "Angle Diversity for an Indoor Cellular Visible Light Communication System," in *2014 IEEE 79th Vehicular Technology Conference (VTC Spring)*, May 2014, pp. 1–5.
- [17] Z. Chen, D. Tsonev, and H. Haas, "A Novel Double-Source Cell Configuration for Indoor Optical Attocell Networks," in *2014 IEEE Global Communications Conference*, Dec 2014, pp. 2125–2130.
- [18] Z. Zeng, M. D. Soltani, M. Safari, and H. Haas, "Angle Diversity Receiver in LiFi Cellular Networks," in *ICC 2019 - 2019 IEEE International Conference on Communications (ICC)*, May 2019, pp. 1–6.
- [19] Z. Zeng, M. D. Soltani, X. Wu, and H. Haas, "Access Point Selection Scheme for LiFi Cellular Networks using Angle Diversity Receivers," in *2019 IEEE Wireless Communications and Networking Conference (WCNC)*, 2019, pp. 1–6.
- [20] A. Nuwanpriya, S. W. Ho, and C. S. Chen, "Indoor MIMO Visible Light Communications: Novel Angle Diversity Receivers for Mobile Users," *IEEE Journal on Selected Areas in Communications*, vol. 33, no. 9, pp. 1780–1792, Sept 2015.
- [21] C. Chen, W. D. Zhong, H. Yang, S. Zhang, and P. Du, "Reduction of SINR Fluctuation in Indoor Multi-Cell VLC Systems Using Optimized Angle Diversity Receiver," *Journal of Lightwave Technology*, pp. 1–1, 2018.
- [22] M. D. Soltani, A. A. Purwita, Z. Zeng, H. Haas, and M. Safari, "Modeling the Random Orientation of Mobile Devices: Measurement, Analysis and LiFi Use Case," *IEEE Transactions on Communications*, vol. 67, no. 3, pp. 2157–2172, March 2019.
- [23] Z. Zeng, M. D. Soltani, H. Haas, and M. Safari, "Orientation Model of Mobile Device for Indoor VLC and Millimetre Wave Systems," *Accepted in 2018 IEEE 88th Vehicular Technology Conference (VTC2018-Fall)*, Chicago, USA, August 2018.
- [24] C. Chen, D. A. Basnayaka, and H. Haas, "Downlink Performance of Optical Attocell Networks," *Journal of Lightwave Technology*, vol. 34, no. 1, pp. 137–156, Jan 2016.
- [25] H. Schulze, "Frequency-Domain Simulation of the Indoor Wireless Optical Communication Channel," *IEEE Transactions on Communications*, vol. 64, no. 6, pp. 2551–2562, June 2016.
- [26] C. Chen, D. Basnayaka, and H. Haas, "Downlink Performance of Optical Attocell Networks," *Journal of Lightwave Technology*, vol. 34, no. 1, pp. 137–156, Apr. 2016.
- [27] C. Chen *et al.*, "Downlink Performance of Optical Attocell Networks," *Journal of Lightwave Technology*, vol. 34, no. 1, pp. 137–156, Jan 2016.
- [28] S. Dimitrov and H. Haas, "Information Rate of OFDM-Based Optical Wireless Communication Systems With Nonlinear Distortion," *J. Lightwave Technol.*, vol. 31, no. 6, pp. 918–929, Mar 2013. [Online]. Available: <http://jlt.osa.org/abstract.cfm?URI=jlt-31-6-918>
- [29] S. M. LaValle, *Planning Algorithms*. Cambridge: Cambridge : Cambridge University Press, 2006.
- [30] S. B. Alexander, *Optical communication receiver design*. IET, 1997, no. 37.

DRAFT

July 21, 2021

# A VCSEL Array Transmission System with Novel Beam Activation Mechanisms

Zhihong Zeng, Mohammad Dehghani Soltani, Majid Safari and Harald Haas

## Abstract

Optical wireless communication (OWC) is considered to be a promising technology which will alleviate traffic burden caused by the increasing number of mobile devices. In this study, a novel vertical-cavity surface-emitting laser (VCSEL) array is proposed for indoor OWC systems. To activate the best beam for a mobile user, two beam activation methods are proposed for the system. The method based on a corner-cube retroreflector (CCR) provides very low latency and allows real-time activation for high-speed users. The other method uses the omnidirectional transmitter (ODTx). The ODTx can serve the purpose of uplink transmission and beam activation simultaneously. Moreover, systems with ODTx are very robust to the random orientation of a user equipment (UE). System level analyses are carried out for the proposed VCSEL array system. For a single user scenario, the probability density function (PDF) of the signal-to-noise ratio (SNR) for the central beam of the VCSEL array system can be approximated as a uniform distribution. In addition, the average data rate of the central beam and its upper bound are given analytically and verified by Monte-Carlo simulations. For a multi-user scenario, an analytical upper bound for the average data rate is given. The effects of the cell size and the full width at half maximum (FWHM) angle on the system performance are studied. The results show that the system with a FWHM angle of  $4^\circ$  outperforms the others.

## I. INTRODUCTION

The sixth-generation (6G) communication is required to support a variety of services such as the Internet of things (IoT), augmented reality, virtual reality, video streaming and online gaming with extremely high data and low latency. However, the current sub-6 GHz band is already congested, and lower-band communication is hard to support the high data rate transmission. The optical wireless communication (OWC) is a promising solution to support the extremely

The authors are with the University of Edinburgh, LiFi R&D Centre, Edinburgh, EH9 3JL, UK, (e-mail: {zhihong.zeng, m.dehghani, Majid.Safari, h.haas}@ed.ac.uk.) This publication was made possible by the funding from PureLiFi Ltd. The statements made herein are solely the responsibility of the author[s]. Professor Harald Haas acknowledges support from the EPSRC under Established Career Fellowship Grant EP/R007101/1. He also acknowledges the financial support of his research by the Wolfson Foundation and the Royal Society.

1  
2  
3 [high rate transmission in a new band](#). There are two main indoor OWC technologies: visible  
4 light communication (VLC) and the beam-steered infrared light communication (BS-ILC) [1].  
5  
6 The VLC systems use wide-spread beams emerging from illumination systems while the BS-ILC  
7  
8 systems use narrow well-directed beams emerging from a dedicated source.

9  
10 The VLC systems uses the visible light spectrum of 400 to 700 nm, which provides a  
11 bandwidth greater than 320 THz. Light-fidelity (LiFi) is a promising and novel bidirectional,  
12 high-speed and fully networked VLC technology [2], [3]. By using orthogonal frequency division  
13 multiplexing (OFDM), a single light emitting diodes (LEDs) can achieve a data rate of 10 Gbit/s  
14 [4]. In addition, LiFi is able to provide data rates of 15.73 Gbit/s using off-the shelf LEDs [5].  
15  
16 Due to the wide coverage of the LED, multiple user equipment (UE) may be served by the same  
17 LED and may share the same resources, which may lead to traffic congestion when the load is  
18 high. In [6], an angle diversity transmitter (ADT) which consists of multiple narrow-beam visible  
19 light LEDs has been proposed for optical wireless networks with the space division multiple  
20 access scheme (SDMA). Multiple users at different locations can be served simultaneously by  
21 activating different LED elements on an ADT. The result shows that SDMA schemes can mitigate  
22 co-channel interference and thus greatly increase the average spectral efficiency (ASE). However,  
23 the VLC systems requires the illumination to be switched-on, which may not always be desired  
24 and thus increase the power consumption. Moreover, typically, the white light emitting LED,  
25 which is used for illumination, have limited bandwidth as it is based on a blue LED with  
26 phosphor coating [1].

27  
28 The deployment of narrow infrared beams in BS-ILC systems leads to small cell coverage,  
29 which implies that it is more likely that each beam only serves a single UE. Therefore, capacity  
30 sharing among multiple UEs as well as traffic congestion can be avoided. By only activating  
31 beams that point towards the UEs, the BS-ILC systems provide better energy-efficiency as  
32 narrow beams with high directivity can send a greater portion of the transmitted power to the  
33 corresponding UE. Therefore, a higher signal-to-noise ratio (SNR) can be achieved. Moreover,  
34 due to the high bandwidth of narrow beam sources, such as optical fiber, laser diode and  
35 vertical-cavity surface-emitting laser (VCSEL), the link can support higher capacity. In addition,  
36 compared with wide-spread beams, the narrow beams provide better privacy as UEs outside the  
37 coverage area cannot receive the transmitted signals. The BS-ILC systems have been explored  
38 in [1], [7]–[9]. Wavelength-controlled 2D beam-steered systems based on fully-passive crossed-  
39 grating devices are introduced and 1D beam steering has been demonstrated in [7], which shows

a multi-beam system with a capacity of 2.5 Gbit/s. The 2D steering of the multi-beam system has been first demonstrated in [8] and with adaptive discrete multitone modulation (DMT) using 512 tones, a gross bit rate of 42.8 Gbit/s has been achieved. In addition, by using 60 GHz radio signal in the uplink, upstream delivery of 10 Gbit/s per upstream has been presented. In [9], the authors proposed a novel OWC receiver concept, which can enlarge the receiver aperture without reducing the bandwidth. Also, a multi-beam system with downstream capacities of up to 112 Gbit/s per infrared beam was demonstrated. In [1], an alternative approach, which is based on a high port count arrayed waveguide grating router (AWGR) and a high-speed lens, is proposed. With pulse amplitude modulation (PAM)-4 modulation, a total system throughput beyond 8.9 Gbit/s over 2.5 m can be achieved by using 80-ports C-band AWGR. Moreover, the localization and tracking of the UE are achieved based on a 60 GHz ultra-wideband (UWB) radio link. However, all these studies consider fixed user location without mobility and the latency is high in these systems. When a mobile UE is considered, due to the small confined coverage area of the narrow beam, the beam that serves a UE may vary fast and frequently. Therefore, a high-accuracy and low-latency beam activation system or user tracking system is required to achieve a seamless connection.

Ordinary radio based indoor positioning techniques based on WiFi, Bluetooth, UWB and radio frequency identification (RFID) are not suitable candidates in this study due to their low accuracy, high latency and high hardware cost [10]. In recent years, visible light positioning (VLP) has emerged and various algorithms for VLP systems have been proposed, which include received signal strength (RSS), time differential of arrival (TDOA) and angle of arrival (AOA) methods. Due to being able to achieve high positioning accuracy and low cost, VLP is attracting more and more attention. Some studies have shown that the VLP technologies can achieve centimeter-level accuracy [10]–[14], which is way more accurate compared to Bluetooth (2-5 m), WiFi (1-7 m) and other technologies [15]. The VLP systems can be divided into two categories based on the receiving device: photodiode (PD) based VLP or image sensor (IS) based VLP. The PD-based VLP system has low latency but is sensitive to the device rotation, and hence cannot achieve high positioning accuracy for UEs without fixed orientation. The IS-based VLP systems are more robust to device rotation. However, due to the high computational latency of image processing or the communication latency of transmitting image data for server-assisted computation, the real-time performance of these systems are limited [10].

Also, when VLP is adopted, the UE is required to autonomously transmit location information

to the access points (APs) owing to the lack of a real-time backward channel from UE to APs. This adds an unnecessary burden on the UE and leads to the inevitable latency in real-time tracking. As the VLP system requires illumination devices and real-time backward channels, it may not be suitable for the VCSEL array system proposed in this study. To address the issue of power consumption and latency caused by UE localization, two beam activation schemes are proposed in this study. The first method is a passive beam activation scheme using a corner-cube reflector (CCR). The CCR is a light-weight small device, which can reflect light back to its source with minimal scattering. By using CCR, immediate feedback can be obtained for beam activation which minimizes the latency and leads to almost zero delay. The CCR has been proposed for the VLP system in [16]. Compared with the method in [16], no illumination equipment is required in our method and the power consumption for the localization system is almost zero. The second method utilizes the omnidirectional transmitter (ODTx) in the uplink communication. By using the uplink RSS matrix, this method does not require any extra signal power for localization. Compared with the PD-based VLP system, the beam activation system with ODTx is robust to the device orientation, that is to say the user can be located accurately without concerning the random orientation of the UE. Compared with the IS-based system, image sensor is not required, which reduces the cost. And the computation latency is reduced as the positioning algorithm is based on the RSS, which is the simplest and most cost effective schemes.

Among different types of laser diodes, vertical cavity surface emitting lasers (VCSELs) are one of the promising candidates to ensure high-data rate communications due to several outstanding features such as [17]: high-speed modulation (bandwidths of larger than 10 GHz), high power conversion efficiency, low cost and compact in size. These attributes make VCSELs appealing to many applications, particularly for high-speed indoor networks [18]. In this study, a VCSEL array systems with novel beam activation methods are proposed. Compared with the wavelength-controlled BS-ILC systems, the proposed VCSEL array system removes the requirement of wavelength-tuning, spatial light modulation (SLM), microelectromechanical systems (MEMS) and coherence of beams and fiber connection to the AP. End-point devices may include virtual reality devices, smartphones, televisions, computers and IoT applications. In summary, the main contributions of this work are listed as follows:

- We propose a VCSEL array system which can support high data rate, low latency and multiple UEs without the requirement of expensive/complex hardware, such as SLM, MEMS, fiber and so on.



- Two beam activation methods are proposed based on the small cell property of the VCSEL array system. The beam activation based on the CCR can achieve low power consumption and almost-zero delay, allowing real-time beam activation for high-speed users. The other beam activation is based on the ODTx, which serves the purpose of the uplink transmission and beam activation simultaneously. By collecting the RSS values, an artificial neural network (ANN) is trained to predict the index of serving beam directly without estimating the UE position first. This method is robust against random device orientation and is suitable for low-speed users.
- For a single UE scenario, regarding the central beam, the probability density function (PDF) of the SNR is derived. The analytical derivation for the average data rate is provided for the central beam and an upper bound is presented for the VCSEL array system.
- In terms of scenarios with multiple users, the optical SDMA is adopted and an analytical upper bound for the average data rate is developed.
- The effects of the cell size and beam divergence angle are considered in this study. By evaluating the system performance, the choices of cell size and beam divergence angle are proposed for the VCSEL array system.

The rest of the paper is organized as follows. The VCSEL array system model is introduced in Section II. In Section III, two beam activation methods are proposed. Analytical derivations for the system level performance are presented in Section IV. The performance evaluation and discussion are presented in Section V. Conclusions are drawn in Section VI.

## II. SYSTEM MODEL

A VCSEL array system is presented in Fig. 1. The AP of the system is composed of  $N_{\text{beam}}$  narrow-beam Tx's and each Tx is a VCSEL with a beam divergence of  $\theta_{\text{beam}}$ . The position of the  $n$ -th Tx is denoted as  $\mathbf{p}_{\text{tx}}^n$ . The  $n$ -th Tx is slightly tilted so that it is directed towards the center of its corresponding cell,  $\mathbf{p}_{\text{cell}}^n$ . Hence, the normal vector of the  $n$ -th Tx is denoted as  $\mathbf{n}_{\text{tx}}^n = (\mathbf{p}_{\text{cell}}^n - \mathbf{p}_{\text{tx}}^n) / \|\mathbf{p}_{\text{cell}}^n - \mathbf{p}_{\text{tx}}^n\|$ , where  $\|\cdot\|$  denotes the norm operator. The side length of each cell is denoted as  $d_{\text{cell}}$ . The location of the UE is denoted as  $\mathbf{p}_{\text{UE}}$  and for the downlink communication, an avalanche photodiode (APD) is used as the receiver (Rx) at the UE side.

### A. Gaussian Beam

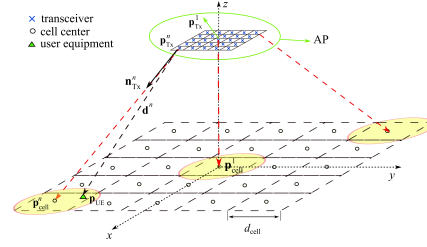


Fig. 1: The downlink geometry of a VCSEL array system.

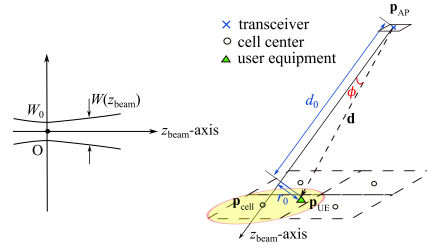


Fig. 2: Geometrical representation of the elliptical Gaussian beam.

Depending on the bias current, the VCSEL output beam profile can be Gaussian [19]. The geometrical representation of the Gaussian beam is shown in Fig. 2 and the Gaussian beam intensity can be expressed as given in [20]:

$$I(r_0, d_0) = \frac{2P_{\text{tx,opt}}}{\pi W^2(d_0)} \exp\left(-\frac{2r_0^2}{W^2(d_0)}\right), \quad (1)$$

where  $P_{\text{tx,opt}}$  is the transmitted optical power of a single beam and  $r_0$  is the distance from the UE to the beam axis, which is represented as  $z_{\text{beam-axis}}$ ; the distance from the Tx to the UE along the beam axis is given as  $d_0$ ; the beam width at  $z_{\text{beam}} = d_0$  is denoted as  $W(d_0)$  and it can be obtained as:

$$W(d_0) = W_0 \sqrt{1 + \left(\frac{\lambda d_0}{\pi W_0^2}\right)^2}, \quad (2)$$

where  $\lambda$  is the operating wavelength of the VCSEL. The beam waist is denoted as  $W_0 = \frac{\lambda}{\pi \theta_{\text{beam}}}$ , where  $\theta_{\text{beam}}$  is the divergence angle. The relation between the beam divergence and the angle for full width at half maximum (FWHM) intensity points,  $\theta_{\text{FWHM}}$ , is given as  $\theta_{\text{beam}} = \theta_{\text{FWHM}} / \sqrt{2 \ln(2)}$ , where  $\ln(\cdot)$  represents the natural logarithm. The distance vector from the

VCSEL to the UE is denoted as  $\mathbf{d} = \mathbf{p}_{\text{UE}} - \mathbf{p}_{\text{Tx}}$  and the distance is  $d = \|\mathbf{d}\|$ . The radiance angle of the Tx is denoted as  $\phi = \cos^{-1} \frac{\mathbf{n}_{\text{Tx}} \cdot \mathbf{d}}{d}$ . It should be noted that  $r_0 = d \sin \phi$  and  $d_0 = d \cos \phi$ . Hence, the intensity of the beam at the position of the UE can be reformulated as:

$$I(d, \phi) = \frac{2P_{\text{Tx,opt}}}{\pi W^2(d \cos \phi)} \exp\left(-\frac{2d^2 \sin^2 \phi}{W^2(d \cos \phi)}\right). \quad (3)$$

The received optical power at the Rx of a UE is denoted as:

$$\begin{aligned} P_{\text{Tx,UE}} &= I(d, \phi) A_{\text{eff}} G_{\text{APD}} g(\psi) \cos(\psi) \text{rect}\left(\frac{\psi}{\Psi_c}\right) \\ &= \frac{2g(\psi) \cos(\psi) P_{\text{Tx,opt}} A_{\text{eff}} G_{\text{APD}}}{\pi W^2(d \cos \phi)} \exp\left(-\frac{2d^2 \sin^2 \phi}{W^2(d \cos \phi)}\right) \text{rect}\left(\frac{\psi}{\Psi_c}\right), \end{aligned} \quad (4)$$

where  $G_{\text{APD}}$  is the gain of the APD;  $A_{\text{eff}}$  is the effective area of the APD, and  $\psi$  is the angle between the normal vector of Rx on the UE, i.e.,  $\mathbf{n}_{\text{UE}}$ , and the distance vector  $\mathbf{d}$ . Therefore,  $\psi = \cos^{-1} \frac{\mathbf{n}_{\text{UE}} \cdot (-\mathbf{d})}{d}$ . Furthermore,  $\text{rect}\left(\frac{\psi}{\Psi_c}\right) = 1$ , for  $0 \leq \psi \leq \Psi_c$  and 0 otherwise, where  $\Psi_c$  is the field of view (FOV) of the receiver. The gain of the optical concentrator is given as  $g(\psi) = \varsigma^2 / \sin^2 \Psi_c$ , where  $\varsigma$  is the refractive index. Due to the eye safety consideration, the transmit optical power should be limited. A detailed discussion about eye safety is given in the Appendix, where the beam wavelength  $\lambda$  is chosen to be 1550 nm. The maximum allowable transmitted power for  $\theta_{\text{FWHM}}$  of  $2^\circ$ ,  $4^\circ$  and  $6^\circ$  are 19, 60 and 129 mW, respectively.

In this system, the Tx and Rx use intensity modulation (IM) and direct detection (DD), respectively, and the transmit signals are required to be positive and real. The direct current biased optical (DCO)-OFDM is used in this study to achieve high data rates. The sequence number of OFDM subcarriers is denoted by  $m \in \{0, \dots, M-1\}$ , where  $M$  is an even and positive integer which denotes the number of OFDM subcarriers. To ensure real and positive signals, two constraints should be satisfied: i)  $X(0) = X(M/2) = 0$ , and ii) the Hermitian symmetry constraint, i.e.,  $X(m) = X^*(M-m)$ , for  $m \neq 0$ , where  $(\cdot)^*$  denotes the complex conjugate operator [21]. Hence, the effective subcarrier set bearing information data is defined as  $\mathcal{M}_e = \{m | m \in [1, M/2-1], m \in \mathbb{N}\}$ , where  $\mathbb{N}$  is the set of natural numbers. For the DCO-OFDM signal,  $x_{\text{DC}} = \kappa \sqrt{P_{\text{elec}}}$ , where  $x_{\text{DC}}$  is the DC bias,  $P_{\text{elec}}$  is the electrical power and  $\kappa$  is the conversion factor. By setting  $\kappa = 3$ , it is guaranteed that less than 0.3% of the signals are clipped and therefore the clipping noise is neglectable [22]. Therefore, the electrical SNR of the

UE at each effective subcarrier  $m$  can be denoted as:

$$\gamma_m = \frac{(R_{\text{APD}} P_{\text{rx,UE}})^2}{(M-2)\kappa^2 \sigma_n^2}, \quad m \in \{1, 2, \dots, M/2 - 1\}, \quad (5)$$

where  $P_{\text{rx,UE}}$  is given in (4);  $R_{\text{APD}}$  is the APD responsivity;  $\sigma_n^2$  is the total noise power for each subcarrier and the detailed discussion of  $\sigma_n^2$  will be given in the next subsection. Based on the Shannon capacity, the data rate for the UE can be expressed as [23]:

$$\zeta = \sum_{m=1}^{M/2-1} \frac{B_L}{M} \log_2(1 + \gamma_m) = \frac{(M/2-1)}{M} B_L \log_2 \left( 1 + \frac{(R_{\text{APD}} P_{\text{rx,UE}})^2}{(M-2)\kappa^2 \sigma_n^2} \right), \quad (6)$$

where  $B_L$  is the baseband modulation bandwidth.

### B. Receiver Noise

At the receiver, we utilize a high-bandwidth Indium gallium arsenide (InGaAs) APD (G8931-10), where it can work in the spectral range of 950 nm to 1700 nm. The peak sensitivity wavelength is 1550 nm. Parameters of this APD are given in Table I [24]. It is noted that the receiver bandwidth inversely depends on the capacitance of APD, i.e.,  $B_L = 1/(2\pi R_F C_T)$ , where  $C_T$  is the capacitance of the APD and  $R_F$  is the feedback resistor of the transimpedance amplifier. Therefore, small-area APDs are required to achieve wide bandwidth at the receiver. However, for small-area APDs, a lens is required at the receiver to collect enough power and consequently enhance the SNR. Optical receivers that use an APD are able to provide high SNR. This enhancement in SNR is due to the internal gain of the APD,  $G_{\text{APD}}$ . If the noise of the receiver was independent of the internal gain, the SNR would increase by a factor of  $G_{\text{APD}}^2$ .

TABLE I: APD parameters.

Parameter	Symbol	Value
Bandwidth	$B_L$	1.5 GHz
Spectral response range	-	950 to 1700 nm
Peak sensitivity wavelength	-	1550 nm
Physical area of APD	$A$	$\pi \times 0.07 \times 0.07 \times 10^{-6} \text{ m}^2$
Area of APD with lens	$A_{\text{eff}}$	$\pi \times 0.25 \times 0.25 \times 10^{-4} \text{ m}^2$
Receiver FOV	$\Psi_c$	60°
Gain of APD	$G_{\text{APD}}$	30
Responsivity	$R_{\text{APD}}$	0.9 A/W
Refractive index	$\varsigma$	1
Laser noise	RIN	-155 dB/Hz

Unfortunately, the noise depends on  $G_{\text{APD}}$  so that the SNR improvement is less than  $G_{\text{APD}}^2$  [25]. The noise at the receiver is due to three factors, namely thermal noise, shot noise and relative intensity noise (RIN). In the following, we will characterize the different types of noise at the receiver.

1) *Thermal Noise*: Thermal noise is characterized for an APD the same as other PDs. The power spectral density (PSD) of thermal noise is given as [26]:

$$S_{\text{thermal}}(f) = \frac{4k_{\text{B}}T}{R_{\text{F}}}, \quad (7)$$

where  $k_{\text{B}}$  is the Boltzmann's constant,  $T$  is absolute temperature.

2) *Shot Noise*: In optical communication, shot noise is due to the random nature of photon arrivals with an average rate determined by the incidence optical power. The PSD of the shot noise for an APD is given as:

$$S_{\text{shot}}(f) = 2qG_{\text{APD}}^2 F_{\text{A}} R_{\text{APD}} (P_{\text{rx,UE}} + P_{\text{n}}), \quad (8)$$

where  $q$  denotes the electron charge and the average ambient power is represented by  $P_{\text{n}}$ . We note that under the condition of  $P_{\text{n}} \gg P_{\text{rx,UE}}$  the shot noise is signal independent and is only affected by the ambient light. In (8),  $F_{\text{A}}$  is called the excess noise factor and can be obtained as:

$$F_{\text{A}} = k_{\text{A}} G_{\text{APD}} + (1 - k_{\text{A}}) \left( 2 - \frac{1}{G_{\text{APD}}} \right), \quad (9)$$

where  $0 < k_{\text{A}} < 1$  is a dimensionless parameter.

3) *Relative Intensity Noise*: RIN is another type of noise induced mainly due to the instability in the transmit power of the VCSEL. Cavity variation and fluctuations in the laser gain are two major contributors to the RIN. The variance of power fluctuations is given as [27]:

$$\sigma_{\text{I}}^2 = (R_{\text{APD}} P_{\text{rx,UE}} r_{\text{I}})^2, \quad (10)$$

where  $r_{\text{I}}$  is a measure of the noise level of the optical signal and is given as:

$$r_{\text{I}}^2 = \int_{-\infty}^{\infty} \text{RIN}(f) df, \quad (11)$$

where  $\text{RIN}(f)$  is the intensity noise spectrum. For a limited bandwidth receiver, the above integral should be calculated over the receiver bandwidth. It is noted that  $r_{\text{I}}$  is simply the inverse

of the transmit optical power. For simplicity, we assume that  $\text{RIN}(f)$  is a constant value over the whole bandwidth, i.e.,  $\text{RIN}(f) = \text{RIN}$ . Hence, the PSD of the relative noise intensity can be denoted as:

$$S_{\text{RIN}}(f) = \text{RIN}(R_{\text{APD}}P_{\text{rx,UE}})^2. \quad (12)$$

4) *Total Noise*: Finally, the total noise power for each subcarrier at the receiver can be expressed as:

$$\sigma_n^2 = \frac{4k_B T}{R_F} B_L/M + 2qG_{\text{APD}}^2 F_A R_{\text{APD}}(P_{\text{rx,UE}} + P_n) B_L/M + \text{RIN}(R_{\text{APD}}P_{\text{rx,UE}})^2 B_L/M. \quad (13)$$

### C. Retroreflector

A retroreflector can reflect part of the incident beam back to the direction it came from. The retroreflector can be realized by a CCR, retroreflective sheeting or even retroreflective spray paint [28]. In this paper, the property of a CCR is studied. As the distance between the Tx and the CCR,  $d$ , is much larger than the size of a CCR, all the incident rays can be considered to be

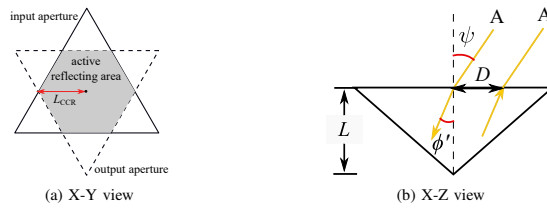


Fig. 3: Corner-Cube retroreflector

parallel with an incident angle of  $\psi$ . According to Snell's law, the refracted angle  $\phi' = \sin^{-1} \frac{\sin \psi}{n_{\text{re}}}$ , where  $n_{\text{re}}$  is the refractive index of the retroreflector. Fig. 3a shows the result for a triangular corner-cube reflector at normal incidence. The solid line is the input aperture, which is the shape of the CCR face, and the dotted line is the output aperture which is the outline of the retroreflected beam. The overlap area of the input and output aperture is the active reflecting area, and the incident rays outside this area will not be retroreflected. Fig. 3b shows the result for a triangular corner-cube reflector at oblique incidence. The displacement of input and output apertures,  $D$ , can be obtained as:

$$D = 2L \tan \phi', \quad (14)$$

where  $L$  is the length of the CCR. The size of the active reflecting area mainly depends on  $L_{CCR}$ , which is shown in Fig. 3a.

### III. BEAM ACTIVATION

For a VCSEL array system, it is important to determine which beam should be activated to optimize the system performance. The beam selection strategy considered in this study is the signal strength strategy (SSS), which only selects the beam providing the highest received power. Other beam selection strategies can be applied to activate two or more beams simultaneously to achieve better performance. However, two or more beams consume more power, which may not be energy efficient. The trade of between spectrum and energy efficiency will be considered in our future work. Therefore, the index of the serving beam for the user is expressed as:

$$I = \arg \max_{n \in \mathcal{N}} P_{rx,UE}^n, \quad (15)$$

where  $\mathcal{N}$  is the set of beams and  $P_{rx,UE}^n$  is the received optical power of the user from the  $n$ -th beam. To solve (15), the knowledge of user location is required. The cell size is very small in the VCSEL array system, therefore, an accurate localization technique is needed. For the mobile UE, the user tracking system is required to update the location of the UE quickly and frequently. The VLP can easily achieve sub-meter accuracy. However, most VLP localization technologies utilize the downlink transmission of the VLC system [1], which requires extra light setting for the proposed system. In addition, the location information needs to be processed and sent back to the server, which causes extra delays to the real-time beam activation system. Two beam activation schemes are proposed in this study to address the power consumption and delay issue. The first method is a passive beam activation scheme, which uses a CCR to obtain a power matrix and then find the serving beam. The second method uses the ODTx in the uplink communication. The details of these two schemes are presented in the following subsections.

#### A. Systems with a CCR

A CCR can reflect part of the incident light to the opposite direction. Based on this property, a passive beam activation is proposed to reduce the power consumption of the battery-operated UE and the latency. A CCR will be mounted next to the Rx of a UE and will reflect part of the transmitting light back to the source beam. As shown in Fig. 4, a PD, which is referred to as RxAP, is mounted next to each source beam to detect the light reflected by the CCR. The

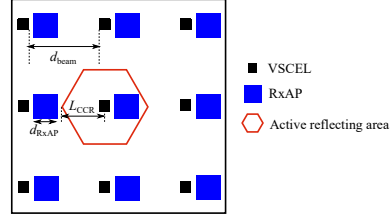


Fig. 4: The setup of the AP in the VCSEL array system using a CCR ( $N_{\text{beam}} = 9$ ).

area bounded by the red line in Fig. 4 is the active reflecting area, which is the area hit by the retroreflected light. As discussed in Section II-C, the size of the active reflecting area is determined by  $L_{\text{CCR}}$ , which mainly depends on the size of the retroreflector. To make sure the light transmitted by the source beam, after being reflected by the CCR, will only be received by the RxAP next to this source beam, the source beams need to be separated from each other with a distance of  $d_{\text{beam}} \geq L_{\text{CCR}} + d_{\text{RxAP}}$ . In this study, the orientation of the Rx and CCR are assumed to be fixed and vertically upward. However, it should be noted that due to the limitation of the maximum incident angle of the CCR and the rotation of the UE, a single Rx may not always receive the signal and a single CCR may not always reflect the light back to the reversed direction. As a result, when a UE's orientation is considered, multiple Rxs and CCRs should be mounted in different directions to solve the issue. The structure of multiple Rxs and CCRs, which ensures that the system is robust against random orientation, will be a subject for future studies. In terms of beam activation mechanism, before transmitting the data packet, all the beams will send test signals simultaneously. By monitoring the power matrix, which is the power received by the array of RxAPs, the beam corresponds to the RxAP receiving the maximum reflected power will be activated to transmit the data packet. Therefore, the index of the source beam for the UE in (15) can be reformulated as:

$$I = \arg \max_{n \in \mathcal{N}} P_{\text{RxAP}}^n, \quad (16)$$

where  $P_{\text{RxAP}}^n$  is the received power, reflected by the UE's CCR, of the  $n$ -th RxAP.

By covering the front face of the CCR with a liquid crystal display (LCD), the retroreflected light can be modulated [16]. In addition, the power consumption of the LCD with its driver circuit is only in the order of tens of  $\mu\text{W}$ . The use of the LCD serves multiple purposes. First,



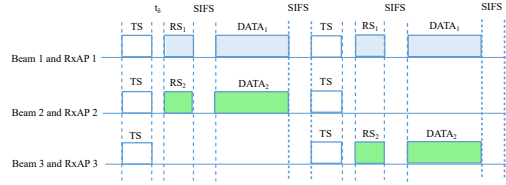


Fig. 5: Beam activation mechanism.

it can be used to determine whether a UE is active and requires data communication. Second, it helps to distinguish the active UE from mirrors or CCRs in the environment. Finally, for a multi-user scenario, the active UEs can be distinguished among each other through modulating the retroreflected light differently.

The beam activation mechanism is shown in Fig. 5. At the beginning, all the beams send test signals (TS) simultaneously. It is noted that the TS can be unmodulated light. The UE will retroreflect and modulate the TS into the reflected signal (RS), and the RS will be received by the corresponding RxAP after a mean propagation delay of  $t_\delta$ . The beam will be activated based on (16). Then, the data frame will be transmitted by the serving beam after a short inter-frame space (SIFS). In Fig. 5, firstly, beams 1, 2, and 3 send TS simultaneously. Then, the RxAP 1 and 2 receive RS retroreflected by the UE 1 and UE 2, respectively, while the RxAP 3 does not receive any reflected signal. Therefore, beams 1 and 2 are activated to transmit data frames to UE 1 and UE 2, respectively. After the SIFS, all the beams send TS again. Here, the RxAP 3 receives RS retroreflected by the UE 2, which means that UE 2 moved to the cell served by the beam 3. Hence, the beam 3 is activated to transmit data to the UE 2 while the beam 2 is deactivated. As a consequence, real-time tracking of UEs and real-time beam activation can be executed with almost zero-delay for a UE with ultra-low power and no computational capability. In addition, the proposed system with CCR does not first require the estimation of the position of UEs.

*Signaling Cost Analysis:* The effective throughput can be obtained based on the ratio of the time allocated for data transmission and the total time including that used for the signaling. Accordingly, we have:

$$t_{\text{Data}} = \frac{L_{\text{Data}}}{\zeta_{\text{down}}}, \quad t_{\text{tot}} = t_{\text{Data}} + t_{\text{delay}}, \quad (17)$$

$$t_{\text{delay}} = t_{\text{TS}} + t_\delta + t_{\text{RS}} + t_{\text{SIFS}} + t_{\text{SIFS}},$$

TABLE II: Parameters of beam activation mechanism.

Parameter	Symbol	Value
Test signal time	$t_{TS}$	0.3 micro-seconds
Reflected signal time	$t_{RS}$	0.3 micro-seconds
Average length of data packet [29]	$L_{Data}$	64 Kbytes
Mean propagation delay [30]	$t_{\delta}$	3 ns
SIFS [29]	SIFS	2 micro-seconds

where  $t_{Data}$  is the average data transmission time;  $L_{Data}$  is the average data packet length;  $\zeta_{down}$  is the average downlink data rate which can be obtained based on (6); the  $t_{delay}$  is the delay time; and  $t_{tot}$  is the total time required to complete the transmission of a packet;  $t_{TS}$  and  $t_{RS}$  are the signaling periods;  $t_{SIFS}$  is the time required for the SIFS. Assuming there is no collision, the effective throughput can be obtained as:

$$\mathcal{T}_{eff} = \frac{t_{Data}}{t_{tot}} \zeta_{down}. \quad (18)$$

#### B. Systems with ODTx on the UE

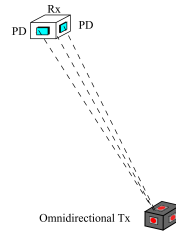


Fig. 6: Localization using the ODTx.

In this study, an alternative scheme is proposed for beam activation by using ODTx for the wireless infrared uplink transmission. An ODTx, which achieves omnidirectional transmission characteristics by using multiple transmitting elements, is first proposed for LiFi systems in [31]. The structure of this ODTx is shown in Fig. 6. There is one infrared LED located on each side of the UE. It is assumed that the infrared LED follows Lambertian radiation and  $m$  is the Lambertian order which is given as  $m = 2$ . The received optical power of a PD from the ODTx can be written as [31]:

$$P_{rx,OD} = \begin{cases} \frac{(m+1)P_{tx,OD}A_{OD}n_{ref}^2 \cos(\psi_{OD})}{2\pi d^2 \sin^2(\Psi_{OD})}, & \psi_{OD} \leq \Psi_{OD} \\ 0, & \text{otherwise} \end{cases}, \quad (19)$$

where  $R_{PD}$  is the PD responsivity and  $P_{tx,OD}$  is the transmitted optical power of a single infrared LED in the ODTx;  $A_{OD}$  represents the physical area of the PD;  $n_{ref}$  denotes the internal refractive index; the incidence angle of the PD is  $\psi_{OD}$  and the FOV of the PD is  $\Psi_{OD}$ . Based on (19), it can be observed that the received optical power is independent of the irradiance angle of the ODTx, which means that the rotation of the UE will not change  $P_{rx,OD}$ . Consequently, the received optical power only depends on the position of the UE,  $p_{UE}$ .

By mounting multiple PDs in different orientations on the ceiling, multiple RSS values,  $P_{rx,OD}$ , can be collected. In indoor positioning systems, RSS-based methods have been widely adopted since RSS values are easy to obtain [15]. In this study, the ANN algorithm is used to estimate the user position. The main motivation of using ANN is that it can estimate the beam activation directly without estimating the UE location, which reduces the latency. Other methods require the prediction of the user position using techniques, such as fingerprinting, proximity and trilateration first and then complete the beam activation. Conventionally, the ANN is adopted to estimate the user position and after finding the position of the UE,  $p_{UE}$ , the beam that needs to be activated can be obtained based on (15). Fig. 7a shows the layout of the ANN for the UE localization. The input of the ANN is the RSS from 5 receiving PDs facing in different directions. There are  $N_{hidden}$  neurons in the hidden layer and the activation function is a rectified linear unit (ReLU). In the output layer, the sigmoid activation function is adopted and the output is the position of the UE  $p_{UE}$ , which should be normalized. Then, the index of the serving beam can be calculated based on (15). In this study, the proposed ANN predicts the index of serving beam directly without the need of positioning first. The layout of the ANN for beam activation is shown in Fig. 7b. The input and hidden layer is the same as the counterpart in the ANN for

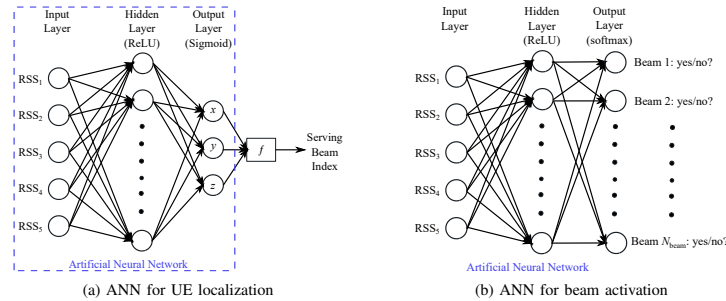


Fig. 7: The ANN structures

1  
2  
3  
4  
5  
6  
7  
8  
9  
10  
11  
12  
13  
14  
15  
16  
17  
18  
19  
20  
21  
22  
23  
24  
25  
26  
27  
28  
29  
30  
31  
32  
33  
34  
35  
36  
37  
38  
39  
40  
41  
42  
43  
44  
45  
46  
47  
48  
49  
50  
51  
52  
53  
54  
55  
56  
57  
58  
59  
60

UE localization, while the output layer uses the softmax activation function and the number of output neurons equals the number of beams  $N_{\text{beam}}$ . The value of each output neuron represents the probability of activating the corresponding beam. As the SSS is adopted here, the beam with highest probability should be selected as the serving beam for the UE. The beam activation can be executed in two steps: the offline training of ANN and then the online activating of beams. The RSS data in this study can be generated based on the ideal channel model in (19). However, the Lambertian irradiation model is not exactly accurate in real applications. To ensure the accuracy of the beam activation, the ANN can be pre-trained using the data from the ideal model and then trained with the on-site data [32].

Users can access the uplink and receive the data on downlink simultaneously since the uplink and downlink are operating on different wavelengths and there would be no interference between them. It is assumed that the uplink is always active for data or TS transmission. By using the collected uplink RSS values, the index of the serving beam can be predicted. However, the delay time,  $t_{\text{delay}}$ , of the system is caused by the signal propagation from the ODTx to the AP and the ANN processing time to estimate the active beam index. The signal propagation time, which is in the order of tens of ns, can be ignored when compared with the ANN processing time. Hence, the  $t_{\text{delay}}$  is mainly determined by the ANN processing. For a static user, the effect of  $t_{\text{delay}}$  can be ignored. If the user is moving,  $t_{\text{delay}}$  should be taken into account when evaluating the system performance. It is noted that this method can be still applied to mobile users with low speed however for those users with high speed the delay due to ANN mechanism can cause the location information be outdated and a wrong beam might be activated. When there are multiple UEs, multiple access schemes such as time division multiple access (TDMA), frequency division multiple access (FDMA), or carrier sense multiple access with collision avoidance (CSMA/CA) should be adopted.

#### IV. SYSTEM LEVEL ANALYSIS

##### A. System with single user

In a VCSEL array system, the total number of beams is denoted as  $N_{\text{beam}}$  and the beams are pointing in different directions. Therefore, the channel gain distribution is different for each beam. The central beam, which points vertically downward, provides the best channel as it has the shortest distance to the UE. Hence, initially, we will start with the central beam and then we extend the analysis to the whole system. In a single user system, the SNR and average data rate of the  $n$ -th beam are represented as  $\gamma_{\text{single}}^n$  and  $\bar{\zeta}_{\text{single}}^n$ , respectively. The central beam is

assumed to be the 1<sup>st</sup> beam and its SNR and average data rate are denoted as  $\gamma_{\text{single}}^1$  and  $\zeta_{\text{single}}^1$ , respectively. For the central beam, the horizontal distance between an active user and the cell center is denoted as  $r$ . The PDF of  $r$  can therefore be given as:

$$f_r(r) = \frac{2r}{R^2}, \quad r \leq R, \quad (20)$$

where  $R$  is the radius of the service region of the central beam and  $R = \sqrt{d_{\text{cell}}^2/\pi}$ . As the central beam is pointing vertically downward,  $\cos \phi = \cos \psi = h/\sqrt{h^2 + r^2}$ ,  $\sin \phi = r/\sqrt{h^2 + r^2}$  and  $d = \sqrt{h^2 + r^2}$ . Hence, for UEs served by the central beam, (4) can be reformulated as:

$$P_{\text{rx,UE}}(r) = \frac{2g(\psi)P_{\text{tx,opt}}A_{\text{eff}}G_{\text{APD}}}{\pi W^2(h)} \frac{h}{\sqrt{h^2 + r^2}} \exp\left(-\frac{2r^2}{W^2(h)}\right). \quad (21)$$

For a single user case, the system is noise-limited and there is no interference. Therefore, the SNR given in (5) for the user served by the central beam can be obtained as:

$$\gamma_{\text{single}}^1(r) = \frac{(R_{\text{APD}}P_{\text{rx,UE}}(r))^2}{(M-2)\kappa^2\sigma_n^2} = \frac{\gamma_0}{h^2 + r^2} \exp\left(-\frac{4r^2}{W^2(h)}\right). \quad (22)$$

where  $\gamma_0 = \left(\frac{2R_{\text{APD}}g(\psi)P_{\text{tx,opt}}A_{\text{eff}}G_{\text{APD}}h}{\pi W^2(h)\sqrt{M-2}\kappa\sigma_n}\right)^2$ . The SNR in decibel (dB) can be expressed as:

$$\gamma_{\text{db}}^1(r) = 10 \log_{10}(\gamma_{\text{single}}^1(r)). \quad (23)$$

Recalling from the fundamental theorem of a function of a random variable [33], the PDF of  $\gamma_{\text{db}}^1$  can be written as:

$$f_\gamma(\gamma) = \frac{f_r(r_0)}{\left|\frac{d}{dr}\gamma_{\text{db}}^1(r)\right|_{r=r_0}} = \frac{\log(10)(h^2 + r_0^2)W^2(h)}{10R^2(4h^2 + 4r_0^2 + W^2(h))}, \quad (24)$$

where

$$r_0 = f_r^{-1}(\gamma) = \frac{1}{2} \sqrt{W^2(h)W_k\left(\frac{4\gamma_0 \exp\left(\frac{4h^2}{W^2(h)} - \gamma \log(10)/10\right)}{W^2(h)}\right) - 4h^2}, \quad \gamma_{\text{db}}^1(R) \leq \gamma \leq \gamma_{\text{db}}^1(0), \quad (25)$$

where  $W_k(\cdot)$  is the Lambert W function, also called as the omega function or product logarithm.

As  $0 \leq r_0 \leq R \ll h$ , the PDF of  $\gamma_{\text{db}}^1$  in (24) can be approximated as:

$$f_\gamma(\gamma) \approx \frac{\log(10)(h^2)W^2(h)}{10R^2(4h^2 + W^2(h))}, \quad \gamma_{\text{db}}^1(R) \leq \gamma \leq \gamma_{\text{db}}^1(0), \quad (26)$$

Therefore, the approximated PDF of  $\gamma_{\text{db}}^1$  is a uniform distribution function between  $\gamma_{\text{db}}^1(R)$  and  $\gamma_{\text{db}}^1(0)$ , where  $\gamma_{\text{db}}^1(R)$  and  $\gamma_{\text{db}}^1(0)$  can be obtained from (23).

Based on (6) and (22), the data rate of the central beam at radius  $r$  can be represented as:

$$\zeta_{\text{single}}^1(r) = \frac{M/2 - 1}{M} B_L \log_2\left(1 + \frac{\gamma_0}{h^2 + r^2} \exp\left(-\frac{4r^2}{W^2(h)}\right)\right). \quad (27)$$

Therefore, the average data rate of the central beam can be written as:

$$\begin{aligned}
 \bar{\zeta}_{\text{single}}^1 &= \mathbb{E}[\zeta_{\text{single}}^1(r)] \\
 &= \int_0^R \frac{M/2-1}{M} B_L \log_2 \left( 1 + \frac{\gamma_0}{h^2+r^2} \exp \left( -\frac{4r^2}{W^2(h)} \right) \right) f_r(r) \, dr \\
 &= \frac{M-2}{2M} B_L \int_0^R \log_2 \left( 1 + \frac{\gamma_0}{h^2+r^2} \exp \left( -\frac{4r^2}{W^2(h)} \right) \right) \frac{2r}{R^2} \, dr \\
 &\approx \frac{M-2}{2 \log(2) M R^2} B_L \int_0^R 2r \log \left( \frac{\gamma_0}{h^2+r^2} \exp \left( -\frac{4r^2}{W^2(h)} \right) \right) \, dr \\
 &= \frac{M-2}{2 \log(2) M R^2} B_L \left[ (h^2 + R^2) \log \left( \frac{\gamma_0}{h^2 + R^2} \right) + R^2 - h^2 \log \left( \frac{\gamma_0}{h^2} \right) - \frac{2R^4}{W^2(h)} \right].
 \end{aligned} \tag{28}$$

For a single-user case, the average data rate of the VCSEL array system,  $\bar{\zeta}_{\text{single}}^{\text{sys}}$ , is the mean of the average data rate of all beams, which can be expressed as:

$$\bar{\zeta}_{\text{single}}^{\text{sys}} = \frac{1}{N_{\text{beam}}} \sum_n^{N_{\text{beam}}} \bar{\zeta}_{\text{single}}^n \leq \frac{1}{N_{\text{beam}}} \sum_n^{N_{\text{beam}}} \bar{\zeta}_{\text{single}}^1 = \bar{\zeta}_{\text{single}}^1 = \bar{\zeta}_{\text{single}}^{\text{UB}}, \tag{29}$$

where  $\bar{\zeta}_{\text{single}}^{\text{UB}}$  denotes the upper bound of the system average data rate in a single-user scenario.

According to (29), the upper bound is the average data rate of the central beam,  $\bar{\zeta}_{\text{single}}^1$ .

### B. System with Multiple users

The performance of a multi-user system is limited by two factors: noise and inter-cell interference (ICI). When multiple UEs are served by the same beam, due to the high-directionality of each Tx in the VCSEL array system, SDMA proposed in [6] will be adopted. Based on (15), the UEs served by the same beam are grouped together. Multiple beams can serve corresponding UEs simultaneously within the same time slot as the interference between these narrow beams can be significantly mitigated. Active UEs served by the same beam share the bandwidth resource equally. Hence, the data rate of the optical SDMA system can be expressed as:

$$\zeta_{\text{multi}}^{\text{sys}} = \sum_{n=1}^{N_{\text{beam}}} \sum_{\mu=1}^{N_{\text{UE}}^n} \zeta_{\text{multi},\mu}^n = \sum_{n=1}^{N_{\text{beam}}} \sum_{\mu=1}^{N_{\text{UE}}^n} \frac{1}{N_{\text{UE}}^n} \zeta_{\text{single},\mu}^n \tag{30}$$

where  $\zeta_{\text{multi},\mu}^n$  is the data rate of user  $\mu$  served by  $n$ -th beam in the multi-user scenario;  $N_{\text{UE}}^n$  is the number of active UEs served by the  $n$ -th beam; and  $\zeta_{\text{single},\mu}^n$  is data rate of user  $\mu$  served by  $n$ -th beam in a single-user scenario. For the best-case scenario, it is assumed that all the beams are utilizing different wavelengths, which should be perfectly distinguished by the optical

receiver. Therefore, the system is noise limited as ICI is completely avoided and the signal to interference-plus-noise ratio (SINR) is represented as shown in (22). Hence, the average data rate of the central beam can be written as:

$$\bar{\zeta}_{\text{multi}}^1 = \mathbb{E}\left[\sum_{\mu=1}^{N_{\text{UE}}^1} \zeta_{\text{multi},\mu}^1\right] = \sum_{\mu=1}^{N_{\text{UE}}^1} \frac{1}{N_{\text{UE}}^1} \mathbb{E}\left[\zeta_{\text{single}}^1(r_{\mu})\right] = \bar{\zeta}_{\text{single}}^1, \quad (31)$$

where  $\zeta_{\text{multi},\mu}^1$  is the data rate of user  $\mu$  served by the central beam, and  $r_{\mu}$  is the horizontal distance between the user  $\mu$  and the center of central cell. We can see that the average data rate of the central beam for the multi-user scenario is the same as the one for the single-user scenario. It should be noted that the average data rate of other beams is less than the average data rate of the central beam. Hence, the average data rate of the entire system for multi-user scenario will be upper bounded as follows:

$$\bar{\zeta}_{\text{multi}}^{\text{sys}} = \sum_{n=1}^{N_{\text{beam}}} \bar{\zeta}_{\text{multi}}^n \leq \bar{N}_{\text{a}} \bar{\zeta}_{\text{multi}}^1 = \bar{\zeta}_{\text{multi}}^{\text{UB}}, \quad (32)$$

where  $\bar{N}_{\text{a}}$  denotes the average number of active beams and  $\bar{\zeta}_{\text{multi}}^{\text{UB}}$  denotes the upper bound of the average data rate in the VCSEL array system. The value of  $\bar{N}_{\text{a}}$  depends on the total number of active UEs,  $N_{\text{UE}}$ , in the system as well as the total number of beams,  $N_{\text{beam}}$ , on the Tx, and it can be calculated as follows [34]:

$$\bar{N}_{\text{a}} = N_{\text{beam}} - N_{\text{beam}}(1 - 1/N_{\text{beam}})^{N_{\text{UE}}}. \quad (33)$$

If the number of active UEs are infinite,  $N_{\text{UE}} = \infty$ , the average number of active beams,  $\bar{N}_{\text{a}}$ , is equal to the total number of beams on the Tx. On the other hand, when there is only one active UE,  $\bar{N}_{\text{a}} = 1$ .

## V. SIMULATION RESULTS

First of all, it should be noted that for all simulations in this study, the corresponding transmit power of beams for different values of  $\theta_{\text{FWHM}}$  are based on the eye safety regulations given in Appendix. Hence, the transmit power for  $\theta_{\text{FWHM}}$  of  $2^\circ$ ,  $4^\circ$  and  $6^\circ$  are 19, 60 and 129 mW,

TABLE III: Parameters in Zemax simulation

$d_{\text{beam}}$	$L_{\text{CCR}}$	$d_{\text{RxAP}}$	AP height	UE height	$\theta_{\text{FWHM}}$
12 mm	5 mm	5 mm	3.5 m	1.5 m	$4^\circ$

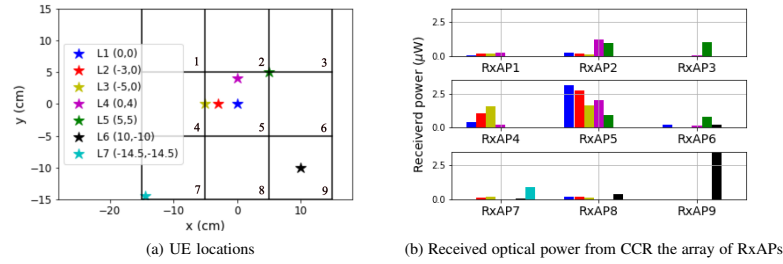


Fig. 8: The UE locations and received power matrix,  $N_{\text{beam}} = 9$ .

respectively. To test the accuracy of the beam activation using CCR, the simulation with a beam number of  $N_{\text{beam}} = 9$  is carried out in Zemax and the result is presented in Fig. 8. The parameters are listed in Table III. Each beam is pointed to the center of each square cell and the cell size is  $10 \text{ cm} \times 10 \text{ cm}$ . Seven UE positions are assumed as shown in Fig. 8a and the received power of each PD in the array of RxAPs is shown in Fig. 8b. When the UE is in L1, L2 or L4, which are inside cell 5, it can be seen that the RxAP 5 receives much higher power than other RxAPs and thus beam 5 should be activated. When the UE is at L3, which is in the boundary of cell 4 and 5, the RxAP 4 and RxAP 5 receives similar power. Therefore, based on the beam activation algorithm, either beam 4 or beam 5 or both of them should be activated. When the UE is inside cell 9 such as L6, RxAP 9 has the highest power and beam 9 will be activated. L7 is located in the corner of cell 7, for this case, only the RxAP 7 collects power from the retroreflected light. These simulation results show that by using the CCR, the system can activate the corresponding beam for the UE accurately. The IS-based VLP system proposed in [10] is selected as the benchmark scheme. According to (17) and Table II, the average latency, caused by the system can be calculated. Therefore, the average latency of the system using CCR is in the order of a few micro-seconds, which is significantly lower than the average positioning time, 44.3 ms, of the IS-based VLP system proposed in [10]. Hence, real-time fast tracking can be enabled by using the retroreflector. In the traditional VLP systems, if the position estimation is completed in the UE, the computation will add a high power burden to the UE. Also, in order to activate the best beam, it requires the autonomous transmission of users' location information from UE to APs. If the position estimation is done at the AP side, the UE needs to transmit data collected by the ISs or PDs to the AP for server-assisted computation. In conclusion, when the



traditional VLP system is applied for the beam activation, it always requires a real-time backward channel from UE to APs. However, with the utilization of a retroreflector, the backward channels can be replaced by the RS reflected by the retroreflector. In addition, no additional illumination devices are required as the TS is transmitted by the VCSEL array system, which severs the dual functionality of communication and positioning. Hence, the proposed beam activation method based on a retroreflector has the advantage of low latency, low power consumption and low cost.

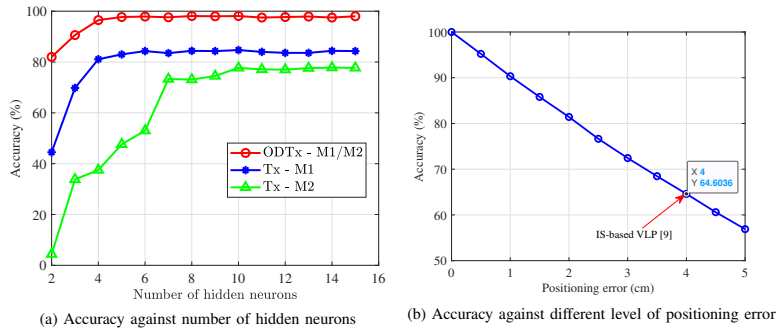


Fig. 9: Beam activation accuracy

The accuracy of the beam activation is analyzed in this part. The effect of device orientation is studied and two orientation models are considered here. The first orientation model (M1) is the Gaussian model proposed in [35] for elevation angle of the UE and the second orientation model (M2) is the uniform model, which assumes uniform distribution in all movement directions. To train the ANN,  $10^5$  samples, are generated based on the analytical model in (4) and (19). 80% of the data is used for the training set and 20% of the data is used for the test set. In a real scenario, the accuracy can be further increased by training the on-site data. As shown in Fig. 9a, the system with ODTx achieves 98% accuracy when  $N_{\text{hidden}} = 5$ . The selected benchmarks for comparison include: a) a single infrared-LED for uplink transmission and beam activation (which is called a single Tx in the rest of the paper), b) the IS-based VLP [10]. Systems with a single Tx can only achieve an accuracy of 82% and 78% for orientation models M1 and M2, respectively. The position error of the IS-based VLP system is around 4 cm [10], which leads to a poor activation accuracy of 64.6%, as shown in Fig. 9a. To achieve an accuracy of more than 90%, the positioning error is required to be less than 1 cm according to Fig. 9b. In terms of the beam activation latency for the system using ODTx, the delay time,  $t_{\text{delay}}$ , is mainly

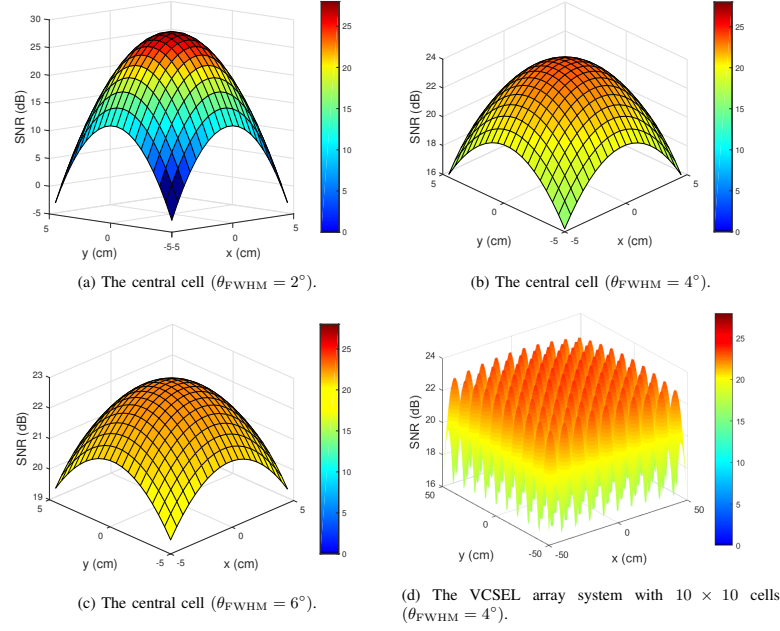


Fig. 10: SNR distribution in a single user system.

caused by the ANN processing time. In a laptop with Intel(R) Core(TM) i7-7700HQ CPU @ 2.8 GHz, the processing time of ANN with  $N_{\text{hidden}} = 5$  for user positioning is 29.7 ms, which is lower than the 44.3 ms of the IS-based VLP systems. In addition, no additional illumination device is required for the ODTx as it serves the purpose of uplink communication and beam activation simultaneously. In conclusion, the ODTx is much more robust against random device orientation compared with the single Tx system, while it has the advantage of higher accuracy, lower latency, lower power consumption and lower cost compared with the IS-based VLP.

The simulation results for systems with a single user scenario are shown in Fig. 10-12. In the central cell with a size of  $10 \text{ cm} \times 10 \text{ cm}$ , the SNR distribution is illustrated in Fig. 10a-10c for different values of  $\theta_{FWHM}$ . When  $\theta_{FWHM} = 2^\circ$ , the UE achieves the highest SNR, 27.7 dB, in the cell center. However the SNR at the cell corner is almost 0 dB. This is because the beam divergence angle is small and thus most of the power is focused around the beam center. By

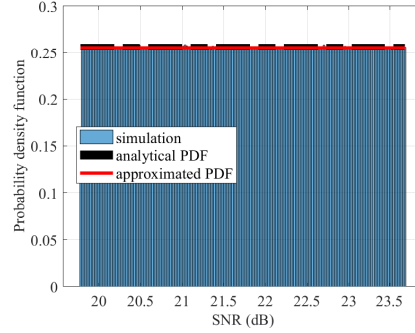


Fig. 11: Probability density function of the SNR for the central beam ( $\theta_{FWHM} = 4^\circ$ ).

increasing  $\theta_{FWHM}$  from  $2^\circ$  to  $4^\circ$ , although the transmit power increases from 19 mW to 60 mW, the peak SNR decreases to 23.7 dB since the beam is more diverged. However, the wider divergence angle leads to a great increase, 16 dB, in the SNR for the UE at the cell corner. With the further increase of  $\theta_{FWHM}$  to  $6^\circ$ , the transmit power doubles to 120 mW but the SNR slightly decreases to 22.7 dB. The advantage is that the UE at the cell corner can achieve a SNR of 19.4 dB. The SNR distribution of the VCSEL array system with  $10 \times 10$  beams is plotted in Fig. 10d. It can be seen that the distributions of all other cells have similar distributions to the central cell with a slight decrease in the SNR values.

To verify the PDF of the SNR derived for the central beam in (24), Monte-Carlo simulations are carried out and the histogram of SNR are plotted by the blue bars in Fig. 11. The analytical PDF in (24) is plotted by the black dash-dot line while the approximated PDF in (26) is plotted by the red line. As the red line, black dash-dot line and the histogram are well matched, the PDF of the SNR for the central beam can be well approximated by the uniform distribution expressed in (26).

Fig. 12 shows the average data rate for the central cell with different cell size. It can be seen that for different values of  $\theta_{FWHM}$ , the analytical derivation in (28) matched the Monte-Carlo simulation results. When the cell size is small, the central beam with  $\theta_{FWHM} = 2^\circ$  provides higher average data rate. However, with the increase in cell size, its average data rate decreases faster than the others. This is because with a smaller  $\theta_{FWHM}$ , the beam power is more focused on the center, which leads to high power in the cell center and low power in the edge, as shown

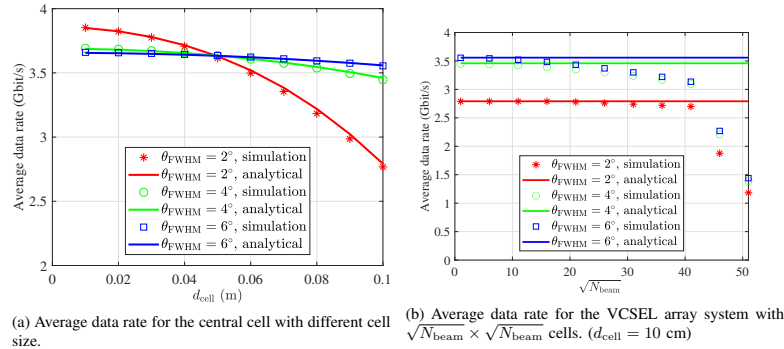


Fig. 12: Average data rate in a single user system.

in Fig. 10a. By increasing  $\theta_{\text{FWHM}}$ , the beam power is less focused. Therefore, the average data rate decreases slower when the cell size increases. When the cell size  $d_{\text{cell}}$  is 5 cm, the beam with  $\theta_{\text{FWHM}} = 2^\circ$  provides the highest data rate, 3.8 Gbit/s. However, when the cell size  $d_{\text{cell}}$  is 10 cm, the average data rate for  $\theta_{\text{FWHM}} = 4^\circ$  and  $\theta_{\text{FWHM}} = 6^\circ$  are 3.4 Gbit/s and 3.5 Gbit/s, respectively, which are higher than the average data rate for  $\theta_{\text{FWHM}} = 2^\circ$ , 2.7 Gbit/s. Fig. 12b demonstrates the average data rate for the VCSEL array system with  $N_{\text{beam}}$  beams and  $d_{\text{cell}} = 10$  cm. The number of beams along one axis is denoted as  $\sqrt{N_{\text{beam}}}$ . It can be seen from Fig. 12b that by varying the number of beams along one axis, the value of average data rate for the simulation results will be upper bounded by  $\bar{\zeta}_{\text{single}}^{\text{UB}}$  in (29). The result indicates that, in a VCSEL array system,  $\bar{\zeta}_{\text{single}}^{\text{UB}}$  is actually a good approximation of the average data rate when the number of cells is small. This occurs because the distance between the central cell and the edge cell is small, the SNR distribution of other cells will be similar to the SNR distribution of the central cell as shown in Fig. 10d. However, with the further increase of  $\sqrt{N_{\text{beam}}}$ , the distance between the central cell and the edge cell increases, which will lead to higher path loss and a decrease in the average data rate. In such cases,  $\bar{\zeta}_{\text{single}}^{\text{UB}}$  can only be considered as the upper bound instead of a well-approximation. It should be noted that for a single UE scenario with  $d_{\text{cell}} = 10$  cm, a VCSEL array system with  $\theta_{\text{FWHM}} = 4^\circ$  and  $6^\circ$  can provide similar performance, which is better than the system with  $\theta_{\text{FWHM}} = 2^\circ$ .

The simulation for systems with multiple users are carried out. The relationship between the number of UEs,  $N_{\text{UE}}$ , and the average data rate of the VCSEL array system ( $N_{\text{beam}} = 100$

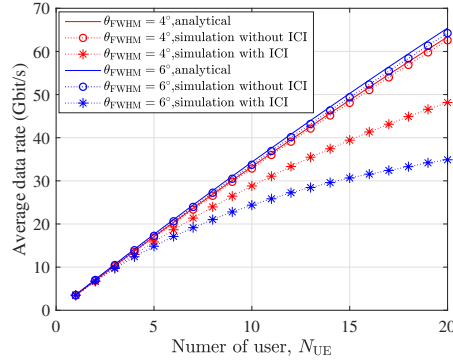


Fig. 13: Average data rate for the VCSEL array system with multiple users. ( $N_{\text{beam}} = 10 \times 10$ ,  $d_{\text{cell}} = 10$  cm).

and  $d_{\text{cell}} = 10$  cm) is shown in Fig. 13. For the ideal case without ICI, where each beam uses a different wavelength, the analytical derivation in (32) matches with the simulations without ICI for both  $\theta_{\text{FWHM}} = 4^\circ$  and  $6^\circ$ . This also gives the upper bound of the average data rate,  $\bar{\zeta}_{\text{multi}}^{\text{UB}}$ , for the VCSEL array system with multiple UEs. When all the beams are using the same wavelength, the ICI needs to be taken into consideration as the ICI will degrade the system performance. When the number of UEs,  $N_{\text{UE}}$ , is less than 6, we can see the average data rate of the system with ICI is very close to the average data rate of the system without ICI, and thus the average data rate of the system with ICI can be well approximated by (32) for small value of  $N_{\text{UE}}$ . With the increase of  $N_{\text{UE}}$  from 6 to 20, the chance of having ICI rises, which widens the gap between the average data rate of simulations with ICI and the average data rate of a system without ICI. Further increases in  $N_{\text{UE}}$  from 20 will lead to a larger gap between systems with and without ICI. It should be noted that in a VCSEL array system with multiple UEs, the system with  $\theta_{\text{FWHM}} = 4^\circ$  achieves a higher data rate than the system with  $\theta_{\text{FWHM}} = 6^\circ$ . When the cell size is fixed, a larger divergence angle means more power will reach the adjacent cells and will be treated as interference noise by UEs in the adjacent cells. Therefore, a small divergence angle can alleviate the ICI and increase the average data rate. When  $N_{\text{UE}} = 20$ , a throughput of around 50 Gbit/s can be achieved by systems with  $\theta_{\text{FWHM}} = 4^\circ$ , while only 33 Gbit/s can be achieved for a systems with  $\theta_{\text{FWHM}} = 6^\circ$ .

To calculate the system throughput, the user mobility should be considered and hence the

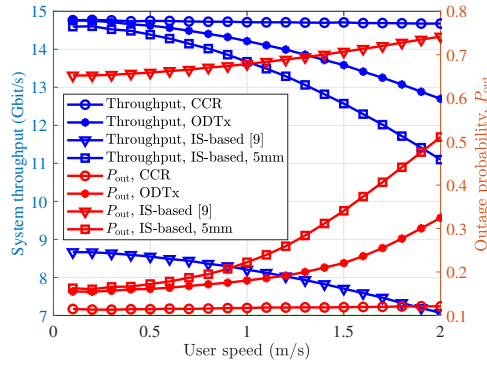


Fig. 14: Evaluation of system throughput and outage probability corresponding to user speed. ( $N_{\text{beam}} = 10 \times 10$ ,  $d_{\text{cell}} = 10$  cm,  $\theta_{\text{FWHM}} = 4^\circ$ ),  $N_{\text{UE}} = 5$ .

effect of the delay caused by the beam activation should be evaluated. It is assumed that all of the users are moving randomly following the random waypoint model [36]. In terms of the mechanism using CCR, the effective throughput,  $\mathcal{T}_{\text{eff}}$ , can be obtained based on (18). According to the parameters in Table II, it can be obtained that  $\mathcal{T}_{\text{eff}} = 0.98 \times \zeta_{\text{down}}$ . For the mechanism using ODTx, the latency,  $t_{\text{delay}}$ , is majorly caused by the ANN processing time. Hence, the beam activated at current time will be based on the user location in  $t_{\text{delay}}$  ms ago. In a laptop with Intel(R) Core(TM) i7-7700HQ CPU @ 2.8 GHz, the processing time of ANN with  $N_{\text{hidden}} = 5$  is 30 ms. The selected benchmarks for comparison include: a) the IS-based VLP proposed [10], b) the IS-based VLP system in which the position error is assumed to be 5 mm. The evaluation of system throughput and outage probability corresponding to the user speed is presented in Fig. 14. The outage probability,  $P_{\text{out}}$ , is defined as the probability that the user throughput is less than the required threshold data rate,  $R_T$ , where  $R_T$  is assumed to be 2.5 Gbit/s. When the IS-based VLP [10] is adopted for positioning and beam activation, due to the high positioning error and high latency, the effective system throughput is much lower than the other schemes while the outage probability is more than 60%. When the user speed is 0.1 m/s, by decreasing the positioning error of the IS-based scheme from 3.97 cm to 5 mm, the system throughput increases substantially from 8.7 Gbit/s to 14.5 Gbit/s, which achieves similar performance as the system with CCR and the system with ODTx. However, for high-speed users, the latency, caused by beam activation and positioning, can lead to outdated location information, and the wrong beam

may be activated. Therefore, when the user speed increases to 2 m/s, the system throughput of the IS-based scheme (5 mm positioning error) decreases rapidly to 11 Gbit/s. In comparison, due to the lower latency, the system throughput of the ODTx-based scheme only decreases to 12.8 Gbit/s. In terms of the CCR-based scheme, the system throughput and outage probability is independent of the user speed, which indicates the CCR mechanism has a extremely low latency and thus the effect of delay can be ignored.

## VI. CONCLUSION

In this study, a novel VCSEL array system, which supports high data rate, low latency and multiple user access without the requirement of expensive/complex hardware, is proposed. In addition, the choices of cell size and beam divergence angle are recommended. In order to support mobile users, two beam activation methods are proposed. The beam activation based on the CCR can achieve low power consumption and almost-zero delay, allowing real-time beam activation for high-speed users. The mechanism based on the ODTx is suitable for low-speed users and very robust to random orientation. The proposed methods exhibits significantly superior data rate and outage probability performance than the benchmark schemes. For a single UE scenario, regarding the central beam, the PDF of the SNR in dB can be considered as a uniform distribution. In addition, the analytical derivations for the average data rate of the central beam and its upper bound are presented and proved by simulations. This study may have great potential in guiding the designs in future experiment studies and performance analysis on the VCSEL array system. The research area is still broadly open for research and could be extended in many interesting directions, such as utilizing the spatial and multiplexing gain, designing the omnidirectional CCR and optimizing the resource management in a multi-VCSEL-array network.

## APPENDIX

When laser diodes or VCSEIs are deployed, it is necessary to consider eye safety, which will limit the value of the transmit power,  $P_{\text{tx,opt}}$ . In this section, the maximum allowable transmit optical power  $P_{\text{tx,max}}$  will be calculated based on regulations in the eye safety standard [37]. The Gaussian beam intensity at the distance  $z$  is:

$$I(r, z) = \frac{2P_{\text{tx,opt}}}{\pi W^2(z)} \exp\left(-\frac{2r^2}{W^2(z)}\right). \quad (34)$$

The aperture diameter of cornea is denoted as  $d_a$ . The exposure level of the cornea at distance  $z$  can be calculated as:

$$\begin{aligned} E_{\text{exp}}(z) &= \frac{1}{\pi(d_a/2)^2} \int_0^{d_a/2} I(r, z) 2\pi r \, dr \\ &= \frac{1}{\pi(d_a/2)^2} \int_0^{d_a/2} \frac{2P_{\text{tx,opt}}}{\pi W^2(z)} \exp\left(-\frac{2r^2}{W^2(z)}\right) 2\pi r \, dr. \\ &= \frac{P_{\text{tx,opt}}}{\pi(d_a/2)^2} \left(1 - \exp\left(-\frac{d_a^2}{2W^2(z)}\right)\right) \end{aligned} \quad (35)$$

The level of radiation to which persons may be exposed without suffering adverse effects is called the maximum permissible exposure (MPE). Exposures above the MPE will lead to eye injuries. Instead of actually performing an MPE analysis for all locations along the beam, the exposure level at the most hazardous position (MHP),  $z_{\text{mph}}$ , can be calculated and compared with the MPE. If the exposure level at the MHP,  $E_{\text{exp}}(z_{\text{mph}})$ , is less than the MPE, then the MPE is not exceeded anywhere else in the beam [38]. Hence, when considering eye safety,  $E_{\text{exp}}(z_{\text{mph}}) \leq E_{\text{mpe}}(t_{\text{exp}})$ , where  $t_{\text{exp}}$  represents the exposure duration and  $E_{\text{mpe}}(t_{\text{exp}})$  represents the MPE value corresponding to  $t_{\text{exp}}$ . Therefore, the maximum allowable transmit optical power  $P_{\text{tx,max}}$  can be written as:

$$P_{\text{tx,max}}(t_{\text{exp}}) = \frac{\pi d_a^2 E_{\text{mpe}}(t_{\text{exp}})}{4 \left(1 - \exp\left(-\frac{d_a^2}{2W^2(z_{\text{mph}})}\right)\right)}. \quad (36)$$

When the angular subtense of the apparent source is less than 1.5 mrad, the MPH,  $z_{\text{mph}}$ , is 10 cm. The MPE value  $E_{\text{mpe}}(t_{\text{exp}})$  can be calculated based on parameters in Table IV [37]. The maximum allowable transmit optical power,  $P_{\text{tx,max}}$  is plotted against the exposure duration  $t_{\text{exp}}$  in Fig. 15 for different wavelengths and different  $\theta_{\text{FWHM}}$ . The  $P_{\text{tx,max}}$  for  $\lambda = 1550$  nm is much larger than the  $P_{\text{tx,max}}$  for  $\lambda = 850$  nm so that  $\lambda = 1550$  nm is chosen in this study for higher data rate communication. The maximum allowable transmitted power,  $P_{\text{tx,max}}$ , for  $\theta_{\text{FWHM}} = 2^\circ$ ,  $4^\circ$ ,  $6^\circ$  are 20 mW, 60 mW, and 130 mW, respectively.

TABLE IV: Parameters for eye safety

	$\lambda = 1550$ nm		$\lambda = 850$ nm	
Exposure duration, $t_{\text{exp}}$ (s)	0.35 to 10	10 to $10^3$	$10^{-3}$ to 10	10 to $10^3$
MPE, $E_{\text{mpe}}$ ( $\text{W} \cdot \text{m}^{-2}$ )	$10^4/t_{\text{exp}}$	1000	$18t_{\text{exp}}^{0.75}C_4/t_{\text{exp}}$	$10C_4C_7$
Aperture stop (mm) $d_a$	$1.5t_{\text{exp}}^{3/8}$	3.5	7	7
$C_4$	-	-	$10^{0.002(\lambda-700)}$	$10^{0.002(\lambda-700)}$
$C_7$	-	-	1	1



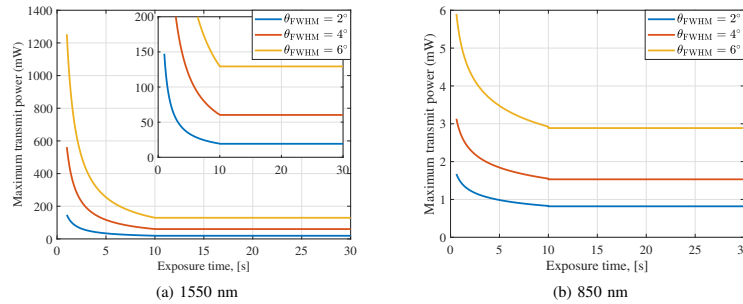


Fig. 15: Maximum transmit power considering eye safety

## REFERENCES

- [1] T. Koonen, F. Gomez-Agis, F. Huijskens, K. A. Mekonnen, Z. Cao, and E. Tangdionga, "High-Capacity Optical Wireless Communication Using Two-Dimensional IR Beam Steering," *Journal of Lightwave Technology*, vol. 36, no. 19, pp. 4486–4493, Oct 2018.
- [2] H. Haas, L. Yin, Y. Wang, and C. Chen, "What Is LiFi?" *Journal of Lightwave Technology*, vol. 34, no. 6, pp. 1533–1544, March 2016.
- [3] S. Ma, R. Yang, H. Li, Z.-L. Dong, H. Gu, and S. Li, "Achievable rate with closed-form for siso channel and broadcast channel in visible light communication networks," *Journal of Lightwave Technology*, vol. 35, no. 14, pp. 2778–2787, 2017.
- [4] M. S. Islim, R. X. Ferreira, X. He, E. Xie, S. Videv, S. Viola, S. Watson, N. Bamiedakis, R. V. Pentty, I. H. White, A. E. Kelly, E. Gu, H. Haas, and M. D. Dawson, "Towards 10 Gb/s Orthogonal Frequency Division Multiplexing-based Visible Light Communication Using a GaN Violet Micro-LED," *Photon. Res.*, vol. 5, no. 2, pp. A35–A43, Apr 2017.
- [5] R. Bian, I. Tavakkolnia, and H. Haas, "15.73 gb/s visible light communication with off-the-shelf leds," *J. Lightwave Technol.*, vol. 37, no. 10, pp. 2418–2424, May 2019. [Online]. Available: <http://jlt.osa.org/abstract.cfm?URI=jlt-37-10-2418>
- [6] Z. Chen, D. A. Basnayaka, and H. Haas, "Space Division Multiple Access for Optical Attocell Network Using Angle Diversity Transmitters," *Journal of Lightwave Technology*, vol. 35, no. 11, pp. 2118–2131, June 2017.
- [7] A. M. J. Koonen, C. W. Oh, and E. Tangdionga, "Reconfigurable free-space optical indoor network using multiple pencil beam steering," in *2014 OptoElectronics and Communication Conference and Australian Conference on Optical Fibre Technology*, July 2014, pp. 204–206.
- [8] T. Koonen, J. Oh, K. Mekonnen, Z. Cao, and E. Tangdionga, "Ultra-High Capacity Indoor Optical Wireless Communication Using 2D-Steered Pencil Beams," *Journal of Lightwave Technology*, vol. 34, no. 20, pp. 4802–4809, Oct 2016.
- [9] T. Koonen, F. Gomez-Agis, Z. Cao, K. Mekonnen, F. Huijskens, and E. Tangdionga, "Indoor ultra-high capacity optical wireless communication using steerable infrared beams," in *2017 International Topical Meeting on Microwave Photonics (MWP)*, Oct 2017, pp. 1–4.
- [10] P. Lin, X. Hu, Y. Ruan, H. Li, J. Fang, Y. Zhong, H. Zheng, J. Fang, Z. L. Jiang, and Z. Chen, "Real-time visible light positioning supporting fast moving speed," *Opt. Express*, vol. 28, no. 10, pp. 14 503–14 510, May 2020. [Online]. Available: <http://www.opticsexpress.org/abstract.cfm?URI=oe-28-10-14503>
- [11] J. Xu, C. Gong, and Z. Xu, "Experimental indoor visible light positioning systems with centimeter accuracy based on a commercial smartphone camera," *IEEE Photonics Journal*, vol. 10, no. 6, pp. 1–17, 2018.
- [12] W. Guan, S. Chen, S. Wen, Z. Tan, H. Song, and W. Hou, "High-accuracy robot indoor localization scheme based on robot operating system using visible light positioning," *IEEE Photonics Journal*, vol. 12, no. 2, pp. 1–16, 2020.
- [13] N. Hassan, A. Naeem, M. Pasha, T. Jadoon, and C. Yuen, "Indoor Positioning Using Visible LED Lights: A Survey," *ACM Computing Surveys (CSUR)*, vol. 48, no. 2, pp. 1–32, 2015.
- [14] S. Ma, R. Yang, Y. He, S. Lu, F. Zhou, N. Al-Dhahir, and S. Li, "Achieving channel capacity of visible light communication," *IEEE Systems Journal*, vol. 15, no. 2, pp. 1652–1663, 2021.
- [15] Y. Zhuang, L. Hua, L. Qi, J. Yang, P. Cao, Y. Cao, Y. Wu, J. Thompson, and H. Haas, "A Survey of Positioning Systems Using Visible LED Lights," *IEEE Communications Surveys Tutorials*, vol. 20, no. 3, pp. 1963–1988, thirdquarter 2018.

- [16] S. Shao, A. Khreishah, and I. Khalil, "RETRO: Retroreflector Based Visible Light Indoor Localization for Real-time Tracking of IoT Devices," in *IEEE INFOCOM 2018 - IEEE Conference on Computer Communications*, April 2018, pp. 1025–1033.
- [17] K. Iga, "Surface-Emitting Laser-Its Birth and Generation of New Optoelectronics Field," *IEEE Journal of Selected Topics in Quantum Electronics*, vol. 6, no. 6, pp. 1201–1215, 2000.
- [18] A. Liu, P. Wolf, J. A. Lott, and D. Bimberg, "Vertical-Cavity Surface-Emitting Lasers for Data Communication and Sensing," *Photon. Res.*, vol. 7, no. 2, pp. 121–136, Feb 2019.
- [19] L. M. A. Plouzenec, L. J. Sargent, R. V. Penty, I. H. White, P. J. Heard, M. R. T. Tan, S. W. Corzine, and S.-Y. Wang, "Gaussian beam profile and single transverse mode emission from previously multimode gain-guided VCSEL using novel etch," in *Vertical-Cavity Surface-Emitting Lasers IV*, K. D. Choquette and C. Lei, Eds., vol. 3946, International Society for Optics and Photonics. SPIE, 2000, pp. 219 – 229. [Online]. Available: <https://doi.org/10.1117/12.384378>
- [20] M. C. Teich, *Beam Optics*. John Wiley and Sons, Ltd, 2001, ch. 3, pp. 80–107. [Online]. Available: <https://onlinelibrary.wiley.com/doi/abs/10.1002/0471213748.ch3>
- [21] C. Chen, D. Basnayaka, and H. Haas, "Downlink Performance of Optical Attocell Networks," *Journal of Lightwave Technology*, vol. 34, no. 1, pp. 137–156, Apr. 2016.
- [22] M. Dehghani Soltani, X. Wu, M. Safari, and H. Haas, "Bidirectional User Throughput Maximization Based on Feedback Reduction in LiFi Networks," *IEEE Transactions on Communications*, vol. 66, no. 7, pp. 3172–3186, July 2018.
- [23] S. Dimitrov and H. Haas, "Information Rate of OFDM-Based Optical Wireless Communication Systems With Nonlinear Distortion," *J. Lightwave Technol.*, vol. 31, no. 6, pp. 918–929, Mar 2013. [Online]. Available: <http://jlt.osa.org/abstract.cfm?URI=jlt-31-6-918>
- [24] "InGaAs APD: G8931 series," Hamamatsu, Hamamatsu, Jul. 2019.
- [25] G. P. Agrawal, *Lightwave technology: telecommunication systems*. John Wiley and Sons, 2005.
- [26] J. M. Kahn and J. R. Barry, "Wireless Infrared Communications," *Proceedings of the IEEE*, vol. 85, no. 2, pp. 265–298, 1997.
- [27] S. Shin, U. Sharma, H. Tu, W. Jung, and S. A. Boppart, "Characterization and Analysis of Relative Intensity Noise in Broadband Optical Sources for Optical Coherence Tomography," *IEEE Photonics Technology Letters*, vol. 22, no. 14, pp. 1057–1059, July 2010.
- [28] A. Lundvall, F. Nikolajeff, and T. Lindstrom, "High Performing Micromachined Retroreflector," *Opt. Express*, vol. 11, no. 20, pp. 2459–2473, Oct 2003. [Online]. Available: <http://www.opticsexpress.org/abstract.cfm?URI=oe-11-20-2459>
- [29] E. Khorov, A. Kiryanov, A. Lyakhov, and G. Bianchi, "A tutorial on ieee 802.11ax high efficiency wlans," *IEEE Communications Surveys Tutorials*, vol. 21, no. 1, pp. 197–216, 2019.
- [30] M. D. Higgins, R. J. Green, and M. S. Leeson, "A genetic algorithm method for optical wireless channel control," *Journal of Lightwave Technology*, vol. 27, no. 6, pp. 760–772, March 2009.
- [31] C. Chen, R. Bian, and H. Haas, "Omnidirectional Transmitter and Receiver Design for Wireless Infrared Uplink Transmission in LiFi," in *2018 IEEE International Conference on Communications Workshops (ICC Workshops)*, May 2018, pp. 1–6.
- [32] S. Zhang, P. Du, C. Chen, W. Zhong, and A. Alphones, "Robust 3D Indoor VLP System Based on ANN Using Hybrid RSS/PDOA," *IEEE Access*, vol. 7, pp. 47 769–47 780, 2019.
- [33] A. Papoulis and S. U. Pillai, *Probability, Random Variables, and Stochastic Processes*. McGraw-Hill, 2002.
- [34] P. P. Williamson, D. P. Mays, G. A. Asmerom, and Y. Yang, "Revisiting the Classical Occupancy Problem," *The American Statistician*, vol. 63, no. 4, pp. 356–360, 2009. [Online]. Available: <https://doi.org/10.1198/tast.2009.08104>
- [35] M. D. Soltani, A. A. Purwita, Z. Zeng, H. Haas, and M. Safari, "Modeling the Random Orientation of Mobile Devices: Measurement, Analysis and LiFi Use Case," *IEEE Transactions on Communications*, vol. 67, no. 3, pp. 2157–2172, March 2019.
- [36] C. Tsao *et al.*, "Link Duration of the Random Way Point Model in Mobile Ad Hoc Networks," in *IEEE Wireless Communications and Networking Conference (WCNC)*, vol. 1, Apr. 2006, pp. 367–371.
- [37] *BS EN 60825-1:2014 - Safety of laser products. Equipment classification and requirements*, 2014.
- [38] A. R. Henderson, *Laser Safety*. Bristol: Institute of Physics, 2003.



---

## Bibliography

---

- [1] Z. Zeng, M. Dehghani Soltani, M. Safari, and H. Haas, "Interference Mitigation using Optimized Angle Diversity Receiver in LiFi Cellular network," *Submitted to IEEE Transaction on Communications*, July. 2021.
- [2] H. Burchardt, S. Sinanovic, Z. Bharucha, and H. Haas, "Distributed and Autonomous Resource and Power Allocation for Wireless Networks," *IEEE Transactions on Communications*, vol. 61, no. 7, pp. 2758–2771, July 2013.
- [3] Z. Zeng, M. Dehghani Soltani, C. Chen, M. Safari, and H. Haas, "A VCSEL Array Transmission System with Novel Beam Activation Mechanisms," *Submitted to IEEE Transaction on Communications*, July. 2021.
- [4] D. C. O'Brien, "Visible Light Communications: Challenges and potential." IEEE, October 2011, pp. 365–366.
- [5] H. Haas, L. Yin, Y. Wang, and C. Chen, "What is LiFi?" *Journal of Lightwave Technology*, vol. 34, no. 6, pp. 1533–1544, 2016.
- [6] S. Wu, H. Wang, and C. H. Youn, "Visible Light Communications for 5G Wireless Networking Systems: from Fixed to Mobile Communications," *IEEE Network*, vol. 28, no. 6, pp. 41–45, Nov 2014.
- [7] M. S. Alouini and A. J. Goldsmith, "Area Spectral Efficiency of Cellular Mobile Radio Systems," *Vehicular Technology, IEEE Transactions on*, vol. 48, no. 4, pp. 1047–1066, 1999.
- [8] T. Borogovac, M. Rahaim, and J. B. Carruthers, "Spotlighting for Visible Light Communications and Illumination," in *2010 IEEE Globecom Workshops*, Dec 2010, pp. 1077–1081.
- [9] G. W. Marsh and J. M. Kahn, "Channel Reuse Strategies for Indoor Infrared Wireless Communications," *Communications, IEEE Transactions on*, vol. 45, no. 10, pp. 1280–1290, 1997.
- [10] K. Cui, J. Quan, and Z. Xu, "Performance of Indoor Optical Femtocell by Visible Light Communication," *Optics Communications*, vol. 298-299, pp. 59–66, 2013.
- [11] C. Chen, S. Videv, D. Tsonev, and H. Haas, "Fractional Frequency Reuse in DCO-OFDM-based Optical Attocell Networks," *Journal of Lightwave Technology*, vol. 33, no. 19, pp. 3986–4000, Oct. 2015.
- [12] C. Chen, D. Tsonev, and H. Haas, "Joint Transmission in Indoor Visible Light Communication Downlink Cellular Networks," in *2013 IEEE Globecom Workshops (GC Wkshps)*, Dec 2013, pp. 1127–1132.
- [13] Z. Chen, D. A. Basnayaka, and H. Haas, "Space Division Multiple Access for Optical Attocell Network Using Angle Diversity Transmitters," *Journal of Lightwave Technology*, vol. 35, no. 11, pp. 2118–2131, June 2017.
- [14] J. M. Kahn and J. R. Barry, "Wireless Infrared Communications," *Proceedings of the IEEE*, vol. 85, no. 2, pp. 265–298, 1997.
- [15] J. Carruthers and J. Kahn, "Angle Diversity for Nondirected Wireless Infrared Communication," in *ICC '98. 1998 IEEE International Conference on Communications. Conference Record. Affiliated with SUPERCOMM'98 (Cat. No.98CH36220)*, vol. 3, 1998, pp. 1665–1670 vol.3.

- [16] J. Carruther and J. Kahn, "Angle Diversity for Nondirected Wireless Infrared Communication," *IEEE Transactions on Communications*, vol. 48, no. 6, pp. 960–969, 2000.
- [17] G. Yun and M. Kavehrad, "Spot-diffusing and fly-eye receivers for indoor infrared wireless communications," in *1992 IEEE International Conference on Selected Topics in Wireless Communications*, 1992, pp. 262–265.
- [18] Z. Chen, D. Basnayaka, X. Wu, and H. Haas, "Interference Mitigation for Indoor Optical Attocell Networks using Angle Diversity Receiver," *Journal of Lightwave Technology*, pp. 1–1, 2018.
- [19] Z. Chen, N. Serafimovski, and H. Haas, "Angle Diversity for an Indoor Cellular Visible Light Communication System," in *2014 IEEE 79th Vehicular Technology Conference (VTC Spring)*, May 2014, pp. 1–5.
- [20] Z. Chen, D. Tsonev, and H. Haas, "A Novel Double-Source Cell Configuration for Indoor Optical Attocell Networks," in *2014 IEEE Global Communications Conference*, Dec 2014, pp. 2125–2130.
- [21] Z. Zeng, M. D. Soltani, M. Safari, and H. Haas, "Angle Diversity Receiver in LiFi Cellular Networks," in *ICC 2019 - 2019 IEEE International Conference on Communications (ICC)*, May 2019, pp. 1–6.
- [22] Z. Zeng, M. D. Soltani, X. Wu, and H. Haas, "Access Point Selection Scheme for LiFi Cellular Networks using Angle Diversity Receivers," in *2019 IEEE Wireless Communications and Networking Conference (WCNC)*, 2019, pp. 1–6.
- [23] A. Nuwanpriya, S. W. Ho, and C. S. Chen, "Indoor MIMO Visible Light Communications: Novel Angle Diversity Receivers for Mobile Users," *IEEE Journal on Selected Areas in Communications*, vol. 33, no. 9, pp. 1780–1792, Sept 2015.
- [24] C. Chen, W. D. Zhong, H. Yang, S. Zhang, and P. Du, "Reduction of SINR Fluctuation in Indoor Multi-Cell VLC Systems Using Optimized Angle Diversity Receiver," *Journal of Lightwave Technology*, pp. 1–1, 2018.
- [25] W. Wu, Q. Shen, M. Wang, and X. S. Shen, "Performance Analysis of IEEE 802.11.ad Downlink Hybrid Beamforming," in *2017 IEEE International Conference on Communications (ICC)*, May 2017, pp. 1–6.
- [26] Y. Wang, X. Wu, and H. Haas, "Distributed Load Balancing for Internet of Things by Using Li-Fi and RF Hybrid Network," in *IEEE 26th Annual International Symposium on Personal, Indoor, and Mobile Radio Communications (PIMRC)*, HongKong, China, Aug 2015, pp. 1289–1294.
- [27] Y. Wang and H. Haas, "Dynamic Load Balancing With Handover in Hybrid Li-Fi and Wi-Fi Networks," *Journal of Lightwave Technology*, vol. 33, no. 22, pp. 4671–4682, Nov 2015.
- [28] T. Koonen, F. Gomez-Agis, F. Huijskens, K. A. Mekonnen, Z. Cao, and E. Tangdionga, "High-Capacity Optical Wireless Communication Using Two-Dimensional IR Beam Steering," *Journal of Lightwave Technology*, vol. 36, no. 19, pp. 4486–4493, Oct 2018.
- [29] Z. Zeng, M. D. Soltani, H. Haas, and M. Safari, "Orientation Model of Mobile Device for Indoor VLC and Millimetre Wave Systems," in *IEEE Veh. Technol. Conf. (VTC Fall)*, Chicago, USA, August 2018.
- [30] Z. Zeng, M. Dehghani Soltani, Y. Wang, X. Wu, and H. Haas, "Realistic Indoor Hybrid WiFi and OFDMA-Based LiFi Networks," *IEEE Transactions on Communications*, vol. 68, no. 5, pp. 2978–2991, 2020.
- [31] Z. Ghassemlooy, W. Popoola, and S. Rajbhandari, *Optical Wireless Communications: System and Channel Modelling with Matlab*. CRC press, 2012.
- [32] F. R. Gfeller and U. Bapst, "Wireless in-house data communication via diffuse infrared radiation," *Proceedings of the IEEE*, vol. 67, no. 11, pp. 1474–1486, Nov 1979.

- [33] G. Marsh and J. Kahn, "Performance evaluation of experimental 50-Mb/s diffuse infrared wireless link using on-off keying with decision-feedback equalization," *IEEE Transactions on Communications*, vol. 44, no. 11, pp. 1496–1504, 1996.
- [34] R. Hou, Y. Chen, J. Wu, and H. Zhang, "A brief survey of optical wireless communication," in *Proc. Australas. Symp. Parallel Distrib. Comput. (AusPDC 15)*, vol. 163, 2015, pp. 41–50.
- [35] A. G. Bell, "Selenium and the Photophone," *Nature*, vol. 22, no. 569, pp. 500–503, Sep. 1880.
- [36] Y. Tanaka, S. Haruyama, and M. Nakagawa, "Wireless Optical Transmissions with White Colored LED for Wireless Home Links," in *11th IEEE International Symposium on Personal Indoor and Mobile Radio Communications. PIMRC 2000. Proceedings (Cat. No.00TH8525)*, vol. 2, London, UK, Sept 2000, pp. 1325–1329 vol.2.
- [37] T. Komine and M. Nakagawa, "Fundamental Analysis for Visible-Light Communication System Using LED Lights," *IEEE Transactions on Consumer Electronics*, vol. 50, no. 1, pp. 100–107, Feb 2004.
- [38] M. S. Islim, R. X. Ferreira, X. He, E. Xie, S. Videv, S. Viola, S. Watson, N. Bamiedakis, R. V. Penty, I. H. White, A. E. Kelly, E. Gu, H. Haas, and M. D. Dawson, "Towards 10 Gb/s Orthogonal Frequency Division Multiplexing-based Visible Light Communication Using a GaN Violet Micro-LED," *Photon. Res.*, vol. 5, no. 2, pp. A35–A43, Apr 2017.
- [39] R. Bian, I. Tavakkolnia, and H. Haas, "15.73 Gb/s Visible Light Communication With Off-the-Shelf LEDs," *J. Lightwave Technol.*, vol. 37, no. 10, pp. 2418–2424, May 2019. [Online]. Available: <http://jlt.osa.org/abstract.cfm?URI=jlt-37-10-2418>
- [40] H. Haas, "Wireless data from every light blub," *TEDGlobal TalkEdinburgh*, 2011.
- [41] M. Dehghani Soltani, X. Wu, M. Safari, and H. Haas, "Bidirectional User Throughput Maximization Based on Feedback Reduction in LiFi Networks," *IEEE Transactions on Communications*, vol. 66, no. 7, pp. 3172–3186, July 2018.
- [42] A. M. J. Koonen, C. W. Oh, and E. Tangdiongga, "Reconfigurable free-space optical indoor network using multiple pencil beam steering," in *2014 OptoElectronics and Communication Conference and Australian Conference on Optical Fibre Technology*, July 2014, pp. 204–206.
- [43] T. Koonen, J. Oh, K. Mekonnen, Z. Cao, and E. Tangdiongga, "Ultra-High Capacity Indoor Optical Wireless Communication Using 2D-Steered Pencil Beams," *Journal of Lightwave Technology*, vol. 34, no. 20, pp. 4802–4809, Oct 2016.
- [44] T. Koonen, F. Gomez-Agis, Z. Cao, K. Mekonnen, F. Huijskens, and E. Tangdiongga, "Indoor ultra-high capacity optical wireless communication using steerable infrared beams," in *2017 International Topical Meeting on Microwave Photonics (MWP)*, Oct 2017, pp. 1–4.
- [45] Y. Tanaka, T. Komine, S. Haruyama, and M. Nakagawa, "Indoor visible communication utilizing plural white LEDs as lighting," in *12th IEEE International Symposium on Personal, Indoor and Mobile Radio Communications. PIMRC 2001. Proceedings (Cat. No.01TH8598)*, vol. 2, 2001, pp. F–F.
- [46] M. Dyble, N. Narendran, A. Bierman, and T. Klein, "Impact of dimming white LEDs: chromaticity shifts due to different dimming methods," in *Fifth International Conference on Solid State Lighting*, I. T. Ferguson, J. C. Carrano, T. Taguchi, and I. E. Ashdown, Eds., vol. 5941, International Society for Optics and Photonics. SPIE, 2005, pp. 291 – 299. [Online]. Available: <https://doi.org/10.1117/12.625924>
- [47] K.-D. Langer, J. Vucic, C. Kottke, L. F. del Rosal, S. Nerreter, and J. Walewski, "Advances and prospects in high-speed information broadcast using phosphorescent white-light LEDs," in *2009 11th International Conference on Transparent Optical Networks*, 2009, pp. 1–6.

- [48] M. D. Soltani, Z. Zeng, H. Kazemi, C. Chen, H. Haas, and M. Safari, "A Study of Sojourn Time for Indoor LiFi Cellular Networks," in *2019 IEEE 30th Annual International Symposium on Personal, Indoor and Mobile Radio Communications (PIMRC)*, 2019, pp. 1–6.
- [49] D. Tsonev, H. Chun, S. Rajbhandari, J. McKendry, S. Videv, E. Gu, M. Haji, S. Watson, A. Kelly, G. Faulkner, M. Dawson, H. Haas, and D. O'Brien, "A 3-Gb/s Single-LED OFDM-Based Wireless VLC Link Using a Gallium Nitride uLED," *IEEE Photonics Technology Letters*, vol. 26, no. 7, pp. 637–640, Apr. 2014.
- [50] J. J. D. McKendry, D. Massoubre, S. Zhang, B. R. Rae, R. P. Green, E. Gu, R. K. Henderson, A. E. Kelly, and M. D. Dawson, "Visible-Light Communications Using a CMOS-Controlled Micro-Light-Emitting-Diode Array," *Journal of Lightwave Technology*, vol. 30, no. 1, pp. 61–67, 2012.
- [51] A. Neumann, J. J. Wierer, W. Davis, Y. Ohno, S. R. J. Brueck, and J. Tsao, "Four-color Laser White Illuminant Demonstrating High Color-rendering Quality," *Opt. Express*, vol. 19, no. S4, pp. A982–A990, Jul 2011. [Online]. Available: <http://www.opticsexpress.org/abstract.cfm?URI=oe-19-104-A982>
- [52] K. Iga, "Surface-Emitting Laser-Its Birth and Generation of New Optoelectronics Field," *IEEE Journal of Selected Topics in Quantum Electronics*, vol. 6, no. 6, pp. 1201–1215, 2000.
- [53] A. Liu, P. Wolf, J. A. Lott, and D. Bimberg, "Vertical-Cavity Surface-Emitting Lasers for Data Communication and Sensing," *Photon. Res.*, vol. 7, no. 2, pp. 121–136, Feb 2019.
- [54] L. M. A. Plouzenec, L. J. Sargent, R. V. Penty, I. H. White, P. J. Heard, M. R. T. Tan, S. W. Corzine, and S.-Y. Wang, "Gaussian Beam Profile and Single Transverse Mode Emission from Previously Multimode Gain-guided VCSEL using Novel Etch," in *Vertical-Cavity Surface-Emitting Lasers IV*, K. D. Choquette and C. Lei, Eds., vol. 3946, International Society for Optics and Photonics. SPIE, 2000, pp. 219 – 229. [Online]. Available: <https://doi.org/10.1117/12.384378>
- [55] M. D. Soltani, E. Sarbazi, N. Bamiedakis, P. de Souza, H. Kazemi, J. M. Elmirghani, I. H. White, R. V. Penty, H. Haas, and M. Safari, "Safety Analysis for Laser-based Optical Wireless Communications: A Tutorial," *arXiv preprint arXiv:2102.08707*, 2021.
- [56] H. Kazemi, E. Sarbazi, M. D. Soltani, M. Safari, and H. Haas, "A Tb/s Indoor Optical Wireless Backhaul System Using VCSEL Arrays," in *2020 IEEE 31st Annual International Symposium on Personal, Indoor and Mobile Radio Communications*, 2020, pp. 1–6.
- [57] M. C. Teich, *Beam Optics*. John Wiley and Sons, Ltd, 2001, ch. 3, pp. 80–107. [Online]. Available: <https://onlinelibrary.wiley.com/doi/abs/10.1002/0471213748.ch3>
- [58] H. Elgala, R. Mesleh, and H. Haas, "Indoor Optical Wireless Communication: Potential and State-of-the-Art," *IEEE Communications Magazine*, vol. 49, no. 9, pp. 56–62, September 2011.
- [59] S. Schmid, G. Corbellini, S. Mangold, and T. R. Gross, "An LED-to-LED Visible Light Communication System with Software-Based Synchronization," in *2012 IEEE Globecom Workshops*, Dec 2012, pp. 1264–1268.
- [60] J. Liu, W. Noonpakdee, H. Takano, and S. Shimamoto, "Foundational Analysis of Spatial Optical Wireless Communication Utilizing Image Sensor," in *2011 IEEE International Conference on Imaging Systems and Techniques*, May 2011, pp. 205–209.
- [61] P. Djahani and J. M. Kahn, "Analysis of Infrared Wireless Links Employing Multibeam Transmitters and Imaging Diversity Receivers," *IEEE Transactions on Communications*, vol. 48, no. 12, pp. 2077–2088, Dec 2000.
- [62] Z. Wang, D. Tsonev, S. Videv, and H. Haas, "On the Design of a Solar-Panel Receiver for Optical Wireless Communications With Simultaneous Energy Harvesting," *IEEE Journal on Selected Areas in Communications*, vol. 33, no. 8, pp. 1612–1623, Aug 2015.

- [63] Y. Li, M. Safari, R. Henderson, and H. Haas, "Optical OFDM With Single-Photon Avalanche Diode," *IEEE Photonics Technology Letters*, vol. 27, no. 9, pp. 943–946, 2015.
- [64] N. A. W. Dutton, I. Gyongy, L. Parmesan, S. Gneccchi, N. Calder, B. R. Rae, S. Pellegrini, L. A. Grant, and R. K. Henderson, "A SPAD-Based QVGA Image Sensor for Single-Photon Counting and Quanta Imaging," *IEEE Transactions on Electron Devices*, vol. 63, no. 1, pp. 189–196, 2016.
- [65] S. Cova, M. Ghioni, A. Lacaita, C. Samori, and F. Zappa, "Avalanche photodiodes and quenching circuits for single-photon detection," *Appl. Opt.*, vol. 35, no. 12, pp. 1956–1976, Apr 1996. [Online]. Available: <http://ao.osa.org/abstract.cfm?URI=ao-35-12-1956>
- [66] G. P. Agrawal, *Lightwave Technology: Telecommunication Systems*. John Wiley and Sons, 2005.
- [67] S. Shin, U. Sharma, H. Tu, W. Jung, and S. A. Boppart, "Characterization and Analysis of Relative Intensity Noise in Broadband Optical Sources for Optical Coherence Tomography," *IEEE Photonics Technology Letters*, vol. 22, no. 14, pp. 1057–1059, July 2010.
- [68] D. Lubin Zeng, G. Brien, G. Hoa Minh, G. Faulkner, G. Kyungwoo Lee, G. Daekwang Jung, G. Yunje Oh, and G. Eun Tae Won, "High Data Rate Multiple Input Multiple Output (MIMO) Optical Wireless Communications using White Led Lighting," *Selected Areas in Communications, IEEE Journal on*, vol. 27, no. 9, 2009.
- [69] S. B. Alexander, *Optical Communication Receiver Design*. IET, 1997, no. 37.
- [70] A. M. Khalid, G. Cossu, R. Corsini, P. Choudhury, and E. Ciaramella, "1-Gb/s Transmission Over a Phosphorescent White LED by Using Rate-Adaptive Discrete Multitone Modulation," *IEEE Photonics Journal*, vol. 4, no. 5, pp. 1465–1473, Oct 2012.
- [71] D. Tsonev, H. Chun, S. Rajbhandari, J. J. D. McKendry, S. Videv, E. Gu, M. Haji, S. Watson, A. E. Kelly, G. Faulkner, M. D. Dawson, H. Haas, and D. O'Brien, "A 3-Gb/s Single-LED OFDM-Based Wireless VLC Link Using a Gallium Nitride  $\mu$ LED," *IEEE Photonics Technology Letters*, vol. 26, no. 7, pp. 637–640, April 2014.
- [72] S. Dimitrov and H. Haas, "Optimum Signal Shaping in OFDM-Based Optical Wireless Communication Systems," in *Vehicular Technology Conference (VTC Fall), 2012 IEEE*, Sept 2012, pp. 1–5.
- [73] C. Chen *et al.*, "Downlink Performance of Optical Attocell Networks," *Journal of Lightwave Technology*, vol. 34, no. 1, pp. 137–156, Jan 2016.
- [74] G. Miao, J. Zander, K. W. Sung, and S. Ben Slimane, *Fundamentals of Mobile Data Networks*. Cambridge: Cambridge University Press, 2016.
- [75] H. Schulze, "Frequency-Domain Simulation of the Indoor Wireless Optical Communication Channel," *IEEE Transactions on Communications*, vol. 64, no. 6, pp. 2551–2562, June 2016.
- [76] L. Wu, Z. Zhang, J. Dang, and H. Liu, "Adaptive Modulation Schemes for Visible Light Communications," *Journal of Lightwave Technology*, vol. 33, no. 1, pp. 117–125, Jan. 2015.
- [77] H. L. Minh, D. O'Brien, G. Faulkner, L. Zeng, K. Lee, D. Jung, Y. Oh, and E. T. Won, "100-Mb/s NRZ Visible Light Communications Using a Postequalized White LED," *IEEE Photonics Technology Letters*, vol. 21, no. 15, pp. 1063–1065, Aug 2009.
- [78] Y. Wang, X. Wu, and H. Haas, "Resource Allocation in LiFi OFDMA Systems," in *GLOBECOM 2017 - 2017 IEEE Global Communications Conference*, Dec 2017, pp. 1–6.
- [79] H. S. Dhillon, R. K. Ganti, F. Baccelli, and J. G. Andrews, "Modeling and Analysis of K-Tier Downlink Heterogeneous Cellular Networks," *IEEE Journal on Selected Areas in Communications*, vol. 30, no. 3, pp. 550–560, 2012.
- [80] S. Sesia, I. Toufik, and M. Baker, "LTE-The UMTS Long Term Evolution: From Theory to Practice," A John Wiley and Sons, Ltd, Publication, 2009.



- [81] P. Yang, Y. Xiao, Y. Yu, L. Li, Q. Tang, and S. Li, "Simplified Adaptive Spatial Modulation for Limited-Feedback MIMO Systems," *IEEE Transactions on Vehicular Technology*, vol. 62, no. 6, pp. 2656–2666, 2013.
- [82] G. Bianchi, "Performance analysis of the IEEE 802.11 distributed coordination function," *IEEE Journal on Selected Areas in Communications*, vol. 18, no. 3, pp. 535–547, March 2000.
- [83] M. D. Soltani, A. A. Purwita, Z. Zeng, H. Haas, and M. Safari, "Modeling the Random Orientation of Mobile Devices: Measurement, Analysis and LiFi Use Case," *IEEE Transactions on Communications*, vol. 67, no. 3, pp. 2157–2172, March 2019.
- [84] S. M. LaValle, *Planning Algorithms*. Cambridge: Cambridge : Cambridge University Press, 2006.
- [85] F. Bai and A. Helmy, "A Survey of Mobility Models," *Wireless Adhoc Networks. University of Southern California, USA*, vol. 206, p. 147, 2004.
- [86] J. Broch, D. A. Maltz, D. B. Johnson, Y.-C. Hu, and J. Jetcheva, "A Performance Comparison of Multi-hop Wireless Ad Hoc Network Routing Protocols," in *Proceedings of the 4th Annual ACM/IEEE International Conference on Mobile Computing and Networking*, ser. MobiCom '98. New York, NY, USA: ACM, 1998, pp. 85–97.
- [87] M. Dehghani Soltani, A. A. Purwita, Z. Zeng, C. Chen, H. Haas, and M. Safari, "An Orientation-Based Random Waypoint Model for User Mobility in Wireless Networks," in *2020 IEEE International Conference on Communications Workshops (ICC Workshops)*, 2020, pp. 1–6.
- [88] M. Dehghani Soltani, "Analysis of random orientation and user mobility in LiFi networks," 2019.
- [89] M. D. Soltani, M. A. Arfaoui, I. Tavakkolnia, A. Ghayeb, M. Safari, C. Assi, M. Hasna, and H. Haas, "Bidirectional Optical Spatial Modulation for Mobile Users: Toward a Practical Design for LiFi Systems," *IEEE Journal on Selected Areas in Communications*, vol. 37, no. 9, pp. 2069–2086, Sep. 2019.
- [90] A. A. Purwita, M. D. Soltani, M. Safari, and H. Haas, "Terminal Orientation in OFDM-based LiFi Systems," *IEEE Transactions on Wireless Communications*, vol. 18, no. 8, pp. 4003–4016, Aug. 2019.
- [91] S. Dimitrov and H. Haas, "Information Rate of OFDM-Based Optical Wireless Communication Systems With Nonlinear Distortion," *J. Lightwave Technol.*, vol. 31, no. 6, pp. 918–929, Mar 2013. [Online]. Available: <http://jlt.osa.org/abstract.cfm?URI=jlt-31-6-918>
- [92] X. Wu, M. D. Soltani, L. Zhou, M. Safari, and H. Haas, "Hybrid LiFi and WiFi Networks: A Survey," *IEEE Communications Surveys Tutorials*, vol. 23, no. 2, pp. 1398–1420, 2021.
- [93] M. B. Rahaim, A. M. Vegni, and T. D. C. Little, "A Hybrid Radio Frequency and Broadcast Visible Light Communication System," in *IEEE Global Communications Conference Workshop (GLOBECOMW)*, Dec. 2011, pp. 792–796.
- [94] S. Shao, A. Khreishah, M. B. Rahaim, H. Elgala, M. Ayyash, T. D. C. Little, and J. Wu, "An Indoor Hybrid WiFi-VLC Internet Access System," in *IEEE International Conference on Mobile Ad Hoc and Sensor Systems (MASS)*, Oct. 2014, pp. 569–574.
- [95] X. Li, R. Zhang, and L. Hanzo, "Cooperative Load Balancing in Hybrid Visible Light Communications and WiFi," *IEEE Transactions on Communications*, vol. 63, no. 4, pp. 1319–1329, April 2015.
- [96] F. Jin, R. Zhang, and L. Hanzo, "Resource Allocation under Delay-Guarantee Constraints for Heterogeneous Visible-Light and RF Femtocells," *IEEE Transactions on Wireless Communications*, vol. 14, no. 2, pp. 1020 – 1034, Feb. 2014.

- [97] D. Basnayaka and H. Haas, "Hybrid RF and VLC Systems: Improving User Data Rate Performance of VLC Systems," in *IEEE 81st Vehicular Technology Conference (VTC Spring)*, Glasgow, UK, May 2015, pp. 1–5.
- [98] M. D. Soltani, A. A. Purwita, I. Tavakkolnia, H. Haas, and M. Safari, "Impact of Device Orientation on Error Performance of LiFi Systems," *IEEE Access*, vol. 7, pp. 41 690–41 701, 2019.
- [99] M. Bennis, S. Guruacharya, and D. Niyato, "Distributed Learning Strategies for Interference Mitigation in Femtocell Networks," in *IEEE Global Telecommunications Conference (GLOBECOM)*, Houston, USA, Dec. 2011, pp. 1–5.
- [100] P. Semasinghe, E. Hossain, and K. Zhu, "An Evolutionary Game for Distributed Resource Allocation in Self-Organizing Small Cells," *IEEE Transactions on Mobile Computing*, vol. 14, no. 2, pp. 274–287, Feb. 2015.
- [101] Y. Wang, X. Wu, and H. Haas, "Load Balancing Game With Shadowing Effect for Indoor Hybrid LiFi/RF Networks," *IEEE Transactions on Wireless Communications*, vol. 16, no. 4, pp. 2366–2378, April 2017.
- [102] X. Wu, M. Safari, and H. Haas, "Joint Optimisation of Load Balancing and Handover for Hybrid LiFi and WiFi Networks," in *IEEE Wireless Communications and Networking Conference (WCNC)*, March 2017, pp. 1–5.
- [103] F. Seguel, I. Soto, D. Iturralde, P. Adasme, and B. Nuez, "Enhancement of the QoS in an OFDMA VLC System," in *International Symposium on Communication Systems, Networks and Digital Signal Processing (CSNDSP)*, July 2016, pp. 1–5.
- [104] J. Fakidis, D. Tsonev, and H. Haas, "A Comparison between DCO-OFDMA and Synchronous One Dimensional OCDMA for Optical Wireless Communications," in *IEEE International Symposium on Personal, Indoor, and Mobile Radio Communications (PIMRC)*, Sept 2013, pp. 3605–3609.
- [105] G. Cossu, R. Corsini, and E. Ciaramella, "High-Speed Bi-directional Optical Wireless System in Non-Directed Line-of-Sight Configuration," *J. Lightwave Technol.*, vol. 32, no. 10, pp. 2035–2040, May 2014. [Online]. Available: <http://jlt.osa.org/abstract.cfm?URI=jlt-32-10-2035>
- [106] C. Chen, R. Bian, and H. Haas, "Omnidirectional Transmitter and Receiver Design for Wireless Infrared Uplink Transmission in LiFi," in *2018 IEEE International Conference on Communications Workshops (ICC Workshops)*, May 2018, pp. 1–6.
- [107] M. A. Dastgheib, H. Beyranvand, J. A. Salehi, and M. Maier, "Mobility-Aware Resource Allocation in VLC Networks Using T-Step Look-Ahead Policy," *Journal of Lightwave Technology*, vol. 36, no. 23, pp. 5358–5370, Dec 2018.
- [108] L. Li, Y. Zhang, B. Fan, and H. Tian, "Mobility-Aware Load Balancing Scheme in Hybrid VLC-LTE Networks," *IEEE Communications Letters*, vol. 20, no. 11, pp. 2276–2279, Nov 2016.
- [109] R. Wang, J. Zhang, S. H. Song, and K. B. Letaief, "Mobility-Aware Caching in D2D Networks," *IEEE Transactions on Wireless Communications*, vol. 16, no. 8, pp. 5001–5015, Aug 2017.
- [110] J. Chen, I. Tavakkolnia, C. Chen, Z. Wang, and H. Haas, "The Movement-Rotation (MR) Correlation Function and Coherence Distance of VLC Channels," *Journal of Lightwave Technology*, vol. 38, no. 24, pp. 6759–6770, 2020.
- [111] H. Elgala and T. D. C. Little, "SEE-OFDM: Spectral and Energy Efficient OFDM for Optical IM/DD Systems," in *2014 IEEE 25th Annual International Symposium on Personal, Indoor, and Mobile Radio Communication (PIMRC)*, Sep. 2014, pp. 851–855.
- [112] D. Tsonev, S. Videv, and H. Haas, "Unlocking Spectral Efficiency in Intensity Modulation and Direct Detection Systems," *IEEE Journal on Selected Areas in Communications*, vol. 33, no. 9, pp. 1758–1770, Sep. 2015.

- [113] S. W. Kim, B.-S. Kim, and Y. Fang, "Downlink and Uplink Resource Allocation in IEEE 802.11 Wireless LANs," *IEEE Transactions on Vehicular Technology*, vol. 54, no. 1, pp. 320–327, Jan 2005.
- [114] Y. Wang, D. A. Basnayaka, X. Wu, and H. Haas, "Optimization of Load Balancing in Hybrid LiFi/RF Networks," *IEEE Transactions on Communications*, vol. 65, no. 4, pp. 1708–1720, April 2017.
- [115] M. Kassab, J. M. Bonnin, and A. Belghith, "Fast and Secure Handover in WLANs: An Evaluation of the Signaling Overhead," in *2008 5th IEEE Consumer Communications and Networking Conference*, Jan 2008, pp. 770–775.
- [116] M. D. Soltani, X. Wu, M. Safari, and H. Haas, "On Limited Feedback Resource Allocation for Visible Light Communication Networks," in *Proceedings of the 2nd Int. Workshop on Visible Light Communications Systems*. Paris, France: ACM, 2015, pp. 27–32.
- [117] D. J. Love, R. W. Heath, V. K. N. Lau, D. Gesbert, B. D. Rao, and M. Andrews, "An Overview of Limited Feedback in Wireless Communication Systems," *IEEE Journal on Selected Areas in Communications*, vol. 26, no. 8, pp. 1341–1365, October 2008.
- [118] Q. Ye, B. Rong, Y. Chen, M. Al-Shalash, C. Caramanis, and J. Andrews, "User Association for Load Balancing in Heterogeneous Cellular Networks," *IEEE Transactions on Wireless Communications*, vol. 12, no. 6, pp. 2706–2716, June 2013.
- [119] J. Mo and J. Walrand, "Fair End-to-End Window-Based Congestion Control," *IEEE/ACM Transactions on Networking*, vol. 8, no. 5, pp. 556–567, Oct. 2000.
- [120] P. Lin, X. Hu, Y. Ruan, H. Li, J. Fang, Y. Zhong, H. Zheng, J. Fang, Z. L. Jiang, and Z. Chen, "Real-time visible light positioning supporting fast moving speed," *Opt. Express*, vol. 28, no. 10, pp. 14 503–14 510, May 2020. [Online]. Available: <http://www.opticsexpress.org/abstract.cfm?URI=oe-28-10-14503>
- [121] J. Xu, C. Gong, and Z. Xu, "Experimental Indoor Visible Light Positioning Systems With Centimeter Accuracy Based on a Commercial Smartphone Camera," *IEEE Photonics Journal*, vol. 10, no. 6, pp. 1–17, 2018.
- [122] W. Guan, S. Chen, S. Wen, Z. Tan, H. Song, and W. Hou, "High-Accuracy Robot Indoor Localization Scheme Based on Robot Operating System Using Visible Light Positioning," *IEEE Photonics Journal*, vol. 12, no. 2, pp. 1–16, 2020.
- [123] N. Hassan, A. Naeem, M. Pasha, T. Jadoon, and C. Yuen, "Indoor Positioning Using Visible LED Lights: A Survey," *ACM Computing Surveys (CSUR)*, vol. 48, no. 2, pp. 1–32, 2015.
- [124] Y. Zhuang, L. Hua, L. Qi, J. Yang, P. Cao, Y. Cao, Y. Wu, J. Thompson, and H. Haas, "A Survey of Positioning Systems Using Visible LED Lights," *IEEE Communications Surveys Tutorials*, vol. 20, no. 3, pp. 1963–1988, thirdquarter 2018.
- [125] S. Shao, A. Khreishah, and I. Khalil, "RETRO: Retroreflector Based Visible Light Indoor Localization for Real-time Tracking of IoT Devices," in *IEEE INFOCOM 2018 - IEEE Conference on Computer Communications*, April 2018, pp. 1025–1033.
- [126] "InGaAs APD: G8931 Series," Hamamatsu, Hamamatsu, Jul. 2019.
- [127] A. Lundvall, F. Nikolajeff, and T. Lindstrom, "High Performing Micromachined Retroreflector," *Opt. Express*, vol. 11, no. 20, pp. 2459–2473, Oct 2003. [Online]. Available: <http://www.opticsexpress.org/abstract.cfm?URI=oe-11-20-2459>
- [128] E. Khorov, A. Kiryanov, A. Lyakhov, and G. Bianchi, "A Tutorial on IEEE 802.11ax High Efficiency WLANs," *IEEE Communications Surveys Tutorials*, vol. 21, no. 1, pp. 197–216, 2019.
- [129] M. D. Higgins, R. J. Green, and M. S. Leeson, "A Genetic Algorithm Method for Optical Wireless Channel Control," *Journal of Lightwave Technology*, vol. 27, no. 6, pp. 760–772, March 2009.

- [130] S. Zhang, P. Du, C. Chen, W. Zhong, and A. Alphones, “Robust 3D Indoor VLP System Based on ANN Using Hybrid RSS/PDOA,” *IEEE Access*, vol. 7, pp. 47 769–47 780, 2019.
- [131] A. Papoulis and S. U. Pillai, *Probability, Random Variables, and Stochastic Processes*. McGraw-Hill, 2002.
- [132] P. P. Williamson, D. P. Mays, G. A. Asmerom, and Y. Yang, “Revisiting the Classical Occupancy Problem,” *The American Statistician*, vol. 63, no. 4, pp. 356–360, 2009. [Online]. Available: <https://doi.org/10.1198/tast.2009.08104>
- [133] C. Tsao *et al.*, “Link Duration of the Random Way Point Model in Mobile Ad Hoc Networks,” in *IEEE Wireless Communications and Networking Conference (WCNC)*, vol. 1, Apr. 2006, pp. 367–371.
- [134] C. Song, Z. Qu, N. Blumm, and A.-L. Barabási, “Limits of Predictability in Human Mobility,” *Science*, vol. 327, no. 5968, pp. 1018–1021, 2010. [Online]. Available: <https://science.sciencemag.org/content/327/5968/1018>
- [135] *BS EN 60825-1:2014 - Safety of laser products. Equipment classification and requirements*, 2014.
- [136] A. R. Henderson, *Laser Safety*. Bristol: Institute of Physics, 2003.